

Quantum coherent control of laser-kicked molecular rotors

by

Martin Bitter

B.Sc., Technische Universität Darmstadt, 2008

M.Sc., Technische Universität Darmstadt, 2010

A THESIS SUBMITTED IN PARTIAL FULFILLMENT OF
THE REQUIREMENTS FOR THE DEGREE OF

DOCTOR OF PHILOSOPHY

in

The Faculty of Graduate and Postdoctoral Studies

(Physics)

THE UNIVERSITY OF BRITISH COLUMBIA

(Vancouver)

October 2016

© Martin Bitter 2016

Abstract

The objective of this dissertation is the experimental study and control of laser-kicked molecular rotors. Nonresonant rotational Raman excitation of linear molecules by periodic sequences of ultra-short laser pulses allows for the realization of a paradigm system - the periodically kicked rotor. This apparently simple physical system has drawn much interest within the last decades, especially due to its role in the field of quantum chaos.

This thesis presents an experimental apparatus capable of producing long sequences of high-energy femtosecond pulses. Rotation of diatomic molecules, the most basic version of quantum rotors, is investigated under multi-pulse excitation. In the case of periodic kicking, the wave function of the quantum rotor dynamically localizes in the angular momentum space, similarly to Anderson localization of the electronic wave function in disordered solids. We present the first direct observation of dynamical localization in a system of true rotors. The suppressed growth of rotational energy is demonstrated, as well as the noise-induced recovery of diffusion, indicative of classical dynamics. We examine other distinct features of the quantum kicked rotor and report on quantum resonances, the phenomena of rotational Bloch oscillations and Rabi oscillations. In addition, multi-pulse excitation is investigated in the context of creating broad rotational wave packets.

Another goal of the reported study is the coherent control of quantum chaos. We demonstrate that the relative phases in a superposition of rotational states can be used to control the process of dynamical localization. We specify the sensitivity to external parameters and illustrate the loss of control in the classical limit of laser-molecule interaction.

Our work advances the general understanding of the dynamics of laser kicked molecules and complements previous studies of the quantum kicked rotor in a system of cold atoms. The results encourage further studies, e.g. of quantum phenomena which are unique to true rotors. The possibility of control in classically chaotic systems has far reaching implications for the ultimate prospect of using coherence to control chemical reactions.

Preface

All the work presented in this thesis was conducted in “The Laboratory for Advanced Spectroscopy and Imaging Research” (LASIR) at the University of British Columbia, Vancouver, Canada. I designed and constructed the apparatus with help of Kamil Krawczyk, Andrej Machnev and Jonathan Morrison. All the data taking and analysis of the results was done by me. For the theoretical analysis of the δ -kicked rotor I used a *Matlab* program. The core of the code, the interaction of a single kick with a diatomic molecule, was written by Johannes Floß. I adapted the program for multiple kicks. All the simulations in this thesis were done by me.

The methods to create long sequences of high-energy femtosecond pulses are described in chapter 3. The main ideas are published in Applied Optics [M. Bitter, V. Milner, “Generating long sequences of high-intensity femtosecond pulses”, Appl. Opt. **55**, 830 (2016)] [23]. A version of Sec. 5.4 including all the figures has been published in Physical Review A [M. Bitter, V. Milner, “Rotational excitation of molecules with long sequences of intense femtosecond pulses”, Phys. Rev. A **93**, 013420 (2016)] [24]. The key results of chapter 6, described in Sec. 6.4, have been published in Physical Review Letters [M. Bitter, V. Milner, “Experimental Observation of Dynamical Localization in Laser-Kicked Molecular Rotors”, Phys. Rev. Lett. **117**, 144104 (2016)] [22]. Further investigations on the same topic, discussed in Sec. 6.4.4, are presented in a follow-up manuscript [M. Bitter, V. Milner, “Control of quantum localization and classical diffusion in laser-kicked molecular rotors”] [20], which has been submitted for publication. Chapter 7 is heavily based on a manuscript [M. Bitter, V. Milner, “Experimental demonstration of coherent control in quantum chaotic systems”] [21], which has been submitted for publication.

The work on Bloch oscillations in Sec. 5.3 and 6.5, and the results on Rabi oscillations in Sec. 5.2 are currently being prepared for two separate manuscripts, to be submitted shortly.

Table of Contents

Abstract	ii
Preface	iii
Table of Contents	iv
List of Tables	viii
List of Figures	ix
List of Abbreviations	xii
1 Introduction	1
1.1 Main research objectives	4
1.2 Outline of the thesis	6
2 The kicked rotor	8
2.1 Classical kicked rotor	9
2.1.1 The standard map	10
2.1.2 Classical diffusion	11
2.2 Quantum kicked rotor	11
2.2.1 Quantum resonance	12
2.2.2 Dynamical localization	12
2.2.3 Stochasticity	13
2.2.4 Atom-optics kicked rotor	13
2.3 Laser-kicked molecular rotor	14
2.3.1 Light-molecule interaction	14
2.3.2 Kick strength	17
2.3.3 Hamiltonian	17
2.3.4 Wave function	18
2.3.5 Density matrix	18
2.3.6 Numerical analysis	20

Table of Contents

2.3.7	Revival time	23
2.3.8	Resonance map	23
2.3.9	Choice of molecule	26
2.4	Correspondence to crystalline solids	26
2.4.1	The one-dimensional lattice	27
2.4.2	Bloch's theorem	28
2.4.3	Floquet's theorem	29
2.4.4	Tight-binding model	30
2.4.5	Anderson model	32
2.4.6	Mapping the kicked-rotor onto the Anderson model	34
2.4.7	Anderson model of the laser kicked rotor	37
3	Techniques I: Generation of pulse sequences	40
3.1	Laser pulses and pulse sequences	42
3.1.1	Transform-limited pulse	42
3.1.2	Linearly-chirped pulse	44
3.1.3	Pulse sequences	45
3.2	Laser source	50
3.2.1	Pulse characterization	51
3.3	Pulse shaping I: The pulse shaper	53
3.3.1	Optical setup	54
3.3.2	Implementation of pulse sequences	55
3.3.3	Demonstration of pulse sequences	58
3.4	Pulse shaping II: The Michelson interferometer	58
3.5	Multi-pass amplification	60
3.5.1	Compressed versus chirped amplification	62
3.5.2	Amplification of pulse sequences	64
3.5.3	Demonstration of amplified pulse sequences	67
4	Techniques II: Rotational Raman spectroscopy	69
4.1	Raman spectroscopy	69
4.1.1	Raman spectrogram	72
4.2	Molecular beam source	75
4.2.1	Theory of supersonic expansion	75
4.2.2	Beam setup	77
4.2.3	Beam characterization	80
5	Resonant excitation of molecular rotation	86
5.1	Demonstration of the resonance map	87
5.1.1	Excitation of single coherences	89

Table of Contents

5.2	Rabi oscillations in molecular rotation	92
5.2.1	Theory and simulation	93
5.2.2	Experiment	99
5.2.3	Observation of Rabi oscillations	100
5.2.4	Kick strength calibration	107
5.3	Bloch oscillations in molecular rotation	107
5.3.1	Theory I: Bloch oscillations in crystalline solids . . .	109
5.3.2	Theory II: Bloch oscillations in a molecular rotor . .	110
5.3.3	Numerical simulation	112
5.3.4	Experiment	113
5.3.5	Observation of Bloch oscillations	115
5.4	Generation of broad rotational wave packets	121
5.4.1	Periodic excitation	122
5.4.2	Non-periodic excitation	125
5.4.3	Propagation effects	129
5.5	Conclusion	133
6	Dynamical localization in molecular rotation	135
6.1	Experiments on Anderson localization	136
6.2	Theory	137
6.3	Experiment	138
6.3.1	Calibration of experimental parameters	139
6.3.2	Population retrieval from the experiment	140
6.4	Observation of dynamical localization	141
6.4.1	Dependence on the number of kicks	145
6.4.2	Dependence on the kick strength	147
6.4.3	Rotational energy	148
6.4.4	Dependence on the period	148
6.5	Transition from Bloch oscillations to dynamical localization .	153
6.5.1	Anderson wall	153
6.5.2	Evolution of angular momentum	157
6.5.3	Evolution of rotational energy	161
6.6	Conclusion	162
7	Coherent control of quantum chaos	164
7.1	Theory	165
7.1.1	Coherent control	165
7.1.2	Quantum-to-classical transition	165
7.2	Experiment	166
7.3	Demonstration of coherent control in quantum chaotic system	169

Table of Contents

7.3.1	Robustness of control	171
7.3.2	Quantum-to-classical transition	172
7.4	Conclusion	173
8	Outlook	175
	Bibliography	178
 Appendices		
A	List of Publications	196
B	Classical dynamics of the kicked rotor	198
	B.1 Equations of motion	198
C	Spectral decomposition of the kicked rotor wave function	200
	C.1 The kicked rotor	200
	C.2 The periodically kicked rotor	201
	C.2.1 The wave function ψ^+	201
	C.2.2 Decomposition of ψ^+	201
	C.2.3 The coupling matrix	202
D	Fourier transform of shaped pulses	204
	D.1 Fourier transform of a TL pulse	204
	D.2 Fourier transform of a chirped pulse	205
	D.3 Fourier transform of a pulse train	206
	D.4 Convolution theorem	208
E	Semi-classical model of rotational Bloch oscillations	209
	E.1 Non-rigid rotor on quantum resonance	210
	E.2 Rigid rotor detuned from quantum resonance	210

List of Tables

2.1	Molecular constants and parameters for N ₂ and O ₂	26
2.2	Anderson localization versus dynamical localization	39

List of Figures

2.1	Standard map of the classical kicked rotor.	10
2.2	Illustration of a diatomic molecule in a laser field.	14
2.3	Field-free alignment of linear molecules.	15
2.4	Rotational Raman transitions in linear molecules.	16
2.5	Resonance map.	24
2.6	Dispersion relation of the 1D tight-binding model.	28
2.7	Extended Bloch wave versus localized wave.	33
2.8	Real lattice versus rotational lattice.	35
3.1	Electric field of a TL pulse in the spectral and time domains.	43
3.2	Electric field of a chirped pulse in the spectral and time domains.	45
3.3	Schematic of a flat pulse train in the time domain.	46
3.4	Pulse sequences in the spectral and time domains.	47
3.5	Pulse sequences in the spectral and time domains (PAP).	49
3.6	(Cross-correlation) frequency-resolved optical gating (X)FROG.	52
3.7	XFROG spectrograms of single pulses.	53
3.8	Pulse shaper in '4f'-folded design	54
3.9	Discretization of the SLM amplitude mask.	56
3.10	Optimization protocol to shape flat pulse sequences.	57
3.11	Demonstration of flexibility in shaping pulse trains.	59
3.12	Diagram of the Michelson interferometer setup.	60
3.13	Diagram of the home-built multi-pass amplifier.	61
3.14	The effect of amplification on the pulse spectrum.	63
3.15	Diagram of the setup to create long, high-energy pulse trains.	65
3.16	XFROG spectrogram of a high-intensity pulse train.	66
3.17	Temporal profile of long, high-intensity pulse trains.	68
4.1	Scheme of the Raman spectroscopy setup.	70
4.2	Raman spectrum of N ₂ after a single kick.	73
4.3	Raman spectrum of O ₂ after a single kick.	74
4.4	Diagram of a supersonic jet expansion.	76
4.5	Diagram of the molecular beam setup.	78

List of Figures

4.6	Temperature and pressure as a function of nozzle distance. . .	79
4.7	Rotational spectroscopy of N ₂ and O ₂	82
4.8	Collisional decay of the Raman signal.	83
4.9	Rotational distribution as a function of nozzle distance. . . .	85
5.1	Raman spectrogram after a periodic pulse train (I).	88
5.2	Raman spectrogram after a periodic pulse train (II).	90
5.3	Selective excitation with periodic pulse trains.	91
5.4	Energy diagram of a two-level system.	93
5.5	Rabi oscillations: Simulation at 0 K	96
5.6	Rabi oscillations: Resonance map	96
5.7	Rabi oscillations: Simulation at 25 K	98
5.8	Rabi oscillations: Raman spectrograms.	101
5.9	Rabi oscillations: Dependence on detuning.	103
5.10	Rabi oscillations: Dependence on kick strength.	104
5.11	Rabi oscillations: Effect of bandwidth.	106
5.12	Bloch oscillations: Simulation at 25 K	113
5.13	Bloch oscillations: Dependence on detuning.	115
5.14	Bloch oscillations: Dependence on kick strength.	116
5.15	Bloch oscillations: Dependence on energy & detuning.	118
5.16	Bloch oscillations: Effect of bandwidth.	120
5.17	Limited excitation due to centrifugal distortion.	124
5.18	Scheme of an optimized pulse train.	126
5.19	Excitation with an optimized pulse train.	127
5.20	Propagation effects: Cascaded Raman scattering.	130
5.21	Propagation effects: Spectral broadening.	132
6.1	Dynamical localization: Resonance map.	140
6.2	Dynamical localization & timing noise.	142
6.3	Dynamical localization & amplitude noise.	144
6.4	Dynamical localization: Dependence on pulse number.	146
6.5	Dynamical localization: Dependence on kick strength.	147
6.6	Dynamical localization: Rotational energy.	149
6.7	Dynamical localization: Dependence on pulse period.	150
6.8	Diffusive growth: Dependence on pulse period.	152
6.9	Dynamical behaviour near the quantum resonance (I).	158
6.10	Dynamical behaviour near the quantum resonance (II).	159
6.11	Localized population near the quantum resonance.	160
6.12	Rotational energy near the quantum resonance (I).	161
6.13	Rotational energy near the quantum resonance (II).	162

List of Figures

7.1	Control of quantum chaos: Pulse train diagram.	167
7.2	Control of quantum chaos: Resonance map.	167
7.3	Control of the rotational energy.	168
7.4	Control of the rotational population.	170
7.5	Sensitivity of the control scheme.	171
7.6	Quantum to classical transition.	172

List of Abbreviations

AOKR	Atom-Optics Kicked Rotor
BBO	Barium Borate
CCD	Charge-Coupled Device
CGC	Clebsch-Gordan Coefficients
FROG	Frequency Resolved Optical Gating
FT	Fourier Transform
FWHM	Full Width at Half Maximum
KAM	Komolgorov-Arnold-Moser
KR	Kicked Rotor
MIIPS	Multiphoton Intrapulse Interference Phase Scan
MKR	Modified Kicked Rotor
MPA	Multi-Pass Amplifier
Nd:YAG	Neodymium-doped yttrium aluminium garnet ($\text{Nd:Y}_3\text{Al}_5\text{O}_{12}$)
OPA	Optical Parametric Amplifier
PAP	Piecewise Adiabatic Passage
QKR	Quantum Kicked Rotor
SLM	Spatial Light Modulator
Ti:Sapph	Titanium-doped sapphire (Ti^{3+} :sapphire)
TL	Transform-limited
XFROG	Cross-correlated Frequency Resolved Optical Gating

Chapter 1

Introduction

Control of molecular rotation with ultra-short laser pulses is an active research area of experimental and theoretical molecular science. Interests are ranging from studying molecular dynamics to chemical reactivity of molecules [164, 126, 56] and from implementing model systems like the kicked rotor to exploring quantum chaotic systems [28, 59, 63, 70, 71].

The rotation of molecules in the gas phase can be excited coherently by intense non-resonant laser fields. The manipulation with ultra-short laser pulses in particular allows for time-dependent control and field-free studies [152]. If the duration of the laser pulse is short with respect to the period of molecular rotation, the excited molecules will exhibit complex dynamics. The evolution of the rotational wave packet is characterized by “quantum revivals”, a consequence of the discreteness of the angular momentum spectrum [151].

Many techniques to control molecular rotation exist that use two time-delayed ultra-short pulses, and several techniques are based on pulse sequences with more than two pulses, e.g. to enhance molecular alignment [41], to control the alignment of asymmetric molecules [139] or to initiate unidirectional rotation [193]. The reasons behind implementing multi-pulse schemes are often to improve the selectivity of excitation or to increase the efficiency. Both are achieved by tailoring the timing between the pulses in accordance with the rotational dynamics. A few schemes of using long sequences of pulses, so-called “pulse trains”, have been proposed theoretically [12, 103, 104, 166, 187], and implemented experimentally with sequences of up to eight laser pulses [41, 192, 64, 88].

The impulsive excitation of linear molecules with a sequence of periodic high-intensity ultra-short pulses presents the realization of a paradigm system known as the “kicked rotor” [59]. In this theoretically well-studied model a rotor is subject to an external driving field of periodic δ -kicks. Classically, the system is described by a set of two simple equations of motion for the angle and angular momentum of the rotor, which despite being strictly deterministic, turn chaotic beyond a certain strength of the kicks [31].

In his ground-breaking paper from 1969, Boris Chirikov introduced the famous “standard map” to describe a large number of classically chaotic systems [35]. Among them is the periodically delta-kicked rotor. Ten years later, Chirikov and collaborators discovered a totally new and unexpected effect: the stochastic behavior of the classical rotor becomes non-stochastic for the quantum kicked rotor (QKR) [31]. Two fundamentally different regimes emerge depending on the period of the external driving field. If the external frequency matches the natural frequency of the quantum rotor, the rotational excitation becomes highly efficient [84]. In this case of an excitation on “quantum resonance” the angular momentum grows linearly with time, rather than diffusively ($\propto \sqrt{\text{time}}$) like in the case of a classical rotor. However, if the external frequency is incommensurable with the natural frequency of the quantum rotor, the surprising result is a complete suppression of angular momentum growth. Despite a continued kicking, the rotor does not accept any rotational energy. This effect has later been called the “dynamical localization”.

In 1982 Shmuel Fishman and collaborators [52] pointed out that the mechanism of dynamical localization is related to the phenomenon of “Anderson localization” [6] known from solid state physics. Philip Anderson, in 1958, had shown that the propagation of an electron in a one-dimensional disordered lattice is completely suppressed¹. Fishman *et.al.* formulated a theory that proved the deep underlying connection between the two types of localization. They considered the rotational quantum number of a quantum rotor as an effective site number in a rotational lattice. The disorder could be linked to the periodic kicking with a nonlinear potential. In both cases, the effect of localization stems from the destructive interference of quantum pathways: in the real space of the lattice [6] and in the angular momentum space of the rotor [31, 84].

Research on the effect of Anderson localization in a variety of different systems is very active and constantly growing [98]. As it relies on the destructive interference of waves, it has been observed with classical waves, i.e. photons [68, 42, 183, 33, 165, 150, 99] and sound [178, 80], as well as with matter waves [39, 50, 18, 143]. Dynamical localization of the QKR presents an alternative model to study the fundamental aspects of Anderson localization. In 1992, Graham *et.al.* suggested the realization of a QKR in a related system by observing periodically kicked ultracold atoms in the momentum space [74]. The “atom-optics kicked rotor” (AOKR), first demonstrated in 1995 [121], has since evolved to a standard approach for studying many in-

¹For this and related work, Anderson was awarded the Nobel Prize in Physics in 1977.

interesting effects, from dynamical localization and quantum resonances, to the effects of noise and dissipation, etc. [135]. Yet until now, more than 30 years after Chirikovs and Fishmans papers, the fundamental effect of dynamical localization has never been observed in a system of true quantum rotors, i.e. quantum objects that actually rotate in space.

Besides being an ideal testing ground for effects related to Anderson localization, the QKR plays another important role in the field of quantum chaos [71], a synonym for quantum systems whose classical counterparts are chaotic. One question of interest is whether the evolution of a chaotic system can be steered one way or another by adjusting its initial state. The very definition of classical chaos, i.e. the exponential sensitivity to initial conditions, seems to leave no room for such controllability. Yet quantum mechanics teaches us that quantum trajectories, leading to the same final state, will interfere with one another no matter how stochastic they are. Adjusting the relative phase of these trajectories to make their interference either constructive or destructive should then provide full control [157], contrary to the classical expectations. The question is not new and has been discussed in many theoretical works for more than 20 years (for reviews, see Ref. [142, 71]). Gong and Brumer considered the QKR to study the controllability of classically chaotic dynamics in the quantum limit [69, 70, 71]. They showed theoretically that the energy of the localized state can indeed be controlled by modifying the initial quantum state of the rotor. However, the experimental study of the predicted controllability has been lacking. Control in the regime of quantum chaos is of immediate relevance for the general goal of controlling molecular dynamics with external fields, since many complex molecules often display chaotic behaviour.

Several theoretical works suggested diatomic molecules repeatedly kicked by a pulsed external field (microwave, optical or THz) as a realization of the QKR [28, 70, 59, 114]. In their proposal, Averbukh and coworkers used ultra-short laser pulses to periodically excite linear molecules [59]. They investigated several QKR phenomena [59, 63, 60, 61] and effects related to the quantum resonance have been experimentally verified since [41, 192, 64]. An onset of dynamical localization in laser-induced molecular alignment was reported [88], but the direct evidence of the exponentially localized states and the suppressed growth of the rotational energy have not been shown.

Laser-kicked molecules as QKR provide some advantages over the cold-atom analogue. The angular momentum of true rotors is inherently quantized, in contrast to the continuous spectrum of the translational momentum

in the case of the AOKR [135]. To reach sufficiently narrow momentum distributions the atoms need to be cooled down to ultra-cold temperatures, which requires a complicated experimental setup. On the other hand, supersonic molecular jets are easier to construct, and they provide low enough temperatures for the molecular QKR experiments.

Furthermore, the suggested system enables the study of quantum phenomena which are unique to true rotors. The effect of centrifugal distortion of spinning molecules leads to oscillations in the angular momentum distribution, similar to Bloch oscillations in solids [25]. This has been predicted by Floss and Averbukh [60, 62] and recently demonstrated [64]. Molecules experience an “edge” in the semi-infinite lattice of rotational states, since only positive rotational quantum numbers are allowed. Floss and Averbukh theoretically showed the existence of localized edge states [61], which has not been observed yet.

1.1 Main research objectives

The goal of our research is the study of the quantum kicked rotor with laser-kicked linear molecules. In the last decade some of the many predicted phenomena, i.e. the quantum resonance [41, 192], the existence of Bloch oscillations [64] and some first indirect signs for the presence of localization [88] have been explored experimentally. In order to investigate other fundamental effects, in particular the demonstration of a localized angular momentum distribution, all of the above experiments lacked a few key requirements, the most important one being a sufficiently long pulse sequence of high energy ultra-short pulses.

We designed and built a new tool to create pulse sequences of twenty or more pulses; up until now the sequences were limited to eight pulses. The technique is based on the principles of femtosecond pulse shaping and interferometric multiplexing. While other techniques often suffer from insufficient pulse intensities, we use multi-pass amplification to compensate for the severe energy losses. This approach excels in almost full controllability over the profile of the generated pulse train: The amplitudes as well as the temporal spacing of all sub-pulses can be adjusted individually.

In our experiments we use long pulse sequences to excite linear molecules, i.e. nitrogen or oxygen, at rotational temperatures around 25 K. Prior experiments have exclusively been done at room temperature, which prohibits the observation of many effects due to broad angular momentum distributions. In contrast to previously implemented detection techniques, we employed

a frequency-resolved method allowing for the resolution of individual rotational states.

Complimenting previous work with AOKR, we directly observed the effect of dynamical localization, demonstrating the characteristic exponential distribution of the localized wave function and the suppression of the rotational energy growth. We introduced noise in a sequence of rotational kicks to show the expected destruction of localization and the recovery of classically diffusive behaviour.

In addition, we continued the research of molecular excitation on quantum resonances. We improved the existing studies on Bloch oscillations in molecular rotation [64] and documented a new phenomenon of Rabi oscillations between two rotational states. The prospects of creating broad rotational wave packets by means of molecular interaction with long pulse sequences were explored. The timing of the pulses could be optimized to partially mitigate the limitations stemming from the centrifugal distortion.

Another objective was to explore the possibility of coherent control in a system that is classically chaotic. We established the first experimental demonstration of “quantum chaos under control”. In the verification of the Gong-Brumer control scheme [69, 70], our unique ability to fine-tune the initial rotational state was used to control the rotation of a molecule at later times. By varying the relative phases of the initial states we effectively changed the localization process of the QKR. We proved the quantum nature of the demonstrated controllability by showing its disappearance in the classical regime of laser-molecule interaction.

Many of the demonstrated phenomena, e.g. dynamical localization and Bloch oscillations, establish an intimate connection between the two fundamental aspects of modern physics: the motion of a quantum particle in a disordered solid and the motion of a quantum pendulum under periodic kicking [52]. Our work opens new opportunities for investigating quantum phenomena which are unique to true rotors, e.g. edge localization [61] or the effects of centrifugal distortion and rotational decoherence on QKR dynamics [60]. We believe that our results are important to the general fields of laser technology, quantum control of light-matter interaction, nonlinear dynamics and quantum chaos.

1.2 Outline of the thesis

The goal of this thesis is to give a complete overview on the subject of “Quantum coherent control of laser-kicked molecular rotors”.

Chapter 2 describes the kicked rotor model, classically (Sec. 2.1) as well as its quantum mechanical counterpart (Sec. 2.2). Important concepts to characterize different interaction regimes, the stochasticity of the system and the transition from a quantum-to-classical rotor are discussed. We become more rigorous when we discuss the QKR model of interest - the laser-kicked molecular rotor (Sec. 2.3). We introduce the physics behind laser-molecule interaction and the relevant Hamiltonian. We give details how we model the system numerically to analyse our results. The kicked rotor model can be mapped onto a one-dimensional tight-binding problem (Sec. 2.4). We introduce the concepts to describe quantum particles in crystalline solids, before we derive the correspondence between a periodically-kicked quantum rotor and a quantum particle in a disordered lattice.

In chapter 3 we give a detailed description of the technique that we developed to create long sequences of high-intensity ultra-short laser pulses and demonstrate its unique abilities. A second technical chapter 4 introduces other techniques that proved to be crucial for the implementation of many experiments. Rotational Raman spectroscopy (Sec. 4.1) enabled a quantum-state selective detection with a dynamic range over several orders of magnitude. This Raman technique was implemented to work with rotationally cold molecules produced in a supersonic jet expansion (Sec. 4.2). We analyse the performance and characterize the experimental conditions.

Chapter 5 is dedicated to molecular excitation via quantum resonances. At first, an intuitive “resonance map” is recorded and used to explain the existence of various (fractional) quantum resonances (Sec. 5.1). An immediate implication of the periodic excitation on fractional quantum resonances are rotational Rabi oscillations in an effective two-level system of two rotational states (Sec. 5.2). The excitation on full quantum resonances leads to the phenomenon of Bloch oscillations in the angular momentum space (Sec. 5.3). The effect is studied and compared to the solid state analogue. Finally, the quantum resonances are explored with the objective of exciting broad rotational wave packets (Sec. 5.4), which is desirable for creating strongly aligned molecular samples.

Dynamical localization in a system of true rotors is the subject of chapter 6. Starting with a theoretical picture of dynamical localization (Sec. 6.2) and the intricacies of the experimental realization (Sec. 6.3), we present direct evidence of localized molecular rotation and test its dependency on

multiple experimental parameters and the transition to classical behaviour under the influence of noise (Sec. 6.4). In addition, we establish a connection between the phenomenon of dynamical localization and Bloch oscillations by studying the regime around the quantum resonance (Sec. 6.5).

The final experimental chapter 7 discusses the topic of controlling quantum chaos. We describe the idea of coherent control and the unique opportunity to tune the QKR dynamics from quantum mechanical to classical (Sec. 7.1). We detail the scheme that we use to control the dynamical localization process (Sec. 7.2) and show the observed controllability (Sec. 7.3). We demonstrate that the control relies on quantum coherences by driving the system closer to the classical limit. At last, we outline the future directions of this work in chapter 8.

Chapter 2

The kicked rotor

The one-dimensional kicked rotor (KR) is a well-studied paradigm system, classically as well as in quantum mechanics [31, 138, 77]. Although it is a strictly deterministic Hamiltonian system, it exhibits chaotic motion in certain regimes. Its simplicity and the fact that the transition to chaos can be controlled by the external driving field make it a popular model system [138].

The interaction of a diatomic molecule subject to N periodic kicks via non-resonant linearly polarized laser pulses, provides an experimental realization of the “quantum kicked rotor” (QKR). It is described by the following Hamiltonian:

$$\hat{H} = \frac{\hat{J}^2}{2I} - \hbar P \cos^2(\theta) \sum_{n=0}^{N-1} \delta(t - nT) . \quad (2.1)$$

The first term, the kinetic energy of the rotor, depends on the angular momentum operator \hat{J} and the moment of inertia I . The second term is dictated by a nonlinear potential with the angle θ between the molecular axis and the laser polarization axis. The period of the driving field is T , the strength of the kicks is P and \hbar is the reduced Planck constant.

In section 2.1 we look at the classical version of this rotor. We explain the fundamental concepts of the kicked rotor model and introduce the “standard map”. Section 2.2 discusses the similarities and the unique differences of the quantum version of the KR. In Sec. 2.3 we return to the system that we will study experimentally, the “laser-kicked molecular rotor”. More details about the light-molecule interaction, the Hamiltonian and the rotational dynamics will be provided.

A second important significance of the KR has been shown by Fishman and coworkers [52, 76]: the QKR can be mapped onto a tight-binding model known from solid state physics. Section 2.4 is dedicated to the correspondence between a crystalline solid and the QKR, which will be used in our analysis of several observed effects.

2.1 Classical kicked rotor

The classical equations of motion of the Hamiltonian in Eq. 2.1 are

$$\begin{aligned}\theta_N &= \theta_{N-1} + \tilde{J}_N \\ \tilde{J}_N &= \tilde{J}_{N-1} - K \sin(2\theta_{N-1}) .\end{aligned}\tag{2.2}$$

In appendix B we show how the equations of motion can be derived from the Hamiltonian of the kicked rotor ². The two coupled equations describe the motion of the KR at discrete steps after each kick N via the two canonical variables, the angle θ and the dimensionless angular momentum \tilde{J} ,

$$\tilde{J} = J \frac{T}{I} .\tag{2.3}$$

The dynamics of the KR is determined by the parameter K - the “stochasticity parameter” - which is a measure of the amplitude of the kicks. In the case of a diatomic molecule exposed to non-resonant linearly polarized laser pulses, the parameter can be calculated as

$$K = \frac{T \cdot \Delta\alpha}{4I} \int \mathcal{E}^2(t) dt ,\tag{2.4}$$

where $\Delta\alpha$ is the polarizability anisotropy of the molecule and $\mathcal{E}(t)$ is the electric field envelope. The integral is evaluated over one full period T of the pulse sequence. Details about the light-molecule interaction for a laser-kicked rotor will be discussed in Sec. 2.3.

The KR dynamics can be distinguished into several regimes depending on the magnitude of K . For weak kicks the classical equations (2.2) represent periodic motion. Here, the angle and the angular momentum only change in small quantities from one kick to the next, resulting in a deterministic motion. However, if the amplitude of the kicks becomes large enough, the motion turns chaotic. The behaviour of the KR is no longer regular but rather stochastic, hence the name of the stochasticity parameter. We can understand the chaos as a consequence of the nonlinear angle-dependent potential [135]. At high K values each kick is effectively quasi-random in its direction and its amplitude.

² The traditional equations of motion for the planar kicked rotor have a slightly modified form $\theta_N = \theta_{N-1} + \tilde{J}_N$ and $\tilde{J}_N = \tilde{J}_{N-1} + K \sin(\theta_{N-1})$ [70]. However, the physical interpretation remains the same.

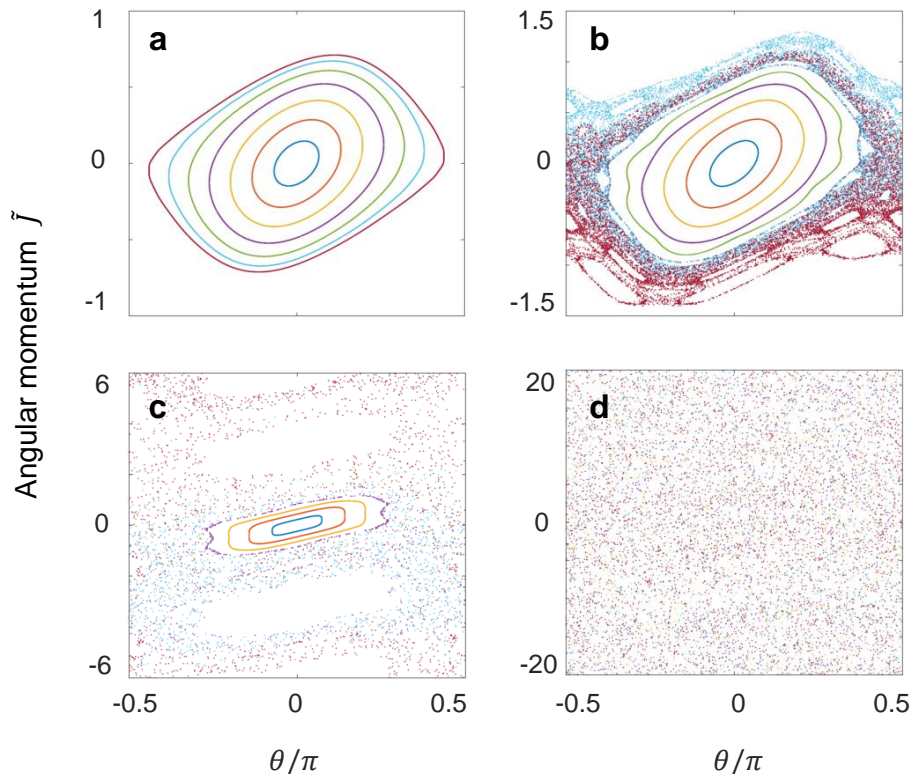


Figure 2.1: Sections of the standard map of the kicked rotor for different values of the stochasticity parameter (a) $K = 0.25$, (b) $K = 0.5$, (c) $K = 1$ and (d) $K = 3$.

2.1.1 The standard map

The recursion equations (2.2) are called the “standard map” [31]. Stroboscopically one can follow the motion of the rotor on classical trajectories in the phase space. The map depends solely on the stochasticity parameter K .

In Fig. 2.1 we show four different maps obtained from Eq. 2.2 corresponding to different K parameters. All maps are constructed starting from the same initial conditions: seven points in phase space at $\tilde{J}_0 = 0$ and $\theta_0 = \pi p/16$ with $p = 1, 2, \dots, 7$ (plotted in different colours). Then the system is evolved in time up to $N = 10000$, which yields either stable trajectories, visible as closed ellipsoids, or chaotic trajectories. Due to the periodicity of $\sin(2\theta)$ the complete dynamics can be portrayed on a cylinder, modulo π .

The KR behaviour is analysed in different regimes, controlled by the

stochasticity parameter. Small values of $K \ll 1$ lead to periodic motion, seen in Fig. 2.1(a). Once chaos emerges, for small K , it is first isolated in chaotic regions, Fig. 2.1(b). The area of the chaotic regions grows with K , while the regions itself are separated by Komolgorov-Arnold-Moser (KAM) trajectories [75]. Beyond a critical value K_{cr} the last KAM trajectory disappears and the motion is no longer bounded, as in Fig. 2.1(c). Note the different y -scale, shown is only a section of the occupied phase space. The critical value for the planar kicked rotor is cited as $K_c = 0.97164\dots$ [75]. The laser-kicked rotor described in Eq. 2.2, however, turns chaotic twice faster as a function of K ³. Eventually all stable islands disappear in the chaotic sea, shown in Fig. 2.1(d). Although no critical value exists in the literature, it is commonly assumed that the phase space of the planar kicked rotor is globally chaotic for $K \gtrsim 5$ [83]. For the equations of motion (2.2) of the laser-kicked rotor, no periodic trajectories should be expected for $K \gtrsim 2.5$.

2.1.2 Classical diffusion

In the regime of global chaos, the classical rotor performs a random walk in angular momentum space, despite being perfectly deterministic. The mean-square value of the angular momentum grows as $\langle \tilde{J}^2 \rangle \propto DN$ with a characteristic diffusion rate $D \approx K^2/2$ in the globally chaotic regime [36]. The mean energy of the rotor $\langle E \rangle \propto \langle \tilde{J}^2 \rangle$ therefore increases linearly with the kick number.

The diffusive growth is unbounded for the idealistic δ -kicks. As long as the rotor does not rotate much during the duration of the kick, the δ -KR is still a good approximation [28, 63]. If the rotational period is on the same time scale as the kicking period, the momentum transfer averages out to zero. As a consequence, the achievable angular momentum is bounded.

2.2 Quantum kicked rotor

The main interest in the quantum kicked rotor (QKR) is stimulated by the study of the effects of quantization on classically stochastic behaviour - a field of physics known as “quantum chaos” [31, 138, 77]. Unless otherwise noted, in this work we will be concerned with the globally chaotic regime.

For a finite amount of time, the quantum motion resembles the chaotic classical motion. However, after a critical number of kicks N_b - the “quan-

³ This is a consequence of the symmetry of linear molecules and an angle dependence of 2θ in (2.2).

tum break time” - the quantization of angular momenta becomes noticeable and leads to quasi-periodic dynamics. Interferences in the quantum system prohibit stochasticity [31, 84]. Unlike in the classical case, one has to distinguish two regimes: one where the period of the kicks is commensurable with the periodicity of the quantum rotor, and one where it is incommensurable. The respective excitations result in two different phenomena: *quantum resonance* and *dynamical localization*.

2.2.1 Quantum resonance

We introduce a dimensionless time which relates the period of the kicks T to the revival period of the rotor $T_{\text{rev}} = 2\pi I/\hbar$,

$$\tau = \hbar \frac{T}{I} = 2\pi \frac{T}{T_{\text{rev}}} . \quad (2.5)$$

The time τ acts as the effective Planck constant of the system. The discreteness of the rotational spectrum of the QKR results in quantum resonances whenever $\tau = 2\pi p/q$, where p and q are integers [84, 184, 59]. Equivalently, this condition can be expressed as $T/T_{\text{rev}} = p/q$. Tuning the period to match a quantum resonance enables an efficient excitation of multiple rotational states. Owing to constructive interference, the rotational energy grows quadratically from kick to kick. This “ballistic” growth exceeds the classical diffusive growth.

2.2.2 Dynamical localization

On the other hand, away from quantum resonances, the quantum interferences are destructive and suppress the increase in rotational energy after the quantum break time. The growth is completely halted due to a mechanism called dynamical localization. It has been shown that this phenomenon is related to the absence of diffusion in a one-dimensional disordered lattice due to Anderson localization [52]. According to the commonly accepted terminology, *Anderson localization* always refers to a quantum particle in a real lattice, and *dynamical localization* to the QKR ⁴.

The angular momentum of the QKR localizes around the initial momentum. The resulting distribution of the angular momentum states falls off exponentially with a characteristic length called the “localization length”. (The characteristic length scale of the classical KR was given as the diffusion constant D .)

⁴In the literature it is also common to find the QKR localization under the synonym of Anderson localization.

2.2.3 Stochasticity

Looking back at the classical definition of the stochasticity in Eq. 2.4, we observe that the motion of the QKR is governed by two separate parameters, the effective Planck constant τ and a dimensionless kick strength P . The rigorous definition of P will be given in Sec. 2.3.2. The stochasticity parameter is thus derived by their product

$$K = \tau P . \tag{2.6}$$

We can reduce the quantum effects by decreasing τ while keeping K constant. The underlying classical dynamics stays unchanged, but we approach the classical limit, i.e. the standard map. For quantum effects to become noticeable the period has to be on the order of the revival time $T \rightarrow T_{\text{rev}}$, see Eq. 2.5. For $T \ll T_{\text{rev}}$, on the other hand, the discreteness of the energy spectrum is not yet noticeable in the system's dynamics.

The quantum-classical correspondence can also be achieved by introducing noise or dissipation into the system. Since all quantum effects crucially rely on the interference of coherent pathways, such processes of decoherence will lead to the destruction of dynamical localization and the recovery of classical diffusion.

2.2.4 Atom-optics kicked rotor

In 1992 Graham *et.al.* proposed to study the QKR by kicking ultracold atoms with a standing wave of far-detuned light. [74]. The momentum of ultracold atoms interacting with a pulsed standing wave will spread diffusively in a classical description. However, they demonstrated theoretically that the momentum transfer is quantum mechanically limited by dynamical localization. The first experimental demonstration of dynamical localization in this system was reported in 1995 [121] and has in fact been the first observation of one-dimensional Anderson localization with atomic matter waves. Since then this system, which we will refer to as the atom-optics kicked rotor (AOKR), has become the standard setup for studying the QKR. Much research has been done to investigate different aspects of the QKR, dynamical localization and quantum chaos. More information can be found in multiple reviews [135, 136].

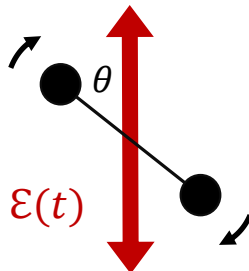


Figure 2.2: Diatomic molecule interacting with linearly polarized electric field.

2.3 Laser-kicked molecular rotor

We implement the QKR by exposing linear molecules to ultra-short laser pulses. The goal of this section is to understand the underlying physics of the system: We describe the light-molecule interaction and the idea of “kicking” molecules. We introduce the Hamiltonian of a kicked rotor, its wave function and the resulting dynamics. A vital part of our work is the comparison of the experimental results with the respective simulations, we describe the numerical methods to simulate the kicked rotor in Sec. 2.3.6. To finish, we discuss the particular diatomic molecules that were used as quantum rotors. We give relevant molecular constants and useful derived parameters in Sec. 2.3.9.

2.3.1 Light-molecule interaction

At first, we need to understand the interaction between linear molecules and a non-resonant laser field, see Fig. 2.2. We start with a **classical description**. The interaction potential of a molecule with a permanent dipole moment μ has the nonlinear form

$$V(\theta, t) = -\mu\mathcal{E}(t) \cos \theta , \quad (2.7)$$

with the angle θ between the molecular axis and the polarization axis of the electric field $\mathcal{E}(t)$. Since we look exclusively at molecules without a permanent dipole moment, $\mu(t) = \alpha(t)\mathcal{E}(t)$ is the induced dipole moment in the presence of the laser field. The resulting dipole will interact with the electric field itself. After averaging over the fast oscillations, the interaction potential becomes [12]

$$V(\theta, t) = -\frac{1}{4}\mathcal{E}^2(t) [(\alpha_{\parallel} - \alpha_{\perp}) \cos^2 \theta + \alpha_{\perp}] . \quad (2.8)$$

2.3. Laser-kicked molecular rotor

The full derivation can be found in the “Nonlinear Optics” book by Boyd [29]. The second term of $V(\theta, t)$ does not depend on the angle θ . Hence, it will not affect the rotational dynamics induced by a laser pulse and can be disregarded [63]. The polarizability anisotropy $\Delta\alpha = \alpha_{\parallel} - \alpha_{\perp}$ is determined by the parallel α_{\parallel} and the perpendicular α_{\perp} components of the polarizability with respect to the molecular axis.

Most molecules have $\Delta\alpha > 0$ and the *potential energy* of the system is minimized when the angle is $\theta = 0$. This implies, that a thermal ensemble of randomly oriented molecules will, in the presence of a *long* laser pulse, feel a torque that will align all molecules. For more details about “adiabatic alignment” see Refs. [66, 164]. Here, we work with ultra-short pulses. In this impulsive regime, the molecules merely feel a “kick” towards the field polarization direction [12], shown in Fig. 2.3. For a classical rotor, the gain in the angular velocity is proportional to $\sin(2\theta)$ [104] - which also appears in the classical equation of motions in Eq. 2.2. Molecules with initial angles $\theta \ll 1$ acquire a velocity that is proportional to the angle. Thus, these molecules arrive at $\theta = 0$ at the same time [12] resulting in a “field-free alignment”. Different speeds of molecules in the ensemble result in rich dynamics, including further molecular alignments. For more details on the topic of impulsive alignment we refer to Refs. [151, 126, 56].

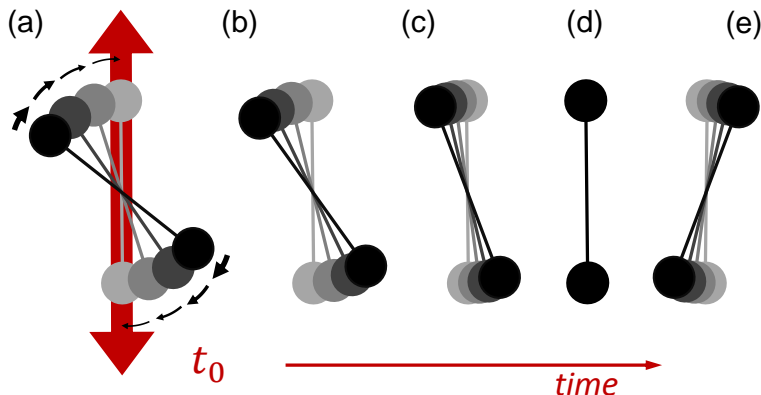


Figure 2.3: Field-free alignment of an ensemble of molecules after the excitation with an ultra-short laser pulse.

In the **quantum mechanical description** we need to include the quantization of the angular momentum. In the simplest approximation linear molecules are viewed as rigid rotors with a moment of inertia $I = \hbar(4\pi cB)^{-1}$

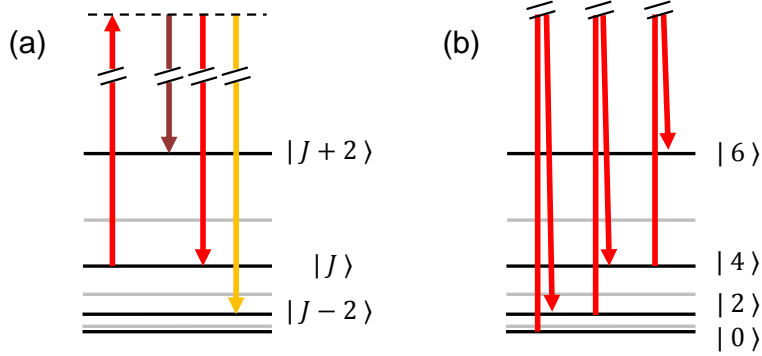


Figure 2.4: **(a)** Non-resonant two-photon Raman transitions in a rotational system. The quantum number changes by $\Delta J = 0, \pm 2$. **(b)** Rotational ladder climbing via consecutive Raman processes.

[63], where B is the rotational constant and c is the speed of light. The rotational energy spectrum is expressed as

$$E_J = hcBJ(J + 1) . \quad (2.9)$$

However, once real molecules occupy higher rotational quantum numbers J , they no longer behave like rigid rotors. Owing to the fast rotation, the molecular bond stretches, which is reflected by a centrifugal distortion term with the centrifugal constant D ,

$$E_J = hc[BJ(J + 1) - DJ^2(J + 1)^2] . \quad (2.10)$$

An ultra-short, non-resonant laser pulse induces two-photon Raman transitions via an intermediate virtual level. In each transition, the rotational quantum number J changes by either $\Delta J = +2$ (Stokes Raman scattering), $\Delta J = -2$ (anti-Stokes Raman scattering) or $\Delta J = 0$ (Rayleigh scattering), as drawn in Fig. 2.4**(a)**. If the pulse is strong, it is possible to climb up the “rotational ladder” with many consecutive Raman transitions, provided that the bandwidth of the pulse is wide enough to support all the required frequencies, see Fig. 2.4**(b)**.

Finally, we connect the classical and the quantum picture. If a molecule, whose polarizabilities α_{\parallel} and α_{\perp} are different, is rotating, then the effective polarizability of the medium $\alpha(t)$, experienced by a linearly polarized light, changes periodically [112]. The refractive index $n(t)$ of a collection of coherently rotating molecules will be modulated in time $n(t) = \sqrt{1 + N\alpha(t)}$,

where N is the number density of molecules [29]. This temporal modulation of n results in the frequency modulation of the carrier wave, and the corresponding Raman sidebands.

2.3.2 Kick strength

Our ultra-short laser pulses are of a Gaussian shape. The electric field envelope of a single pulse is described by $\mathcal{E}(t) = \mathcal{E}_0 \exp(-t^2/2\sigma^2)$, with the peak value of \mathcal{E}_0 at the center of the pulse at time $t = 0$ and a width σ . When a short pulse interacts with a molecule it creates a rotational wave packet. This interaction can be described as an instantaneous “kick”, if the duration of the pulse is substantially shorter than the time scales of the dynamics in the rotational wave packet.

The width of the prepared wave packet is a measure of the strength of the pulse. One can define a dimensionless *kick strength* [57]

$$P = \frac{\Delta\alpha}{4\hbar} \int \mathcal{E}^2(t) dt . \quad (2.11)$$

The kick strength reflects the typical amount of angular momentum (in units of \hbar , the reduced Planck’s constant) transferred from the laser pulse to the molecule [57]. Solving the integral for a Gaussian pulse, simplifies the expression to $P = \Delta\alpha/4\hbar \cdot \mathcal{E}_0^2 \sqrt{\pi}\sigma$. On the other hand, if we numerically simulate the effect of δ -kicks, Eq. 2.11 can be reformulated with Dirac’s delta function $\frac{\Delta\alpha}{4\hbar} \mathcal{E}^2(t) = P\delta(t)$.

2.3.3 Hamiltonian

The Hamiltonian for a three-dimensional rigid rotor is $H = \frac{\hat{J}^2}{2I} + V(\theta, t)$. It has a kinetic term, with the angular momentum operator \hat{J} , and a potential term $V(\theta, t)$ taken from Eq. 2.8 (without the θ -independent term), such that

$$H = \frac{\hat{J}^2}{2I} - \frac{\Delta\alpha}{4} \cos^2(\theta) \mathcal{E}^2(t) . \quad (2.12)$$

The Hamiltonian for a periodically kicked rotor simply follows by introducing a summation over N pulses with the period T

$$H = \frac{\hat{J}^2}{2I} - \frac{\Delta\alpha}{4} \cos^2(\theta) \sum_{n=0}^{N-1} \mathcal{E}^2(t - nT) . \quad (2.13)$$

2.3. Laser-kicked molecular rotor

The Hamiltonian can be written in terms of the kick strength (Eq. 2.11), for a pulse sequence of Gaussian pulses

$$H = \frac{\hat{J}^2}{2I} - \frac{P\hbar}{\sqrt{\pi}\sigma} \cos^2(\theta) \sum_{n=0}^{N-1} \exp\left(-\frac{(t-nT)^2}{\sigma^2}\right), \quad (2.14)$$

or similarly in the case of δ -pulses

$$\hat{H} = \frac{\hat{J}^2}{2I} - \hbar P \cos^2(\theta) \sum_{n=0}^{N-1} \delta(t-nT). \quad (2.15)$$

2.3.4 Wave function

The natural choice to describe the rotational wave function of a linear molecule interacting with a light pulse are the eigenfunctions of a three-dimensional rotor: the spherical harmonics $|J, M\rangle = Y_J^M(\theta)$. The quantum numbers J and M are the molecular angular momentum and its projection on the quantization axis, respectively. The wave function of a rotor is expanded in spherical harmonics

$$|\psi^M(t)\rangle = \sum_{J=0}^{\infty} c_J^M e^{-iE_J t/\hbar} |J, M\rangle, \quad (2.16)$$

with the complex amplitudes c_J^M . In the case of a linearly polarized driving field, the quantum number M remains unchanged. The selection rules $\Delta M = 0$ and $\Delta J = 0, \pm 2$ follow from the derivation in appendix C.2. Here, we merely use the fact that the wave functions are independent for each M (we do not need to sum over M). The amplitudes c_J^M can be calculated by solving the Schrödinger equation

$$i\hbar \frac{\partial \psi}{\partial t} = H\psi, \quad (2.17)$$

with the Hamiltonian of a kicked rotor given in Eq. 2.14. The mathematical procedure is described in appendix C.1.

2.3.5 Density matrix

Two important quantities that we will often refer to are the rotational “population” and the rotational “coherence”. Both are conveniently defined in the *density matrix formalism*, presented here.

2.3. Laser-kicked molecular rotor

Let the operator \mathbf{A} represent an observable of the quantum mechanical system, described by a wave function $|\psi(t)\rangle = \sum_J c_J(t) |J\rangle$. In comparison to Eq. 2.16, we omitted the magnetic quantum number M and included the phase term in $c_J(t)$. The ensemble average $\langle \mathbf{A} \rangle$ is given by

$$\langle \mathbf{A} \rangle = \langle \psi | \mathbf{A} | \psi \rangle = \sum_{J,J'} c_J^* c_{J'} \langle J | \mathbf{A} | J' \rangle = \sum_{J,J'} c_J^* c_{J'} A_{JJ'} . \quad (2.18)$$

The coefficients c_J contribute to the expectation value of \mathbf{A} as quadratic terms $c_J^* c_{J'}$ which are the matrix elements of the operator $\rho = |\psi\rangle\langle\psi|$

$$c_J^* c_{J'} = \langle J' | \psi \rangle \langle \psi | J \rangle = \rho_{J'J} . \quad (2.19)$$

The operator ρ is known as the ‘density matrix’.

Population: The diagonal elements $\rho_{JJ} = |c_J|^2$ are the populations. They specify the probability of finding the system in a quantum state $|J\rangle$. The total probability is conserved $\sum_J |c_J|^2 = 1$.

Coherence: The off-diagonal elements $\rho_{J'J} = c_J^* c_{J'}$ for all $J \neq J'$ are the coherences. These crossterms are responsible for the interference effects and appear whenever the wave function is in a superposition of the states $|J\rangle$ and $|J'\rangle$. Coherences satisfy two important properties [147]: First, $\rho_{JJ'}^* = \rho_{J'J}$ a consequence of the Hermitian nature of the density matrix. Second, $\rho_{JJ} \rho_{J'J'} \geq |\rho_{J'J}|^2$, i.e. coherences only exist, if the population of the corresponding levels is non-zero.

Statistical mixture: The density operator of a statistical mixture is $\rho = \sum_k p_k \rho_k$ where ρ_k are the density matrices for the pure states $|\psi_k\rangle$ and p_k their statistical weights. The same properties as mentioned above still apply. It can be shown [147] that the population is now $\rho_{JJ} = \sum_k p_k |c_J^{(k)}|^2$ and similarly that the coherence is $\rho_{J'J} = \sum_k p_k c_J^{(k)*} c_{J'}^{(k)}$.

The observable in our experiment is proportional to the modulus squared of the coherences $|c_J^* c_{J+2}|^2$. More details will be given in Sec. 2.3.6. We will talk about the detection technique of rotational Raman spectroscopy in Sec. 4.1.

2.3.6 Numerical analysis

It has been essential to simulate the dynamics of the QKR, not only to show the correspondence between experiment and theory but also to test hypotheses or to make predictions. The simulations are done in the programming language *Matlab* for a δ -kicked rotor. In this section we describe the numerical procedure.

The δ -kicked rotor

We solve the Schrödinger equation (Eq. 2.17) with the Hamiltonian for a single pulse (Eq. 2.12). Owing to the impulsive approximation, meaning that the duration of the pulse is much shorter than the relevant rotational time scale, we approximate the laser pulse by a δ -function. The wave function immediately before the kick is labelled as $|\psi^-\rangle$, whereas the one after the δ -kick is labelled $|\psi^+\rangle$. During the δ -pulse, the potential is so strong, that the kinetic energy term in the Hamiltonian can be neglected. Thus, the Schrödinger equation simplifies to

$$i\hbar \frac{\partial |\psi^+\rangle}{\partial t} = -\frac{1}{4} \mathcal{E}^2(t) \Delta\alpha \cos^2\theta |\psi^+\rangle. \quad (2.20)$$

In appendix C.2.1 we prove that an analytic solution of Eq. 2.20 is

$$|\psi^+\rangle = \exp(iP \cos^2\theta) |\psi^-\rangle. \quad (2.21)$$

Next, we want to rewrite $|\psi^+\rangle$ in the basis of spherical harmonics,

$$|\psi^+\rangle = \sum_{J,M} c_J^M e^{-iE_J t/\hbar} |J, M\rangle \quad (2.22)$$

to find its complex amplitudes c_J^M . This decomposition into the eigenstates of the kicked rotor is a non-trivial exercise. The approach used in our code, taken from Ref. [57] is outlined in appendix C.2.2. Alternative methods are presented in Ref. [12, 104]. We introduce an artificial time τ , defined such that before the kick ($\tau = 0$) and immediately after the kick ($\tau = 1$). Eventually, we obtain a set of coupled ordinary differential equations (ODE)

$$\frac{\partial}{\partial t} c_{J'}^{M'}(\tau) = iP \sum_{J,M} c_J^M \langle J', M' | \cos^2\theta | J, M \rangle, \quad (2.23)$$

that are solved numerically by means of the ‘*ode45 solver*’ in *matlab*. The eigenstates before the kick are $|J, M\rangle$ and after the kick $|J', M'\rangle$. The

resulting amplitude coefficients $c_{J'}^{M'}(\tau)$ are evaluated at ($\tau = 1$) to get the wave function of the created rotational wave packet immediately after the kick.

Selection rules: In appendix C.2.3 we further investigate the expression $\langle J', M' | \cos^2 \theta | J, M \rangle$, which contains all transition matrix elements for the relevant two-photon transitions, the Clebsch-Gordan coefficients (CGC). The selection rules follow directly from the CGC

$$\Delta J = 0, \pm 2 \quad \text{and} \quad \Delta M = 0 . \quad (2.24)$$

Statistical averaging: In the experiment, we work with a thermal ensemble of molecules. We calculate the final wave function individually for each initially populated state $|J_0, M_0\rangle$. The results are then added with the proper statistical weights $\omega = \omega_B \omega_N$. The weight of the thermal Boltzmann distribution $\omega_B = Z^{-1} \exp(-hcE_J/k_B T_0)$ depends on the initial temperature T_0 . Here, k_B is the Boltzmann constant and $Z = \sum_J (2J + 1) \exp(-hcE_J/k_B T_0)$ is the partition function. The weight of the appropriate nuclear spin statistic ω_N is given in Sec. 2.3.9.

Sequence of δ -kicks: So far, we mentioned only the wave function of the rotor after a single δ -kick. In order to get the wave function for a sequence of kicks, we implement the following procedure: (1) Calculate the wave function after a single kick individually for each initially populated state $|J_0, M_0\rangle$. (2) Evolve each wave function for the field-free time period T to the next δ -kick. A free evolution corresponds to the J -dependent phase term $e^{-iE_J T/\hbar}$. (3) Apply the next kick to the new wave functions. Again calculate it individually for all of the wave functions which originated from the different $|J_0, M_0\rangle$. (4) Repeat step (2-3) iteratively for each pulse in the sequence. (5) Sum over all wave functions with the proper statistical weights.

Experimental observable

Our experimental observable, the coherent Raman signal, depends on the coherences $c_J^{M*} c_{J+2}^M$ excited in an ensemble of molecules. More about the detection technique of Raman spectroscopy will be discussed in section 4.1. Here, we only point out that the J -dependent observable is referred to as “Raman spectrum”.

Consider a coherent superposition of two rotational states,

$$|\psi_J^M(t)\rangle = c_J^M e^{-iE_J t/\hbar} |J, M\rangle + c_{J+2}^M e^{-iE_{J+2} t/\hbar} |J+2, M\rangle, \quad (2.25)$$

created by a laser pulse. The coherent dynamics of such a wave packet is J -dependent. Owing to the selection rules for a two-photon excitation process (Eq. 2.24) the superposition $|\psi_J^M(t)\rangle$ can originate from any initially populated thermal state $|J_0 = J \pm 2k, M_0 = M\rangle$, where k is an integer. The intensity of the observed Raman spectrum will be proportional to the modulus squared of the induced coherence,

$$I_J \propto \sum_M \langle |c_J^{M*} c_{J+2}^M|^2 \rangle_{J_0, M_0}, \quad (2.26)$$

summed over all M -sublevels and averaged over the initial thermal mixture. It is important to realize that the Raman signal I_J as a function of the quantum number J , does in fact depend on both rotational states J and $J+2$.

M -degeneracy

Each rotational state J is $(2J+1)$ -fold degenerate in the field-free case. The degenerate states are described by the magnetic quantum number $M = -J, -J+1, \dots, J-1, J$. The axes of the polar coordinates are determined by the polarization direction of the electric field, which is taken along the z -direction. The quantum number M refers to the projection of the angular momentum J on the z -axis.

One important point about the M -substates is that they interact differently with the laser pulses - the kick strength P will effectively vary for different M -substates. For multiply-degenerate states the kicks are felt weaker if $|M|$ approaches its maximal value J . In this case the corresponding angular momentum vector is oriented closer to the z -axis, and the rotating molecules are thus confined closer to the xy -plane. One can see from Eq. 2.8 that for such polar angles θ the interaction potential decreases.

Another difference between M -sublevels has its origins in the “dynamic Stark effect”, i.e. the AC Stark effect, which leads to a shift in the energy levels due to the non-resonant laser field. During the interaction of the laser pulse, the M -degeneracy is lifted, because the energy shift will vary for different M -substates.

It is obvious now, that in the experiments it is important to lower the initial rotational temperature to have fewer M -sublevels populated. This

will result in a more accurate extraction of the molecular wave function (details in Sec. 6.3.2) because of a reduced averaging over states with different dynamics.

2.3.7 Revival time

The discreteness of the rotational energy spectrum leads to periodic dynamics of any wave packet and the so called quantum revivals [13], which have been observed in many different contexts, e.g. Refs [144, 108, 45, 141] to give just a few examples.

The revival time is inversely proportional to the second derivative of the rotational energy $E(J)$ with respect to the angular momentum J [105, 151]. In the case of a rigid rotor we obtain

$$T_{\text{rev}} = \frac{1}{2cB}, \quad (2.27)$$

an expression that is independent of the rotational quantum number J . Fast molecular rotation leads to a non-negligible centrifugal distortion and therefore a J -dependent revival time, which will become important for high quantum numbers.

2.3.8 Resonance map

An ultra-short laser ‘kick’ creates a rotational wave packet. We are looking at its dynamics and want to develop an understanding, how the wave packet will change once it is exposed to a series of periodic kicks and how it depends on the periodicity. The following arguments are based on the perturbative regime of light-molecule interaction.

The first laser pulse in a sequence of pulses induces a coherent rotational wave packet $|\psi(t)\rangle = \sum_J c_J e^{-iE_J t/\hbar} |J\rangle$. Consider a wave packet of only two states, $|J\rangle$ and $|J+2\rangle$. It can be assigned a classical rotation period $\tau_J = 2\hbar(E_{J+2} - E_J)^{-1}$ with Planck’s constant \hbar . Given a symmetric molecule (e.g. N_2 or O_2), the wave function of such a coherent superposition repeats itself every integer multiple of a half-rotation, i.e. at times $T_J = N_J \tau_J / 2$ with $N_J \in \mathbb{N}$. Figure 2.5 indicates all these time moments T_J for all the $(|J\rangle, |J+2\rangle)$ wave packets. Black and red markers represent the two independent rotational progressions of even and odd quantum numbers J , respectively. Note that due to the nuclear spin statistics some spin isomers may not be allowed, e.g. in oxygen $^{16}\text{O}_2$ even values of J are prohibited

2.3. Laser-kicked molecular rotor

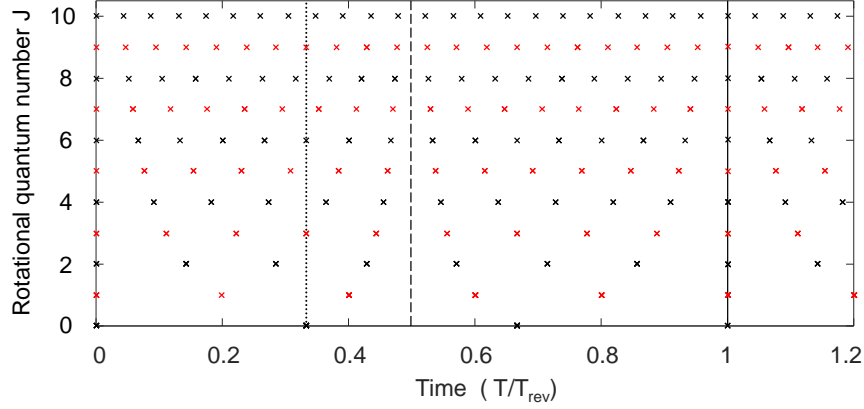


Figure 2.5: Resonance map: Markers indicate all time moments at which a coherent rotational wave packet consisting of two states, $|J\rangle$ and $|J+2\rangle$, completes half a classical rotation τ_J . Time is expressed in units of the molecular revival time T_{rev} . The dotted, dashed and solid lines indicate the third, half and full quantum resonance, respectively.

(Sec. 2.3.9). We refer to all the individual times T_J as “fractional quantum resonances” and we address the plot itself as the “resonance map”.

For a rigid rotor, $E_J = hcBJ(J+1)$ and the rotational period becomes $\tau_J = T_{\text{rev}}(J+3/2)^{-1}$, with the J -independent revival time $T_{\text{rev}} = (2cB)^{-1}$. The map is universal since it is plotted as a function of the dimensionless time T/T_{rev} . For a non-rigid rotor, however, the map will depend on the choice of the molecule and its centrifugal terms. In Fig. 2.5 for the low quantum numbers $J \leq 10$ the effect of centrifugal distortion is not yet visible.

Every laser pulse in a periodic sequence will interfere with the rotational wave packet created by the previous pulses. Again, we start by looking at the excited ($|J\rangle, |J+2\rangle$) wave packet between two neighbouring states. If the time T between two consecutive laser kicks coincides with a fractional resonance T_J , then this wave packet has evolved by $N_J = T/T_{\text{rev}} \times (2J+3)$ half rotations during its free evolution. This means that the next laser pulse ‘kicks’ the molecule in the same direction as the previous pulse, enhancing the rotational excitation of the corresponding wave packet. At all other times $T \neq T_J$ the period of the pulse train is out of phase with the ($|J\rangle, |J+2\rangle$) wave packet and the rotational excitation is suppressed.

Quantum resonance

At the timing known as the quantum resonance, when $T = T_{\text{rev}}$, all wave packets perform an integer number of half-rotations with $N_J = 2J + 3$. In Fig. 2.5, these times $T_J = (2J + 3) \times \tau_J/2$ lie on a vertical trajectory (solid line). Thus, a resonant pulse train with a period $T = T_{\text{rev}}$ is equally efficient in exciting all molecules in the ensemble, regardless of their angular momentum [192]. However, this is only true for rigid rotors. For non-rigid rotors, the quantum resonance T_{rev} becomes J -dependent and, therefore, impossible to satisfy for all quantum states simultaneously. In our map, the dots will no longer line up along a vertical line above $T/T_{\text{rev}} = 1$. Consequences of the centrifugal distortion are investigated in Sec. 5.3 and 5.4.

Fractional quantum resonance

Back to Fig. 2.5, we point out that all the $(|J\rangle, |J+2\rangle)$ wave packets complete an integer number of half-rotations at different time moments. However, there are times when several wave packets corresponding to different values of J are in phase simultaneously. Those are called “fractional resonances”, because a fraction of the total wave function revives to its initial state. An example of a lower-order fractional resonance, $T/T_{\text{rev}} = 1/3$, is plotted as the dotted line. Here, the quantum states $J = 0, 3, 6, \dots$ are resonantly excited, as they complete $N_J = 1, 3, 5, \dots$ half rotations, respectively. All other states are out of phase. At higher-order fractions with $T_J/T_{\text{rev}} = N_J/(2J + 3)$, fewer states are simultaneously resonant.

The resonance map, although quite simple, proves to be very helpful in the explanation of many observations. In section 5.1, we present Raman spectra after the excitation with different periodic pulse trains. By tuning the train period and having a detection accuracy of individual rotational states, we experimentally verify the resonance map of Fig. 2.5. The study of the kicked rotor crucially depends on the choice of the pulse train period, in particular whether it coincides with a fractional resonance or not. We will return to the resonance map in several instances, e.g. in Sec. 5.2 to study periodic excitations on fractional quantum resonances, in Sec. 5.3 to investigate periodic excitation around the full quantum resonance, and in chapters 6 & 7 to examine the phenomenon of dynamical localization via off-resonant periodic excitation.

2.4. Correspondence to crystalline solids

	B_e [cm ⁻¹]	α_e [cm ⁻¹]	B [cm ⁻¹]	D [cm ⁻¹]	T_{rev} [ps]	$\Delta\alpha$ [Å ³]
¹⁴ N ₂	1.9982	0.0173	1.9896	5.76E-6	8.383	0.69
¹⁶ O ₂	1.4376	0.0159	1.4297	4.84E-6	11.666	1.08

Table 2.1: Molecular constants and parameters for N₂ and O₂.

2.3.9 Choice of molecule

All experiments are conducted with either oxygen or nitrogen molecules for several reasons: (1) Our Raman detection technique (see Sec. 4.1) is capable of resolving individual rotational states, whose spacing is given by the energy separation of neighbouring rotational states and is bigger for lighter molecules. (2) The revival times T_{rev} are on the order of 10 ps, which allows the generation of multiple pulses in a periodic sequence via our pulse shaping techniques (see Sec. 3.3). (3) Both molecules are non-toxic gases that are easy and safe to handle in the laboratory.

Necessary molecular constants are taken from the NIST Chemistry Webbook [81] and shown in the table with other derived parameters. The rotational constant $B = B_e - \alpha_e(v + 1/2)$ is calculated for the vibrational ground state $v = 0$. Higher order terms, beyond the centrifugal constant D , are not necessary. And to calculate the kick strength of our laser pulses we require the polarizability anisotropy $\Delta\alpha$, whose values are taken from Ref. [8].

Molecules can often exist in different states, called nuclear spin isomers. These are found by evaluating the symmetry of the total wave function with respect to the exchange of two identical nuclei. Oxygen ¹⁶O has a zero nuclear spin ($I = 0$). Oxygen molecules (¹⁶O₂) can therefore only exist in odd rotational states. The nuclear spin of ¹⁴N is $I = 1$ which yields a 2:1 statistical ratio of even to odd rotational states in molecular nitrogen (¹⁴N₂) [79].

2.4 Correspondence to crystalline solids

In this section we outline the similarities of our kicked rotor system to that of a seemingly unrelated crystalline solid, which was first analysed by Fishman and coworkers in 1982 [52].

We start with the solid state system of an electron in a periodic crystal, Sec. 2.4.1, to introduce the important concepts of reciprocal lattice, Brillouin zone and Bragg reflection. Note, that in this work we will always refer to a

one-dimensional lattice, where vectors like \vec{k}, \vec{r}, \dots reduce to scalars k, r, \dots . Bloch's theorem (Sec. 2.4.2) and Floquet's theorem (2.4.3) are essential tools to solve Schrödinger equations for periodic problems. The first one is applied to periodic potentials like the electron in a lattice, while the latter one simplifies periodic time-dependent problems like the QKR.

The physical framework in all of our efforts is the tight-binding model. In Sec. 2.4.4 we go over the simplest case for a one-dimensional periodic lattice with only nearest neighbour interactions. Introducing disorder into the system yields the Anderson model, subject of Sec. 2.4.5. We explain the emerging phenomenon of Anderson localization in its original context of electron conduction in metals. Finally, we are ready to make the connection back to the QKR in Sec. 2.4.6. We derive how a quantum rotor in a lattice of angular momentum states can be mapped onto a quantum particle in a one-dimensional lattice. In other words, we show how the QKR can be expressed in the formalism of the Anderson model. Section 2.4.7 describes some specific details for our system of laser-kicked molecular rotors.

2.4.1 The one-dimensional lattice

Free electrons are described by plane waves e^{ikr} with energies $E(k) = \hbar^2 k^2 / 2m$, where k is the wave vector. Once an electron is inside a periodic lattice of atoms, its dynamics becomes 'more interesting'. The equilibrium distance between identical atoms is given by the lattice constant a , which establishes a periodicity $r \rightarrow r + a$. The relationship between the energy of an electron (or frequency $\omega = E/\hbar$) and its wave vector k is described by a dispersion relation, which is also periodic, but in $k \rightarrow k + 2\pi/a$. We stress the importance: Any system that is periodic in *real space* with period a , will also be periodic in *reciprocal space* with periodicity $2\pi/a$ [161, 9, 91]. We define a lattice vector $R = na$ and a reciprocal lattice vector $G = m2\pi/a$ with integers n, m .

The unit cell in the reciprocal lattice is called a *Brillouin zone*. The excitation spectrum of waves in periodic media is given as the dispersion relation $E(k)$. The entire spectrum can be described in the first Brillouin zone, which spans from $-\pi/a \leq k \leq \pi/a$ [161]. A quantity that will be of importance later is the group velocity $v_G = d\omega/dk$: it is the speed at which a wave packet moves. The group velocity vanishes ($v_G = 0$) at the Brillouin zone boundary $\pm\pi/a$ [161, 9, 91]. Here, the electrons, i.e. plane waves, are scattered back due to a mechanism called *Bragg reflection* [161, 9, 91]. This feature of wave propagation in periodic lattices leads to band gaps, i.e. there are energies in the spectrum that do not support any wave-like solutions of

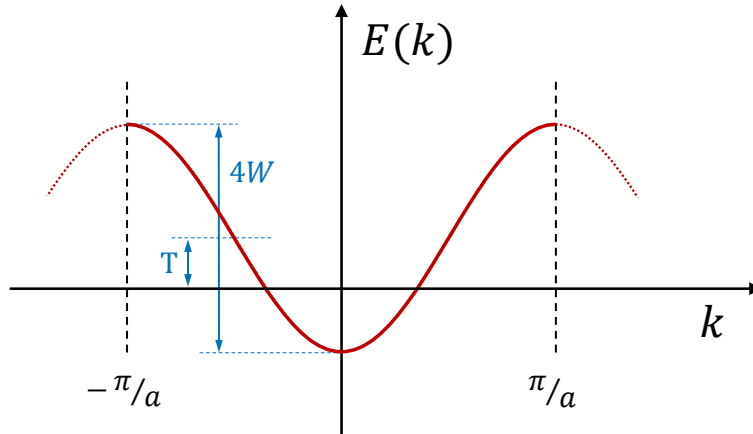


Figure 2.6: Dispersion relation of the one-dimensional tight-binding model.

the Schrödinger equation. In solid state physics, the band structure is used to phenomenologically describe the existence of metals, semi-conductors and insulators. We will be able to connect some of these ideas to the angular momentum lattice of a kicked rotor.

An exemplary dispersion relation, illustrating the concepts of reciprocal space and Brillouin zone, can be seen in Fig. 2.6. Shown is the solution to the one-dimensional tight-binding model with only nearest neighbour interactions, which will be discussed later in the corresponding Sec. 2.4.4.

2.4.2 Bloch's theorem

A Bloch wave ψ_k is the solution of the Schrödinger equation for a periodic potential, i.e. an electron in a periodic lattice. Bloch's theorem states that all Bloch functions can be expressed as a plane wave multiplied by a periodic function $u_k^\alpha(r)$ with the period a of the lattice [162, 161, 91, 9].

$$\begin{aligned}\psi_k^\alpha(r) &= e^{ikr} u_k^\alpha(r) \\ u_k^\alpha(r) &= u_k^\alpha(r+a) .\end{aligned}\tag{2.28}$$

The subscript k is referred to as “quasi-momentum”; it can always be chosen within the first Brillouin zone. Note that $\hbar k$ is not the momentum of an electron but rather a *crystal momentum*. It can be seen as a quantum number describing the electron's state within a band α [162, 9]. Each k can present different states α that belong to different bands. An important

relation follows as

$$\psi_k^\alpha(r+R) = e^{ik(r+R)} u_k^\alpha(r+R) = e^{ikR} e^{ikr} u_k^\alpha(r) = e^{ikR} \psi_k^\alpha(r), \quad (2.29)$$

where we used the invariance of u_k^α towards lattice translations.

Although the atomic potentials that each electron sees are strong, the electron itself still moves like a plane wave through the crystal, modulated by a periodic function. An important difference however, is that the electron momentum has been replaced by a quasi-momentum of the lattice [161].

2.4.3 Floquet's theorem

For time-periodic problems, the Floquet formalism [58] can be utilized to simplify the time-dependent Schrödinger equation $H(t)\psi(t) = i\hbar \frac{\partial \psi(t)}{\partial t}$. It will become obvious that it is closely related to the Bloch formalism used with periodic lattices. Since the QKR presents a periodic problem, we will make use of Floquet's theorem.

If the Hamiltonian $H(t) = H(t+T)$ is invariant under a time translation $t \rightarrow t+T$, then according to Floquet's theorem [78], a solution exists such that

$$\begin{aligned} \psi_\alpha(t) &= e^{-i\omega_\alpha t} u_\alpha(t) \\ u_\alpha(t) &= u_\alpha(t+T). \end{aligned} \quad (2.30)$$

The eigenstates $\psi_\alpha(t)$ are known as *Floquet states* with periodic Floquet modes $u_\alpha(t)$ and the period T . In direct analogy to the quasi-momentum k of Bloch states, the Floquet states are characterized by a quasi-energy $\mathcal{E}_\alpha = \hbar\omega_\alpha$ [189]. Looking at Eq. 2.30, we know that the eigenfunctions can be uniquely defined in a time window of width $\omega = 2\pi/T$ interval. We define the first *Brillouin zone* of the reciprocal lattice as $-\pi/T \leq \omega_\alpha \leq \pi/T$. For different Floquet modes $u_{\alpha'}(t) = u_\alpha(t) \exp(-in\omega t)$ with integers n we merely get shifted energies $\mathcal{E}_{\alpha'} = \mathcal{E}_\alpha + n\hbar\omega$, that can be mapped into the first Brillouin zone. Therefore, the subscript α corresponds to a whole class of solutions with all α' for $n = 0, \pm 1, \pm 2, \dots$.

In other words, if the Hamiltonian is periodic, we can find solutions of the Schrödinger equation that are periodic in time up to a phase factor [189]

$$\psi_\alpha(t+T) = e^{-i\omega_\alpha T} \psi_\alpha(t). \quad (2.31)$$

All linearly independent states with different quasi-energies ($\mathcal{E}_{\alpha'} \neq \mathcal{E}_\alpha + n\hbar\omega$) form a complete basis set [189]. Therefore, the total wave function is a

linear combination of all quasi-energy states $|\Psi(t)\rangle = \sum_{\alpha} c_{\alpha} |\psi_{\alpha}(t)\rangle = \sum_{\alpha} c_{\alpha} e^{-i\omega_{\alpha}t} |u_{\alpha}(t)\rangle$. The time-independent amplitude coefficients are known at time zero $c_{\alpha} = \langle u_{\alpha}(0) | \Psi(0) \rangle$.

Owing to the periodicity of the problem, it is often advantageous to use a stroboscopic description. A one-cycle propagator U is defined such that

$$U(t+T, t) \psi_{\alpha}(t) = \psi_{\alpha}(t+T) . \quad (2.32)$$

Substituting the right-hand side by Eq. 2.31 reveals that the Floquet states are eigenstates of the one-cycle propagator

$$U(t+T, t) \psi_{\alpha}(t) = e^{-i\omega_{\alpha}T} \psi_{\alpha}(t) . \quad (2.33)$$

This means that the Floquet states remain unchanged after each period apart from a phase factor. In practice, we numerically calculate the propagator $U(t+T, t)$ and diagonalize it to find the quasi-energies.

2.4.4 Tight-binding model

We have a one-dimensional periodic chain of atoms located at sites r with a spacing a . The potentials are so large that the electrons spend most of their time close to the core and only occasionally jump to a neighbouring atom - they are tightly bound [162]. Here, we go through the deviation of the most basic tight-binding model, following Ref. [161]. This serves to establish the formalism and our notations. At multiple occasions in this thesis we will map the kicked rotor model onto such a one-dimensional tight-binding model.

The atomic wave function (atomic orbital) $\phi_m(r)$ of the m -th atom satisfies the Schrödinger equation $H_{at} \phi_m(r) = E_{at} \phi_m(r)$, where H_{at} is the Hamiltonian for an isolated atom. In a lattice, however, the electron sees not only the atomic potential but also a contribution $V^{(j)}$ from neighbouring atoms $j \neq m$. Due to the strong binding these contributions are considered small. The tight-binding Hamiltonian for the m -th atom is

$$H = H_{at} + \sum_{j \neq m} V^{(j)} . \quad (2.34)$$

We assume that the wave function of the one-dimensional lattice can be expressed as a linear combination of all individual atomic wave functions

$$|\Psi\rangle = \sum_m c_m |\phi_m\rangle . \quad (2.35)$$

2.4. Correspondence to crystalline solids

In the case of isolated atoms the orbitals are orthogonal $\langle \phi_n | \phi_m \rangle = \delta_{n,m}$, but when the atoms get closer - as it is the case in a lattice - the orthogonality is lifted. Fortunately, the solution of the problem is not much affected by whether the wave functions are orthogonal or not. Thus, we assume orthonormal orbitals for simplicity [161].

We try to solve the time-independent Schrödinger equation $H|\Psi\rangle = E|\Psi\rangle$. Using the linear combination of states and the orthogonality, we arrive at an effective Schrödinger equation

$$\sum_m H_{n,m} c_m = E c_n, \quad (2.36)$$

with the matrix elements $H_{n,m} = \langle \phi_n | H | \phi_m \rangle$.

In the simplest model of only nearest-neighbour interactions, we set $\sum_{j \neq m} V_{n,m}^{(j)} = -W$ for $n = m \pm 1$. This describes a hopping of the electron from the m -th atom to the n -th via the interaction of all $j \neq m$ atoms. We will refer to W as the *hopping term* (dimension of energy). Further, $\sum_{j \neq m} V_{n,m}^{(j)} = T_0$ for $n = m$, which presents an on-site energy shift. We will refer to $T = T_0 + E_{at}$ as the *on-site energy*. The matrix elements of this Hamiltonian are

$$H_{n,m} = T\delta_{n,m} - W(\delta_{n+1,m} + \delta_{n-1,m}). \quad (2.37)$$

This model is in accordance with Bloch's theorem (Sec. 2.4.2). In fact, one can show that the wave function $\Psi(r)$ is indeed a Bloch wave that matches the periodicity of the lattice $\phi(r) = \phi(r + R)$ for all lattice translations R [162]. The tight-binding approach is often used to approximate electronic band structures in solids.

Solution

The ansatz $c_n = \exp(-ikna)$ presents a solution to the effective Schrödinger equation (Eq. 2.36 and 2.37) [161]. The obtained energy spectrum

$$E(k) = T - 2W \cos(ka) \quad (2.38)$$

is periodic in k -space with the period $2\pi/a$ ⁵. Figure 2.6 shows the dispersion relation, with the boundaries of the first Brillouin zone marked by dashed vertical lines. Electrons only have energies in a band spanning a width

⁵We will return to this dispersion relation in Sec. 5.3 when we address the phenomenon of Bloch oscillations.

of $4W$. At a hopping strength $W = 0$, we are at the atomic limit. For increasing W , the atomic orbital spread into bands.

The implications of this model become obvious when we compare the energy $E_e = \frac{\hbar^2 k^2}{2m_e}$ of a free electron with mass m_e , to the dispersion relation. For $ka \ll 1$ equation 2.38 is parabolic $E(k) \propto Wa^2 k^2$. This suggests that electrons near the bottom of the band move like free electrons with an effective mass $m_W = \frac{\hbar^2}{2Wa^2}$ [161]. The larger the hopping term, the smaller the effective mass, and the more freely move the electrons.

2.4.5 Anderson model

We showed that for a periodic (infinite) lattice the electrons can move quasi-freely through the entire lattice. The system experiences no attenuation due to scattering, because the periodic order of scatterers is responsible for a constructive interference of all scattering events. This will no longer be true if we introduce disorder into the lattice.

The Anderson model describes a quantum particle in a lattice where all the lattice sites m have random potentials T_m . As in the standard tight-binding model the hopping term W_r is responsible for the transfer of the particle to the r -th neighbour. The probability amplitude u_m to find the particle at site m is given by the Schrödinger equation

$$T_m u_m + \sum_r W_r u_{m+r} = 0 . \quad (2.39)$$

All solutions u_m , belonging to different quasi-energies, are localized eigenstates. This means that rather than being extended Bloch states that spread over the full periodic lattice, illustrated in Fig. 2.7(a), the eigenstates are now exponentially localized in a disordered lattice with $u_m \sim e^{-|n-m|/l}$, illustrated in Fig. 2.7(b). The probability amplitude to find a particle at site m away from the localization center at n falls off exponentially with a characteristic localization length l .

A simplistic explanation for this intriguing effect can be given as follows. The solutions of the Anderson model are quasi-energy states as we have shown above. The initial system is a wave packet comprised of a finite number of states. At any point of time, we can only populate quasi-energy states that overlap with the initially populated states. It is known that nearly-identical quasi-energies localize at different sites, whereas states with similar localization centers (compared with the localization length) have different quasi-energies [52, 76]. We conclude that the final wave packet will have a discrete energy spectrum with a finite amount of peaks. The wave

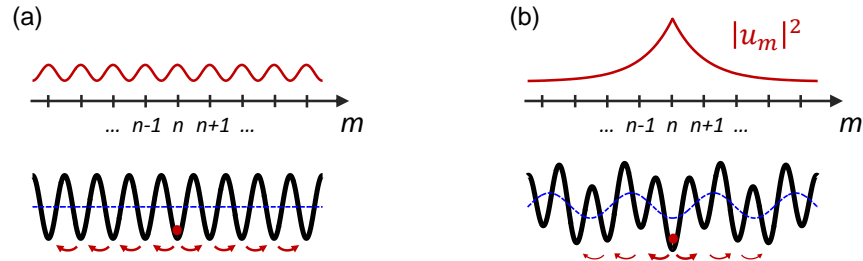


Figure 2.7: (a) Extended Bloch waves (red curve) describe a quantum particle in a periodic lattice (black curve), with lattice sites m . (b) The quantum particle is localized in a disordered lattice (black curve), with a probability (red curve) to find it at site m , which is decreasing exponentially away from the localization center at $m = n$. The disorder in this so-called *bi-chromatic lattice* is produced by adding two periodic lattices of incommensurable periods: here, the one (black curve) from (a) and a second weaker one (blue curve).

packet dynamics associated with such a spectrum must be quasi-periodic. An initial diffusive spreading of the wave packet will turn into a quasi-periodic motion after a certain time, approximately when the wave packet spread has reached the localization length [77]. An unbounded growth of the wave packet is prohibited by Anderson localization.

Anderson localization in one-dimension

The theory of Anderson localization originated more than 50 years ago to describe electron conduction in solid states [6]. Nowadays, the effect has been observed in many different materials using classical as well as matter waves, and the same theory has been applied to other physical systems, for instance the kicked rotor. A brief overview will be given later in the motivation of chapter 6. Here, we discuss the phenomenon in disordered electronic systems, for reviews see Ref. [97, 98].

Electrons do not scatter on ions of a regular lattice, scattering only occurs at random impurities, resulting in a diffusive motion of the electrons, a random walk. In earlier models it was believed that more impurities lower the conductivity according to Ohm's law [9], which did not capture the real behaviour. The conductivity completely vanishes beyond a critical amount of impurities [6], an effect that could only be explained with the wave character of the electron. All scattered waves for each electron self-interfere destruc-

tively, such that the electronic wave function becomes spatially localized, with the probability amplitudes falling off exponentially to the sides. Anderson’s theory describes a disorder-induced phase transition from classical diffusion to complete localization which prohibits any charge transport.

Anderson localization in higher dimensions

In a one dimensional disordered system *all* quantum states are localized [6, 7]. The generalization of Anderson’s theory to higher dimensions took another 15 years [1]. The formulation of a *scaling theory* of localization in 1979 [2] was another milestone. A scaling parameter was introduced that governed the dependence of the localization transition on the size of the material. It was proven that any one- or two-dimensional system localizes regardless of the disorder strength, provided the system size is large enough, a fact that is not true in three-dimensions. Here, the disorder strength determines a critical energy, called the *mobility edge*. Energy states can either be localized (insulator) or extended (conductor) depending on the magnitude of the energy with respect to the mobility edge [153] ⁶.

The observation of Anderson localization in a solid lattice is extremely hard due to several decoherence mechanisms, e.g. lattice vibrations or electron-electron interactions. Signs of “weak localization” (reduced conductivity) have been demonstrated, but “strong localization” (suppressed conductivity) has not been observed in atomic crystals, read the review in Ref. [98].

2.4.6 Mapping the kicked-rotor onto the Anderson model

In the seminal paper from 1982, Fishman *et.al.* gave a mathematical proof that the periodically kicked quantum rotor can be mapped onto the Anderson problem of electronic transport in a one-dimensional disordered lattice [52], drawn in Fig. 2.8(a). The equivalent rotational lattice in Fig. 2.8(b) is built of the “ J -sites” with the occupation probabilities $|c_J|^2$ known through the rotor wave function $|\psi\rangle = \sum_J c_J |J\rangle$. We are going to outline this mapping for the relevant case of laser-kicked molecules. Our derivation is based on the original work of a planar rotor [52, 76], also see the book on quantum chaos by Haake [77]. The extension to real three-dimensional rotors has been made for the case of linear molecules exposed to either periodic microwave fields [28] or ultra-short laser pulses [63].

⁶In general, each energy band of a disordered solid has two mobility edges: The extended states are around the center of each band with the localized states in the wings.

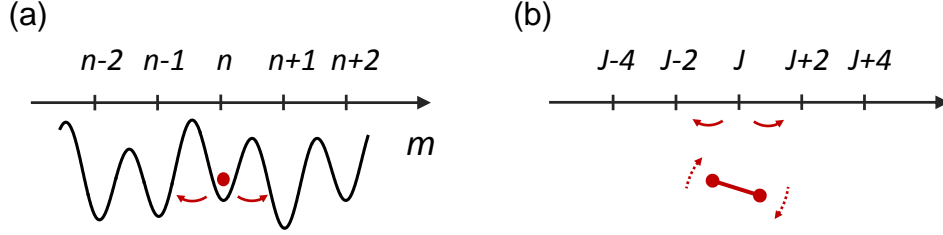


Figure 2.8: (a) Quantum particle in a disordered lattice of lattice sites m . (b) Quantum rotor as an angular momentum lattice with rotational sites J .

We are investigating linear molecules exposed to periodic laser pulses. The pulses are approximated by δ -functions to simplify the mathematics; we refer to Ref. [28, 63] for a treatment with real pulses. The wave function immediately before an instantaneous kick is labelled as ψ^- and the one after a δ -kick is labelled ψ^+ . Due to the periodicity of the kicking, the solutions of the time-dependent Schrödinger equation ψ^\pm must be Floquet states ψ_α^\pm . We look at the evolution over one period T in two independent steps. In the first step, the time between kicks is a free evolution when the Floquet state accumulates a phase. The Floquet state is represented in the basis of the free rotor (spherical harmonics $|J, M\rangle$) with the Hamiltonian H_0

$$\psi_\alpha^-(t+T) = e^{-iH_0T/\hbar} \psi_\alpha^+(t) = e^{-i\mathcal{E}_\alpha T/\hbar} \psi_\alpha^-(t). \quad (2.40)$$

The second part of the equation takes advantage of Floquet's theorem, see Eq. 2.31, with the quasi-energy \mathcal{E}_α . We define the phase $\phi = (\mathcal{E}_\alpha - H_0)T/\hbar$ and reorganize to get

$$\psi_\alpha^-(t) = e^{i\phi} \psi_\alpha^+(t) \quad (2.41)$$

$$u_\alpha^- = e^{i\phi} u_\alpha^+. \quad (2.42)$$

In Eq. 2.42 we rewrote the Floquet states via $\psi_\alpha^\pm(t) = e^{-i\mathcal{E}_\alpha t/\hbar} u_\alpha^\pm(t)$, see Eq. 2.30, and note that it is sufficient to study u_α^\pm [52, 76]. We dropped the t -dependence in the notation of u_α^\pm for simplicity. In the second step, the evolution from immediately before to immediately after the δ -kick is given as

$$\psi_\alpha^+(\theta, t) = e^{iP \cos^2 \theta} \psi_\alpha^-(\theta, t) \quad (2.43)$$

$$u_\alpha^+(\theta) = e^{iP \cos^2 \theta} u_\alpha^-(\theta), \quad (2.44)$$

2.4. Correspondence to crystalline solids

which is written in the angle representation (Eq. 2.21) ⁷. To show the connection to the Anderson model we need to use the one-cycle propagator U , which was introduced earlier in Eq. 2.33. We find [28, 63]

$$U u_{\alpha}^{\pm} = e^{-i\mathcal{E}_{\alpha}T/\hbar} u_{\alpha}^{\pm} \quad (2.45)$$

$$U = e^{-iH_0T/\hbar} e^{iP \cos^2 \theta} . \quad (2.46)$$

Next, we have to transform Eq. 2.42 into the angle representation, which can be done by means of the propagator. We start with the reverse of Eq. 2.44 $e^{-iP \cos^2 \theta} u_{\alpha}^{+}(\theta) = u_{\alpha}^{-}(\theta)$ and propagate it by one cycle by multiplying U from the left side [77]. The left-hand side collapses to $e^{-iH_0T/\hbar} u_{\alpha}^{+}(\theta)$ because of Eq. 2.46 and the right-hand side yields $e^{-i\mathcal{E}_{\alpha}T/\hbar} u_{\alpha}^{-}(\theta)$ due to Eq. 2.45. The combination yields the desired expression in angle representation:

$$u_{\alpha}^{-}(\theta) = e^{i\phi} u_{\alpha}^{+}(\theta) . \quad (2.47)$$

A new vector is defined $u_{\alpha}(\theta) = \frac{1}{2}[u_{\alpha}^{+}(\theta) + u_{\alpha}^{-}(\theta)]$ as well as an Hermitian operator $W(\theta)$ [52, 76, 77], its relevance will be discussed shortly

$$u_{\alpha}(\theta) = \frac{u_{\alpha}^{+}(\theta)}{1 + iW(\theta)} = \frac{u_{\alpha}^{-}(\theta)}{1 - iW(\theta)} . \quad (2.48)$$

Using these relations, we substitute $u_{\alpha}^{\pm}(\theta)$ in Eq. 2.47.

$$[1 - iW(\theta)] u_{\alpha}(\theta) = e^{i\phi}[1 + iW(\theta)] u_{\alpha}(\theta) , \quad (2.49)$$

which is followed by a separation into two terms, with and without $W(\theta)$ dependence

$$i \frac{1 - e^{i\phi}}{1 + e^{i\phi}} |u_{\alpha}\rangle + W(\theta) |u_{\alpha}\rangle = 0 . \quad (2.50)$$

The states are $|u_{\alpha}\rangle \equiv u_{\alpha}(\theta)$ in angle representation and $|J, M\rangle$ in angular-momentum representation, which are the eigenstates of the free rotor with E_J the eigenvalues, $H_0|J, M\rangle = E_J|J, M\rangle$. Per definition $i \frac{1 - e^{i\phi}}{1 + e^{i\phi}} = \tan(\frac{\phi}{2})$ and we relate the tangent function to an energy $T_J^{(\alpha)} \equiv \tan(\frac{\phi}{2})$. All that is left to do is a projection onto the angular momentum states

$$\begin{aligned} \langle J, M | T_J^{(\alpha)} | u_{\alpha} \rangle + \langle J, M | W(\theta) | u_{\alpha} \rangle &= 0 \\ T_J^{(\alpha)} \langle J, M | u_{\alpha} \rangle + \sum_{J'} \langle J, M | W(\theta) | J', M \rangle \langle J', M | u_{\alpha} \rangle &= 0 . \end{aligned} \quad (2.51)$$

⁷A verification of this equation and details were discussed earlier in Sec. 2.3.6.

2.4. Correspondence to crystalline solids

Since the quantum number M does not change in the interaction (Sec. 2.3.6) it is treated as a parameter.

$$T_J^{(\alpha)} u_J^{(\alpha, M)} + \sum_{J'} W_{J, J'}^{(M)} u_{J'}^{(\alpha, M)} = 0 . \quad (2.52)$$

The mapping between Anderson's tight binding model and the periodically kicked rotor is complete. The equation for $u_J^{(\alpha, M)} = \langle J, M | u_\alpha \rangle$ matches the Schrödinger equation of a quantum particle in a lattice with the *on-site energy* $T_J^{(\alpha)}$ and the *hopping term* $W_{J, J'}^{(M)}$ [63]

$$T_J^{(\alpha)} = \tan \left[\frac{(\mathcal{E}_\alpha - E_J)T}{2\hbar} \right] \quad (2.53)$$

$$W_{J, J'}^{(M)} = \langle J, M | W(\theta) | J', M \rangle . \quad (2.54)$$

The probability amplitude to find the quantum particle at site J is given by $u_J^{(\alpha, M)}$. Considering Eq. 2.44 and 2.48 we can express the kicking operator in terms of $W(\theta)$ as [77, 28, 63]

$$e^{iP \cos^2 \theta} = \frac{1 + iW(\theta)}{1 - iW(\theta)} , \quad (2.55)$$

which tells us more about the 'hopping operator' $W(\theta) = \tan \left[\frac{P \cos^2 \theta}{2} \right]$.

2.4.7 Anderson model of the laser kicked rotor

We evaluate the details of the Anderson model (Eq. 2.52) in the case of linear molecules that are periodically kicked by ultra-short laser pulses. The periodic lattice of this true quantum rotor are the angular momentum states J . The effective lattice constant is $\Delta J = 2$ because only states of the same parity are coupled. The energies of the rotational states are $E_J = hc[BJ(J+1) - DJ^2(J+1)^2]$, with the rotational constant B and the centrifugal constant D . And the on-site energy term (Eq. 2.53) is given by $T(J)$ and $\phi(J)$

$$\begin{aligned} T(J) &= \tan[\phi(J)] \\ \phi(J) &= \pi T \left(\frac{\mathcal{E}_\alpha}{\hbar} - cBJ(J+1) + cDJ^2(J+1)^2 \right) \\ &= \frac{\tau}{4} \left(\frac{\mathcal{E}_\alpha}{\hbar cB} - J(J+1) + \frac{D}{B} J^2(J+1)^2 \right) , \end{aligned} \quad (2.56)$$

2.4. Correspondence to crystalline solids

as a function of the period T , or alternatively, as a function of the effective Planck constant $\tau = 2\pi T/T_{\text{rev}} = 4\pi cBT$. The molecular constants B and D are irrational numbers, which means that under most conditions the values of $\phi(J)$ modulus π uniformly cover all angles. Consequently, the energies T_J that follow from the nonlinear tangent function are distributed in a pseudo-random fashion. The result is dynamical localization in the angular momentum space [59, 63]. Chapter 6 is dedicated to the experimental investigation of this phenomenon.

When we excite the rotor with a period that coincides with the quantum resonance at $T = T_{\text{rev}} = (2cB)^{-1}$, the energies T_J are not pseudo-random anymore. However, this statement applies only to small rotational states J , when we can neglect the centrifugal term

$$\phi_{\text{rev}}(J) = \frac{\pi}{2} \left(\frac{\mathcal{E}_\alpha}{hcB} - J(J+1) \right). \quad (2.57)$$

The phase $\phi_{\text{rev}}(J)$ modulo π is independent of J and the on-site energy of neighbouring states will be constant. Similar non-random energies are obtained at fractional resonances $T = \frac{p}{q}T_{\text{rev}}$ with integers p, q . All these resonance excitation scenarios are studied in chapter 5. In section 5.3 we will investigate how the localized states under non-resonant excitation turn into extended Bloch states when we tune to the quantum resonance. The phenomenon of Bloch oscillations will be demonstrated.

We summarize the mapping between the one-dimensional Anderson model and the QKR and emphasize the connections and differences in table 2.4.7.

2.4. Correspondence to crystalline solids

Electron in a one-dimensional disordered lattice	Quantum kicked rotor (off-resonant)
lattice in real space	ladder of rotational states
stationary potential	time-dependent potential
hopping strength	kick strength
random disorder of on-site energy	pseudo-random rotational on-site energy
Anderson localization in real space	dynamical localization in angular momentum space
interactions between electrons, phonons	non-interacting

Table 2.2: Comparison of the electron in a disordered lattice versus a quantum kicked rotor.

Chapter 3

Techniques I: Generation of a long and high-energy femtosecond pulse sequence

Series of ultra-short laser pulses, also known as “pulse trains”, have found widespread use in the field of quantum coherent control of matter with laser light (for a recent review of this topic, see [177] and references therein). Numerous applications require multiple pulses of relatively high intensity, on the order of 10^{13} to 10^{14} W/cm², to attain the regime of strong-field interaction with each pulse, just below the damage threshold of the material system under study. Using coherent control of molecular rotation - an area of our own expertise - as only one representative example: Sequences of intense ultra-short pulses have been key in enhancing molecular alignment [19, 101, 41] and aligning asymmetric top molecules in three dimensions [102, 139], selective excitation of molecular isotopes and spin isomers [54, 55], initiating uni-directional rotation [57, 90, 193] and controlling gas hydrodynamics [188]. A series of recent works [192, 64, 88] has used high-intensity pulse trains to study the quantum δ -kicked rotor. The great utility of pulse trains stems from two main factors. First, by matching the timing of pulses in the train to the dynamics of the system of interest, e.g. the vibrational or rotational period of a molecule, one can often significantly improve the selectivity of excitation. Second, the ability to redistribute the energy among multiple pulses without losing the cumulative excitation strength enables one to avoid detrimental strong-field effects, such as molecular ionization and gas filamentation.

There are two common techniques to produce a pulse train with variable time separation between transform-limited (TL) pulses. In the first technique, the incoming laser pulse is split into 2^n pulses using n nested Michelson interferometers. Even though sequences of up to 16 pulses [160] have been generated using this method, the scheme becomes increasingly more difficult to implement with the increasing value of n . In addition

the control over the pulse timing is rather limited in that it cannot be changed independently for each individual pulse in the train. Similarly limited flexibility is characteristic of a pulse splitting method based on stacking a number of birefringent crystals [195]. The second common approach is based on the technique of femtosecond pulse shaping where the spatially dispersed frequency components of the pulse are controlled in phase and amplitude [179, 47], or via the direct space-to-time conversion [100]. This offers much higher flexibility at the expense of being limited to the relatively low energy trains. The latter limitation is due to both the damage threshold of a typical pulse shaper, and also the necessity to block multiple spectral components in order to generate a train of pulses in the time domain. Phase-only shaping has been often used to create a series of pulses without the loss of energy [181, 182, 46, 140, 134], but in this case, the distribution of the pulse amplitudes within the train is uneven and no control over this distribution is available.

Our objective was to establish a technique to generate femtosecond pulse trains, which simultaneously satisfies the following specific characteristics: (1) consist of a large number of transform-limited pulses; (2) exhibit a relatively flat amplitude envelope; (3) can be easily tuned in terms of the timing of the constituent pulses; and (4) carry energies in excess of 100 μJ per pulse. The method that we developed is based on the combination of a pulse shaper, which provides the often required flexibility in controlling the timing and amplitudes of individual pulses on the time scale of 50 ps, and a set of Michelson interferometers, which enables extending the overall length of the train to much longer times. Key to this approach is the integration of a multi-pass amplifier (MPA), which compensates the energy loss during the pulse shaping stage. We note that although amplification of shaped pulses is commonly used in chirped-pulse amplifiers [48, 131], and has also been employed to amplify pulse sequences [109, 47, 49, 196], pulse trains with the above mentioned specifications have not been demonstrated before.

This chapter presents all the optical components of our setup and explains all the details necessary to produce the above motivated pulse sequences. First, we introduce the representation of ultra-short pulses in the frequency and time domains, as well as the mathematical concepts of pulse shaping in Sec. 3.1. Experimental details about the laser system are given in Sec. 3.2, where we also elaborate on a technique to characterize our femtosecond pulses. This will be of great importance to confirm the quality and accuracy of the generated pulse trains. Section 3.3 deals with pulse shaping via a femtosecond pulse shaper. We explain the optical setup, which is

based on spatial light modulation, and give details of how the generation of pulse sequences is implemented. Section 3.4 is about pulse shaping by means of Michelson interferometers. This is followed by the description of a multi-pass amplifier in Sec. 3.5 which is crucial to reach high-intensity pulse trains. Besides technical considerations, we discuss the performance and limitations of all essential building-blocks: pulse shaper, Michelson interferometer and MPA. The versatility of our techniques is demonstrated with various different pulse trains, e.g. a long pulse train consisting of 84 equally strong pulses.

3.1 Laser pulses and pulse sequences

We establish the mathematical framework and our notation to work with ultra-short pulses. We show the connection between spectral and temporal representation via a series of diagrams for different pulse shapes: transform-limited pulses (Sec. 3.1.1), frequency-chirped pulses (Sec. 3.1.2) and pulse sequences (Sec. 3.1.3).

3.1.1 Transform-limited pulse

Ultra-short pulses are called transform-limited (TL) if their duration is at the lower limit given by the spectral bandwidth of the pulse. This condition is met when the time-bandwidth product is at its minimum, in other words the spectral phase is constant across the whole spectrum of the pulse. The ultra-short pulses of our laser system are Gaussian pulses. Here, we give the electric field \mathcal{E} of a Gaussian pulse whose phase ϕ is independent of frequency ω

$$\mathcal{E}(\omega) = A_0 \cdot \exp\left(-\frac{(\omega - \omega_0)^2}{2\Gamma^2}\right) \equiv \mathcal{E}_{\text{TL}}(\omega) . \quad (3.1)$$

The amplitude of the TL pulse is A_0 , the constant phase $\phi = \phi_0$ has been omitted. The Gaussian is centred around the frequency ω_0 and has a bandwidth of Γ . Fourier transform results in a Gaussian pulse in the time domain

$$\mathcal{E}(t) = \mathcal{E}_0 \cdot \exp\left(-\frac{t^2}{2\tau^2}\right) \exp(i\omega_0 t) , \quad (3.2)$$

with the amplitude $\mathcal{E}_0 = A_0\Gamma/\sqrt{2\pi}$ and the duration $\tau = 1/\Gamma$. A larger bandwidth will thus yield shorter pulses with higher amplitudes. The exact derivation is given in appendix D.1.

3.1. Laser pulses and pulse sequences

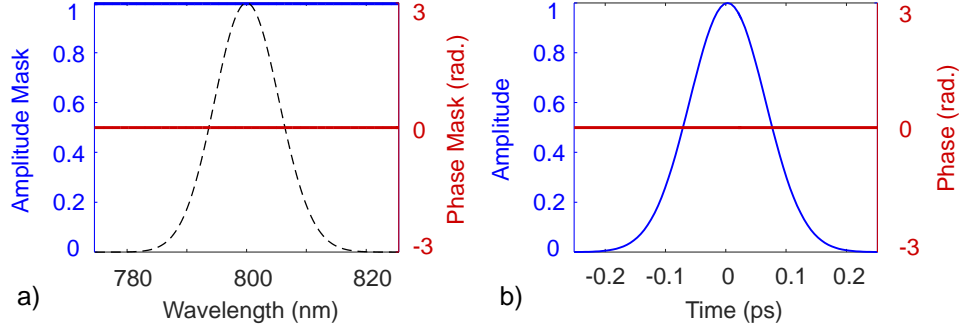


Figure 3.1: **(a)** Amplitude mask (blue line) and phase mask (red line) applied to the electric field of a TL pulse (black dashed line), shown in the spectral domain. **(b)**. Amplitude (blue line) and phase (red line) of the corresponding electric field in the temporal domain. Electric fields are normalized to unity.

The intensity $I(t)$ of a pulse is proportional to $|\mathcal{E}(t)|^2$ and can be calculated with the expression

$$I(t) = \frac{c\epsilon_0}{2} \mathcal{E}(t)^2, \quad (3.3)$$

where ϵ_0 is the vacuum permittivity and c the speed of light.

To illustrate the transformation of the electric field of any laser pulse from the spectral domain to the time domain and vice versa, we introduce a diagram showing both domains in two separate plots. Figure 3.1 illustrates this for a TL pulse. Panel **(a)** presents the electric field of a given pulse \mathcal{E}_{TL} as the black dashed line, normalized to unity. The field is plotted as a function of the wavelength λ , which is related to the frequency as $\omega = 2\pi c/\lambda$. The pulse has a central wavelength of 800 nm with a bandwidth of 9 nm (FWHM), corresponding to the parameters of our Ti:Sapph laser system⁸. Our approach of pulse shaping allows for the individual control of the amplitude and the phase of all spectral components, which is done with the help of a spatial light modulator (SLM). A detailed description of the pulse shaper follows in Sec. 3.3. The SLM consists of two masks that are used to implement an amplitude function A_{SLM} , plotted as the solid blue line (left axis, normalized to unity), and a phase function ϕ_{SLM} , plotted as the solid red line (right axis, in radians). Here, for the trivial case of a TL pulse

⁸ For a Gaussian pulse, the expression $x_{\text{FWHM}} = 2\sqrt{2\ln 2} x_\sigma \approx 2.3548 x_\sigma$ is used to convert the $1/e^2$ width to FWHM.

3.1. Laser pulses and pulse sequences

neither amplitude $A_{\text{SLM}}(\omega) = 1$ nor phase $\phi_{\text{SLM}}(\omega) = 0$ are modulated. Panel **(b)** displays the electric field of the shaped pulse in the time domain $\mathcal{E}(t)$. It is obtained by calculating the Fourier transform of the final electric field in the spectral domain which is given by the expression

$$\mathcal{E}(\omega) = \mathcal{E}_{\text{TL}}(\omega) \cdot A_{\text{SLM}}(\omega) \cdot \exp[i\phi_{\text{SLM}}(\omega)] . \quad (3.4)$$

The phase $\phi(t)$ is plotted as the solid red line (right axis, in radians) and the amplitude $A(t)$ as the solid blue line (left axis). For the case of a TL pulse, shown here, the amplitude is normalized to unity. For all other shaped pulses, shown later, the amplitude is normalized to the amplitude of the TL pulse. This will allow an easy comparison of the absolute pulse amplitudes in each individual pulse of different pulse trains. In the following subsections, we will frequently revisit this type of diagram. The color coding and the axes will always remain the same.

3.1.2 Linearly-chirped pulse

Cutting the bandwidth will lead to longer pulses. Another possibility to *stretch* pulses is to introduce a quadratic phase $\phi(\omega) = \frac{\alpha'}{2}(\omega - \omega_0)^2$ with the spectral chirp α' . This concept is used in the chirped-pulse amplification, see Sec. 3.5.1. Now, the electric field in Eq. 3.1 acquires the additional phase term

$$\mathcal{E}(\omega) = \mathcal{E}_{\text{TL}}(\omega) \cdot \exp[i\phi(\omega)] \quad (3.5)$$

$$= A_0 \cdot \exp\left(-\frac{(\omega - \omega_0)^2}{2\Gamma^2} + i\frac{\alpha'}{2}(\omega - \omega_0)^2\right) . \quad (3.6)$$

A similar Fourier transform shown in appendix D.2 yields the electric field of a Gaussian pulse in the time domain

$$\mathcal{E}(t) = \mathcal{E}_0 \cdot \exp\left(-\frac{t^2}{2\tau^2}\right) \exp\left(i\omega_0 t - i\frac{\alpha}{2}t^2\right) , \quad (3.7)$$

with the temporal phase $\phi(t) = \omega_0 t - \frac{\alpha}{2}t^2$ and the temporal chirp α . These pulses are called linearly-chirped because their instantaneous frequency changes in a linear fashion $\omega(t) = d\phi/dt = \omega_0 - \alpha t$. The relation between bandwidth and duration is given by $\tau^2 = (1 + \alpha'^2\Gamma^4)/\Gamma^2$ and the one between temporal chirp α and spectral chirp α' by $\alpha = \alpha' \Gamma^2/\tau^2$ (for details see appendix D.2). If there is no chirp $\alpha' = \alpha = 0$, we obtain the limit of a TL pulse. For a non-zero chirp, the pulse duration increases with larger chirp values α' .

3.1. Laser pulses and pulse sequences

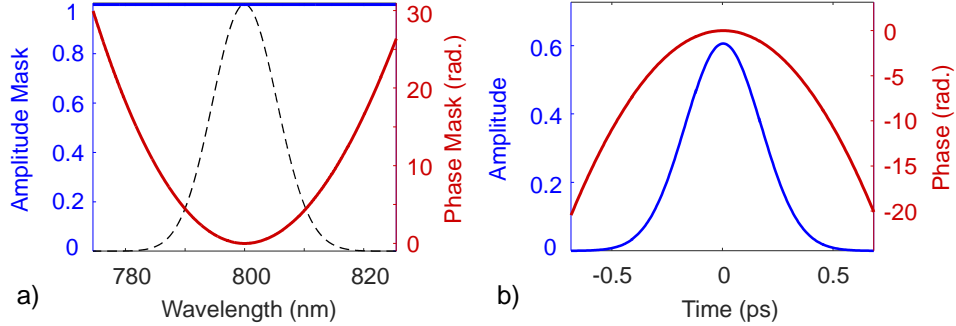


Figure 3.2: **(a)** Amplitude mask (blue line) and phase mask (red line) for a frequency-chirped pulse with $\alpha' = 10.000 \text{ fs}^2$, applied to the electric field of a TL pulse (black dashed line, normalized to unity), shown in the spectral domain. **(b)** Amplitude (blue line, normalized to the TL pulse in Fig. 3.1) and phase (red line) of the corresponding electric field in the temporal domain.

The interplay between the spectral and temporal domains for a linearly-chirped pulse is shown in Fig. 3.2. To achieve such a pulse with the pulse shaper, phase-only shaping is sufficient. This means, that we do not lose any energy in the process; the amplitude mask $A_{\text{SLM}}(\omega) = 1$ does not cut any frequencies. The energy is merely distributed over a longer time, which explains the drop in amplitude of the stretched pulse.

3.1.3 Pulse sequences

We are interested in creating pulse sequences where each individual pulse is a replica of the initial TL pulse with a duration of $\Delta t_{\text{FWHM}} = 130 \text{ fs}$. In the time domain, we design a pulse train of N pulses; $N \in \mathbb{N}$ is a natural number. The train is strictly periodic with a period T and all pulses have the same amplitude. We call this a *flat* pulse train. A schematic is shown in Fig. 3.3. The electric field of such a sequence is described as

$$\mathcal{E}(t) = \sum_k \mathcal{E}_0 \exp\left(-\frac{(t-t_k)^2}{2\tau^2} + i\omega_0 t\right) \cdot \exp\left(i\frac{\beta}{2}k^2\right). \quad (3.8)$$

We need to sum over all N sub-pulses that are labelled with the index $k = [-\frac{N-1}{2}, -\frac{N-1}{2} + 1, \dots, \frac{N-1}{2} - 1, \frac{N-1}{2}]$. Each term in the sum describes a Gaussian pulse at the time $t_k = kT$, which is a TL pulse (Eq.3.2). We also define a quadratic piecewise chirp β across all sub-pulses by adding a phase to each k -th pulse, which depends quadratically on k . This kind of chirp

3.1. Laser pulses and pulse sequences

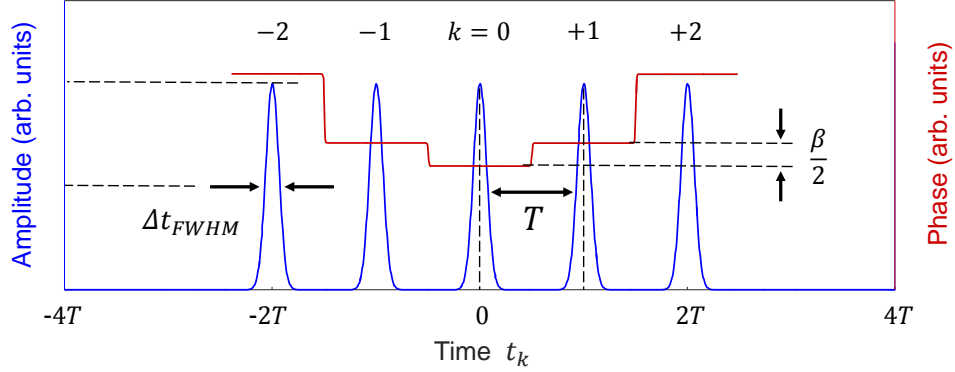


Figure 3.3: Schematic of the amplitude (blue line) and phase (red line) of a flat pulse train in the temporal domain with $N = 5$ pulses and a piecewise quadratic chirp.

has been developed earlier in our group Ref. [154, 156] to execute a process of piecewise adiabatic passage (PAP). In the PAP scheme, population can be transferred in a two-level system in a stepwise adiabatic fashion. In our work, however, the piecewise chirp β plays an important role for a completely different reason: to reduce energy losses in the shaping process (described in this section below).

In appendix D.3 we derive the analytic expression for the corresponding electric field in the spectral domain

$$\mathcal{E}(\omega) = A_0 \exp\left(-\frac{(\omega - \omega_0)^2}{2\Gamma^2}\right) \cdot \sum_k \exp\left(-i(\omega - \omega_0)t_k + i\frac{\beta}{2}k^2\right). \quad (3.9)$$

The term in front of the sum gives the TL spectrum of a single pulse $\mathcal{E}_{\text{TL}}(\omega)$ as in Eq. 3.1. Evaluating the sum and making use of Eq. 3.4 we can then retrieve the spectral amplitude $A_{\text{SLM}}(\omega)$ and the spectral phase $\phi_{\text{SLM}}(\omega)$ needed to obtain the input pulse train

$$A_{\text{SLM}}(\omega) \cdot \exp(i\phi_{\text{SLM}}(\omega)) = \sum_k \exp\left(-i(\omega - \omega_0)t_k + i\frac{\beta}{2}k^2\right). \quad (3.10)$$

Sequences with zero phase

First, we look at the simpler case of $\beta = 0$, when all pulses in the sequence have a zero phase offset with respect to the carrier oscillations ωt . Figure 3.4 plots the spectral and temporal domains of three different pulse trains to

3.1. Laser pulses and pulse sequences

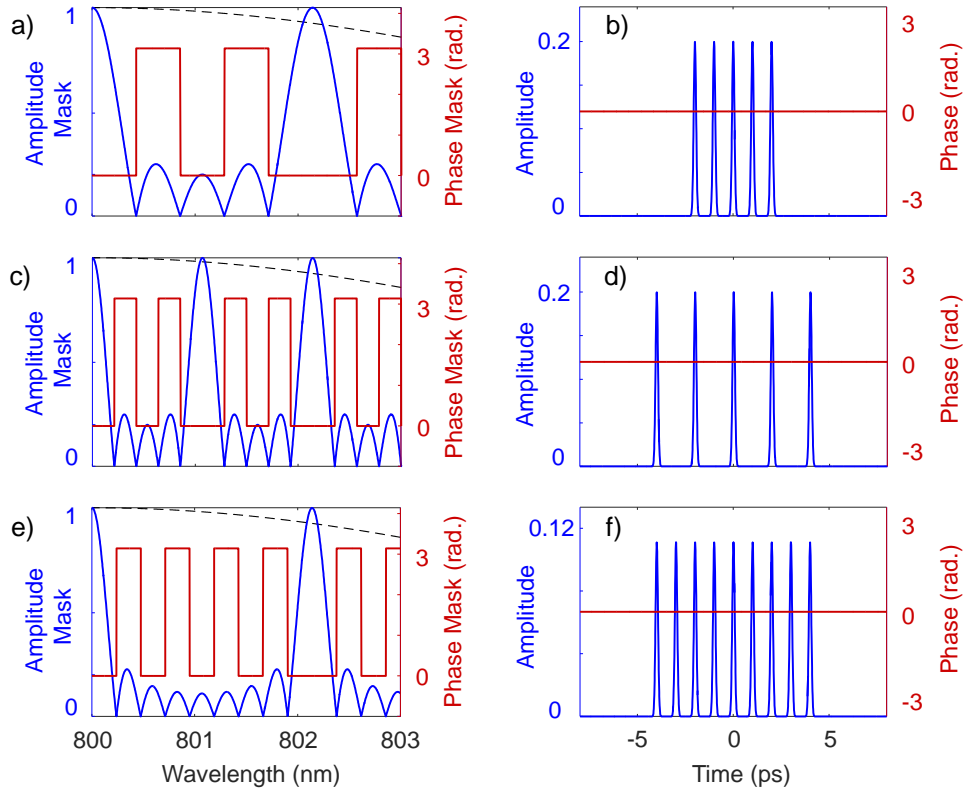


Figure 3.4: **(a,c,e)** Section of the amplitude mask (blue line) and phase mask (red line) for three different pulse trains, applied to the electric field of a TL pulse (black dashed line, normalized to unity), shown in the spectral domain. **(b,d,f)** Amplitude (blue line, normalized to the TL pulse in Fig. 3.1) and phase (red line) of the corresponding electric fields in the temporal domain. The three sequences are characterized by the following pulse numbers and periods: **(a,b)** $N = 5$ & $T = 1$ ps, **(c,d)** $N = 5$ & $T = 2$ ps and **(e,f)** $N = 9$ & $T = 1$ ps.

3.1. Laser pulses and pulse sequences

visualize their dependence on the parameters N and T . From top to bottom, we have a sequence of 5 pulses separated by 1 ps (**a,b**), followed by 5 pulses with twice the period of 2 ps (**c,d**) and at last a train of 9 pulses again spaced out by 1 ps (**e,f**).

To understand the Fourier transformation from one domain to the other, we make use of the *convolution theorem*, see Appendix D.4. A periodic pulse train with a finite number of N pulses that are all of equal amplitude can be described as the multiplication of an infinite pulse train with period T times a squared envelope of width NT . The Fourier transform of a square function yields the sinc function whose width $\delta\omega$ is inversely proportional to NT . We also know, that the spectrum of an infinite pulse train is a frequency comb where the separation of the comb teeth $\Delta\omega$ is inversely proportional to the train period T . Then, according to the convolution theorem (Eq. D.21) this point-wise multiplication in the time domain is equal to the convolution in the frequency domain. Hence, the spectrum of a finite train is a frequency comb convolved with the sinc function, exactly what can be observed in Fig. 3.4. When we double the pulse train period from (**b**) to (**d**), the frequency separation between the main comb teeth $\Delta\omega \propto 1/T$ from (**a**) to (**c**) is split in half. The period from (**b**) to (**f**) remains the same, and so does the spacing $\Delta\omega$ from (**a**) to (**e**). Each main comb tooth has the shape of the sinc function $\sin(x)/x$, when one considers the π phase jumps for its negative values. The width of the sinc function $\delta\omega \propto 1/(NT)$ decreases by a factor of two from (**a**) to (**c,e**) since the total duration of the pulse train increases from 4 ps (**b**) to 8 ps (**d,f**).

The same convolution theorem can be applied a second time in the reverse direction (Eq. D.20) to derive the minimum duration of each individual pulse in the sequence. The electric field due to the amplitude and phase masks has to be multiplied with the electric field of a TL pulse. This Gaussian TL pulse is given by the laser system (dashed black line in (**a,c,e**)). The Fourier transform of a Gaussian function remains a Gaussian function. Therefore, we have to convolve the electric field in the time domain with a Gaussian function. This explains that each sub-pulse in (**b,d,f**) has a duration equal to the single pulse duration prior to shaping.

In conclusion, we apply amplitude and phase shaping to achieve a periodic pulse train. The phase mask is comprised of π -steps, whereas the amplitude mask cuts out a comb-like structure. The (partial) suppression of frequencies leads to a reduced energy in the shaped output pulses. The ratio $\delta\omega/\Delta\omega = 1/N$ estimates the amount of energy remaining in the pulse train (PT) after shaping. We confirm the validity of this approximation by calculating the energy throughput \mathcal{T} . The energy W of each shaped pulse

3.1. Laser pulses and pulse sequences

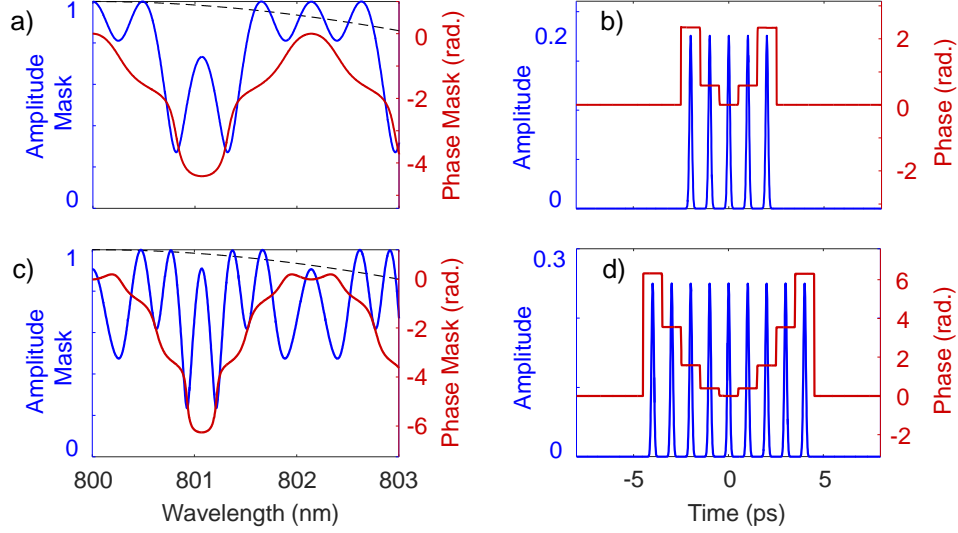


Figure 3.5: **(a,c)** Section of the amplitude mask (blue line) and phase mask (red line) for two different pulse trains in the PAP scheme, applied to the electric field of a TL pulse (black dashed line, normalized to unity), shown in the spectral domain. **(b,d)** Amplitude (blue line, normalized to the TL pulse in Fig. 3.1) and quadratic piecewise phase (red line) of the corresponding electric fields in the temporal domain. The two sequences are characterized by the following parameters: **(a,b)** $N = 5$, $T = 1$ ps & $\beta = 1.17$ and **(c,d)** $N = 9$, $T = 1$ ps & $\beta = 0.79$.

can be calculated by integrating over its intensity spectrum $W \propto \int I(\omega) d\omega$, with $I(\omega) \propto |E(\omega)|^2$. The throughputs $\mathcal{T} = W_{PT}/W_{TL}$ for the three different pulse trains in Fig. 3.4 are **(a)** 20%, **(b)** 20% and **(c)** 11.1%.

Sequences with piecewise quadratic phase

Second, we look at the case of $\beta \neq 0$, when all pulses in the sequence change their phase offset from pulse-to-pulse in a stepwise fashion. Originally, the piecewise quadratic phase was intended to emulate the adiabatic population transfer by a single frequency-chirped pulse. We are interested in this shaping scheme because of its higher energy throughput \mathcal{T} , compared to the same pulse train with $\beta = 0$.

In all our experiments, we are using pulse sequences to impulsively excite rotational states via Raman transitions (Sec. 2.3.1). This two-photon process with the electric field $\mathcal{E}_{\text{Raman}}(t) = \mathcal{E}(t)\mathcal{E}^*(t)$ is phase-independent. The

two photons that are absorbed and emitted in the Raman process stem from the same field $\mathcal{E}(t)$ and as such the phases of both photons are identical and cancel each other. As long as the phase offset of each individual pulse in a pulse train is constant, regardless of its absolute value, the Raman field will stay the same. In other words, a piecewise chirp will not alter the rotational Raman excitation. We benefit from this degree of freedom by optimizing β to minimize our shaping losses. It could be shown empirically that the energy throughput will lie around 60% independently of N or T . We do not claim that a piecewise quadratic chirp yields the optimum energy efficiency. However, we were not able to achieve higher efficiencies, with any other empirically chosen phase profiles. Significantly higher throughputs than what we already obtained cannot be expected, therefore further optimization was deemed unnecessary.

Figure 3.5 plots the spectral and temporal domains of two pulse trains in the PAP scheme. Both sequences have a period of 1 ps, one consists of 5 pulses with $\beta = 1.17$ (**a,b**) and the other of 9 pulses with $\beta = 0.79$ (**c,d**). In either case, β has been optimized to a maximum throughput, reaching 61.7% (**a**) and 56.3% (**b**).

Other shaping techniques to create pulse sequences do exist, many of which are based on the phase-only shaping [181, 182, 46, 140, 134]. However, neither of these methods yield the necessary flexibilities needed for our experiments and will therefore not be introduced. All our pulse trains were built as discussed in this section.

3.2 Laser source

We use a Titanium:Sapphire (Ti:Sapph) femtosecond laser system (SpitFire Pro, Spectra-Physics) producing uncompressed frequency-chirped pulses with the spectral bandwidth of 9 nm (FWHM) at the central wavelength of 800 nm, 1 KHz repetition rate and 2 mJ per pulse. Part of the beam (60% in energy) is compressed to 130 fs pulses (FWHM) via a grating-based pulse compressor. It is used as a reference beam in cross-correlation measurements (see Sec. 3.2.1) or as a probe beam in spectroscopy measurements (see Sec. 4.1). The second part (40% in energy) is used for the generation of high energy pulse sequences, typically as uncompressed pulses of 150 ps (FWHM), as described in Sec. 3.3, 3.4, 3.5.

3.2.1 Pulse characterization

Ultra-short pulses are most commonly characterized with a technique known as frequency-resolved optical gating (FROG) [169]. The idea is to do a correlation measurement in which the pulse to be characterized is gated with another pulse. In FROG, the spectrally-resolved auto-correlation of the unknown pulse yields enough information to numerically retrieve the spectral phase and amplitude of the pulse. Rather than using an auto-correlation function, it is also possible to use a well-characterized reference pulse to perform cross-correlation frequency-resolved optical gating (XFROG). Further information about this technique can be found in Ref. [107].

We elaborate on both techniques with our experimental setup shown in Fig. 3.6. Panel **(a)** is used to characterize a single femtosecond pulse, e.g. as produced by our Ti:Sapphire laser system. The incoming beam is split into two equal parts on a beamsplitter. After travelling some distance, both beams are focused onto a nonlinear BBO crystal where they spatially overlap. The generated second harmonic light of each individual beam is blocked. We are solely interested in measuring the sum-frequency signal with a spectrometer. The spectrum is recorded as a function of the temporal delay between both pulses. This way, the unknown pulse is gated by itself and an iterative algorithm can be used to retrieve the spectral amplitude and phase of the pulse. Panel **(b)** shows a slight variation, known as XFROG. Here, the unknown pulse is gated by a well characterized reference pulse, in an otherwise identical procedure. We use XFROG to characterize our pulse sequences. As the reference pulse we use a TL pulse⁹, that has been characterized via FROG.

Figure 3.7(**a** & **b**) show two different XFROG spectrograms corresponding to two different pulse shapes. The spectrum on the vertical axes is recorded with a spectrometer (Photon Control Inc., SPM-002-B) with a resolution of 0.094 nm at a wavelength of 400 nm. The horizontal axes present the delay between the shaped pulse and the reference pulse which is computer-controlled by a delay line [Newport: Motion Controller, ESP301; translation stage, UTS-100CC (for XFROG) & MFA-CC (for FROG)] with a minimum step size better than 7 fs. We refer to such a two-dimensional representation of a pulse in the spectral and time domains as an XFROG trace. Panel **(a)** shows a transform-limited pulse with a symmetric trace. Panel **(b)**, on the other hand, presents a linearly chirped pulse ($\alpha' = 50.000 \text{ fs}^2$); the instantaneous frequency changes linearly over time, while the total band-

⁹For a definition of *transform-limit* (TL) see Sec. 3.1.1.

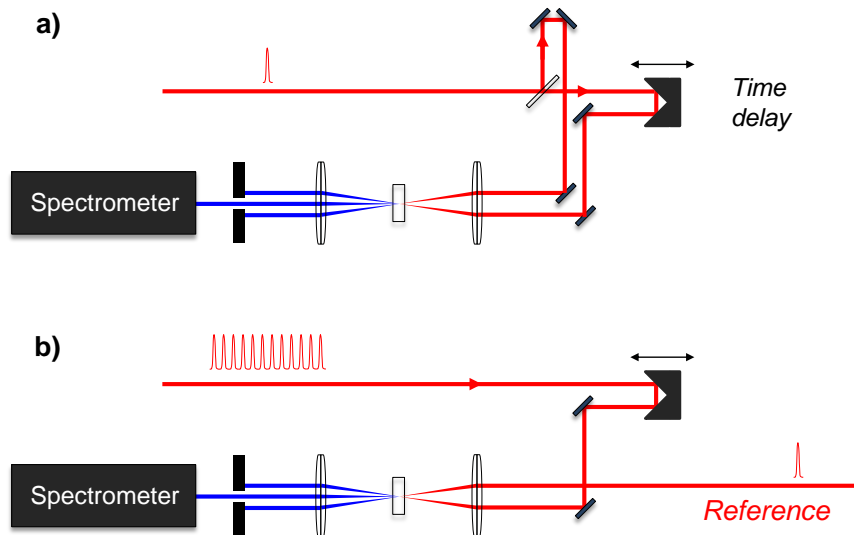


Figure 3.6: Two variations of the experimental setup used for ultra-short pulse characterization: (a) frequency-resolved optical gating (FROG) and (b) cross-correlation frequency-resolved optical gating (XFROG).

width is preserved. To obtain the temporal profile of a pulse, we integrate over the entire spectrum, see Fig. 3.7(c). As expected, frequency chirping (dashed black line) leads to a longer pulse of ≈ 1.4 ps (FWHM) with a lower peak intensity in comparison to the unshaped pulse (red solid line) with a 130 fs duration (FWHM). The procedure equally applies to a pulse sequence. Various examples of different pulse trains will be shown later during the discussion of the shaping techniques.

Compensation of phase distortions

Ultra-short pulses that propagate through any kind of dispersive material, e.g. glass optics, air, etc., do accumulate phase distortions. As a consequence, the spectral phases of a pulse will become frequency dependent, visible in a distorted XFROG trace and leading to longer pulse durations. For the purpose of our experiments, we want to achieve the shortest possible pulse duration, i.e. a transform-limited pulse. We use multiphoton intrapulse interference phase scan (MIIPS) to compensate for all phase distortions [111]. The technique relies on a pulse shaper to apply a spectral phase functions to compensate for the distorted phase of the pulse. The compensation

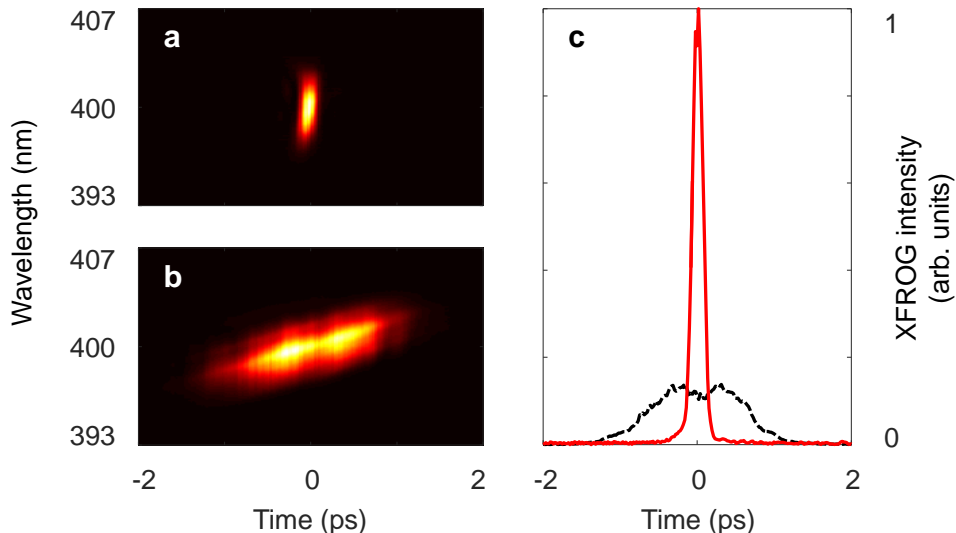


Figure 3.7: XFROG spectrograms: (a) transform-limited 130 fs pulse, (b) linearly chirped 1.4 ps pulse. (c) Their respective temporal profiles as solid-red line and dashed-black line.

function is retrieved iteratively by analysing the second-harmonic spectrum of the pulse. We use the same setup described in Fig 3.6 but measure the second-harmonic signal of the pulse. More details of the MIIPS procedure are given in Ref. [191]. We achieve a 130 fs pulse duration for all pulse shaping scenarios.

3.3 Pulse shaping I: The pulse shaper

The femtosecond pulse shaper allows the creation of pulse sequences with great flexibility. Pulse trains can be formed within certain limitations, namely a minimum pulse duration of 130 fs given by the transform limit of the laser system and a maximum length of the sequence of 50 ps given by the spectral resolution of the shaper, derived below. The ‘magic’ of a pulse shaper is based on spectral phase and amplitude modulation of the femtosecond pulses implemented with a spatial light modulator (SLM). We introduce the optical setup (Sec. 3.3.1), as well as its experimental implementation (Sec. 3.3.2). In particular, we address the method of choice to create pulse sequences and demonstrate the shaping flexibility by showing different pulse trains (Sec. 3.3.3).

3.3. Pulse shaping I: The pulse shaper

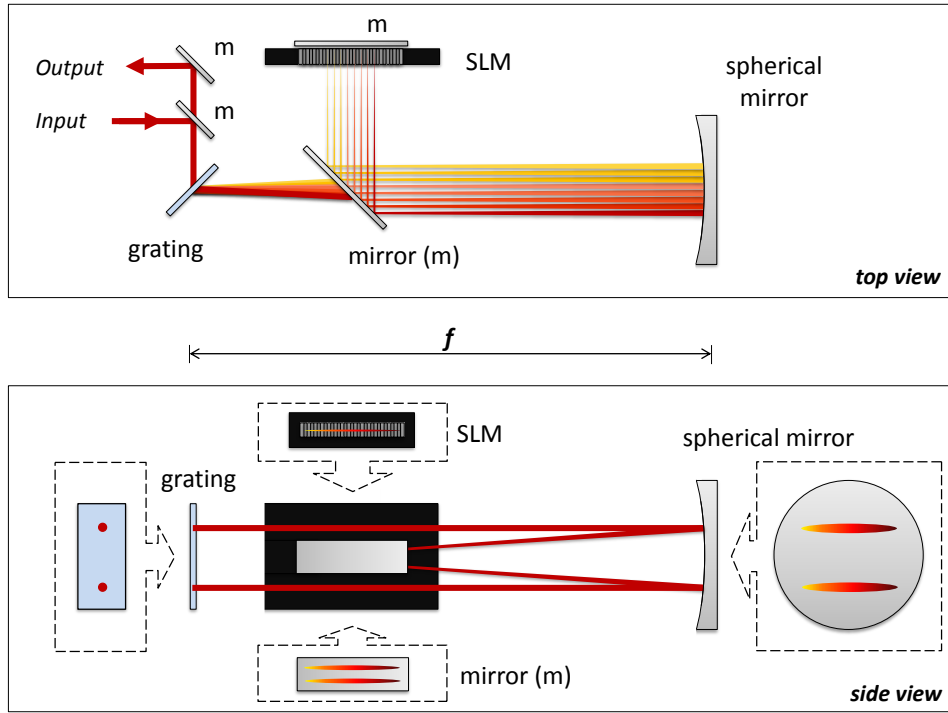


Figure 3.8: Pulse shaper in ' $4f$ '-folded design: top view and side view. The dashed boxes indicate the beam profiles on various optical elements.

3.3.1 Optical setup

We send the laser beam to a femtosecond pulse shaper which is used to split a single pulse into a series of pulses. The shaper, shown schematically in Fig. 3.8, is built in the standard ' $4f$ '-geometry [180] and uses a liquid crystal spatial light modulator (SLM, Cambridge Research and Instrumentation, Inc.).

A transmissive grating (Kaiser Optical Systems, 1800 g/mm) disperses the input beam. A spherical mirror (Edmund Optics, $f = 36$ inch) at the distance f from the grating focuses different frequency components at different locations in the Fourier plane of the shaper, again at the distance f . Here a mirror sends the beam back the same optical path but offset in height, such that we have a non-dispersed, collimated beam at the output of the shaper. The total optical path length sums up to $4f$, hence the name of the design. The optical path can be followed step-by-step in Fig. 3.8 through a top and a side view, which also visualizes the dispersion and focusing of all

spectral components. If no spectral mask is applied in the Fourier plane, the input and output pulses will be identical, in the ideal case that the shaper does not introduce any spatial or spectral distortions due to a misalignment of any optical component. In order to “shape” the femtosecond pulse we introduce a spatial light modulator (SLM) in the Fourier plane, where all frequencies are dispersed and focused. The SLM is the heart of the shaper and it consists of a double-layer 640-pixel mask that is used to control the phase and amplitude of all spectral components of the laser pulse. To achieve any desired waveform of the output pulse, e.g. a pulse train, we first calculate the required frequency masks via the Fourier transform of the target temporal profile and subsequently apply the masks with the SLM. Mathematical details are found in sections 3.1.1 to 3.1.3 and the implementation procedure in section 3.3.2.

The spectral resolution of the pulse shaper of $\Delta\lambda = 0.04$ nm per pixel sets the upper limit for the total duration of the pulse train to $\Delta T = \lambda^2/c\Delta\lambda \approx 50$ ps, where the central wavelength $\lambda = 800$ nm and c is the speed of light in vacuum. Within this window, virtually any pulse shape can be achieved. In this work, we focus on producing pulse sequences.

Pulse shaping can be done with uncompressed pulses, in which case we use a grating compressor at the output of the shaper to compress all pulses in the train. Alternatively, we can compress the pulse prior to the pulse shaping. The choice depends on the amplification process that will follow and is discussed in Sec. 3.5.1. In either case, the minimum duration of each sub-pulse in the train is around 130 fs set by the transform-limited pulse duration of the laser system.

Further details about technical aspects of such a femtosecond pulse shaper have been described in detail in the dissertation of S. Zhdanovich [191]. This includes more information on selecting the appropriate optical components to maximize the shaper resolution, and on aligning and calibrating this specific instrument.

3.3.2 Implementation of pulse sequences

In Sec. 3.1.3, we introduced the mathematical foundation to form a pulse train via phase and amplitude shaping. Here, we will elaborate on the experimental implementation.

The analytically calculated phase and amplitude masks have to be discretized with a step size that matches the resolution of the SLM. Given in units of wavelength, the resolution is $\Delta\lambda = 0.04$ nm per pixel. The peak of the spectrum is placed in the center of the 640-pixel mask. Figure 3.9

3.3. Pulse shaping I: The pulse shaper

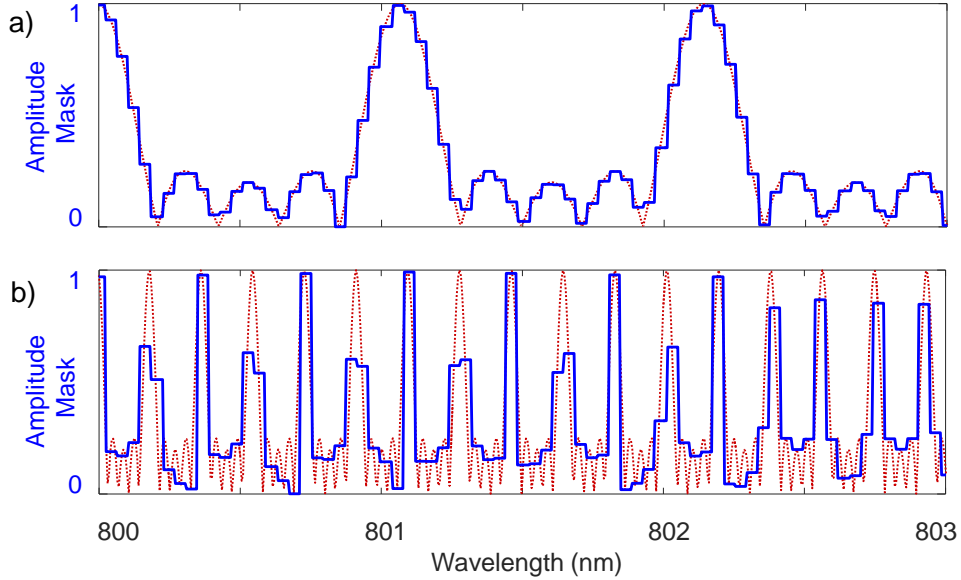


Figure 3.9: Section of an amplitude mask (red dotted line) and its discretized version, matching the experimental SLM resolution, to generate a pulse train with (a) $N = 5$, $T = 2$ ps; $\beta = 0$ or (b) $N = 5$, $T = 11.67$ ps; $\beta = 0$.

shows the discretization of two different pulse sequences. For demonstration purposes, we plot only the amplitude masks in the spectral window from 800 to 803 nm, corresponding to a width of 75 pixels. The center pixel 320 matches the central frequency of $\lambda = 800$ nm. The red dotted lines show the desired amplitude masks, the solid blue lines are the discretized versions. Panel (a) presents the mask to achieve a train of 5 pulses with a 2 ps period. The overall length of the train with 8 ps lies well within the shaper limit of $\Delta T \approx 50$ ps. Panel (b), however, shows an example where the target pulse train reaches the shaper limitation. A train of 5 pulses with a 11.67 ps period spans a total duration of 47 ps. Every comb tooth in the spectrum has the width of only a single pixel of the SLM. A similar pulse train is used e.g. in Sec. 5.4.1, when the period matches the rotational revival time of $^{16}\text{O}_2$ (Sec. 2.3.9).

Figure 3.9(b) reveals one source of inaccuracy in the shape of the experimental pulse train. The discretized function does not describe the amplitude mask well enough and will lead to deviations in the temporal shape. Rather than obtaining a sequence of identical pulses, the amplitudes of the individual pulses will vary. Other discrepancies that we typically observe close

3.3. Pulse shaping I: The pulse shaper

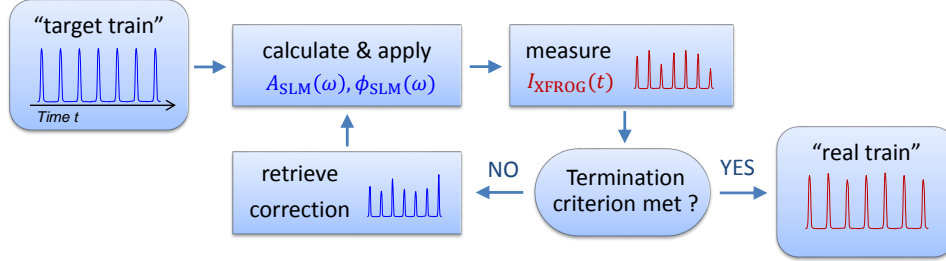


Figure 3.10: Protocol to iteratively compensate for irregularities in the output temporal profile with the objective to reach a flat pulse train.

to the shaper limit are: unwanted pre- and post-pulses appearing outside the 50 ps window, and a spectral chirp of the sub-pulses lying closest to the edge of the 50 ps window.

Pulse train corrections: We developed an approach to minimize shaping errors and inaccuracies in the output pulse sequence. The idea is to pre-compensate for all the discrepancies that occur in the shaping process.

Starting with Eq. 3.8, we introduce more control parameters: Rather than having a flat pulse train, we can adjust the amplitude of each individual pulse; rather than being comprised of TL pulses, each sub-pulse can get a linear chirp; rather than being a strictly periodic pulse train, the period between all pulses can be chosen separately. We use the protocol illustrated in Fig. 3.10 to achieve a flat PT. First, we design the desired pulse train according to the analytic expression in Eq. 3.9 and apply the calculated amplitude and phase masks via the SLM. Next, we measure the intensity profile $I_{\text{XFROG}}(t)$ of the actual shaped pulse via a cross-correlation measurement in the time domain (the technique of XFROG is explained in Sec. 3.2.1). Deviations of all sub-pulses from the ideal are determined and compensated for in the next generation of the pulse train. Via a Fourier transform we obtain the new amplitude and phase masks. The procedure is iteratively repeated until the termination criterion is met and the output shape closely resembles the target pulse train.

The method proved to be very effective, which will be seen in Sec. 3.3.3 and 3.5.3 in several examples. Besides compensating for shaping errors, the procedure also serves to deal with nonlinearities due to the amplification in the MPA, discussed in Sec. 3.5. In addition, the flexibility of the shaping technique enables us to design any arbitrary pulse sequence, e.g. non-periodic sequences or sequences with various sub-pulse amplitudes. Such

sequences will be of importance in almost all of the presented experiments.

3.3.3 Demonstration of pulse sequences

Femtosecond pulse shaping offers the flexibility of creating arbitrary pulse sequences within the limits of the shaper’s temporal and spectral resolution. In Fig. 3.11, we demonstrate this flexibility using the example of a pulse train with nine pulses. The overall energy of the train was set to 1 mJ. A flat train of pulses with almost equal amplitudes (7% flatness) separated by $T = 4$ ps is shown in Fig. 3.11(a). In Fig. 3.11(b), a linear amplitude tilt was applied to the train’s envelope and its sixth pulse was completely suppressed, while the total energy was kept constant at 1 mJ. Figures 3.11(c) and (d) demonstrate our ability to produce high-energy flat-amplitude sequences with multiple periods and completely random timing of pulses, respectively.

3.4 Pulse shaping II: The Michelson interferometer

For some experiments the number of pulses that can be fitted within a 50 ps time frame is not sufficient. In contrast to the pulse shaper, an interferometric setup [160] has no limitation on the overall length of the final pulse train. We built two polarization-based Michelson setups that allow us to quadruple the number of pulses in the sequence and extend its duration to at least four times that produced by the shaper.

In Fig. 3.12, an incoming linearly polarized laser beam is split into two beams with equal amplitude but opposite polarization axes (s & p -polarization) via the combination of a $\lambda/2$ -waveplate and a polarization cube. Each beam is reflected back by a dielectric mirror, passing through a $\lambda/4$ -waveplate twice to flip the polarization axis. The output behind the cube is now a laser beam that consists of two pulses of opposite polarization whose temporal spacing can be adjusted with a computer controlled delay line (Newport: Motion Controller, ESP301; translation stage, MFA-CC). Those optical elements can be put in series n times to split a single pulse into a sequence of 2^n pulses. We implemented this design with two Michelson interferometers $n = 2$. In order to get a final pulse sequence where all pulses share the same polarization we use another $\lambda/2$ -waveplate and a cube to split the pulse train into s & p -polarization. In our setup, we use only p -polarization. Neglecting losses of optical components, polarization multiplexing results in the energy loss of 50%.

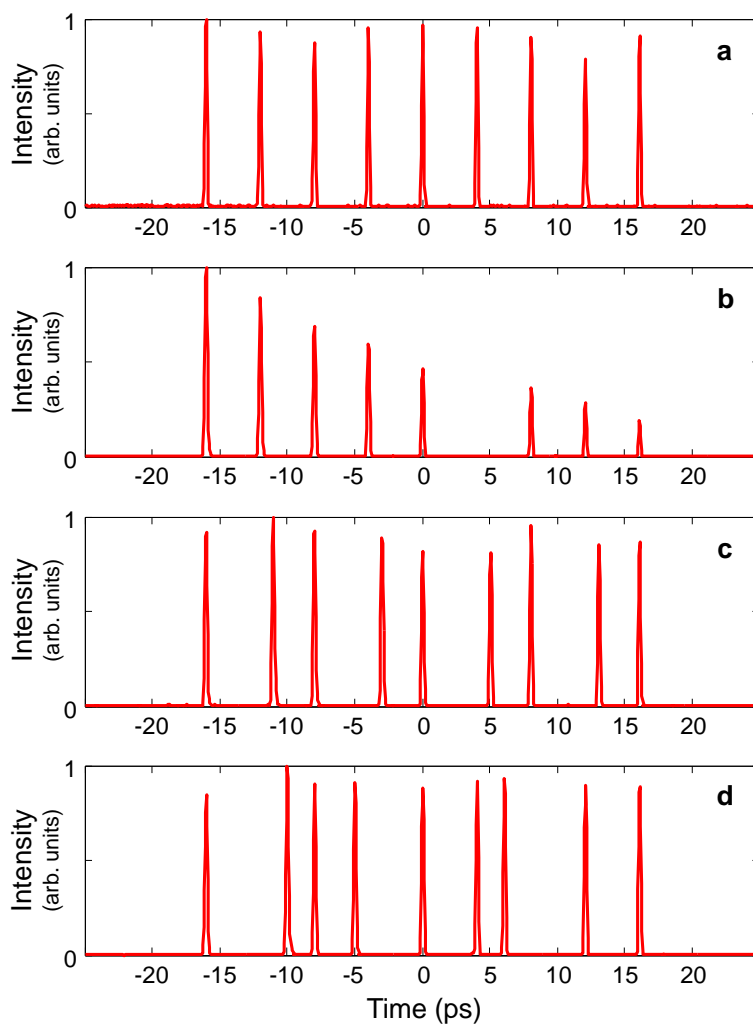


Figure 3.11: Temporal profiles of four different sequences of nine pulses: (a) Periodic train of equal-amplitude pulses separated by 4 ps. (b) Same train with linearly decreasing pulse amplitudes and the sixth pulse suppressed. (c) Flat pulse train with two different time periods of 5 ps and 3 ps. (d) Flat non-periodic pulse sequence with a random timing of pulses.

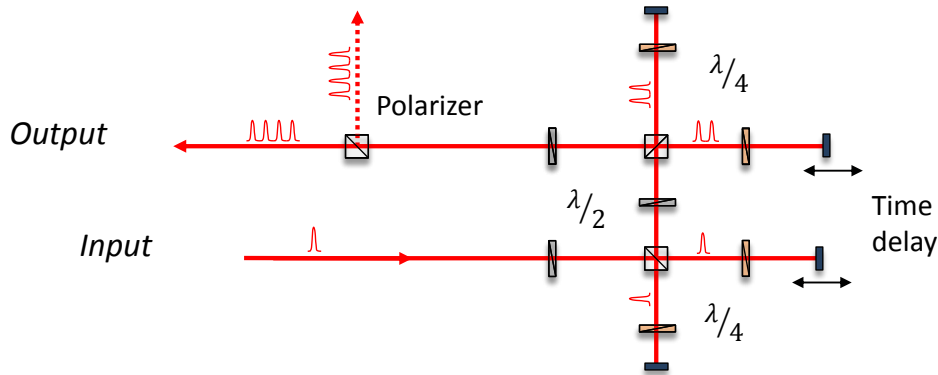


Figure 3.12: Two polarization-based Michelson interferometers quadruple the number of incoming linearly polarized pulses. Computer-controlled delay lines allow variable time delays between the pulses. At the output, half the energy is lost to the opposite polarization.

3.5 Multi-pass amplification

To compensate for the losses of femtosecond pulse shaping and interferometric splitting, we send the long pulse train through a home-built multi-pass amplifier (MPA), see Fig. 3.13. After passing four times through a Ti:Sapph crystal, pumped by a neodymium-doped yttrium aluminium garnet (Nd:YAG) laser (Powerlite Precision II, Continuum, 800 mJ at 532 nm and 10 Hz repetition rate), the weak pulses are amplified to reach energies of more than 100 μJ per pulse. The size and divergence of the 800 nm beam are adjusted with a telescope to control the gain. In the same way, the pumped volume in the crystal can be controlled with another telescope on the 532 nm pump beam. The final gain is set to the desired value by tuning the power of the 532 nm pump beam. The repetition rate of the amplified pulses is limited to 10 Hz, the frequency of the Nd:YAG pump laser. The synchronization with the 1 KHz femtosecond laser systems is done with a home-built pulse generator.

In the following, we give some more technical details for the setup and the alignment of the MPA:

(1) The 800 nm beam should propagate through the Ti:Sapph crystal at the Brewster angle. It is very important, that the pulses are set to a perfect p -polarization, first, to minimize losses due to the reflection of the surface, and second, to achieve a smooth amplified pulse train. In the case

3.5. Multi-pass amplification

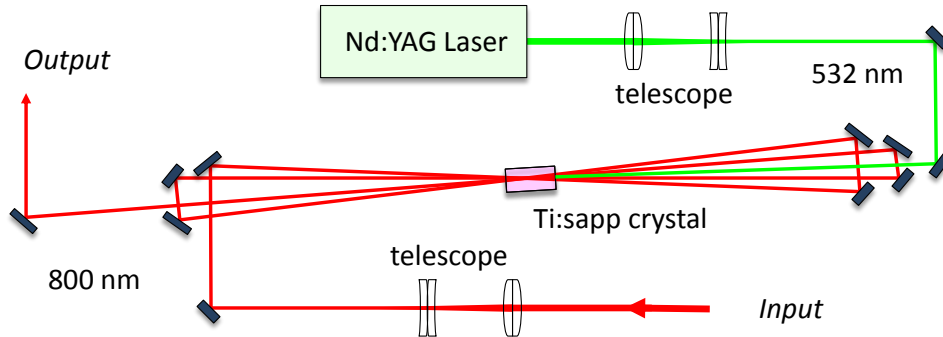


Figure 3.13: Diagram of the home-built multi-pass amplifier.

of a polarization misalignment the birefringence of the Ti:Sapph crystal will lead to a temporal splitting of the input pulse. Recording the final pulse shape via XFROG (Sec. 3.2.1) will reveal undesired pre- and post-pulses if they are present.

(2) The telescope on the 800 nm beam serves primarily to adjust the beam divergence. The actual beam size is chosen as large as possible to minimize the pulse intensities. At the same time, the diameter needs to be smaller than the pump beam diameter to obtain a uniform amplification of the entire beam profile.

(3) Optimal working conditions of the MPA are checked on a weekly (daily) basis. Since our experiment requires long optical beam paths, minuscule changes in the beam alignment can have rather large effects on the nonlinear amplification of the pulses. A rough alignment is guaranteed by multiple sets of irises throughout the setup. The fine adjustment is done by measuring the energy iteratively after each stage of the amplifier with a photo-diode. Tuning the respective optical mirror helps to maximize the amplification of each pass. This procedure is done at low amplifications.

(4) To attain a nice pulse train of equally strong sub-pulses, the alignment of the Michelson interferometers is of crucial importance, too. In order to reach the same gain in each of the four pulse train copies, the four different beams originating in the four arms of the Michelson interferometers must be spatially recombined to travel on an identical path through the MPA. We align the optical beam path for a single arm of the Michelson setup first, as described in (2). In a second step we overlap each other Michelson arm with the first arm in the far field without amplifying the pulses. At last, we check the uniform amplification of all pulses by means of an XFROG measurement.

(5) A potential danger in the nonlinear amplification process lies in self-phase modulation. Self-focusing of the beam can lead to increasing intensities and to the damage of the crystal. We choose a slightly diverging 800 nm beam at the MPA input (diameter about 1 mm) which has increased to about twice the size at the output. Once the MPA is running, we check the amplification at each stage to guarantee an equal amplification throughout the MPA. A sudden increase in amplification is an indicator for decreasing beam sizes and rapidly growing intensities. In this case the beam divergence should be increased to counteract the detrimental self-focusing. Under ideal working conditions, we achieve amplification factors of around 5 per stage, however we did occasionally operate with factors of up to ~ 7 per stage.

3.5.1 Compressed versus chirped amplification

Our laser generates frequency-chirped pulses. Compressing them down to the TL duration and shaping them into a pulse train are two linear-optics operations. As such, they commute with one another and can be executed in either order.

At first, we investigate how the amplification of a single pulse is affected by its compression. The input laser pulse into the multi-pass amplifier can either be an uncompressed frequency-chirped pulse or a compressed TL pulse. Hereby, the compression is done with a standard grating-based pulse compressor. We compare the output pulses when the amplification is done with chirped pulses versus compressed pulses and give a list of arguments for or against each scenario.

Compressed-pulse amplification: Multi-pass amplifiers typically operate with chirped pulses that are recompressed after the amplification. This keeps the peak intensities below the damage threshold of the Ti:Sapph crystal. However, we show that it is possible to amplify 130 fs pulses (FWHM) up to energies of at least 200 μJ . In this configuration, we first compress the chirped pulses down to the Fourier transform limit, before creating and amplifying the pulse train. With beam diameters inside the MPA as small as 1 mm (FWHM), the amplified 800 nm pulse can reach intensities on the order of $10^{11}\text{W}/\text{cm}^2$. Even though this does not damage the Ti:Sapph crystal, it does affect the spectrum. The pulses are propagating through air over a distances of about 7 m inside the MPA and acquire spectral modulations. This propagation effect due to self-phase modulation (SPM) has been studied in detail by Nibbering *et.al.* [125]. In Fig. 3.14(a) we show how the input Gaussian spectrum of a single transform-limited pulse (black solid

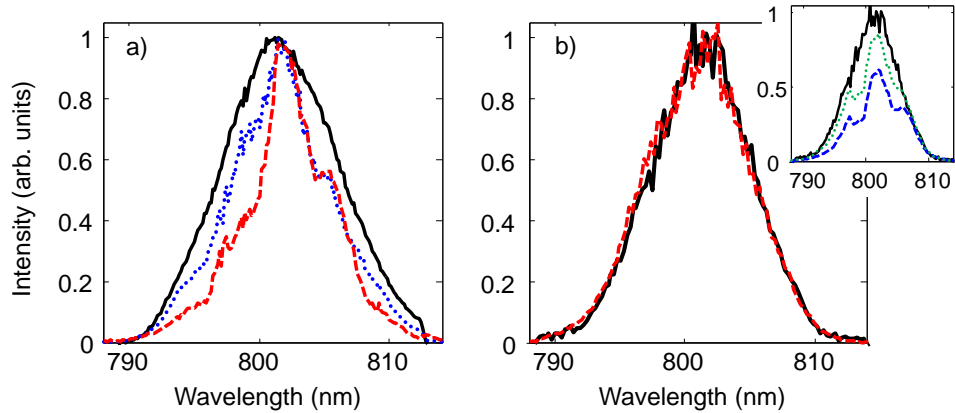


Figure 3.14: (a) Compressed-pulse amplification: spectrum of a single pulse before the MPA (black solid), after the MPA unamplified at $5.4 \mu\text{J}$ (blue dotted) and amplified to $144 \mu\text{J}$ (red dashed). (b) Chirped-pulse amplification: spectrum of a single pulse unamplified at $0.4 \mu\text{J}$ (black solid) and amplified to $100 \mu\text{J}$ (red dashed). The inset shows spectral modulations after the amplified pulse is focused through a cell filled with 6 atm of nitrogen (green dotted) or oxygen (blue dashed) molecules.

line) changes as it propagates through the MPA. At the output, the spectrum is already distorted even if the Nd:YAG laser is turned off and there is no amplification (blue dotted line). The energy of this pulse is measured to be $5.4 \mu\text{J}$. When the same pulse is amplified to an energy of $144 \mu\text{J}$ the modulations become much more severe (red dashed line).

Chirped-pulse amplification: In a second scheme, we use the uncompressed 150 ps pulses (FWHM) from our laser system. The amplification is applied to chirped pulses that are only recompressed to femtosecond pulses at the output. As a consequence, the intensities within the MPA will be decreased by about three orders of magnitude. Since the propagation effects scale with intensity, we can now see a clean output spectrum in Fig. 3.14(b), measured after the pulse compression. The spectrum of a single pulse amplified 250 times to an energy of $100 \mu\text{J}$ (red dashed line) is almost indistinguishable from the spectrum of an unamplified pulse at $0.4 \mu\text{J}$ (black solid line). As a proof that the mentioned SPM effects are due to high intensity pulse propagation in air, we focus ($f = 100\text{mm}$) the same transform-limited pulse into a gas cell filled with 6.5 atm of nitrogen (green dotted line) or Oxygen (blue dashed line) in the inset of Fig. 3.14(b). Spectral modulations

similar to the ones in Fig. 3.14(a) become apparent.

In conclusion, chirped pulse amplification ensures negligible spectral distortions of the output pulses due to propagation effects in air. It also presents the safer option in terms of damaging optical components because of high intensity pulses. Any experiment that requires high pulse energies should therefore implement this scheme. For all other experiments that do not rely on a smooth spectrum or high intensities it is worth considering to work with compressed pulses for technical reasons. First, no energy is lost after the amplification process, as we can send the pulses straight to the gas sample. We do not have to compensate for optical losses of the grating compressor. Second, the optical alignment of the pulse shaper is facilitated with compressed pulses. It becomes a non-trivial task with chirped pulses because the shaper itself can act like a grating compressor. Third, the MPA needs regular (daily) adjustments to maintain optimal amplification. Every change in the beam path through the MPA, necessitates a re-alignment through the compressor. The optimal compression is sensitive to the optical path. Experimentally, we simplified this procedure by setting up several irises throughout the setup to indicate a reference path.

3.5.2 Amplification of pulse sequences

Most of our experiments rely on strong pulses. Thus, we chose the scheme of chirped-pulse amplification. The complete setup is depicted in Fig. 3.15. The chirped pulses from our Ti:Sapph laser system are sent to a pulse shaper followed by two Michelson interferometers (dotted box) to form long pulse sequences, that are then amplified in an MPA (dashed box). At the final stage, a standard grating-based pulse compressor compresses each pulse of the sequence to a 130 fs duration (FWHM). The second part of the beam from the laser system (60% in energy) is immediately compressed with an identical grating compressor and utilized as a reference beam.

Losses and Amplification: Unavoidable optical energy losses in the combined pulse shaper and Michelson interferometer setup can be quantified as follows. In a typical $4f$ pulse shaper, about 50% of energy is lost due to the diffraction efficiency of the gratings. The energy throughput owing to the splitting of the initial pulse into a sequence of N identical pulses by means of the spectral shaping can be estimated as $1/N$. This scaling can be derived from the following consideration of a pulse train in the frequency domain. The spectrum of an infinite pulse train is a frequency comb. The separation

3.5. Multi-pass amplification

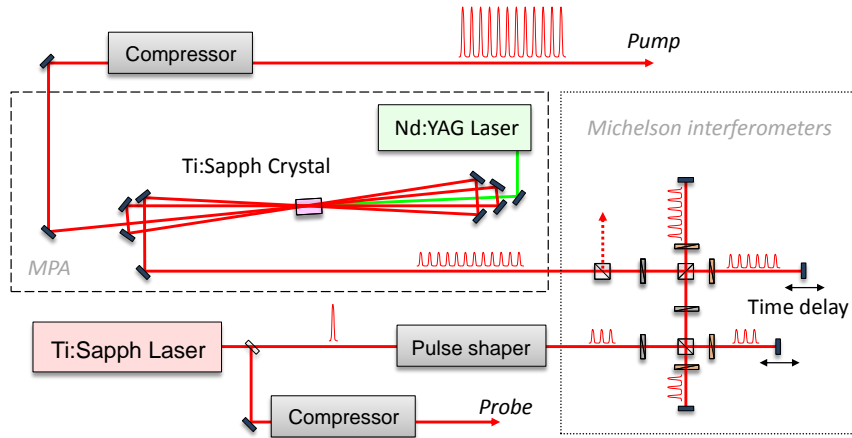


Figure 3.15: Diagram of the optical setup. The output beam of a Ti:Sapph laser with frequency-chirped 150 ps pulses is split into two parts. The pump beam is used to generate long sequences of high-energy pulses; the other beam serves as a probe. Both outputs are compressed to a 130 fs duration (FWHM).

of the comb teeth is inversely proportional to the train period T , $\Delta\omega \propto 1/T$. The spectrum of a finite train of N pulses is the same comb convolved with the sinc function whose width is inversely proportional to NT , $\delta\omega \propto 1/(NT)$. The ratio $\delta\omega/\Delta\omega$ determines the amount of energy remaining in the train after shaping. A more complete mathematical foundation has been derived in Sec. 3.3.2. The polarization multiplexing in the interferometer setup accounts for another energy loss of factor 1/2. In total, each of the $4N$ pulses in the train carries $1/(16N^2)$ of the input energy.

The amount of available energy is typically limited to less than 1 mJ by the damage threshold of a pulse shaper, which in our case corresponded to $300 \mu\text{J}$. For a train of $4N = 84$ pulses demonstrated in Sec. 3.5.3, one ends up with $\lesssim 0.2 \mu\text{J}$ per pulse. Imperfections of various optical components bring this number even further down, well below the typical requirements for a strong-field regime of the laser-molecule interaction. In order to compensate for all the losses, each pulse gets amplified with the MPA. The largest demonstrated amplification factor of 2800 has been for the mentioned train of 84 pulses. Generally, we work with pulse sequences where each pulse exceeds an energy of $100 \mu\text{J}$.

3.5. Multi-pass amplification

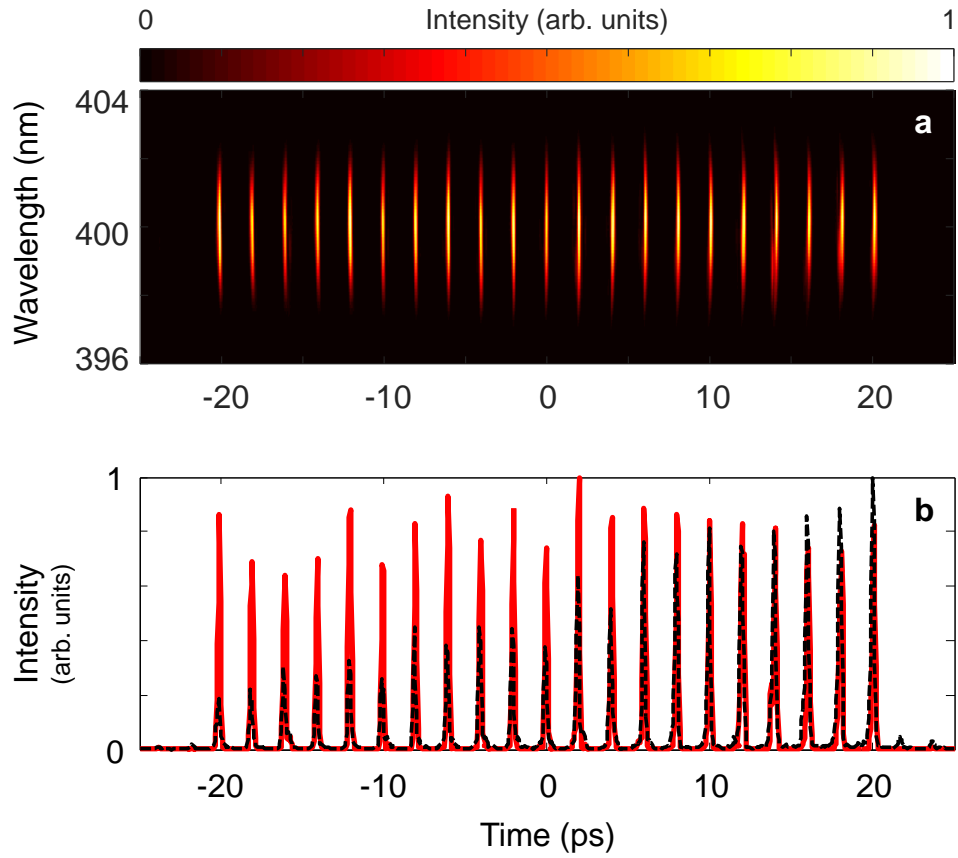


Figure 3.16: (a) XFROG spectrogram of an amplified pulse train with 21 equally spaced pulses and (b) its corresponding temporal profile before (dashed black) and after (solid red) the amplification by a factor of 400.

3.5.3 Demonstration of amplified pulse sequences

Figure 3.16(a) shows an XFROG spectrogram for the pulse train of 21 equally spaced pulses with a period of 2 ps. The spectrogram demonstrates that each pulse in the train is transform-limited with no residual frequency chirp, confirming that proper pulse compression is attainable at the end of the combined shaping and amplification process. Integrating over the whole spectrum, one finds the distribution of energy among the pulses in the train, plotted as the red solid line in Fig. 3.16(b). Here, the gain factor of 400 was required for reaching an average energy of $124 \mu\text{J}$ per pulse. Such high gain levels result in the increased sensitivity of the output pulse sequence to the energy fluctuations in the seed train entering the MPA, as well as in pulse dependent amplification rates. Equalizing the output amplitudes is achieved through the iterative process shown in Fig. 3.10, in which the correction function is fed back to the pulse shaper in order to compensate for the irregularities in the output temporal profile. In the presented example, the corrected seed train is shown in Fig. 3.16(b) by the black dashed line. The final degree of flatness is limited by the nonlinearity of the MPA amplification process and is on the order of 10%, determined as the standard deviation of the pulse-to-pulse energy fluctuations.

Adding a set of nested Michelson interferometers enables us to generate pulse sequences longer than the 50 ps time limit set by the spectral resolution of the shaper and with more pulses, while still maintaining the energy level in excess of $100 \mu\text{J}$ per pulse. In Figures 3.17(a) and (b), we show periodic sequences of 20 and 84 pulses stretching over a duration of ≈ 170 ps (pulse separation of 8 ps and 2 ps, respectively) and carrying $\approx 110 \mu\text{J}$ per pulse. The latter train has been amplified 2800 times to the total energy of 9 mJ. One can see that longer pulse trains suffer from a higher amplitude noise, e.g. standard deviations of 13% and 18% in (a) and (b), respectively. The increasing noise is due to the higher MPA amplification factors and the correspondingly higher nonlinearity of the amplification process. The four colors represent the four different pathways through the Michelson interferometers. Without amplitude noise, each of the four copies would be identical.

3.5. Multi-pass amplification

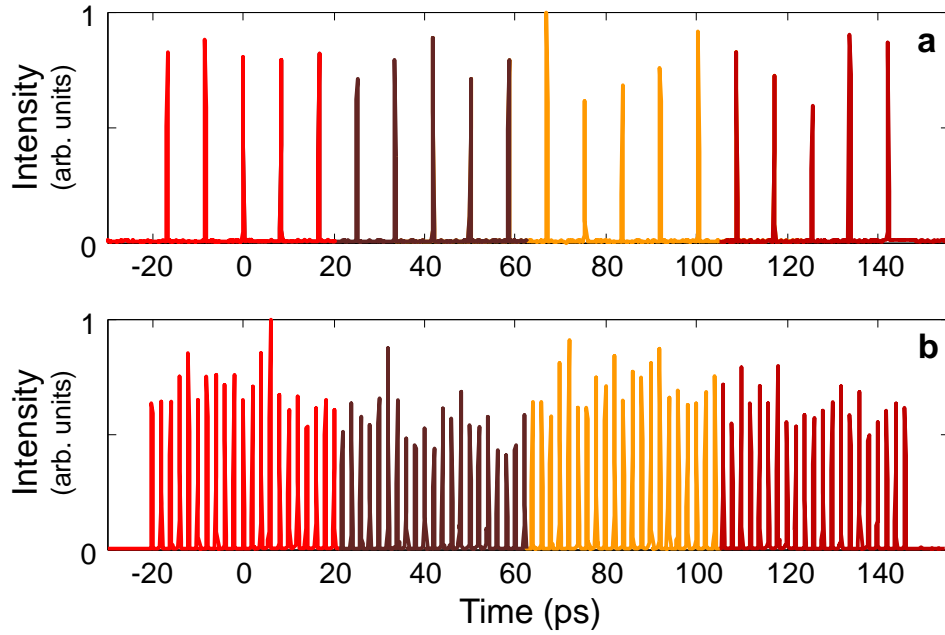


Figure 3.17: Temporal profile of two periodic pulse sequences: (a) 20 pulses separated by 8 ps and amplified 500 times to $114 \mu\text{J}$ per pulse; (b) 84 pulses separated by 2 ps and amplified 2800 times to $107 \mu\text{J}$ per pulse. The four colors represent the four different pathways through the Michelson interferometers.

Chapter 4

Techniques II: Rotational Raman spectroscopy in a molecular jet

In chapter 3 we introduced a method to generate high-intensity pulse sequences, which are necessary to implement the “molecular kicked rotor”. This chapter will present the experimental techniques used to explore and understand the dynamics of the molecular kicked rotor.

All our experiments share the same detection technique: “Rotational Raman spectroscopy”. In Sec. 4.1 we describe how the method works and how it is implemented. We discuss two slightly different variations: one, where the molecular sample is contained in a gas cell; and the other, where the experiments are conducted in a molecular jet. We explain a typical Raman spectrogram as it will reoccur in the presentation of all later results. Experiments that rely on a narrow initial distribution of rotational states have to be done in a molecular jet, topic of Sec. 4.2, where the rotational motion is substantially cooled down. We explain how a molecular beam works and show our experimental realization. We investigate the rotational temperature and the molecular density during a supersonic jet expansion by analysing the Raman spectrum.

4.1 Raman spectroscopy

In order to implement the technique of coherent Raman spectroscopy we need a weak probe pulse with controlled spectral width, which determines our frequency resolution. The experimental scheme is shown in Fig. 4.1. The 800 nm pump pulse, which in almost all of our experiments is a high-intensity sequence of femtosecond pulses, is produced as discussed in chapter 3. The probe, which originates from the Ti:sapphire laser system (for details see Sec. 3.2), is sent through another pulse shaper. This shaper is built in the same folded geometry as the pump shaper in Fig. 3.8 (Sec. 3.3.1), but with

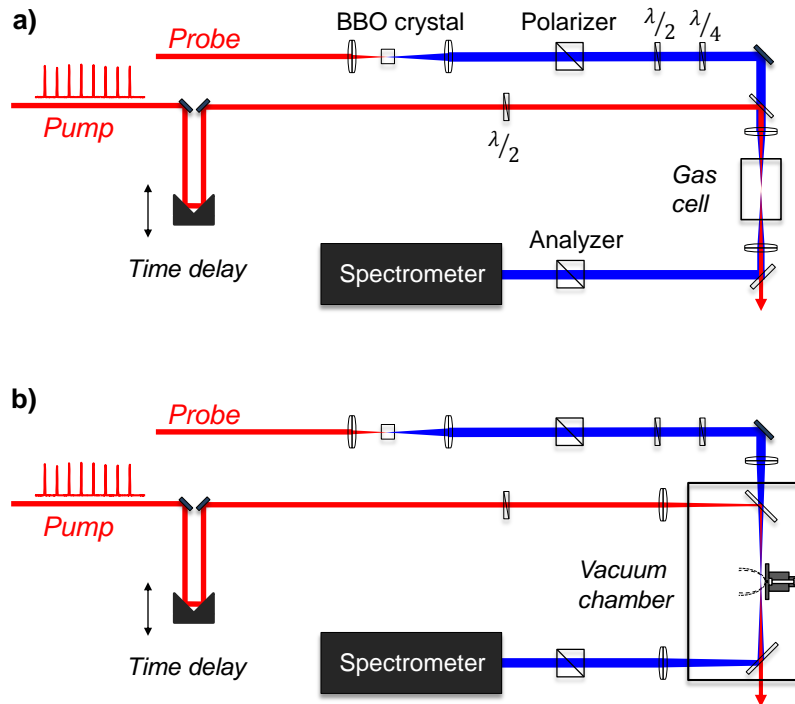


Figure 4.1: Scheme of the experimental setup: A weak probe pulse is frequency-doubled in a nonlinear BBO-crystal and combined with a train of strong femtosecond pulses (pump). Both beams are focused (a) into a cell filled with a molecular gas or (b) onto a supersonic jet of molecules inside a vacuum chamber. The change of probe polarization is analysed as a function of the wavelength by means of two crossed polarizers and a spectrometer, and as a function of the tunable time delay.

some different optical components [reflective grating (1200 g/mm), spherical mirror ($f = 50$ cm)]. In the Fourier plane of the probe shaper, we place a mechanical slit, rather than a liquid-crystal SLM, to withstand higher laser intensities. The slit is used to narrow down the spectrum. The central wavelength is then shifted to 400 nm by means of the second harmonic generation (SHG) in a nonlinear BBO crystal. Finally, the probe pulses of 0.15 nm spectral width (FWHM) are linearly polarized at 45° with respect to the pump pulses. Both beams are combined on a dichroic beamsplitter and focused onto the molecular sample of oxygen O_2 or nitrogen N_2 . Special care is taken to minimize detrimental effects of spatial averaging by making the probe beam significantly smaller than the pump (FWHM beam diameters of 20 μm and 60 μm , respectively).

We distinguish two scenarios illustrated in Fig. 4.1: In panel (a) the gas of linear molecules is contained in a cell at variable pressure. The pump and probe beams are combined prior to entering the cell. This setup is used to conduct experiments at room temperature in dense gases. In panel (b) both beams are first focused into a vacuum chamber, where they are then combined on a dichroic beamsplitter and intersect a supersonic jet of molecules. We use a 500 μm diameter pulsed nozzle, operating at the repetition rate of 10 Hz and the stagnation pressure of 33 bar. We achieve rotational temperatures around $T = 25\text{K}$ at a distance of 1.9 mm from the nozzle. A summary of rotational cooling via a supersonic jet expansion is given in the next section 4.2.

Coherent molecular rotation, produced by a pump pulse, modulates the refractive index of the gas. The mechanism can also be viewed as a two-photon Raman process, introduced earlier in Sec. 2.3. As a result, the spectrum of a weak probe light acquires Raman sidebands shifted from its central frequency and polarized orthogonally to its initial polarization [95, 96]. The Raman sidebands are analysed in a polarization sensitive measurement by passing the output probe light through an analyser set at 90° with respect to the initial probe polarization.

Some of the experiments rely on measuring the Raman spectrum with a dynamic range of three to four orders of magnitude. In chapter 6 for example, we need to demonstrate an exponential shape of the observed Raman spectrum, which would not be possible without such a dynamic range. It is therefore important to suppress the initial probe polarization as much as possible, which in turn will reduce the noise floor. We use two Glan-Thompson polarizers, one before and one after the vacuum chamber, and two additional waveplates. The $\lambda/4$ - and the $\lambda/2$ -waveplates compensate for polarization changes that the probe beam accumulates as it propagates

through the optical windows of the chamber and the dichroic beamsplitters. This results in a lower level of the residual probe light¹⁰.

We record the rotational Raman spectrum with a spectrometer (McPherson Inc., model 2035, with a 1800 grooves/mm diffraction grating) equipped with a CCD camera (Andor iDus, DV401A-BV). The camera has a dynamic range greater than four orders of magnitude. The resolution of the spectrometer of 0.056 nm per pixel (at a wavelength of 400 nm) is good enough to resolve individual rotational states in lighter diatomic molecules (e.g. N₂ or O₂). A computer-controlled translation stage allows for time-resolved spectrograms by scanning the delay between the pump and probe pulses (Newport: Motion Controller, ESP301; translation stage, UTS-100CC; minimum increment ≈ 7 fs). The temporal resolution will be given by the duration of the probe pulse.

4.1.1 Raman spectrogram

When a weak probe pulse follows the pump through a cloud of rotating molecules, its spectrum acquires Raman sidebands. Here, we will explain the interpretation of such a Raman spectrum. The shift of each Raman peak, $\Delta\omega_J$, is equal to the frequency spacing between the rotational levels $|J\rangle$ and $|J+2\rangle$, while its magnitude is proportional to the square of the rotational coherence [96], a more rigorous expression is found in section 2.3.6.

We use oxygen or nitrogen in our experiments, for several reasons described in Sec. 2.3.9. In the first approximation these linear molecules behave as rigid rotors and their rotational energy is given by $E_J = hcBJ(J+1)$. Hence, the frequency shift of each Raman peak is linearly proportional to the rotational quantum number J and can be expressed as $\Delta\omega_J = (E_{J+2} - E_J)/h = 2Bc(2J+3)$.

Figure 4.2 displays a Raman spectrum of N₂ recorded after the rotational excitation by a single pump pulse. Shown are the measurements in a gas cell (solid black line) in comparison to the measurement with a molecular jet (red dashed line). We see a progression of Raman peaks as a function of the wavelength shifted away from the probe wavelength at 400.6 nm. This wavelength shift can be translated to the rotational quantum number J , shown along the lower horizontal axis. According to the nuclear spin statistics of nitrogen, the ratio between even and odd rotational states J must be 2:1 (described in Sec. 2.3.9). Our probe pulse with a spectral width of 0.15 nm (FWHM) is narrower than the line separation $\Delta\omega_{J+2} - \Delta\omega_J \propto 8B$

¹⁰The extinction ratio is greater than five orders of magnitude.

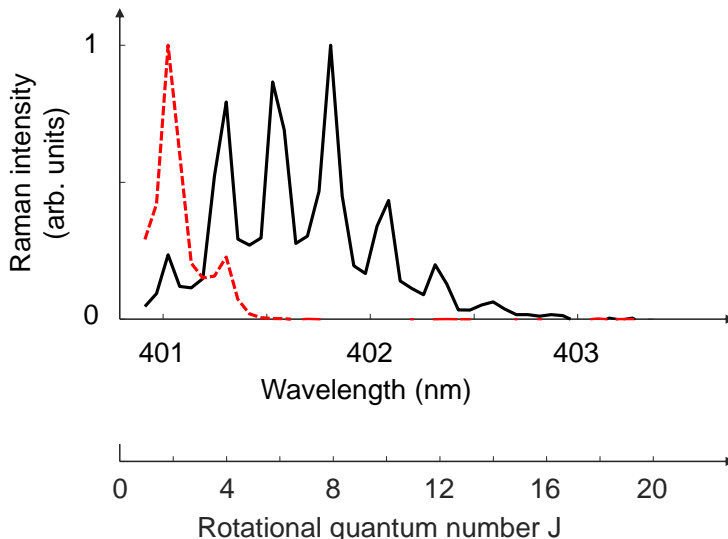


Figure 4.2: Raman spectrum of N_2 after the rotational excitation by a single weak pulse, measured in a gas cell (solid black line) or with a molecular jet (red dashed line).

enabling us to resolve individual rotational states and thus to determine the shape of the excited rotational wave packet.

The entire spectrum consists of a Rayleigh peak, polarized along the input probe polarization (selection rule: $\Delta J = 0$), and two progressions of Raman sidebands shifted up ($\Delta J = +2$) or down ($\Delta J = -2$) with respect to the Rayleigh frequency and polarized in the orthogonal direction. We measure only the red-shifted sidebands. As a consequence of a non-ideal polarization suppression of the input probe light, we detect a Rayleigh peak of substantial magnitude which can exceed that of the scattered Raman spectrum. We set our spectrometer to measure all Raman spectra only for values $J \gtrsim 1$, to truncate the unwanted Rayleigh peak.

In Fig. 4.2 the pump pulse is set to a weak kick strength of $P \ll 1$ which will not lead to much angular momentum transfer. Therefore, the population distribution will hardly change and closely represent the initial thermal distribution. The two plotted lines show the clear difference in the initial rotational temperature. In the case of the gas cell (black solid line) the distribution follows a Boltzmann distribution at room temperature, whereas in the case of the jet (red dashed line) we retrieve a temperature around 25 K (details in Sec. 4.2).

Figure 4.3 shows the Raman spectrum of oxygen, recorded under iden-

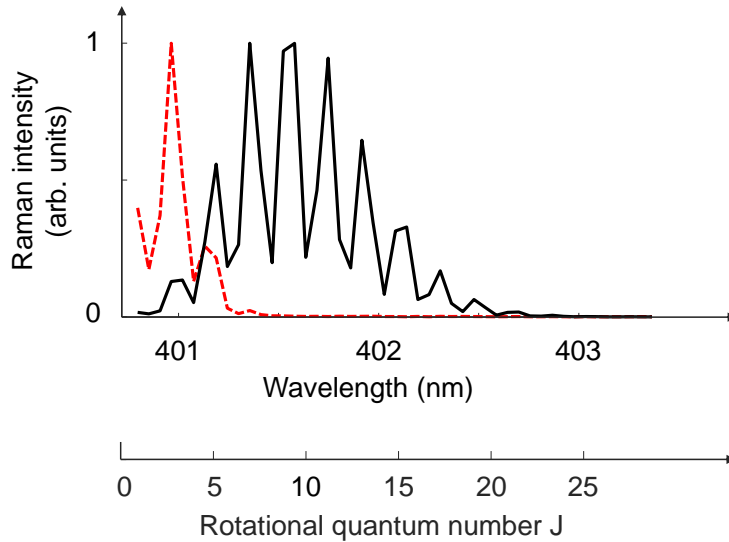


Figure 4.3: Raman spectrum of O_2 after the rotational excitation by a single weak pulse, measured in a gas cell (solid black line) or with a molecular jet (red dashed line).

tical conditions as described above for nitrogen. The main difference with Fig. 4.2 stems from the nuclear spin statistics of O_2 , allowing only odd quantum numbers J .

The interpretation of state-resolved Raman spectra remains the same in all experiments. When the molecules are excited with sequences of strong pulses, however, the assumption of a rigid rotor is not valid anymore. Thus, the exact position of the Raman peaks is calculated with the energy expression of a non-rigid rotor $E_J = hc[BJ(J+1) - DJ^2(J+1)^2]$. The line separation will decrease for higher J values. This change is insignificant for $J < 30$, as they are typically excited in our experiments. All the presented Raman spectra are taken with the probe pulse arriving immediately after the last pulse in the train or after the specific pulse of interest within the train. This way we minimize the decrease in Raman signal due to collisional decay.

4.2 Molecular beam source

A majority of the QKR phenomena that we studied can only be observed in rotationally cold molecular samples. One well established technique to cool molecules is based on a supersonic expansion [115, 5]. A high pressure gas that is passing through a nozzle into a low pressure region will expand adiabatically leading to a drop in temperature. Rotational temperatures of a few Kelvin are routinely achieved.

We implemented a supersonic jet of molecules, which resulted in rotational temperatures around 25 K. First, we present a concise summary of the theory of molecular beams in Sec. 4.2.1. Second, our specific setup with a pulsed nozzle producing a jet suitable for Raman spectroscopy is described in Sec. 4.2.2. Finally, we show experimental Raman spectra of N₂ and O₂ in Sec. 4.2.3, investigating temperatures and densities and their dependence on externally controllable parameters.

4.2.1 Theory of supersonic expansion

All physical concepts and thermodynamic equations in this section were adapted from the books by Miller [115] and Anderson [5].

At first, we introduce the thermodynamic quantity γ . All molecules have a specific heat ratio $\gamma = C_p/C_v$, calculated via the specific heats at constant pressure C_p and constant volume C_v . Next, we look at a beam of diatomic molecules ($\gamma = 7/5$), i.e. N₂ or O₂ entering a vacuum chamber through a nozzle. Initially the gas is at stagnation pressure p_0 and room temperature T_0 . The pressure inside the vacuum chamber is set to p_b . We approximate the beam as a steady-state continuous jet from the nozzle as shown in Fig. 4.4 (in the actual experiment we will be using a pulsed jet.) If the pressure ratio p_0/p_b is greater than a critical value of $G = \left(\frac{\gamma+1}{2}\right)^{\gamma/(\gamma-1)}$, for diatomics $G \approx 1.89$, the speed of the molecules exiting the orifice will be supersonic with a Mach number $M \gg 1$. The Mach number measures the speed v of the gas past the nozzle in relation to the speed of sound a . For an ideal gas $a = \sqrt{\gamma RT/m}$ with the molecular weight m and the universal gas constant R . Before the expansion, the molecules at the orifice of the nozzle have a velocity of $M = 1$. In the subsequent adiabatic expansion of the gas, the velocity will increase, leading to a drop in molecular density and temperature. However, if the pressure ratio p_0/p_b is not sufficiently large, the gas will exit the nozzle at a pressure of p_b with no further expansion.

Different empirical equations exist to calculate the Mach number along the centerline of the jet, see Ref. [115]. We quote one that is suitable for

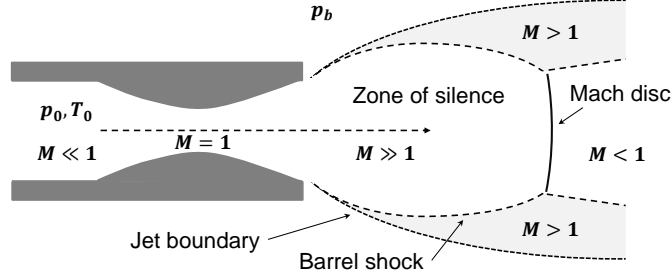


Figure 4.4: Diagram of a supersonic jet expansion. Indicated are the different regions of the beam with their respective molecular speeds given in Mach numbers M .

close distances from the nozzle, relative to the nozzle diameter d

$$M = \left(\frac{x}{d}\right)^{\frac{\gamma-1}{j}} \left[C_1 + \frac{C_2}{x/d} + \frac{C_3}{(x/d)^2} + \frac{C_4}{(x/d)^3} \right]. \quad (4.1)$$

The constants j , C_1 , C_2 , C_3 and C_4 are γ -dependent (molecule-dependent) and can be looked up in tables [115, 167]. The expression is valid for $x/d \geq 0.5$.

The supersonic expansion is an isentropic process, under the assumption that no friction or other dissipative effects occur, which would lead to a change in the entropy. For an ideal gas we can then use known relations to estimate some thermodynamic quantities like temperature T , pressure p and density ρ inside the beam

$$\frac{T}{T_0} = \left(\frac{p}{p_0}\right)^{\frac{\gamma-1}{\gamma}} = \left(\frac{\rho}{\rho_0}\right)^{\gamma-1}. \quad (4.2)$$

Primarily, we are interested in the dependency of those quantities on the distance from the nozzle. We calculate the (translational) temperature as a function of the Mach number which is related to the distance via Eq. 4.1

$$\frac{T}{T_0} = \left(1 + \frac{\gamma-1}{2}M^2\right)^{-1}. \quad (4.3)$$

The temperature and the pressure continue to decrease as long as collisions occur in the flow. This correlates with an asymptotically rising velocity of the molecules. Collisions are also responsible for the rotational cooling. During a free-jet expansion the molecules typically experience around 10^2 to 10^3 binary collisions. This is sufficient to cool the rotational degree of

freedom: Most diatomics require between 10 to 100 collisions to equilibrate with the translational motion. Hence, we estimate the rotational temperature with Eq. 4.3. The vibrational degree of freedom hardly relaxes in a jet expansion as many more collisions are necessary $> 10^4$. Fortunately, almost all molecules in our experiment at room temperature are already in the vibrational ground state. At some point the expansion will transition into a collisionless flow, typically after several nozzle diameters. At this point the terminal velocity is reached and the isentropic description breaks down.

Eventually, the gas will overexpand as a result of the supersonic flow which is unaware of the downstream boundary conditions. Information, i.e. about the pressure p_b inside the chamber, cannot travel faster than the speed of sound ($M = 1$). This results in shock waves indicated in Fig. 4.4, which will recompress the system. For the purpose of our experiment, we have to make sure that the Mach disk location

$$\frac{x_M}{d} = 0.67 \left(\frac{p_0}{p_b} \right)^{1/2}, \quad (4.4)$$

is further away than the interaction region with the laser pulses. The zone of silence is confined within the barrel shock wave with an approximate diameter of $0.75x_M$, the diameter of the Mach disk is about $0.5x_M$ [167].

Often, experimental setups place skimmers inside the zone of silence to extract a small solid angle of the beam. This reduces the momentum spread, enables differential pumping to prevent the formation of shock waves, and generally leads to colder temperatures. Our experiments are done in close proximity to the nozzle, since we rely on high molecular densities for the Raman detection (described in Sec. 4.1). The implementation of a skimmer is not feasible.

4.2.2 Beam setup

Figure 4.5 shows a diagram of our molecular beam setup. We use a pulsed valve (Parker Hannifin, Series9, 009-0582-900) with an orifice of $d = 500 \mu\text{m}$. The valve is operated at a repetition rate of 10 Hz (Newport Corporation, BV100 Beam Valve Driver). The pulse width is set to $\approx 200 \mu\text{s}$. The stagnation pressure p_0 can be regulated up to 33 bar. All our experiments were done at this maximum pressure. The chamber is pumped by a vacuum pump (Edwards, model: E2M40) down to a pressure of $3 \cdot 10^{-2}$ torr without a load. When the pulsed valve is operated, the pressure settles at $p_b \approx 1$ torr. This highlights the importance of working with a pulsed nozzle; the rotary pump could not handle the load in the case of a steady flow.

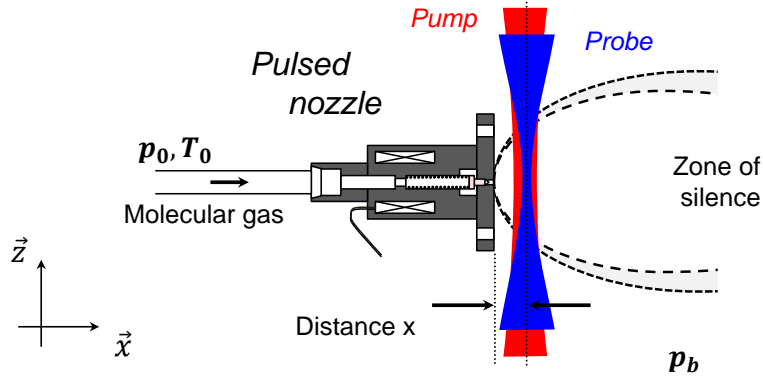


Figure 4.5: Diagram of the molecular beam setup. The pump and probe pulses are both focused onto the supersonic jet of rotationally cold molecules. The probe pulse is focused down to a smaller beam size to reduce spatial averaging over the pump profile in the interaction region.

Our Raman experiments are done at a small distance x from the nozzle, with the exact location being determined as a trade-off between colder rotational temperature and sufficiently high density. Raman spectroscopy relies on the induced birefringence of the gas, which changes the probe polarization [141] (for a detailed explanation see Sec. 4.1). The Raman signal is proportional to the molecular density squared and benefits from a smaller distance. At the same time, we want to maximize the distance to reach lower initial temperatures and not suffer under a collisional decay of the Raman signal. The ideal distance was found at $x = 1.9 \text{ mm} \sim 4d$. All these considerations will be verified with experimental data in Sec. 4.2.3.

The pump and probe beams both propagate through the molecular jet in \vec{z} -direction, see Fig. 4.5. We minimize detrimental effects of spatial averaging by making the probe (400 nm) profile significantly smaller than the pump (800 nm) profile. The FWHM beam diameters D are $20 \mu\text{m}$ and $60 \mu\text{m}$, respectively. This way, the probe beam primarily samples the high-intensity center of the pump beam and the spatial averaging of the Raman signal over the laser profiles is reduced. At the same time, we also improve the confinement in \vec{z} -direction because of the jet. Due to a close proximity to the nozzle, most molecules are present within the Rayleigh range of the laser beams.

In Gaussian beam optics [120], the Rayleigh range $z_R = \pi w_0^2 / \lambda$ is defined as the distance from the smallest beam waist (i.e. the focus) to the point where the beam radius increased by a factor of $\sqrt{2}$. This is the point, where

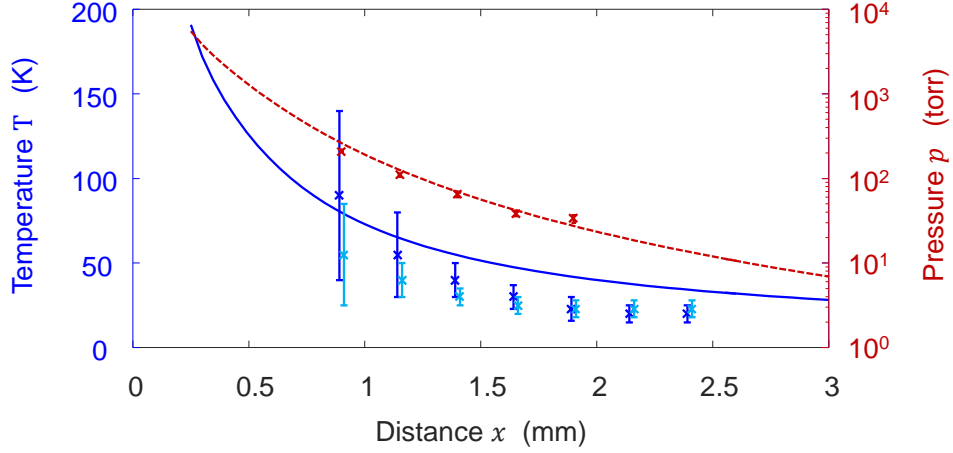


Figure 4.6: Simulated temperature T (blue solid line, left axis) and pressure p (red dashed line, right axis) as a function of the distance to the nozzle x , based on our molecular beam setup. Experimental values retrieved from N_2 measurements are indicated as red crosses (p) and dark-blue crosses (T), the light-blue crosses (T) correspond to O_2 measurements.

the area of the beam cross-section has doubled. The beam radius w_0 is where the Gaussian intensity is $1/e^2$ of its peak value. It can be derived that $w_0 = D/\sqrt{2 \ln 2}$. In our experiment, the Rayleigh range of the probe beam is estimated at 2.3 mm and the one of the pump at 10.2 mm.

Simulation

We simulate the expected temperature and pressure as a function of the distance from the nozzle based on our experimental parameters: $p_0 = 33$ bar ($3.3 \cdot 10^6$ N/m²), $p_b = 1$ torr ($1.3 \cdot 10^2$ N/m²) and $T_0 = 293$ K. At these settings we expect a supersonic flow, because the ratio of $p_0/p_b \approx 2.5 \cdot 10^4 \gg G$ lies well above the threshold value of $G \approx 1.89$. We use Eq.4.1 to calculate the Mach number at a distance x/d with $d = 500$ μm . The empirical constants for the axisymmetric expansion of a diatomic molecule are $j = 1$, $C_1 = 3.606$, $C_2 = -1.742$, $C_3 = 0.9226$ and $C_4 = -0.2069$ [115]. Next, we get the temperature from Eq. 4.3 and subsequently the pressure from Eq.4.2.

The result is plotted in Fig. 4.6 with temperature as the solid blue line (left axis) and pressure as the dashed red line (right axis, log scale). We also retrieved temperatures and pressures experimentally from Raman mea-

measurements at different nozzle distances; the procedure is discussed in the next section 4.2.3. The experimental values are added to the graph with crosses. Note, that only the relative distance between different measurements are known with certainty. The absolute distance x from the nozzle is approximated by shifting the pressure values from the measurements in N_2 (red crosses) to match the simulation. Owing to the retrieval procedure, the obtained pressures are more accurate than the temperatures. There is a discrepancy in the observed temperature which settles at a lower level than expected according to the simulation. The dark blue crosses stem from a measurement in N_2 , the light blue ones from O_2 . (We did not get pressure estimates from the oxygen measurements because of complicated spin-rotation dynamics, more details in the next section.) There are two obvious explanations for inaccuracies: First, our setup works with a pulsed nozzle, whereas the simplistic calculations are based on a continuous jet. Other approximations, that might cause deviations, assume an ideal gas and a frictionless flow without any dissipative effects. Second, the Rayleigh length of the probe pulse $z_R \sim 2.3$ mm is of a similar order than the width of the molecular jet, sketched in Fig 4.5. As a consequence, our Raman spectra yield an average over the spatial temperature and density distributions in \bar{z} -direction, see Ref. [167].

For distances of $x > 3$ mm the local densities become too low for sensitive Raman spectroscopy. All our measurements are done at $x = 1.9$ mm, far before the Mach disk location at $x_M \approx 53$ mm, calculated from Eq. 4.4.

At last, we point out some general relations: The residual pressure p_b inside the chamber determines the Mach disk location, but does not affect the cooling rate. The stagnation pressure p_0 has no influence on the obtained temperature T , but the final pressure depends on it $p \propto p_0$. The nozzle diameter d determines the rate of the cooling process.

4.2.3 Beam characterization

It is possible to map the temperature and density distribution of a supersonic jet expansion using Raman spectroscopy. Rather than creating a complete two-dimensional map as done in Ref. [167], we look only along the center axis of the jet in the region of interest.

Pressure

We use a single high-intensity pump pulse to create strong rotational coherences that we subsequently detect with a weak probe pulse via Raman

spectroscopy (Sec. 4.1). Figure 4.7 shows the mean Raman intensity for nitrogen (**a**) and a state-resolved spectrum for oxygen (**b**) as a function of time. Plotted are the results for two relative distances between the nozzle orifice and the intersecting laser beams, a smaller distance of $x = 0.9$ mm and a larger one of $x = 1.9$ mm. Our goal is to use the decay of the Raman signal due to collisions to estimate the pressure. This is done by comparing the decay times to the decay rates measured in a gas cell at different pressures.

In nitrogen, all individual rotational states behave identically. Thus, we plot their integrated signal in panel (**a**) which decays exponentially with time. The top solid line ($x = 1.9$ mm) and the bottom solid line ($x = 0.9$ mm) are both fitted with an exponential function $f(t) = a \cdot \exp(-t/\tau)$, shown as the red-dotted lines. The decay times are found to be $\tau = (1.13 \pm 0.09)$ ns and (196 ± 6) ps, respectively with the error given by the 95% confidence bounds of the fit.

The same measurements done in oxygen at the distance $x = 0.9$ mm (**b1**) and $x = 1.9$ mm (**b2**) reveal much more complicated dynamics. The collisional decoherence is superimposed on spin-rotational oscillations. Paramagnetic oxygen has a non-zero spin in the electronic ground state ($S = 1$) which is coupled to the molecular rotation (nuclear rotation quantum number N). This coupling splits each rotational level into three levels with the total angular momenta ($J = N, N \pm 1$). It also means that the $N \rightarrow N + 2$ Raman process actually consists of six separate transitions [79]. Owing to the spin-rotation coupling, we observe beat notes that depend on the rotational quantum number N . We plot the state-dependent dynamics for $N = 1$ (blue dashed), $N = 3$ (red dotted) and $N = 5$ (black solid). The spin-rotational dynamics of oxygen has been investigated experimentally¹¹ [116, 117]. For quantum numbers $N > 5$ the dynamics is dominated by branches that lead to the oscillation periods on the order of 600 ps, which is much longer than any time scale that we are concerned with. We are only affected by the spin-rotation coupling at low quantum numbers.

In this thesis, we will disregard the effect of spin-rotation coupling, since we are operating on time scales of 250 ps or less and since we are usually not interested in the very low quantum numbers. For simplicity, we will always label the rotational quantum number with J , for both nitrogen and oxygen.

We calculate the collisional decay times of nitrogen in the jet for a series

¹¹ The fast beating at a period of ~ 17 ps belongs to the two lowest lines of the R-branch ($\Delta J = 1$) and has been observed before [116].

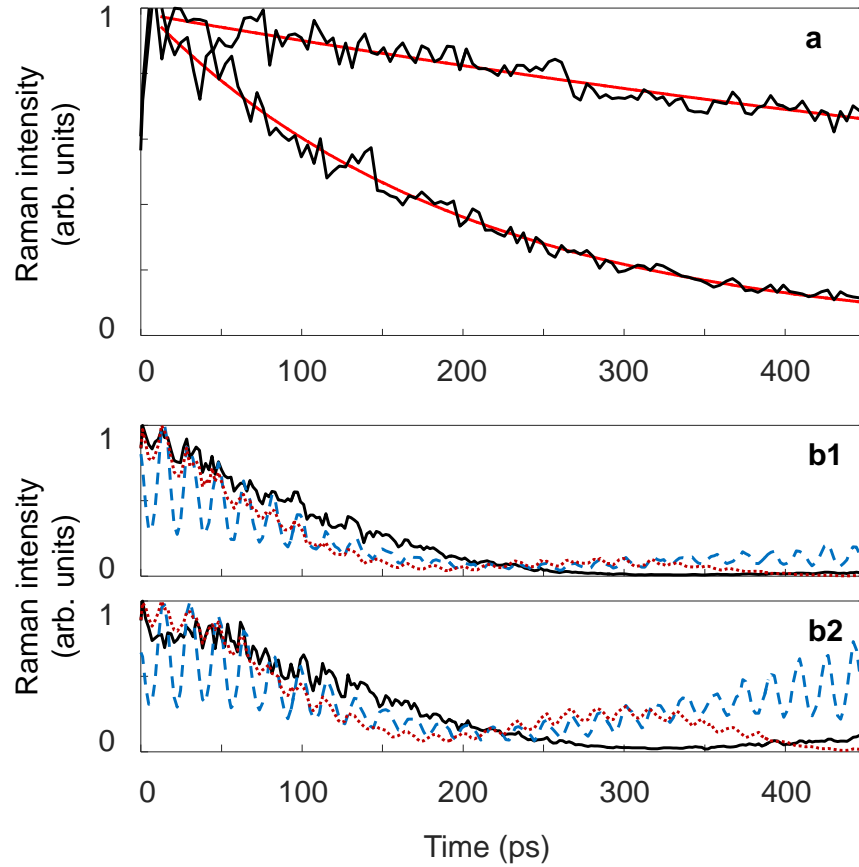


Figure 4.7: (a) Rotational spectroscopy of nitrogen: Mean Raman intensity for nozzle distances of $x = 1.9$ mm (top solid line) and $x = 0.9$ mm (bottom solid line) and their respective exponential fits (red dotted lines). (b) State-resolved spectroscopy in oxygen for $J = 1$ (blue dashed), $J = 3$ (red dotted) and $J = 5$ (black solid) for nozzle distances of $x = 0.9$ mm (b1) and $x = 1.9$ mm (b2). Maximum signals are normalized to unity.

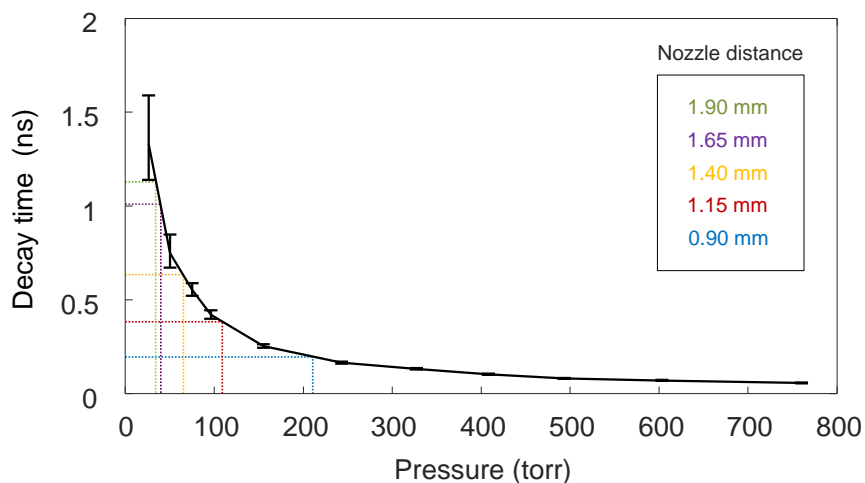


Figure 4.8: Collisional decay times as a function of gas pressure, recorded via Raman spectroscopy in a cell of nitrogen. Horizontal dashed lines indicate the decay rates from molecular jet experiments at various nozzle distances. Their corresponding pressures can be interpolated.

of different nozzle distances **(1)** 0.9 mm, **(2)** 1.15 mm, **(3)** 1.4 mm, **(4)** 1.65 mm, **(5)** 1.9 mm by fitting the Raman signal as a function of time with an exponential, analogous to the description above and Fig. 4.7(a). In order to estimate the corresponding pressure values, we use Fig. 4.8, a graph that shows the relation of pressure versus collisional decay in a cell filled with nitrogen. Based on this set of calibrated data points, we can interpolate the pressure in the jet. The results are **(1)** 210 torr at a decay time of 0.20 ns, **(2)** 110 torr at 0.38 ns, **(3)** 65 torr at 0.64 ns, **(4)** 39 torr at 1.01 ns, **(5)** 34 torr at 1.13 ns. No values exist below the pressure of ~ 30 torr because the collisional decay times become too long to reliably fit an exponential function to our experimental data (maximum time delay was 450 ps). Therefore, the procedure could not be applied to distances of $x > 2$ mm. The interpolated pressure values are the ones that have been added to Fig. 4.6.

Temperature

In a similar fashion we use the Raman spectrum after a single pump pulse to retrieve the rotational temperature. However, this time we use a weak pump pulse with a kick strength of $P \ll 1$, which creates weak coherences but

hardly changes the rotational state distribution. The shape of the Raman spectrum then reflects the initial rotational distribution.

Figure 4.9 demonstrates the narrowing of the spectrum with larger nozzle distances, which corresponds to rotational cooling of the molecules: nitrogen in (a) and oxygen in (b). The six lines from the broadest to the narrowest distribution are measured with distances of $x = 0.9, 1.15, 1.4, 1.65, 1.9$ and 2.15 mm. As a representative example we pick the Raman spectrum at 1.9 mm, shown in the insets. The best matched rotational distribution is marked with crosses and serves to estimate the temperature. These theoretical Raman spectra were calculated numerically based on a thermal Boltzmann distribution of states $P_J = (2J + 1) \exp(-E_J/k_B T)$. Details of our numerical simulation are discussed in section 2.3.6. The rotational temperatures for all nozzle distances have been added to Fig. 4.6. We note, that the Raman spectra, in particular the ones close to the nozzle, deviate from the Boltzmann distribution, leading to large errorbars. One possible explanation lies in the averaging over the temperature profile of the molecular jet along the \bar{z} -direction, the direction in which the laser beams propagate.

In conclusion, we set our distance to $x = 1.9$ mm in all experiments. Here, the pressure is estimated to be around (35 ± 5) torr, sufficient for sensitive measurements, and the rotational temperature is approximated to be (23 ± 7) K, where the most populated state is $J = 2$ in nitrogen or $J = 3$ in oxygen.

Our results are in agreement with the ones found in other Raman spectroscopy methods implemented in beams of N_2 molecules, e.g. coherent anti-stokes Raman spectroscopy (CARS) [26] or spontaneous Raman scattering [137].

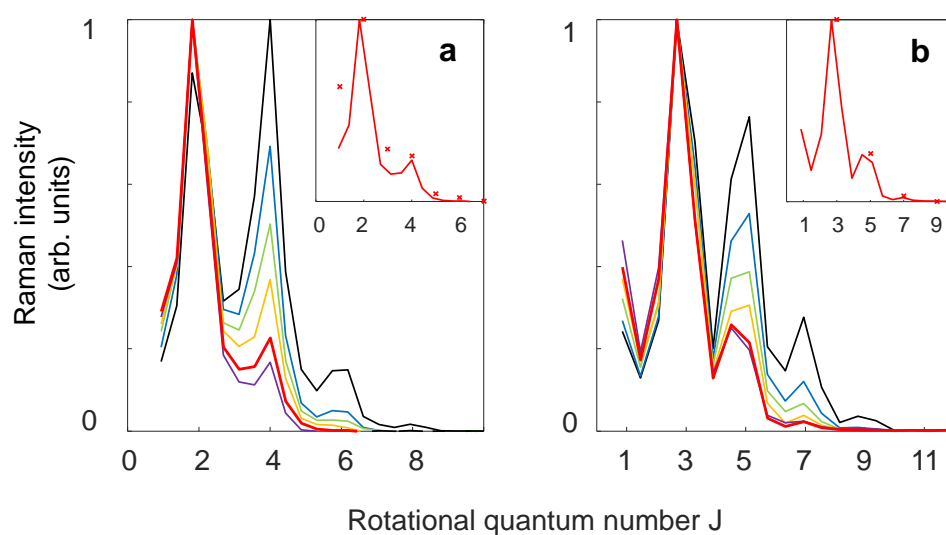


Figure 4.9: Rotational Raman spectra of (a) nitrogen and (b) oxygen, measured in a molecular jet at various distances from the nozzle: $x = 0.9, 1.15, 1.4, 1.65, 1.9$ to 2.15 mm (from broadest to narrowest distribution). The insets compare the experimental spectrum recorded at a distance of 1.9 mm (solid lines), with the simulated distribution at 23 K (crosses). The maximum signals are normalized to unity.

Chapter 5

Resonant excitation of molecular rotation

The periodically kicked rotor exhibits rich dynamics. In the classical limit it is described by the “standard map” (Sec. 2.1.1), which is known as one of the simplest representations of chaotic behaviour. Here, we study the dynamics of periodically kicked linear molecules - a system of quantum rotors. Owing to the discreteness of rotational energies, we need to distinguish between two regimes: the one of periodic excitation on quantum resonances and the one of periodic excitation away from quantum resonances. In this chapter 5, we exclusively investigate various phenomena that are all a consequence of quantum resonances. The following chapter 6 will treat the other case, where the period of the pulse train is chosen to be incommensurable with all quantum resonances of the system.

We established the “resonance map” (Sec. 2.3.8) as a helpful means to study the QKR. In Sec. 5.1, we verify this map experimentally by exposing an ensemble of room temperature molecules to a periodic sequence of pulses. This knowledge is used to set the train period to different resonances in order to demonstrate different effects. To achieve cleaner results, these measurements are typically done in rotationally cold molecules. When the period is chosen to coincide with a single rotational resonance, in Sec. 5.2, we observe Rabi oscillations between the constituent rotational states. We observe that the amplitude and period of the oscillations depend on the detuning from the resonance. If instead of a single rotational resonance the period matches the full quantum resonance, we observe another type of oscillations. In Sec. 5.3, we investigate how the angular momentum of the rotor oscillates in a fashion that has been connected to Bloch oscillations in solid state physics [60, 64, 62]. Again, we can manipulate the dynamics by adjusting the detuning from the quantum resonance.

In Sec. 5.4, our goal is the excitation of broad rotational wave packets, which is commonly done via periodic excitation on quantum resonance [41, 192]. We evaluate the efficiency of this process and assess the limitations for a non-rigid rotor. Despite long sequences with extremely high cumulative

kick strengths, we fail to populate rotational levels that are significantly above thermally excited states. We propose a scheme of a non-periodic pulse train that makes use of fractional resonances to extend the reach of the impulsive excitation. Section 5.5 concludes the topic of impulsive multi-pulse excitation of molecular rotation using fractional and full quantum resonances.

5.1 Demonstration of the resonance map

In this first experimental demonstration, we investigate the rotational coherences created by a periodic pulse sequence. We excite a room temperature ensemble of oxygen molecules with a large number of rotational states thermally populated. This simplifies the observation of many fractional resonances and the study of their ensuing dynamics. We use rotational Raman spectroscopy in a gas cell filled with oxygen, as described earlier in Fig. 4.1(a). The excitation is done via relatively weak femtosecond pulses, in sequences of up to 15 pulses. These sequences were produced by a pulse shaper without interferometric splitting (details of the pulse train generation are given in chapter 3).

In Fig. 5.1, two-dimensional plots show the observed Raman peaks (color coded from dark to bright red) as a function of the pulse train period T . Each Raman spectrum is plotted as a function of wavelength (left vertical axis) or converted to J -numbers (right vertical axis). The apparent pattern of peaks can be interpreted via the resonance map (Sec. 2.3.8). Even J 's are missing due to the oxygen nuclear spin statistics. We set all individual pulses to weak energies, where the accumulated kick strength is $P_N = P \cdot N \lesssim 1$, so as to look at the dynamics in a perturbative regime.

In Fig. 5.1(a), the period of five pulses is varied from 10.8 to 12.6 ps. Oxygen $^{16}\text{O}_2$ has a revival time of $T_{\text{rev}} = 11.67\text{ps}$. If we choose the period to match the revival time $T = T_{\text{rev}}$, then we excite the molecules with a train tuned to the quantum resonance. The result is the generation of a broad rotational wave packet, when all J -states are excited simultaneously. We will investigate this scenario in more detail in Sec. 5.4. The Raman spectrogram matches well with the simulated resonance map, indicated by light blue crosses. Whenever the train period coincides with a fractional resonance, we excite a coherence between the states $|J\rangle$ and $|J+2\rangle$. At all other time periods the rotational coherences are suppressed. This supports the provided interpretation of the coherent accumulation in the rotational multi-pulse excitation.

5.1. Demonstration of the resonance map

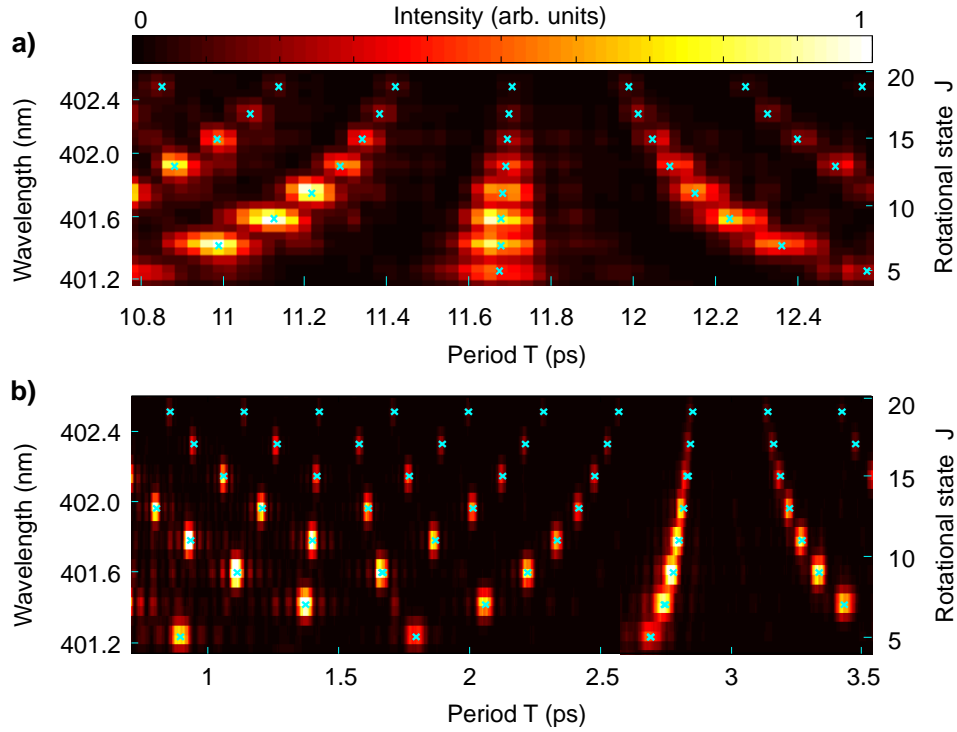


Figure 5.1: State and time resolved Raman spectrogram of room temperature $^{16}\text{O}_2$ after the excitation with a periodic pulse train. The train period T is scanned around the revival time for a sequence of 5 pulses (a) and around a quarter of the revival time for a sequence of 15 pulses (b). Light blue crosses indicate the time moments when a coherent wave packet consisting of two rotational states, $|J\rangle$ and $|J + 2\rangle$, accumulates a phase of π .

Scanning the period from 0.7 to 3.5 ps for a sequence of 15 pulses in Fig. 5.1(b) covers the dynamics around the quarter revival $T \approx 2.92$ ps.¹² In this range, no period exists when all J -states can be excited simultaneously. We point out that we can virtually suppress any coherence completely by choosing a period around 3 ps. This period overlaps with the point in time where the molecules are anti-aligned and thus leads to perfectly destructive interference. Read more about the revival dynamics and molecular alignment in the introduction, Sec. 2.3.7.

5.1.1 Excitation of single coherences

If the chosen period of a pulse train matches a fractional resonance T_J , the population of this state J will be transferred to the state $J + 2$. At the same time, the coherence $\rho_{J,J+2}$ will grow in a stepwise fashion, which we measure as the intensity of the rotational Raman signal. At weak energies, coherences can only be created at thermally populated states. For demonstration purposes, we select seven different periods T_1 , marked with solid vertical lines in the two-dimensional Raman spectrogram of Fig. 5.2. At these times, the train excites one single coherence, $J = 5, 7, 9, 11, 13, 15$ or 17 at the fractional resonances of T_1/T_{rev} equal to $2/13, 3/17, 4/21, 1/5, 6/29, 7/33$ or $8/37$, respectively. In the case of oxygen this corresponds to $T_1 = 1.80$ ps for $J = 5$ (purple), $T_1 = 2.06$ ps for $J = 7$ (blue), $T_1 = 2.22$ ps for $J = 9$ (light blue), $T_1 = 2.33$ ps for $J = 11$ (turquoise), $T_1 = 2.41$ ps for $J = 13$ (yellow), $T_1 = 2.48$ ps for $J = 15$ (orange) and $T_1 = 2.52$ ps for $J = 17$ (red).

Figure 5.3(a) plots the normalized Raman spectra after these periodic sequences of 15 pulses. The respective target states clearly show the strongest coherences. Minor signal can be seen at other J values due to the finite pulse duration of 130 fs leading to a partial overlap with other quantum resonances.

The concept of accumulating coherence over several pulses is not restricted to periodic trains. Building a sequence that alternates between two different periods T_1 and T_2 both of which are resonant with the same target state J will show the same effect. Furthermore, we expect that the selectivity can be enhanced, since the overlap of the finite width pulses with other fractional resonances may be different for T_1 and T_2 . We build three

¹²Both sequences utilized in Fig. 5.1(a) & (b) were created with the pulse shaper, without interferometric splitting, in order to simplify the setup. A pulse train of 5 pulses with a period of 12.6 ps spans a duration of 50 ps, reaching the pulse shaper limit. A pulse train of 15 pulses with a period of 3.5 ps spans a similar duration of 49 ps.

5.1. Demonstration of the resonance map

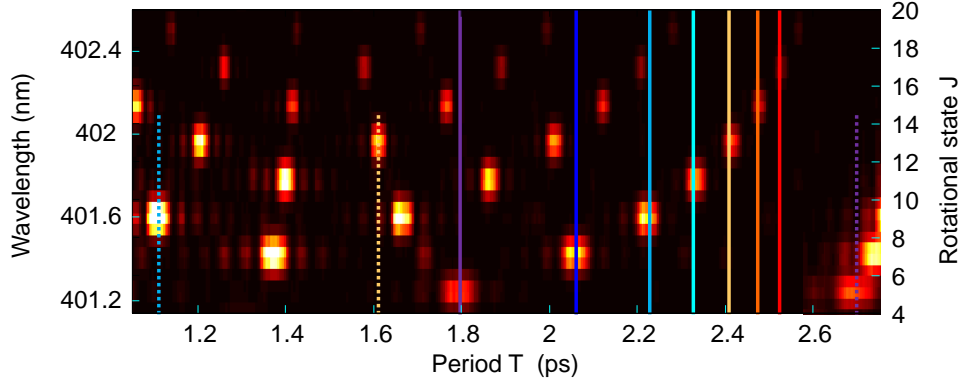


Figure 5.2: Raman spectrogram of room temperature oxygen $^{16}\text{O}_2$ after the excitation with a periodic pulse train of 15 pulses (same color map as Fig. 5.1). Highlighted are selected periods to excite single coherences.

such trains, for $J = 5, 9$ or 13 at the fractional resonances of T_1/T_{rev} and T_2/T_{rev} equal to $2/13$ and $3/13$, $4/21$ and $2/21$, or $6/29$ and $4/29$, respectively. The newly added T_2 timings are marked as dotted vertical lines in Fig. 5.2. The observed Raman spectra in Fig. 5.3(**b-d**) (dashed black lines) prove the increased selectivity compared to the previous results (solid coloured lines) taken from (**a**). The measurements were done with the following periods: (**b**) $T_1 = 1.80$ ps, and $T_2 = 2.69$ ps, (**c**) $T_1 = 2.22$ ps and $T_2 = 1.11$ ps, (**d**) $T_1 = 2.41$ ps and $T_2 = 1.61$ ps.

A number of our studies required periodic sequences of high intensities ($P > 1$). Once the accumulated kick strength of the pulse train is sufficient to transfer more than 50% of the population from the initial state J to the state $J + 2$, the maximum coherence, or the maximum Raman signal, is reached. In the case of even stronger pulses, we observe oscillations between the mentioned states, similar to Rabi oscillations in a two-level system. This phenomenon is discussed in Sec.5.2.

When we investigate the phenomenon of dynamical localization in chapter 6, we examine the angular momentum distribution after the excitation with a high-intensity pulse train, whose period is chosen off-resonance. However, each pulse of the train has a finite duration. Thus, the choice of the train period might affect the shape of the distribution, because of the ‘partial’ overlap of pulses with particular quantum resonances. Peaks in the spectra at certain states J can often be explained by the proximity of a corresponding fractional resonance. For that reason, the simple non-perturbative

5.1. Demonstration of the resonance map

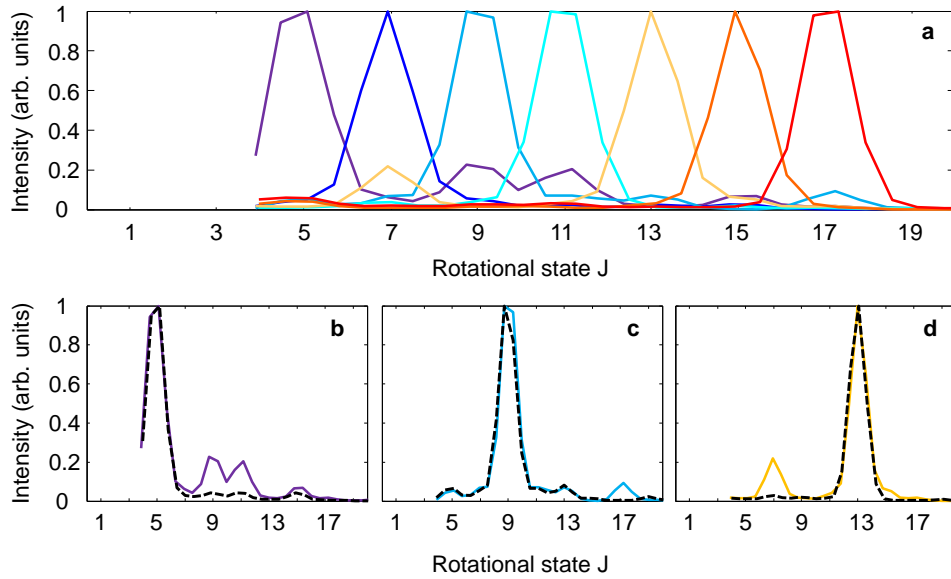


Figure 5.3: Normalized Raman spectrum after the excitation by a sequence of 15 pulses. **(a)** The seven coloured lines are obtained with seven different periodic trains. The periods T_1 are chosen to each excite only a single coherence $\rho_{J,J+2}$. **(b-d)** The black-dashed line shows the improved selectivity using a pulse train with two alternating periods T_1 and T_2 both optimized to excite the same single coherence $\rho_{J,J+2}$ for **(b)** $J = 5$, **(c)** $J = 9$ and **(d)** $J = 13$. The coloured lines are the spectra after the strictly periodic train with $T = T_1$, as shown in **(a)**. All periods are given in the text and marked in Fig. 5.2.

picture of the resonance map is useful in the interpretation of the results.

5.2 Rabi oscillations in molecular rotation

In this section, we demonstrate robust and selective population transfer between two isolated rotational states of the QKR. If the goal is to maximize the population transfer in a simple two-level system, one distinguishes between two approaches: A single pulse that executes half a cycle of a Rabi oscillation (the so-called π -pulse) will invert the population [44, 29], however this method is generally very sensitive to the pulse parameters. A robust alternative is an adiabatic technique [176] which excels in complete population transfer.

Many adiabatic schemes lose their appeal in multi-level systems when they become sensitive to exact frequency chirps or pulse intensities [159, 30, 113]. In a series of theoretical works, Shapiro *et.al.* [154, 156, 155] studied population transfer by a piecewise adiabatic passage and a robust population transfer was demonstrated between two quantum states [194]. The piecewise procedure is transferable to selective excitation in more complex quantum systems. The idea of using pulse sequences to optimize population transfer has also been applied to many non-adiabatic schemes, e.g. Refs. [186, 132], or has been found as a solution via a genetic search algorithm [168].

We present a technique that uses a pulse train of ultra-short pulses to address two-states in a multi-level system. We exploit the fact that a pulse train of broadband ultra-short pulses is a comb in the frequency domain, which enables selective excitation, just like with narrowband continuous-wave lasers [171]. The selectivity of a comb is combined with the accumulative effect of a pulse sequence. More specifically, we choose the pulse train period to pre-select an effective two-level system of two rotational states, $|J\rangle$ and $|J+2\rangle$. In this non-adiabatic approach the number of pulses and their strength can be used to transfer the system into any arbitrary superposition of two states. We demonstrate the effect of Rabi oscillations and study their dependence on the pulse train parameters. The scheme relies on a periodic sequence of many femtosecond pulses and has not been reported yet.

In Sec. 5.2.1 we describe the theory of population transfer in a two-level system and apply it to the QKR. In Sec. 5.2.2 we review the experimental details, before presenting the results in Sec. 5.2.3. The observation of Rabi oscillations was used to calibrate the kick strength of our laser pulses in all

other experiments. Details of this method can be found in Sec. 5.2.4.

5.2.1 Theory and simulation

At first we describe the Rabi formalism in a real two-level system, which is then applied to the case of a kicked molecule. We will then demonstrate the phenomenon via numerical simulations to clarify certain properties that cannot be shown in the experiment.

Two-level system

Monochromatic light of frequency ω is used to excite a transition in a two-level system with the states $|a\rangle$ and $|b\rangle$, whose energy difference is given by $E_b - E_a = \hbar\omega_0$.

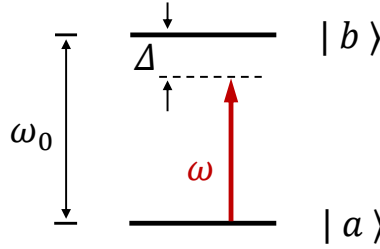


Figure 5.4: Energy diagram of a two-level system.

I.I. Rabi showed that the population in a two-level system will oscillate between both states under the influence of a constant electric field. The potential energy of the interaction is described as the product of the dipole moment μ of the atomic transition and $\mathcal{E}(t)$ the electric field amplitude, $V(t) = \mu\mathcal{E}(t)$. We define the Rabi-frequency as

$$\Omega(t) = \frac{\mu\mathcal{E}(t)}{\hbar}, \quad (5.1)$$

and a *generalized Rabi frequency* Ω' for non-resonant fields with a detuning of $\Delta = \omega_0 - \omega$

$$\Omega' = \sqrt{\Omega^2 + \Delta^2}. \quad (5.2)$$

The time-dependent probability to occupy either of the two states is [44, 29]

$$|c_b(t)|^2 = \frac{\Omega}{\Omega'} \sin^2\left(\frac{\Omega'}{2}t\right) \quad (5.3)$$

$$|c_a(t)|^2 = 1 - |c_b(t)|^2. \quad (5.4)$$

5.2. Rabi oscillations in molecular rotation

with the total wave function $|\Psi(t)\rangle = c_a(t)e^{-iE_a t/\hbar} |a\rangle + c_b(t)e^{-iE_b t/\hbar} |b\rangle$. The population oscillates with the generalized Rabi frequency. For resonant light, the maximum transfer is 100 %. Once we detune from resonance the efficiency drops - the amplitude of Rabi oscillations decreases while the oscillation frequency increases. For time-dependent electric fields it is convenient to introduce the pulse area $A = \int dt \Omega'$. A complete transfer (at $\Delta = 0$) is achieved when the pulse area is an odd multiple of π , referred to as a “ π -pulse”.

Effective two-level system in the periodically kicked rotor

The QKR is a multi-level system with many rotational levels. By taking a long pulse sequence and setting the period to match a specific fractional quantum resonance, the QKR will behave as an effective two-level system.

According to the resonance map (Sec. 2.3.8) we can choose a period which is in resonance with a superposition of two states $|J\rangle, |J+2\rangle$. The excitation of all other states in the vicinity is efficiently suppressed due to the repeated kicking with a period that is incommensurable with their rotational periods. The effective wave function reduces to the form $|\Psi(t)\rangle = c_J(t)e^{-iE_J t/\hbar} |J\rangle + c_{J+2}(t)e^{-iE_{J+2} t/\hbar} |J+2\rangle$. We have isolated a two-level system that is coupled with a two-photon transition within a multi-level system. The number of kicks N , which are spaced out with a period T , represents a unit of time. In the experiment we will demonstrate how the population oscillates between the states $|J\rangle$ and $|J+2\rangle$ as a function of N .

The potential energy of the QKR has been introduced in Eq. 2.8 as $V(\theta, t) = -\frac{\Delta\alpha}{4}\mathcal{E}^2(t)\cos^2\theta$. Similarly to Eq. 5.1, the Rabi-frequency of the QKR behaves according to

$$\Omega_{\text{QKR}}(t) \propto \frac{\Delta\alpha}{4\hbar} \mathcal{E}^2(t). \quad (5.5)$$

We discuss the case where the period of the pulse train is chosen on resonance first. As we learned in the last section, Rabi oscillations depend on the pulse area $A = \int dt \Omega(t)$, which is re-evaluated for the new system by integrating over the duration of the pulse train

$$A_{\text{QKR}} = \int_0^{NT} dt \Omega_{\text{QKR}} \propto \frac{\Delta\alpha}{4\hbar} \int_0^{NT} \mathcal{E}^2(t) dt = PN. \quad (5.6)$$

Here, we used the definition of the kick strength (Eq. 2.11). On resonance, we expect Rabi oscillations with a frequency that is proportional to the kick strength and the number of kicks; complete population transfer is possible.

Detuning from the resonance results in a decrease of the oscillation amplitude and a simultaneous increase of the oscillation frequency, which is best understood in the frequency domain, where the pulse train is represented by a frequency comb. Changing the pulse train period is equivalent to modifying the comb spacing. Thus, it is obvious that a detuning of the train period from a fractional quantum resonance is nothing else but a detuning of the comb teeth from the resonant two-photon frequency.

We stress two points: (1) This discussion is only valid for relatively weak pulses ($P \lesssim 1$), when a single pulse couples only nearest neighbour states. We will show that for larger kick strength values population gets lost to other rotational states. (2) As a consequence of the degenerate M -sublevels, which interact slightly differently with the laser pulses, our system is not a true two-level system, but rather a superposition of several two-level systems. (3) The shift of the levels due to the AC Stark effect cannot be neglected and will become noticeable in an off-resonance excitation.

Rotational population versus coherence

By solving the Schrödinger equation, we obtain the complex amplitudes c_J^M used to calculate the rotational population $P_J = \sum_M \langle |c_J^M|^2 \rangle_{J',M'}$ and the modulus squared of the coherences $C_J^{(2)} = \sum_M \langle |c_J^{M*} c_{J+2}^M|^2 \rangle_{J',M'}$. Both expressions include the summation over the degenerate M -sublevels and the thermal average over initially populated states $|J', M'\rangle$. Check Sec. 2.3.6 for details.

Figure 5.5 shows the intrinsic connection between both quantities, P_J and $C_J^{(2)}$, for the example of nitrogen molecules exposed to a sequence of 60 weak pulses at $P = 0.2$ per pulse. To simplify the picture, we start with the molecules initially being in the rotational ground state at 0 K. Due to a non-zero nuclear spin of $^{14}\text{N}_2$, there are two spin isomers with the corresponding statistical weights of $P_0 = 2/3$ and $P_1 = 1/3$. Both parities are not coupled and evolve independently; we look at even rotational states.

The resonance condition for the quantum state $|J, M\rangle = |0, 0\rangle$ is met exactly when we choose a train period of $T = 0.3354 T_{\text{rev}}$, marked with a solid line in the resonance map, Fig. 5.6. Owing to the AC Stark-shifts of the levels, it deviates from the classical prediction of $1/3$ by 0.62% (more details follow in the next subsection). The excitation dynamics of this idealistic case is plotted in Fig. 5.5(a). We achieve a complete population transfer between the states $J = 0$ and 2, with the respective populations $P_0 = |c_0^0|^2$ (dashed black line) and $P_2 = |c_2^0|^2$ (dotted black line). The strength of the

5.2. Rabi oscillations in molecular rotation

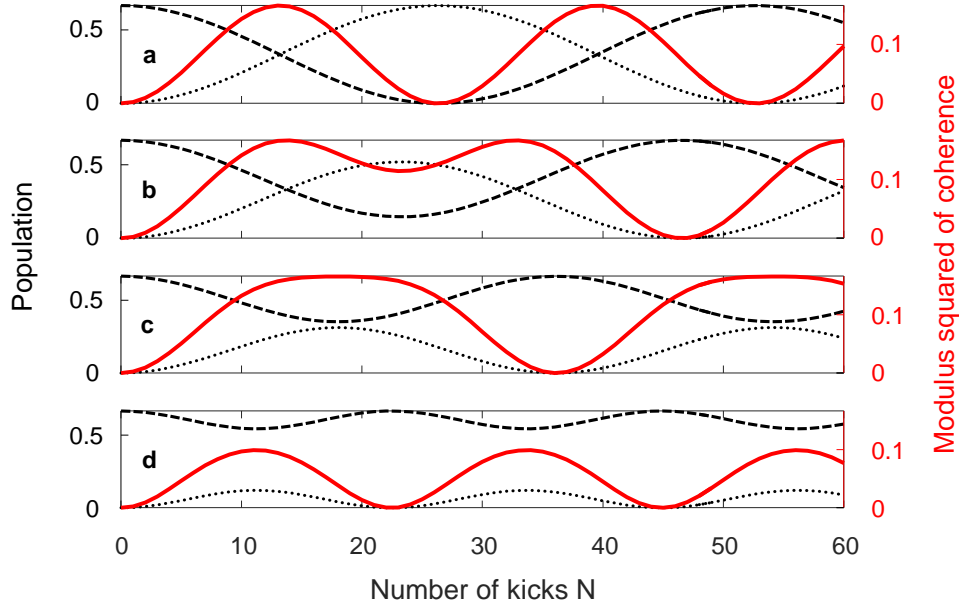


Figure 5.5: Excitation of N_2 molecules, initially in $J = 0$, with a sequence of 60 pulses at $P = 0.2$ per pulse. The population (left axis) oscillates between $J = 0$ (dashed line) and $J = 2$ (dotted line). The quantity of interest is the corresponding modulus squared of the coherence (red solid line, right axis). Shown are different detunings from the period $T/T_{\text{rev}} = 0.3354$ with (a) 0%, (b) 1%, (c) 2% and (d) 4%.

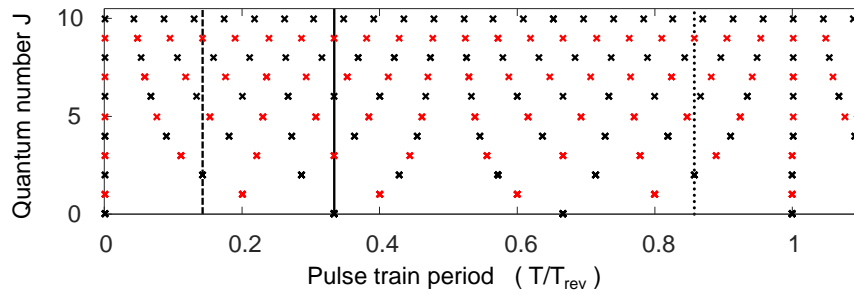


Figure 5.6: Resonance map: A pulse train with period $T/T_{\text{rev}} = 1/3$ (solid line) induces Rabi oscillations between $J = 0$ and 2. For $T/T_{\text{rev}} = 1/7$ (dashed line) or $6/7$ (dotted line) they are between $J = 2$ and 4.

kicks affects the Rabi period, i.e. the number of pulses required to achieve one full cycle. The coherence and its modulus squared $C_0^{(2)} = |c_0^{0*} c_2^0|^2$ (red solid line) is maximized when both states are equally populated and is zero when one of the states has no population.

Figure 5.5**(b-d)** explores the oscillation dynamics for steadily increasing detuning from the particular resonance by 1%, 2% and 4%, respectively. As in the case of a two-level system, we expect faster oscillations with a smaller amplitude for growing detunings. We observe the same behaviour in kicked molecules. The transfer of population \mathcal{T} decreases from **(a)** 100%, **(b)** 78%, **(c)** 47% to **(d)** 18%, while the oscillation frequency increases. The observable $C_0^{(2)}$ contains the same information in a less obvious way: **(a)** On resonance ($\mathcal{T} = 100\%$) we see regular oscillations with half the period of the population oscillations; **(b)** Off resonance ($\mathcal{T} > 50\%$) a double-peak oscillation is visible as two maxima merge, the oscillation amplitude remains unchanged; **(c,d)** Further off resonance ($\mathcal{T} < 50\%$) the regular oscillations have the same period as the population oscillations, but with a decreasing amplitude.

In the experiment, we do not directly detect rotational populations P_J . We use rotational Raman spectroscopy (Sec. 4.1) that yields a state-resolved Raman spectrum whose intensity is proportional to $C_J^{(2)}$. We fit our calculations to match the measured Raman intensities $I_J = b \cdot C_J^{(2)}$ with a single fitting parameter b .

Manifold of M -substates

It is impossible to separate individual M channels *experimentally*. The observed Raman spectra are always an incoherent sum over all initially populated $|J', M'\rangle$ states. In Fig. 5.7 we reveal the individual dynamics *numerically* for N_2 at a realistic temperature of 25 K. The total population in the initial $|2, M'\rangle$ manifold is 0.37, of which one fifth is in each degenerate $M' = 0, \pm 1, \pm 2$ substate. We excite these molecular states with a sequence of 100 weak pulses of $P = 0.2$ with a period of $T = 1/7 T_{\text{rev}}$ (dashed line in Fig. 5.6) and compare the evolution of the population P_2 (dashed black line), the population P_4 (dotted black line) and the modulus squared of their coherence $C_2^{(2)}$ (red solid line).

The dynamics differ significantly for each individual initial state $|J', M'\rangle$ under identical excitation conditions. In Fig. 5.7 we compare the dynamics of molecules initially occupying **(a1)** $|2, 0\rangle$, **(b1)** $|2, 1\rangle$ and **(c1)** $|2, 2\rangle$. Note, that these three plots describe the entire dynamics since each $|2, \pm M'\rangle$ in-

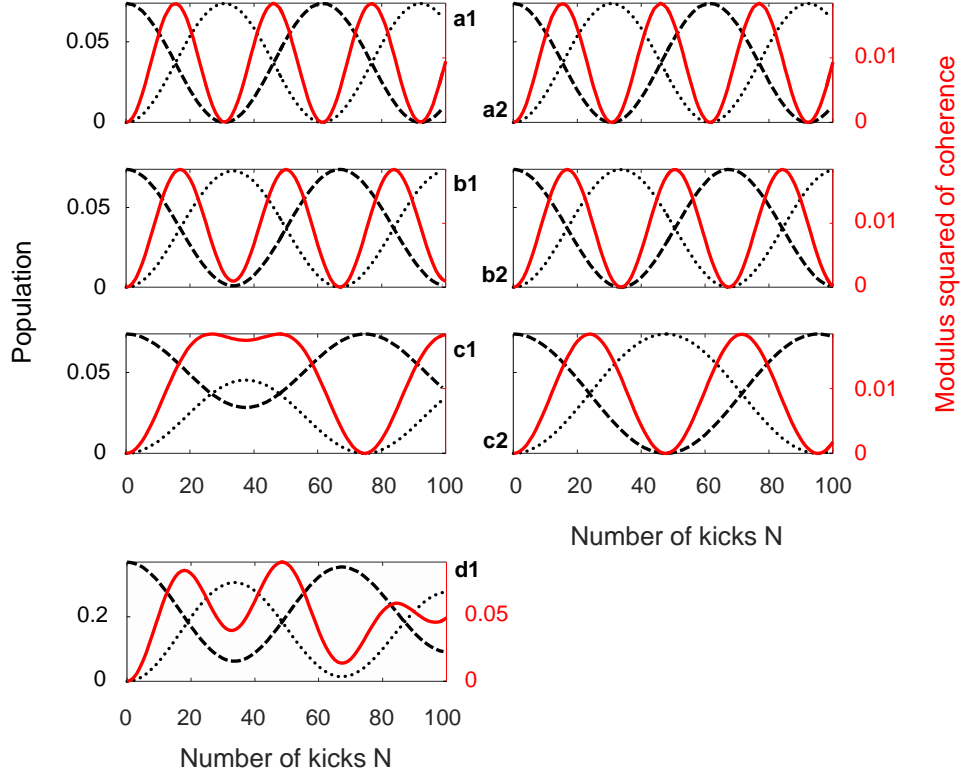


Figure 5.7: Excitation of N_2 molecules at 25 K with a sequence of 100 pulses at $P = 0.2$ per pulse. Plotted are the populations (left axis) oscillating between $J = 2$ (dashed line) and $J = 4$ (dotted line), and the modulus squared of their coherence (red solid line, right axis). In column (1), we set the period to $T = \frac{1}{7} T_{\text{rev}}$ and resolve the dynamics of different initial states $|J', M'\rangle$: (a) $|2, 0\rangle$, (b) $|2, 1\rangle$, (c) $|2, 2\rangle$. (d) is the average of all M' -substates in $|2, M'\rangle$. In column (2), we adjust the period individually for each substate to regain complete population transfer, achieved at the detunings of (a) -0.04% , (b) $+0.17\%$ and (c) $+0.83\%$.

teracts with the pulses in the same way. We emphasize two key signatures, that were both discussed in Sec. 2.3.6 under “ M -degeneracy”. First, the effective kick strength decreases with higher magnetic quantum numbers - more pulses are needed to complete one Rabi cycle. Second, the resonance condition changes due to the dynamic Stark shift. We quantify the difference with the max population transfer \mathcal{T} , which is a measure of the detuning from the resonance. We obtain efficiencies of $\mathcal{T} = 100\%$, 99% and 61% , respectively. The graph (**d1**) is the average over all five M' sub-states starting in the $|2, M'\rangle$ manifold. Since there is no unique period that satisfies the resonance condition for all participating states, we cannot expect pure Rabi oscillations. Instead a quasi-periodic pattern with reduced contrast emerges¹³.

Owing to the quadratic Stark-shift, which is lifting the M -degeneracy, one obtains a resonance condition that depends on the magnetic quantum number. The resonant period is shifted proportionally to the kick strength P . It is possible to compensate the phase shift by detuning the train period away from $T = 1/7 T_{\text{rev}}$. This is done individually for each $|2, M'\rangle$ regaining a 100% population transfer. We empirically retrieve the following detunings (**a2**) -0.04% , (**b2**) $+0.17\%$ and (**c2**) $+0.83\%$.

5.2.2 Experiment

We implement rotational Raman spectroscopy in nitrogen molecules cooled to a rotational temperature around 25 K via a supersonic expansion, as described earlier in Fig. 4.1(**b**). Our pump is a periodic train of intermediate kick strength around $P = 1$ or less. We conducted measurements with two different sequences, one of 29 pulses at a period of $1/7 T_{\text{rev}}$, and the other one with 24 pulses at a period of $6/7 T_{\text{rev}}$. Both timings are marked on the resonance map in Fig. 5.6. The revival time of $^{14}\text{N}_2$ is $T_{\text{rev}} = 8.38$ ps. Owing to the overall length of the pulse train, the generation of the first sequence is done with only the pulse shaper, whereas the latter one requires two additional Michelson interferometers (details are found in chapter 3). The weak probe is a single narrowband pulse with a spectral width small enough to resolve the individual rotational states of nitrogen.

We deliberately choose nitrogen over oxygen as our sample. The phenomenon is independent of the type of molecule, but oxygen bears the disadvantage of spin-rotation coupling (Sec. 4.2.3). In particular at low rotational quantum numbers, where the resulting dephasing of the Raman signal is on

¹³To reproduce the experimental Raman spectrum, we would need to include all other J' -states that can couple to $J = 2$ or 4, as well.

a similar time scale as the length of the pulse train, the data interpretation would be more complicated.

5.2.3 Observation of Rabi oscillations

This section summarizes our experimental investigations regarding Rabi oscillations in a quantum rotational system. We present the dependence of the phenomenon on various pulse train parameters, i.e. the choice of a particular fractional resonance, the detuning from that resonance, the kick strength, the number of pulses and their bandwidth. The results are shown in one of two ways: Either we plot the Raman intensity for a selected J -state as a function of the pump-probe delay, or we plot a two-dimensional Raman spectrogram displaying the entire Raman spectrum along its second axis. The time delay is expressed in the number of pulses N that have interacted with the molecules.

Dependence on the detuning

We study the rotational excitation of nitrogen molecules after a pulse sequence of 29 pulses with a period of $1/7 T_{\text{rev}}$. This fractional resonance is commensurable with the dynamics of the ($|2\rangle, |4\rangle$) wave packet, see Fig. 5.6. It has been chosen because $J = 2$ is the most populated state (37%) at a temperature of 25 K. (The state $J = 4$ holds another 13% of the initial population.) Figure 5.8 analyses the rotational dynamics for different detunings from the resonance, changing from -10% (top left) in 1% steps to $+1\%$ (bottom right). Plotted are the spectra between $J = 0$ and $J = 6$. The only state in the Raman spectrum with a substantial intensity I_J is the one at $J = 2$, which features multiple oscillations with a high contrast. We point out that barely any population escapes to different rotational states, which otherwise would be seen as additional Raman peaks, e.g. at $J = 4$. Although 50% of the population is initially not in $J = 2$ or 4 , the coherent accumulation of a sequence of non-resonant pulses results in virtually no Raman signal away from I_2 .

Looking at the oscillations, we make several key observations. Tuning slowly away from the resonance leads to the merging of two maxima, e.g. at -1% , -2% . The explanation has been given in the theory section. Tuning far away from the resonance leads to faster oscillations and a simultaneous drop of the amplitude. All spectrograms in Fig. 5.8 share the same intensity scale, the absolute amplitudes are therefore comparable. At the detuning of -10% we count three complete oscillations.

5.2. Rabi oscillations in molecular rotation

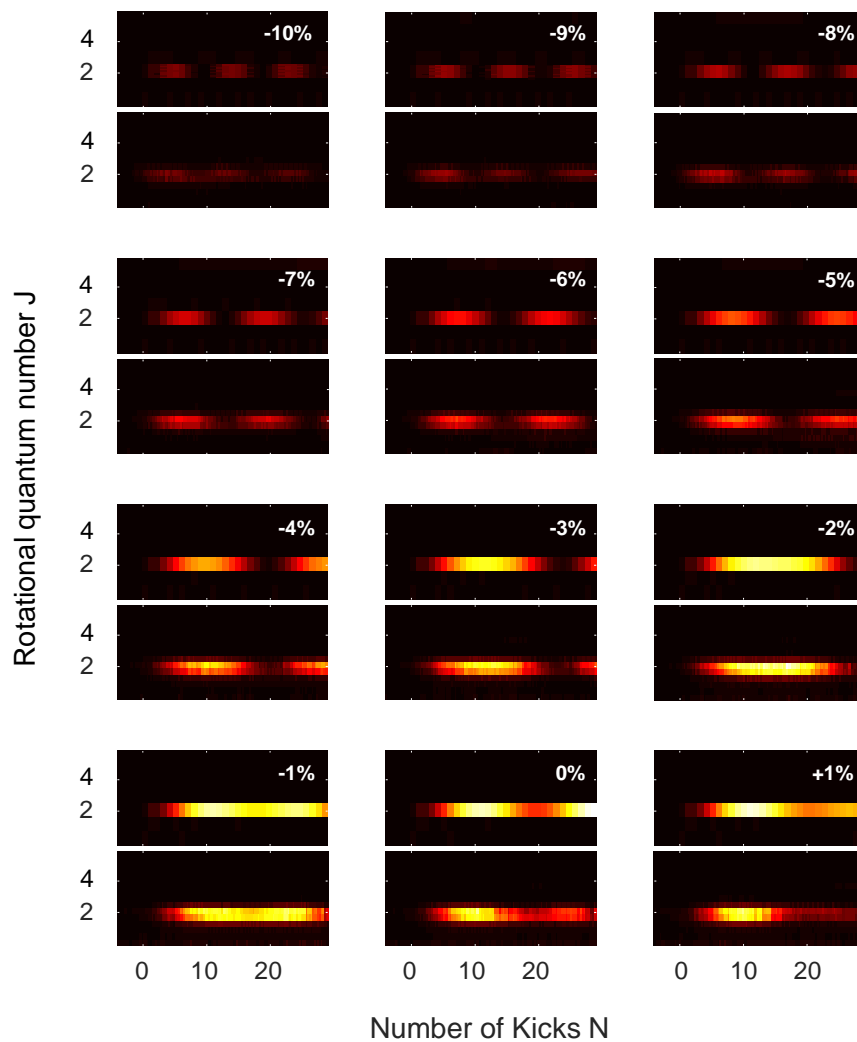


Figure 5.8: Rabi oscillations observed in the Raman spectrum of $^{14}\text{N}_2$ after the excitation with a periodic sequence of $N = 29$ pulses with a kick strength of $P = 0.33$. Amplitude and period of the oscillations are controlled by adjusting the period of the train around the fractional resonance at $T = \frac{1}{7} T_{\text{rev}}$ in twelve 1% steps from -10% (top left) to $+1\%$ (bottom right). Each spectrogram in this table compares numerical simulations at $T = 25$ K (top) with experimental results (bottom).

The experimental Raman spectra (bottom) are compared to the numerically calculated ones (top). The only free parameter in the simulation - the kick strength - has been adjusted to reproduce the observed oscillations. We found the best match at $P = 0.33$. For negative detuning, both graphs are very similar within experimental noise. On resonance and toward positive detuning the experimental contrast decreases with the number of oscillations, which is not reproduced in the simulation. The origin of this discrepancy lies in the finite duration of the pulses, and will be discussed later in the respective subsection.

Figure 5.9 provides a more quantitative comparison between the numerics and the experiment by showing the intensity I_2 for selected periods. The detunings from the resonance are (a) 0%, (b) -3%, (c) -6% and (d) -9%. The graphs represent cross-sections of the two-dimensional Raman spectrograms in Fig. 5.8 at $J = 2$. After determining the kick strength of $P = 0.33$ and rescaling, the simulation (black dots) reproduces the experiment (solid red line) with an error of (a) 44%, (b) 12%, (c) 9% and (d) 32%. We calculated the *root mean square deviation* (RMSD) found from the deviations for all integer values of N . The percentages are the RMSD values divided by the mean experimental signal.

The explanation of the non-zero minima of Rabi oscillations, e.g. in panel (a), is the existence of five individual channels corresponding to the five magnetic quantum numbers $M = 0, \pm 1, \pm 2$. As discussed earlier, in the impulsive multi-pulse excitation, the resonance condition for each non-degenerate M -state is different. Our experiments provide a verification of that discussion in the theory section. At larger detunings from the fractional quantum resonance, e.g. in panel (d), the relative differences in the individual detunings between all M -channels become smaller. Thus, the contrast of the oscillation increases.

Dependence on the kick strength

So far, we have looked at Rabi oscillations at weak kicks of $P \ll 1$. In Fig. 5.10 we examine the dynamics due to a periodic pulse sequence with increasingly higher pulse energies. At $P = 0.6$ (a) we resolve two oscillations within 24 pulses. We provide a direct comparison between simulation (1) and experiment (2) with a reasonable agreement. At larger strengths of $P = 0.83$ (b) and $P = 1.1$ (c) we observe faster oscillations but the correspondence to the simulation becomes increasingly worse. As the number of pulses grows, the Raman intensity of I_2 diminishes. Owing to the finite

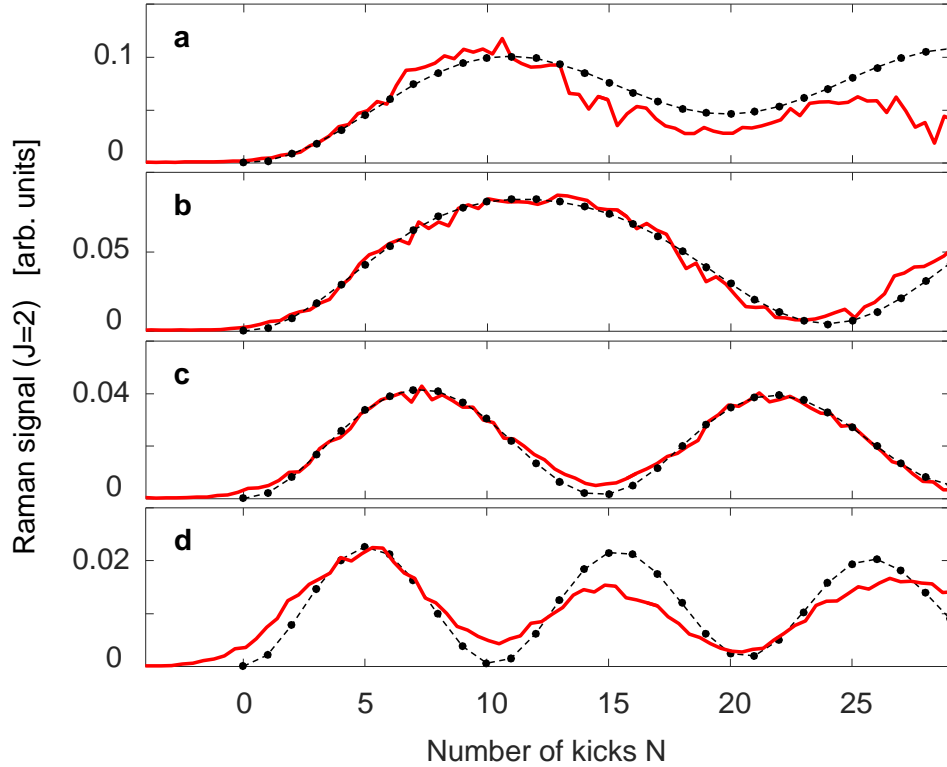


Figure 5.9: Rabi oscillations in $^{14}\text{N}_2$ observed in the Raman signal after the excitation with a periodic sequence of $N = 29$ pulses with a kick strength of $P = 0.33$. Amplitude and period of the oscillations are controlled by detuning the period of the train by (a) 0%, (b) -3% , (c) -6% and (d) -9% with respect to the fractional resonance at $T = 1/7 T_{\text{rev}}$. The intensity of the experimental result (solid red line) is normalized to fit the numerical simulation (black dots, connected with a dashed line).

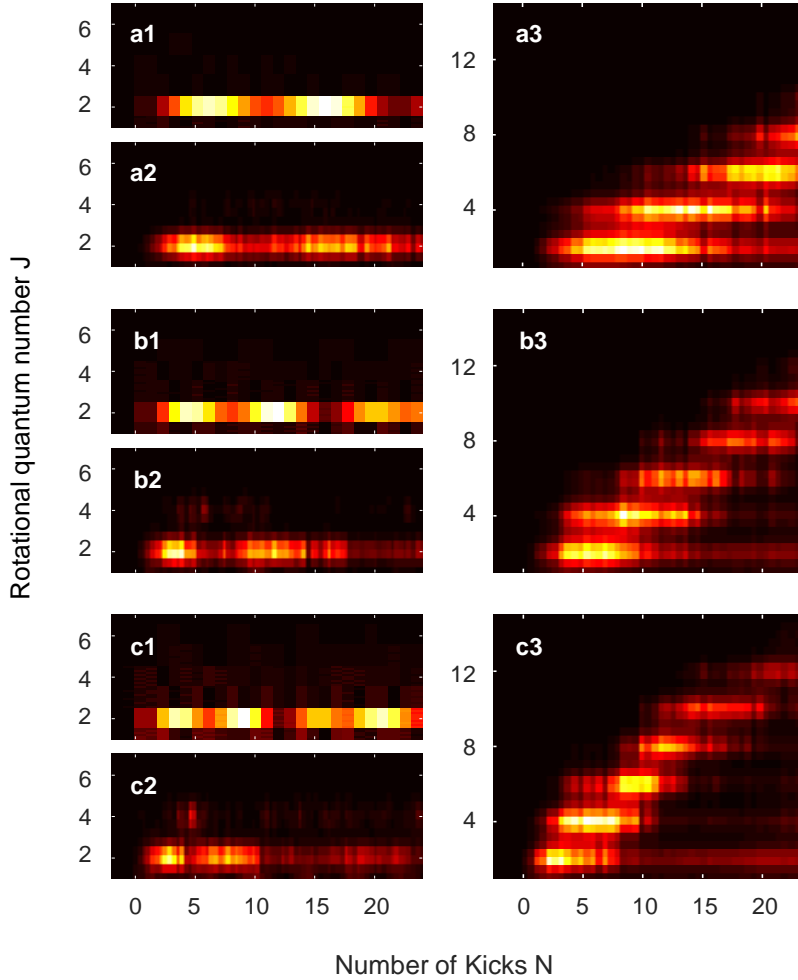


Figure 5.10: The effect of pulse energy on Rabi oscillations observed in the Raman spectrum of $^{14}\text{N}_2$ after the excitation with a periodic sequence of $N = 24$ pulses tuned to the fractional resonance at $T = \frac{6}{7} T_{\text{rev}}$. The period of the oscillations decreases with the kick strength from (a) $P = 0.6$, (b) $P = 0.83$ to (c) $P = 1.1$; shown are numerical simulations at $T = 25$ K (1) and experimental results (2). The same pulse trains with a period tuned to match the quantum resonance at $T = T_{\text{rev}}$ lead to a linear growth in angular momentum; shown are experimental results (3).

pulse duration, the coupling to other states is larger in the experiment than in the idealistic calculation with δ -kicks. Consequently, we detect Raman peaks belonging to higher- J coherences, e.g. I_4 . Further investigations on the subject of pulse duration are performed in the next section.

We want to emphasize that Fig. 5.10 has been recorded for a pulse train whose period is set to $T = 6/7 T_{\text{rev}}$, unlike the train with $T = 1/7 T_{\text{rev}}$ in Fig. 5.8. Both periods are tailored to the same coherent wave packet and exemplify the universality of the process.

Finally, we put the strength of the pulse train in context. For all three scenarios in Fig. 5.10(**a-c**) we include an additional spectrogram (**3**) outlining the linear growth of angular momentum when the period of an otherwise identical pulse train is moved from fractional quantum resonance to the full quantum resonance $T = T_{\text{rev}}$. The total energy in the train is sufficient to reach much higher rotational states. This excitation scenario is discussed in detail in Sec. 5.3.

Effect of finite pulse duration

The finite duration of our 130 fs pulses manifests itself even at the excitation of such low rotational quantum numbers as studied here in the context of Rabi oscillations. We demonstrate consequences of a limited bandwidth by pointing out differences between the experimental results and the δ -kick simulation.

We excite nitrogen with a pulse train similar to those used before, i.e. 29 pulses of medium strength $P = 0.57$, adjusted to the $1/7$ fractional resonance. We fine tune the period by -4% below this resonance, indicated with the dashed line in Fig. 5.11(**1**). Here, the period is as far detuned as possible from the resonances of the next higher Raman peak I_4 . A second pulse train is tuned to $+4\%$ above the resonance, marked by the dotted line, so as to get it closer to the resonance at $J = 4$.

In Fig. 5.11(**2**) we discover that these small relative changes in the train period do matter in the rotational excitation. Specifically, we look at the intensity of the Raman peaks I_2 (blue lines) and I_4 (red lines). According to the simulation (dots, with dashed lines) the expected oscillatory behaviour is apparent for the Raman peak I_2 , whereas the peak I_4 is of virtually zero intensity. This is true for both detunings, -4% (**2a**) and $+4\%$ (**2b**). Hence, the δ -kick excitation is very *selective*. Only in the proximity of a quantum resonance will the respective states be populated. Compared to that are the experimental results (solid lines). We see oscillations in I_2 regardless of the detuning. However, the behaviour of I_4 is sensitive to

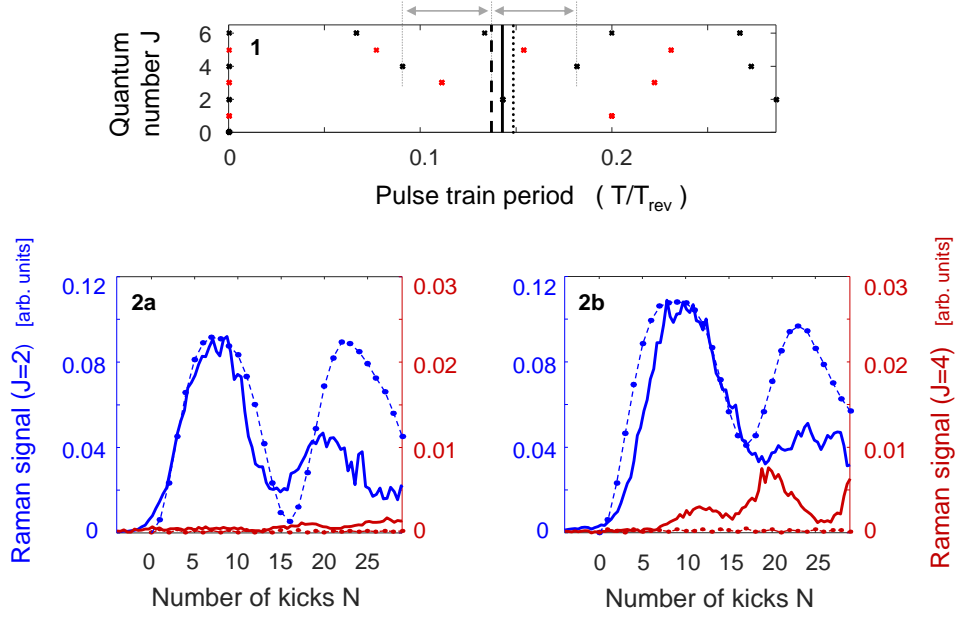


Figure 5.11: **(1)** Resonance map, marked are the train periods matched exactly with the $1/7$ fractional resonance (solid line), and detuned from it by -4% (dashed line) and $+4\%$ (dotted line). **(2)** Compromising effect of the laser bandwidth on Rabi oscillations in $^{14}\text{N}_2$ seen in the Raman signal I_J of the states $J = 2$ (blue lines, left axes) and $J = 4$ (red lines, right axes). A periodic sequence of $N = 29$ pulses with a kick strength of $P = 0.57$ is detuned by **(2a)** -4% and **(2b)** $+4\%$ from the fractional resonance at $T = 1/7 T_{\text{rev}}$. The experimentally measured intensity I_2 (solid blue line) is rescaled to fit the simulation (blue dots, dashed line). The same rescaling is applied to the experimental intensity I_4 (red solid line) and compared to the simulation (red dots, dashed line).

the choice of the period: very little intensity is measured for the optimized detuning of -4% (**2a**) but a significantly higher intensity is seen for $+4\%$ (**2b**). Hence, the experiment with *kicks of finite duration* is more *sensitive* to different quantum resonances, and the population “leaks” more easily to other rotational states.

It is helpful to keep this conclusion in mind for all other QKR studies. For example, when we investigate the phenomenon of dynamical localization in chapter 6, it is important to stay away from all fractional resonances. Owing to the finite pulse width, one will always partially overlap some resonances, which in turn will affect the shape of the Raman spectrum. In order to minimize these effects, we will average over several pulse trains with different periods.

5.2.4 Kick strength calibration

The fact that we can identify multiple Rabi oscillations with high precision is used to calibrate the kick strength of our pulses for all future experiments. We obtain an accurate measure of the kick strength in the interaction region of the experiment, without relying on the (often inaccurate) measurements of the pulse parameters, i.e. beam diameter, pulse energy or pulse duration.

Regardless of the specific experimental requirements, in terms of the number of pulses and the period in a pulse sequence, we can always find a suitable fractional quantum resonance to observe Rabi oscillations nearby. We record oscillations for several different detuning from the chosen resonance to create a compilation of plots similar to Fig. 5.8. The scans are done at weak pulse intensities ($P \ll 1$) where the population is well confined between both target states. The actual kick strength in the interaction region of the experiment is found by matching the simulation to the real data. Knowledge of the input energy of the pulse train, which we measure with an energy meter prior to the vacuum chamber, suffices to extrapolate the final kick strength at higher pulse energies.

5.3 Bloch oscillations in molecular rotation

This section is dedicated to the impulsive excitation of molecules with sequences of high-intensity, ultra-short laser pulses whose periods are tuned on full quantum resonance, i.e. around the rotational revival time of the molecule. Resonant excitation schemes have been studied before in thermal ensembles [41, 192], demonstrating a growing rotational energy. The population of increasingly higher angular momentum states, however, is limited

by the centrifugal distortion. In a series of theoretical works [60, 64, 62] Floss *et.al.* demonstrated that at a critical value of the angular momentum the centrifugal distortion will lead to a “back-scattering” of population towards lower J 's, representing Bloch oscillations in the molecular rotation. These were reported for the first time in 2015 [64], measured indirectly via molecular alignment of room temperature nitrogen exposed to eight periodic pulses.

We present a more detailed investigation of Bloch oscillations in a quantum rotational system. The results demonstrated here improve the previous study in several aspects: (1) The use of rotational Raman spectroscopy allows for a state-resolved detection. For the first time, Bloch oscillations are directly observed in the angular momentum space. (2) Our experiment with molecules cooled to rotational temperatures below 30 K greatly decreases the width of the rotational wave packet, which increases the contrast of Bloch oscillations. (3) Significantly longer pulse sequences enable us to better capture the rotational dynamics. The disadvantage of our approach is a smaller spectral bandwidth of the laser pulses, which imposes a limitation for reaching higher rotational states. Under certain circumstances this prevents the observation of Bloch oscillations.

The phenomenon of Bloch oscillations in angular momentum is unique to real molecules. It does not appear in the case of a kicked rigid rotor. It is also not present in related physical systems like the atom-optic realization of a kicked rotor [121, 135]. Further, our experiment with real molecules offers great controllability over the oscillations. We demonstrate variable oscillation amplitudes and frequencies by detuning the pulse train period from the quantum resonance.

Bloch oscillations were first predicted in 1929 [25] to describe the electron motion in a crystalline solid subject to a DC electric field. The effect is extremely hard to show in real lattices as even small defects will destroy the process. The first experimental realization was done only in 1992 in a semiconductor superlattice [51]. Bloch oscillations have since been shown in a few different systems, i.e. in optical lattices, where ultracold atoms are subject to standing laser waves [17, 123, 93] or in periodic photonic structures [122, 133, 148, 37, 170]. Periodically kicked molecules offer another opportunity to study this effect in a new light.

The section has the following structure. First, we present the necessary theoretical background. In Sec. 5.3.1 we talk about Bloch oscillations in crystalline solids. The example of a one-dimensional crystal serves to show the analogy with the QKR system in Sec. 5.3.2. Section 5.3.3 gives the

details of our numerical simulations and section 5.3.4 the details of our experimental studies. All the results are shown and analysed in Sec. 5.3.5.

5.3.1 Theory I: Bloch oscillations in crystalline solids

Electrons in a crystalline solid subject to an external DC electric field exhibit an oscillatory motion, first discovered by Bloch and Zener [25, 190]. Although 'quasi-free' electrons in a band are exposed to an external force $f = -e\mathcal{E}$, with the electric charge of an electron e and the electric field strength \mathcal{E} , the solid acts as an insulator. The electrons oscillate but no net charge is carried through the crystal. This model only works in a perfectly periodic crystal without impurities.

The electron wave function describes a wave packet, i.e. a superposition of plane waves with the group velocity [162]

$$v = \frac{1}{\hbar} \frac{\partial E}{\partial k} . \quad (5.7)$$

An external force applied to the electrons in a crystal is equal to [162]

$$f = \hbar \frac{\partial k}{\partial t} = -e\mathcal{E} . \quad (5.8)$$

We explain the mechanism using the tight-binding example of a lattice in one dimension with only nearest neighbour interactions of Sec. 2.4.4. The quasi-momentum of the electron is $k(t) = -\frac{e\mathcal{E}}{\hbar}t$ found by integrating Eq. 5.8 with the boundary condition $k(0) = 0$. The dispersion relation $E(k) = T - 2W \cos(ka)$ from Eq. 2.38 is used to calculate the group velocity and the position of the band electron by integrating $v = \partial r / \partial t$ with $r(0) = 0$

$$v(t) = -\frac{2Wa}{\hbar} \sin\left(\frac{ae\mathcal{E}}{\hbar}t\right) \quad (5.9)$$

$$r(t) = \frac{2W}{e\mathcal{E}} \left[\cos\left(\frac{ae\mathcal{E}}{\hbar}t\right) - 1 \right] . \quad (5.10)$$

The electron starts at the bottom of the band at $k = 0$ when we turn on the electric field at $t = 0$. The electron responds by moving in negative r -direction. As k changes uniformly with time, the electron moves up the band $E(k)$. At $k = -\pi/2a$ it has reached the maximum velocity, before the velocity decreases again and reverses the sign at the Brillouin zone boundary $-\pi/a$. At this time the electron has reached its farthest position in real space before it is Bragg scattered in the opposite direction. The quasi-momentum

keeps linearly decreasing but due to the 2π periodicity of the reciprocal lattice, the k value changes to π/a . The process repeats with the velocity and the position of the electron bounded. The electrons oscillate with a Bloch frequency of $\omega_B = ae\mathcal{E}/\hbar$.

5.3.2 Theory II: Bloch oscillations in a molecular rotor

Behaviour similar to that of an electron in a periodic lattice subject to a DC electric field reappears in the angular momentum space of the periodically kicked quantum rotor. The Schrödinger equation governing the dynamics of the QKR is derived in appendix E based on Ref. [62]

$$i\frac{dc_J(n)}{dn} = V(J) c_J^{(n)} - \frac{P}{4} [c_{J+2}^{(n)} + c_{J-2}^{(n)}] . \quad (5.11)$$

In this semi-classical model the discrete number of kicks N is approximated with a continuous dimensionless time n . The parameters $c_J(n)$ are the amplitude coefficients for different eigenstates of the rotor wave function $|\Psi^{(n)}\rangle = \sum_J c_J^{(n)} |J\rangle$ belonging to the ‘ J -sites’ of a one-dimensional rotational lattice. The two terms on the right hand side are the on-site potential $V(J)$ and the kinetic term, which expresses the hopping between neighbouring sites (previously labelled T and W , respectively).

For a periodic lattice, if $V(J)$ is constant, we recover the tight-binding model yielding extended Bloch states; the rotational population will ‘hop’ over the entire lattice. This condition (here, $V(J) = 0$) is fulfilled only for a rigid rotor excited on quantum resonance, but not for realistic molecules, i.e. non-rigid rotors.

Non-rigid rotor, resonant excitation: The period between the kicks is set to match the full quantum resonance $T = T_{\text{rev}}$. The on-site potential calculated in appendix E.1 is approximately [62]

$$V(J) \approx -\pi \frac{D}{B} J^2 (J+1)^2 . \quad (5.12)$$

Compared to Eq. E.9, we neglect the small constant shift $P/2$. The gradient of the potential energy acts as a force, where the spatial coordinate is represented by the J -number $f = -dV(J)/dJ$. To make a connection with the solid state picture, we can also express the external force (Eq. 5.8) as $f = dk/dn$ in dimensionless units [62]

$$\frac{dk}{dn} = -\frac{dV(J)}{dJ} \approx 4\pi \frac{D}{B} J^3 . \quad (5.13)$$

In contrast to a uniform force, the effective force here becomes stronger with increasing J -numbers.

Rigid rotor, non-resonant excitation ($\delta \neq 0$): Let us now assume a period $T = (1 + \delta)T_{\text{rev}}$ with a detuning δ . If it is large enough to dominate over the centrifugal distortion effects, the latter one can be neglected. The on-site potential calculated in appendix E.2 is [62]

$$V(J) = \pi\delta J(J + 1) , \quad (5.14)$$

resulting in an external force

$$\frac{dk}{dn} = -\frac{dV(J)}{dJ} \approx -2\pi\delta J . \quad (5.15)$$

The second quantity of interest is the group velocity (Eq. 5.7) in dimensionless units $v = dE(k)/dk$, which in the lattice frame is $v = dJ/dn$. In direct comparison to the solid state case [$E(k) = T - 2W \cos(ka)$ in Eq. 2.38], the energy dispersion relation becomes

$$E(k) = -\frac{P}{2} \cos(2k) , \quad (5.16)$$

after substituting $T = 0$ as the on-site energy¹⁴ and $W = P/4$ as the strength of the hopping and $a = 2$ for the rotational lattice spacing. The group velocity of the rotational wave packet is therefore

$$\frac{dJ}{dn} = \frac{dE(k)}{dk} = P \sin(2k) , \quad (5.17)$$

displaying the oscillatory motion, equivalent to Bloch oscillations.

The two coupled equations for dJ/dn and dk/dn are equations of motion with the conjugate variables J and k . Floss *et.al.* showed the relation $k = -\theta$ between quasi-momentum and polar angle [62]. The same undulating behaviour manifests itself in the position on the angular momentum lattice $J(n)$, calculated by solving the two coupled equations. The turning points of Bloch oscillations are the edge of the lattice¹⁵ and at the ‘‘Bloch wall’’

¹⁴Strictly speaking, this assumption is only valid on resonance at $\delta = 0$.

¹⁵The edge of the lattice depends on the M -substate and the parity, but cannot lie below $J = |M|$.

J_B , which has been derived semi-classically in Ref. [62]

$$\begin{aligned} \text{Non-rigid rotor}(\delta = 0) : \quad J_B &= \sqrt[4]{J_0^4 + \frac{B P}{D} \frac{P}{2}} \approx \sqrt[4]{\frac{B P}{D} \frac{P}{2}} \\ \text{Rigid rotor}(\delta \neq 0) : \quad J_B &= \sqrt{J_0^2 + \frac{P}{\pi|\delta|}} \approx \sqrt{\frac{P}{\pi|\delta|}}, \end{aligned} \quad (5.18)$$

where J_0 is the initial angular momentum. The approximate expressions are valid if one starts at cold temperatures, close to the rotational ground state ¹⁶.

We interpret the rotational analogue of Bloch oscillations as follows [64]: At time zero, we start with a quasi-momentum $k = \pi/4$ because the initial growth rate $dJ/dn = P$ is determined by the strength of the first kick. The rotor feels an accelerating potential $V(J)$ because of the centrifugal distortion and/or negative detuning. This corresponds to a weak force at low J -states and an increasingly stronger force at higher states. As the quasi-momentum k grows, it eventually reaches the Brillouin zone boundary at $\pi/2$ and the Bloch wave is Bragg reflected because its length is comparable to the lattice spacing of $\Delta J = 2$. We refer to this location as the ‘‘Bloch wall’’ J_B . If the detuning is positive, it will counteract the centrifugal term and push the Bloch wall to higher rotational states, but since the centrifugal force scales as J^3 , Bloch oscillations will always occur. The Bloch wall location can be controlled by the detuning as well as the kick strength.

5.3.3 Numerical simulation

Bloch oscillations in molecular rotation manifest themselves in the rotational populations and coherences. We calculate the rotational population P_J and the modulus squared of the coherences $C_J^{(2)}$, taking into account all the degenerate M -sublevels and the thermal mixture of initially populated states (Sec. 2.3.6).

Figure 5.12 shows a comparison between the calculated population (**a**) and the calculated modulus squared of the coherence (**b**) at a realistic temperature of 25 K. Plotted are the distributions after each δ -kick in a sequence of 30 kicks of $P = 3$ with a period matched to the quantum resonance in ¹⁶O₂. The identical oscillatory behaviour is evident, and expected by the

¹⁶The calculation of the Bloch wall are based on the ϵ -classics approach [62], which cannot treat a non-rigid rotor with a detuning. Nonetheless, the qualitative behaviour is clear from the above two equations.

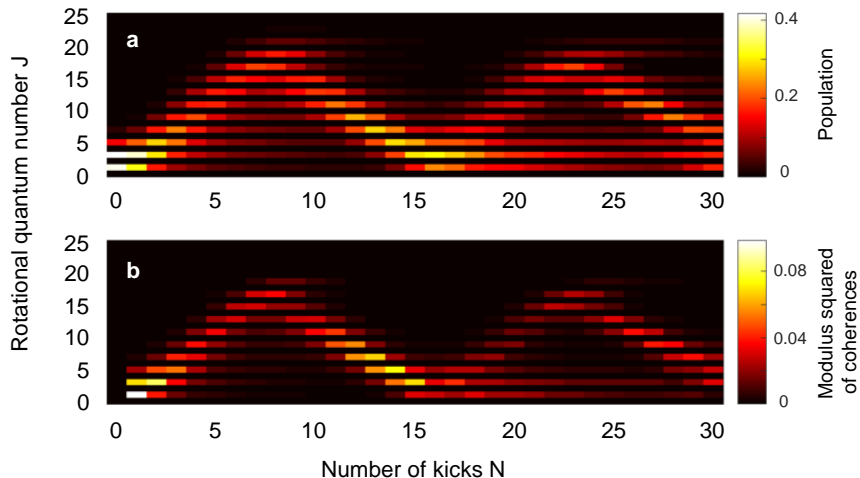


Figure 5.12: Bloch oscillations in molecular rotation: Numerically calculated populations (a) and the modulus of coherences squared (b) for $^{16}\text{O}_2$ at a temperature of 25 K after the excitation with a sequence of $N = 30$ pulses. The pulses have a kick strength of $P = 3$ and are separated by the revival time $T = T_{\text{rev}}$, corresponding to the case of zero detuning from the quantum resonance.

relation of both quantities (Sec. 2.3.5). There is no coherence if the corresponding states are not populated; the coherence is maximal when two Raman-coupled states $|J\rangle$ and $|J+2\rangle$ are equally populated. These simple arguments require that the oscillations of the population of the rotational states must also be present in the coherences (provided the oscillation amplitude is larger than $\Delta J = 2$).

From now on, all our studies concentrate exclusively on the latter quantity $C_J^{(2)}$, because experimentally, the intensity of the observed Raman signal is proportional to it, $I_J \propto C_J^{(2)}$.

5.3.4 Experiment

We decided to study Bloch oscillations in diatomic oxygen instead of nitrogen for the following reason: The D/B ratios of $^{16}\text{O}_2$ and $^{14}\text{N}_2$ are similar, which puts their respective Bloch walls at similar angular momentum values, according to equation 5.18. However, the density of Raman peaks is higher in oxygen due to a smaller rotational constant B , which means that the absolute energy of the Bloch wall will be lower. This is a substantial advantage,

because the maximum reachable rotational energy is restricted by the finite laser bandwidth. Expressed in the rotational quantum number, this limit is $J_{\text{lim}}^{(N_2)} \approx 15$ or $J_{\text{lim}}^{(O_2)} \approx 21$. The explanation is written down in the following subsection. If one can choose the parameters such that $J_B \leq J_{\text{lim}}$, one should be able to demonstrate Bloch oscillations in molecular rotation of oxygen ¹⁷.

We implement rotational Raman spectroscopy in oxygen molecules cooled to a rotational temperature around 25 K via a supersonic expansion, as seen earlier in Fig. 4.1(b). The driving field is a periodic train of 20 high-intensity femtosecond pulses. Each individual pulse is set to the same kick strength, whose value is chosen freely inbetween $P = 0.45$ and $P = 4.4$, depending on the experiment. The exact kick strength is calibrated by measuring Rabi oscillations first and fitting them to the numerical simulation. The pulse sequences with periods tuned around the revival time of ¹⁶O₂ at $T = 11.67$ ps are produced with the combined setup shown in Fig. 3.15 and discussed in Sec. 3.5.2. The weak probe is a single narrowband pulse with a spectral width small enough to resolve the individual rotational states.

Bandwidth limitation

We are limited in the excitation of high values of angular momentum because of the finite duration of our laser pulses, i.e. $\Delta t = 130$ fs (FWHM). If a molecule rotates by $\gtrsim 90^\circ$ during the length of the pulse, the effective kick strength will diminish and further rotational excitation will be suppressed.

The classical rotation period of a rigid rotor has been derived in Sec. 2.3.8 as $\tau_J = T_{\text{rev}}(J + 3/2)^{-1}$. To estimate the bandwidth limit, one needs to set a quarter period equal to the pulse duration $\tau_J/4 = \Delta t$ and solve for the rotational quantum number J . For our laser system, we calculate $J_{\text{lim}} \approx 15$ for nitrogen or $J_{\text{lim}} \approx 21$ for oxygen. If the pulse sequence is strong enough to populate such high rotational states, one will witness a turn-off in the rotational excitation at $J \geq J_{\text{lim}}$, where the impulsive approximation is not applicable anymore. It is referred to as “adiabatic localization” [63]. Our δ -kick simulations do not suffer from a limited bandwidth, and as such do not show adiabatic localization.

¹⁷The detrimental effect due to spin-rotation coupling in oxygen (Sec. 4.2.3) is expected to play a minor role. At most times the population resides in higher rotation states that have a longer dephasing time.

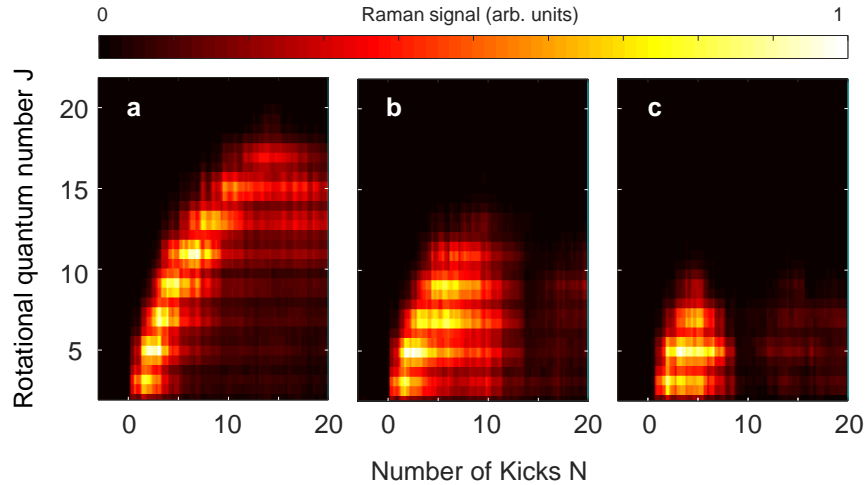


Figure 5.13: Bloch oscillations observed in the Raman spectrum of $^{16}\text{O}_2$ after the excitation with a sequence of $N = 20$ pulses with $P = 2.2$ per pulse. The Raman signal is normalized to unity and colour-coded (color map on top). The amplitude and period of the oscillations are controlled by setting the train period to match the quantum resonance (a), or to be below the quantum resonance by $\delta = -0.2\%$ (b) and -0.6% (c).

5.3.5 Observation of Bloch oscillations

This section is a comprehensive summary of our experimental investigations regarding Bloch oscillation in a quantum rotational system. We present the dependence of the phenomenon on various parameters, i.e. the detuning from resonance, the kick strength, the number of pulses and their bandwidth. The results are presented as two-dimensional Raman spectrograms: Each spectrum is plotted as a function of the rotational quantum number J for a specific pump-probe delay, which is expressed in the number of pulses N that have interacted with the molecules.

Dependence on the detuning

Figure 5.13 displays the predicted oscillatory behaviour for several pulse sequences with different periods $T = (1 + \delta)T_{\text{rev}}$ at a fixed kick strength of $P = 2.2$. The angular momentum increases, following a distinct trace, before its direction is reversed at the Bloch wall and the momentum subsequently decreases again. Such a well-defined trace can only be observed at cold temperatures with a narrow initial distribution. We distinguish a periodic

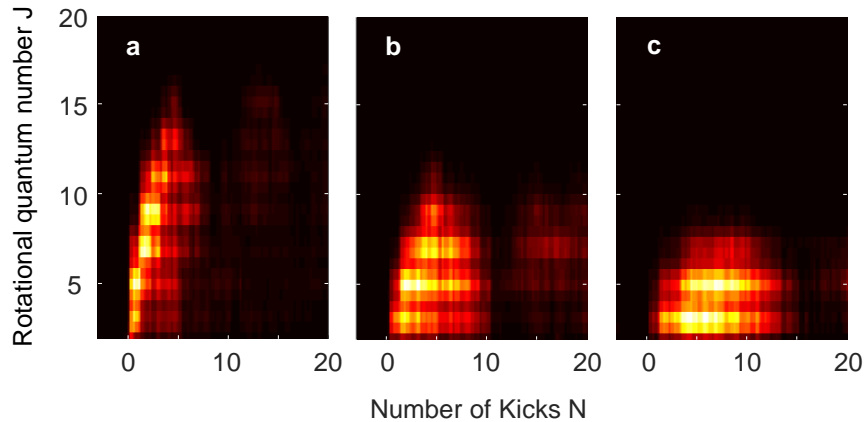


Figure 5.14: Bloch oscillations observed in the Raman spectrum of $^{16}\text{O}_2$ after the excitation with a periodic sequence of $N = 20$ pulses tuned below the quantum resonance by $\delta = -0.4\%$ (same color map as Fig. 5.13). The amplitude and period of the oscillations are controlled by setting the kick strength of each pulse to (a) $P = 4.4$, (b) $P = 2.2$ and (c) $P = 1.1$.

excitation (a) on quantum resonance when $\delta = 0$, (b) with $\delta = -0.2\%$ and (c) -0.6% below resonance, with the Bloch wall shifting from $J_B = 17$ to 13 to 9, respectively. The first case barely resolves the upper turn-around for the given number of 20 pulses, the second case shows one oscillation, whereas the last case exhibits two complete oscillations. The first minimum, where no higher angular momentum states are left excited, is achieved with great fidelity. However, the next oscillation always suffers from a significant drop in Raman intensity. Possible reasons will be discussed later. All Raman spectra start at $J = 2$ to cut off the unwanted Rayleigh peak, see Sec. 4.1.1.

Dependence on the kick strength

Figure 5.14 illustrates the same oscillatory behaviour when the energy of the pulses is changed but the period of the pulse train is fixed at $\delta = -0.4\%$ below quantum resonance. Shown are the dynamics for trains with the kick strength set to (a) $P = 4.4$, (b) $P = 2.2$ and (c) $P = 1.1$, reducing the Bloch wall from $J_B = 15$ to 11 to 7, respectively. The oscillation period decreases from about two oscillations per 20 kicks down to one oscillation per 20 kicks. Again the Raman intensity drops after the first oscillation. This effect seems to intensify for stronger kicks and is not observed in the simulations.

Experiment versus simulation

So far, we have confirmed that Bloch oscillations respond to a change in the periodicity T or the pulse strength P as expected. Now, we will demonstrate that the dynamics is in agreement with our calculations as well. In Fig. 5.15 we explore the two-dimensional parameter space with T (rows) and P (columns), while comparing the experimental Raman spectrum (bottom) with the simulated one (top). For the same pulse train of 20 pulses, the period changes from (a) on quantum resonance to (b) -0.2% to (c) -0.6% below quantum resonance, with a kick strength that varies from (1) $P = 1.8$ to (2) $P = 0.9$ to (3) $P = 0.45$.

The traces in each column have the same slope, which is defined by P . If the kick strength is larger, more angular momentum can be transferred to the molecule per kick. The amplitude of the Bloch oscillations, i.e. the Bloch wall, is smallest in the bottom right corner (c3) and increases with both parameters to its maximum in the top left corner (a1). This trend can be found in both, the simulations and the experiment: the best match is in the bottom right corner, the largest discrepancy is in the top left corner. The culprit is the limited bandwidth of the experimental pulses, which is responsible for adiabatic localization at $J_{\text{lim}} \approx 21$. Once the impulsive approximation breaks down, the effective kick strength declines for higher rotational quantum numbers. This becomes visible in a decreased slope of the trace.

Decay of the signal

Whenever the excited states are close to the bandwidth limit J_{lim} , the intensity of the Raman signal decreases with every consecutive kick. Fast rotating molecules get out of phase with ‘long’ kicks, once the impulsive approximation is failing. It becomes evident in a loss of coherence. Further numerical investigations are necessary to determine the exact effects of the finite frequency bandwidth.

In addition, there is a number of other experimental reasons that result in a decrease of the Raman signal and a loss of contrast in Bloch oscillations. *Spatial averaging* over the Gaussian beam profiles is equivalent to an averaging over different laser intensities, i.e. different molecules experience different kick strengths. This will ‘smear out’ Bloch oscillations with time. We tried to minimize this effect by sampling primarily the high-intensity center of the pump beam with a small probe beam. Experimental *amplitude noise* in the pulse train has similar consequences [63]. In a *thermal ensem-*

5.3. Bloch oscillations in molecular rotation

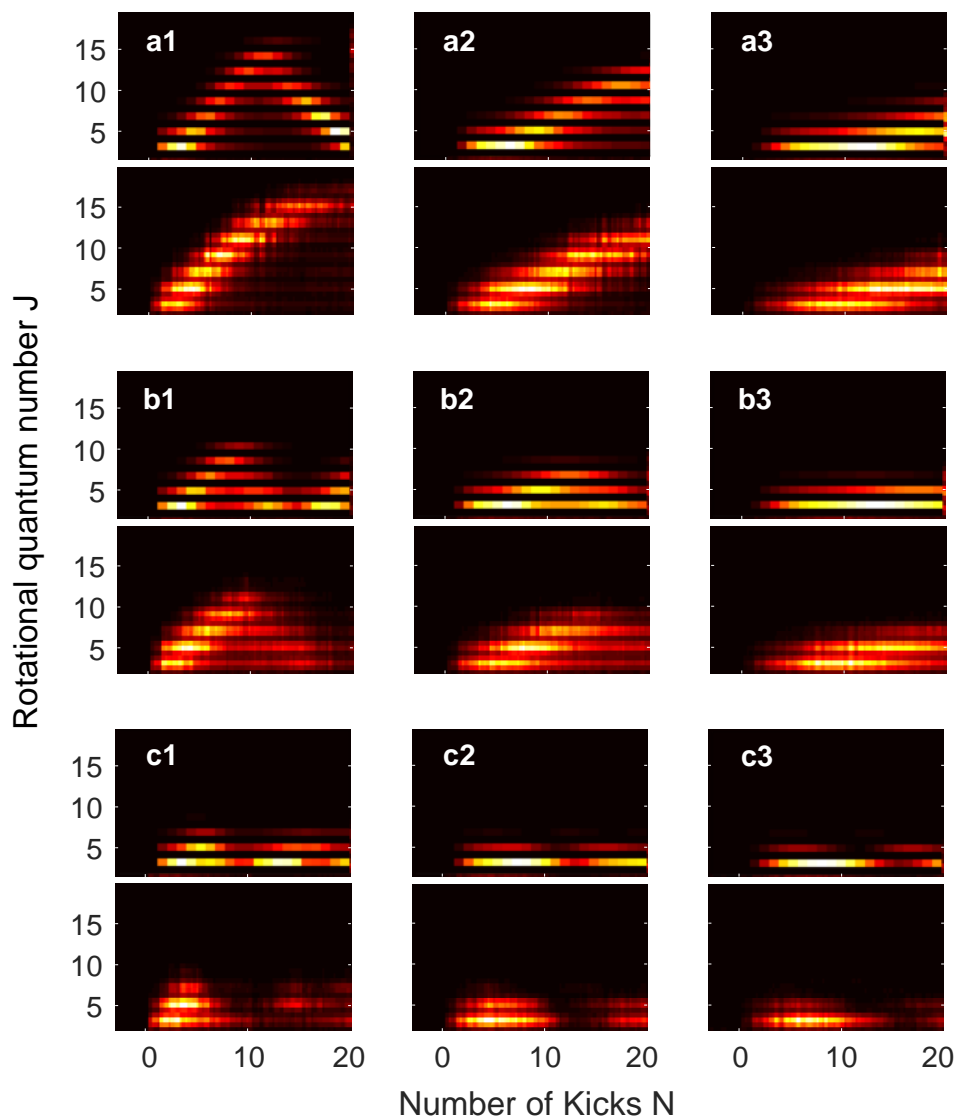


Figure 5.15: Bloch oscillations observed in the Raman spectrum of $^{16}\text{O}_2$ after the excitation with a periodic sequence of $N = 20$ pulses (same color map as Fig. 5.13). Amplitude and period of the oscillations are controlled by two parameters: the kick strength **(1)** $P = 1.8$, **(2)** $P = 0.9$, **(3)** $P = 0.45$; and the train period **(a)** on quantum resonance, **(b)** -0.2% , **(c)** -0.6% below quantum resonance. Each spectrogram in this table compares numerical simulations (top) with experimental results (bottom).

ble of molecules, a multitude of different (J, M) -states are populated. The degenerate M -substates interact differently with the same pulse train, as discussed earlier in Sec. 5.2.1, yielding slightly different Bloch oscillations. At the same time, Bloch oscillation amplitudes vary for the different (J, M) -states because the lower turning points are set by the M -values, as discussed earlier. Any initial state, that is inbetween both turning points can follow a trace toward higher J -values or lower J -values [63], the rotor is either accelerated or decelerated before it is Bragg-reflected. In conclusion, many Bloch oscillations with different amplitudes and periods will ‘wash out’ a clear picture.

We reduced the number of initially populated states by lowering the temperature to ~ 25 K, i.e. about 40% of the total population are each in the $J = 1$ and $J = 3$ manifolds. The previous study of Bloch oscillations in room temperature nitrogen [64] attributed deviations from their simulation to *collisional decoherence*. At our pressures we expect only minor effects from collisions. More research needs to be done to explain why consecutive oscillations suffer from a significant drop in signal strength. This observation seems to intensify for stronger kicks.

Bloch oscillations on quantum resonance

The dynamics of a kicked *rigid rotor* can be described by a tight-binding model. A detuning from the quantum resonance introduces an effective potential that will cause Bloch oscillations in the angular momentum space. Recently, this effect has been demonstrated with a periodic sequence of eight pulses [64]. We expanded this study in the discussion above.

Real molecules - *non-rigid rotors* - will feature Bloch oscillations even when the periodic kicks are tuned to the quantum resonance. In this case, the effective potential stems from the centrifugal distortion, which results in a detuning for higher J -states. This has not been demonstrated yet, since it is harder to show: The period of Bloch oscillations is longer which requires more pulses.

Our Raman spectrogram in Fig. 5.13(a) reveals signs of oscillatory dynamics for periodic excitation on the quantum resonance. We are unable to measure a complete cycle of a single Bloch oscillation as a consequence of the following dilemma: At the kick strength of $P \leq 2.2$, when the Bloch wall is below our laser bandwidth limit ($J_B < J_{\text{lim}}$), we cannot produce enough pulses, due to a technical limitation of the pulse shaping method (Sec. 3.3 & 3.4). However, if we increase the kick strength such that one full Bloch oscillation occurs within 20 pulses, the Bloch wall is out of reach

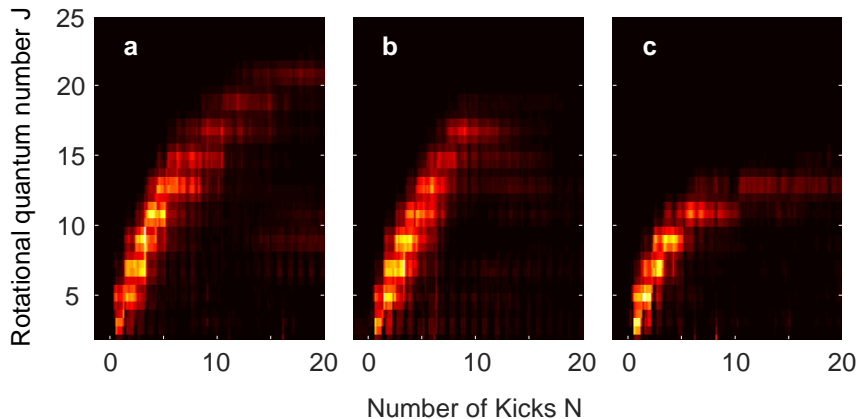


Figure 5.16: Compromising effect of the laser bandwidth on Bloch oscillations observed in the Raman spectrum of $^{16}\text{O}_2$ after the excitation with a sequence of $N = 20$ pulses with $P = 3$ per pulse (same color map as Fig. 5.13). The train period is tuned $\delta = +0.17\%$ above the quantum resonance (**a**) or on quantum resonance (**b,c**). The pulses in the train are transform-limited at 130 fs (**a,b**) or frequency-chirped to ≈ 250 fs (**c**).

($J_B > J_{\text{lim}}$) and oscillations are suppressed by adiabatic localization. The optimized condition to show the onset of Bloch oscillations have been chosen in Fig. 5.13(**a**). Substituting oxygen for another linear molecule, would not help either: The situation for N_2 is similar, but the D/B ratio is less favourable. Heavier molecules are not compromised by our laser bandwidth, but the smaller B constants result in longer time scales which cannot be covered by our pulse shaper.

Effect of bandwidth

We can verify the role that the laser bandwidth plays in the excitation of the rotational states by adjusting the instantaneous bandwidth of the pulses. A sequence of 20 pulses with $P = 3$ per pulse excites a rotational wave packet in oxygen, shown in Fig. 5.16. The plot in the center (**b**) fulfils the quantum resonance condition, the Bloch wall is situated at $J_B^{(b)} = 19$. In comparison with Fig. 5.13(**a**), a smaller portion of the Raman signal reflects off the Bloch wall. The reason lies in stronger kicks resulting in an elevated Bloch wall. Therefore, its position in the angular momentum space is similar to the bandwidth limit of the transform-limited pulses $J_B^{(b)} \sim J_{\text{lim}}^{(TL)}$, which yields a loss of signal as discussed earlier.

In Fig. 5.16(a) we tuned the period by $\delta = +0.17\%$ above the quantum resonance. This pushes the Bloch wall higher ($J_B^{(a)} > J_B^{(b)}$) owing to a cancelling effect between the effective potential caused by the centrifugal distortion and the one caused by the positive detuning. The angular momentum keeps growing and saturates significantly higher at $J \approx 21$.

Instead of lifting the Bloch wall above the bandwidth limit $J_B^{(a)} > J_{\text{lim}}^{(TL)}$, we can also engineer the reversed scenario. In Fig. 5.16(c), for a periodic excitation on resonance, we lowered the bandwidth limit below the Bloch wall $J_{\text{lim}}^{(\text{chirped})} < J_B^{(b)}$. By applying a linear frequency chirp, the instantaneous bandwidth of each individual pulse in the train was reduced, as illustrated in Fig. 3.7(b). With a duration of ≈ 250 fs the chirped pulses correspond to a new $J_{\text{lim}}^{(\text{chirped})} \approx 10$. Indeed, we observe the saturation level in Fig. 5.16(c) drop to $J \sim 13$. All three plots are comparable because the strength of $P = 3$ is maintained.¹⁸

5.4 Generation of broad rotational wave packets

If our goal is to extend the reach of rotational excitation and to excite broad rotational wave packets, one may distinguish “adiabatic” and “non-adiabatic” techniques. One of the most successful adiabatic methods, an *optical centrifuge* [89, 175] has been used to create coherent superpositions of more than 50 rotational quantum states [118]. However, owing to the adiabatic mechanism, controlling the phases of the individual states in such ultra-broad wave packets is difficult and the absolute number of excited molecules can be low. A second alternative route to generate broad rotational wave packets with well defined relative phases uses impulsive excitation with long sequences of pulses [41]. By tuning the period of a pulse train to the quantum resonance we expect a ballistic growth of the wave function (Sec. 2.2.1). Under these conditions, however, we also discussed the limited reach of angular momentum states as a consequence of the centrifugal distortion (Sec. 5.3). In this section, we explore the excitation efficiency with non-periodic pulse sequences and determine strategies of exciting the broadest rotational wave packet.

A femtosecond laser pulse creates a wave packet whose width can be characterized by the dimensionless kick strength P , which is proportional to

¹⁸For chirped pulses, the energy in each pulse is conserved but distributed over a longer duration σ with a smaller peak intensity $I_0 \propto \mathcal{E}_0^2 \propto \sigma^{-1}$. According to Eq. 2.11 for a Gaussian pulse, the kick strength ($P \propto \mathcal{E}_0^2 \sigma$) is constant.

the intensity of the laser field (Sec. 2.3.2). Naively, a broader wave packet can thus be generated by increasingly stronger pulses. In reality, the ionization threshold of a given molecule only allows the excitation of a few rotational states with a single kick. The idea of a pulse train is to remain below the ionization limit by dividing the total energy among N pulses. If the pulses are separated by the quantum revival time T_{rev} , the cumulative kick strength P_N of the whole train is the sum of the kick strengths of its individual pulses [12]. Multiple schemes of using long periodic pulse trains for the controlled rotational excitation of molecules have been proposed theoretically [12, 103, 104, 166, 187], and implemented experimentally, as discussed in the previous section [41, 192, 64, 88].

Here, we investigate the rotational excitation of room temperature oxygen in a gas cell by long sequences up to $N = 28$ pulses with cumulative kick strength up to $P_N \leq 140$. These pulse trains are significantly longer and stronger than previous realizations, most notably $N = 8, P_N \leq 40$ in Ref. [64]. In Sec. 5.4.1, we study the shape of the achieved wave packets and its dependence on the train period with respect to the quantum resonance. As discussed in Sec. 5.3, populating high rotational levels proves impossible due to the centrifugal distortion and despite the high cumulative kick strengths of the periodic train. For fast rotating molecules, the revival time becomes dependent on the angular momentum J and as a result, the resonant condition and the accumulation of the total kick strength from pulse to pulse is inhibited. In Sec. 5.4.2, we exploit fractional revivals and apply four non-periodic kicks per T_{rev} . This optimization for efficient rotational excitation extends our reach to $J \approx 29$. The propagation of such an optimized pulse train through a dense medium is examined in Sec. 5.4.3.

5.4.1 Periodic excitation

To connect with the previous sections, we start by re-examining the rotational coherences created by a periodic pulse sequence on and near the quantum resonance. Here, the goal is the creation of broad rotational wave packets, which can be anticipated on the quantum resonance, i.e. for a period $T = T_{\text{rev}}$ when the excitation of all angular momentum states should be equally efficient. The necessary pulse sequences are produced with the combined setup shown in Fig. 3.15 and discussed in Sec. 3.5.2. We use state-resolved coherent Raman detection in a room temperature ensemble of oxygen molecules, see Fig. 4.1(a), to explicitly demonstrate the effect of the centrifugal distortion as the main reason for the inhibited rotational ladder climbing.

Figure 5.17(a) revisits the 2D Raman spectrogram from Fig. 5.1(a), but this time we analyse the spectrum for much higher quantum numbers $J \approx 40$. The times $T_J = (2J + 3) \times \tau_J/2$, indicated by light blue squares, mark the times when all $(|J\rangle, |J + 2\rangle)$ wave packets perform an integer number $N_J = 2J + 3$ of half-rotations¹⁹. As mentioned before, these times make up an almost vertical “trajectory” originating at the revival time for low values of the rotational quantum number (light blue squares). Away from the quantum resonance, the $N_J = \text{const.}$ trajectories bend away from the vertical lines. For instance, increasing (decreasing) N_J to the next integer value $2J + 4$ ($2J + 2$) results in a curved trajectory marked with triangles (circles), along which no two rotational wave packets corresponding to two different values of J are in phase simultaneously.

Even when the conditions of the quantum resonance are met for the lower rotational states, they no longer hold at higher J 's owing to the centrifugal distortion of the molecular bond. With increasing J , the centrifugal term in the rotational energy $E_J = hc[BJ(J + 1) - DJ^2(J + 1)^2]$ becomes non-negligible, making the resonance J -dependent and, therefore, impossible to satisfy for all quantum states simultaneously. In Fig. 5.17(a), this effect is seen through the apparent curving of the resonant trajectory (light blue squares) away from the vertical line at $T = T_{\text{rev}}$ above $J \approx 15$. As a result, the efficiency of the accumulative rotational excitation by a resonant pulse train ($T = T_{\text{rev}}$) deteriorates with growing J , resulting in Bloch oscillations discussed in Sec. 5.3. To demonstrate the described centrifugal limit we increased the number of kicks as well as their strength. Fig. 5.17(b) shows the detected Raman signal generated by the periodic resonant train of 20 strong pulses with the pulse intensity of $3 \cdot 10^{13} \text{W/cm}^2$ per pulse (black solid line). Despite the increased cumulative kick strength of $P_{20} \approx 140$, the highest excited level remains significantly below that value, $J \approx 17 \ll P_{20}$. In fact, even though the perturbative analysis used earlier is not applicable in the case of strong pulses, the measured limit agrees well with the conclusions of Sec. 5.3.

Utilizing the resonance map further, one arrives at a simple method of extending the reach of rotational excitation by a periodic train of femtosecond pulses. As seen in Fig. 5.17(a), by shifting the train period above the quantum resonance, its overlap with the time of complete half-rotations T_J of the rotational wave packets with higher J 's can be improved. In Section 5.3, this “trick” was introduced in the context of shifting the Bloch wall

¹⁹For a detailed description of the resonance map, see Sec.2.3.8.

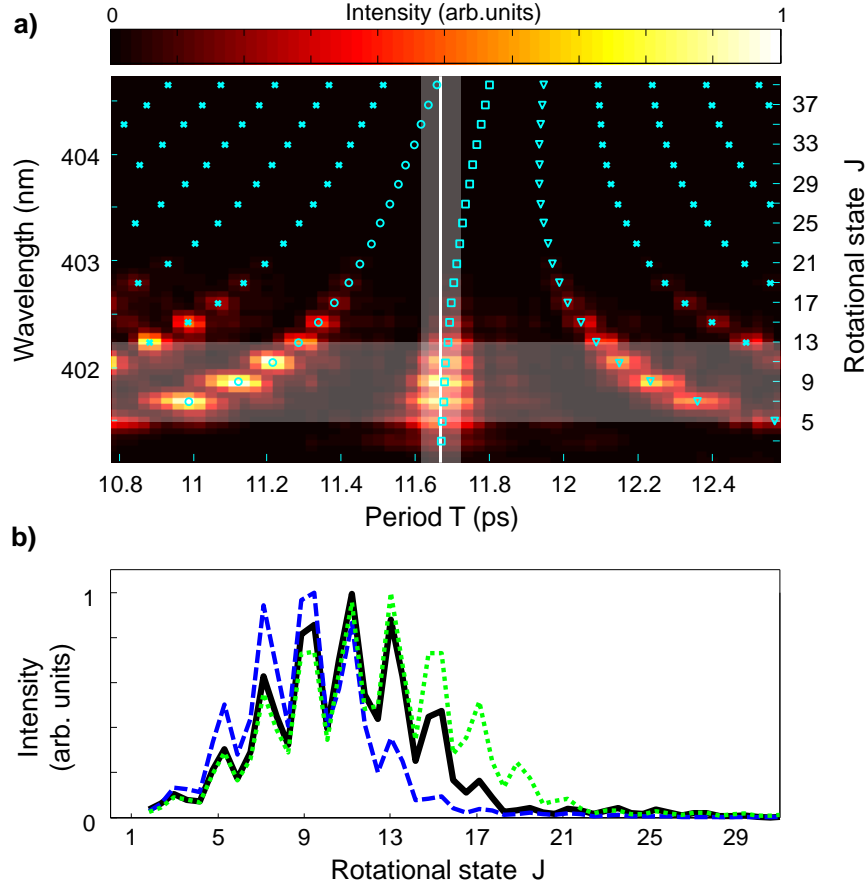


Figure 5.17: (a) State and time resolved Raman spectrogram of $^{16}\text{O}_2$ after the excitation by a sequence of five pulses with a period T scanned around the rotational revival time T_{rev} (vertical solid line). The vertical shaded band represents the length of our Gaussian pulses (FWHM), whereas the shaded horizontal band covers the rotational quantum numbers (shown on the right vertical axis) corresponding to the thermally populated rotational states (population higher than 10 %). Light blue markers indicate the time moments at which a coherent rotational wave packet consisting of two states, $|J\rangle$ and $|J+2\rangle$, completes an integer multiple of half rotations, N_J . The central trajectory (squares) corresponds to $N_J = 2J + 3$, while the two neighbouring sets of circles and triangles represent the cases of $N_J = 2J + 2$ and $N_J = 2J + 4$, respectively. (b) Raman spectra after a sequence of 20 periodic pulses on quantum resonance (black solid), -0.4% below quantum resonance (blue dashed) and $+0.4\%$ above quantum resonance (green dotted).

higher up by compensating the centrifugal term with the positive detuning from the quantum resonance. However, the degree of such control is rather limited, because detuning the pulse train far from the resonance reduces the excitation efficiency of the initially populated low- J states. The limitation can be analysed by inspecting the two shaded bands in Fig. 5.17(a): the vertical one represents the temporal width of our pulses (FWHM), whereas the horizontal one covers the thermally populated rotational states. The length of a continuous set of blue markers under the vertical band tells us about the width of the created rotational wave packet. On the other hand, how many of them are covered by the intersection of the two shaded areas is a qualitative indicator of the thermal fraction of molecules in the wave packet. As the train period shifts to the right of the quantum resonance, higher J states are reached, but the amount of rotationally excited molecules decreases.

For the length and strength of our experimental pulse trains, we found the detuning of +0.4% to result in the highest enhancement of the wave packet’s width, while not causing a significant loss of the overall excitation efficiency. As illustrated in Fig. 5.17(b), by increasing the train period 0.4% above the quantum resonance (green dotted line), we indeed shift the rotational excitation to higher J states. Similarly, setting the train period 0.4% below the resonance (blue dashed line) results in the narrower excited wave packet with the lower “center of mass”.

We note, that due to the power broadening of the individual rotational transitions, higher pulse intensities should allow farther detunings from the quantum resonance and correspondingly broader rotational wave packets. Stronger pulses effectively push the centrifugal limit higher. Nevertheless, as discussed earlier, the ultimate limit for the reach of the rotational excitation is set by the finite width of the laser pulses. Once a molecule rotates too fast for the pulses to act as instantaneous kicks, it does not climb the rotational ladder any further.

5.4.2 Non-periodic excitation

The effect of the centrifugal distortion grows in time as the wave packet spreads out. The dispersion of the revival times with J accumulates, making every next kick less and less efficient [41]. Hence, to fully benefit from the large number of pulses, one needs to apply them on as short of a time scale as possible. To achieve this goal, we employ tunable non-periodic pulse sequences. Here, we make use of fractional quantum revivals [13] and expose molecules to four rotational kicks per T_{rev} . Such an *optimized train*

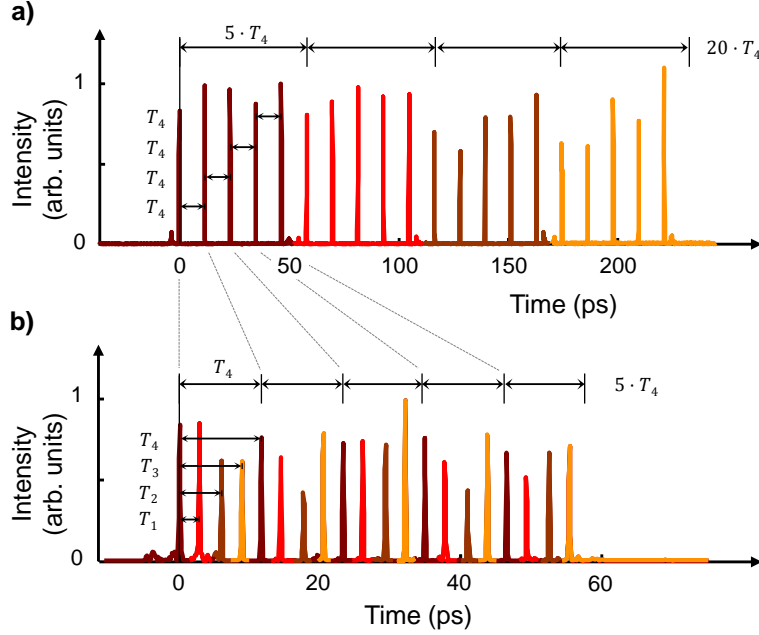


Figure 5.18: Temporal profile of a *long periodic* pulse train (a) and a *dense non-periodic* pulse train (b), 20 pulses each (note different time scale). The four shades of red correspond to one of the four different pathways through the two Michelson interferometers.

allows us to “pack” more pulses within the limited amount of time before the centrifugal distortion suppresses further excitation. By fine tuning the timing around each fractional and full revival, we extend our reach from $J \approx 17$ to $J \approx 29$, utilizing more efficiently the cumulative strength of a long train with 20 pulses.

Such a *dense non-periodic* pulse train optimized for the maximum rotational excitation is generated in the following way: Rather than adding the interferometer copies consecutively one after another to form a *long periodic* pulse train of 20 pulses as shown in Fig. 5.18(a), we interleave those copies with variable timings T_1 , T_2 and $T_3 \equiv T_1 + T_2$ as shown in Fig. 5.18(b). Here, T_k is the time between the beginning of the sequence to its k -th pulse. The procedure to find these timings is described next.

To start, we demonstrate that utilizing two pulses per every revival time can indeed enhance the excitation, if the timing is chosen appropriately. For that purpose, a resonant train of five pulses with a period $T_4 = T_{\text{rev}}$ is produced with the pulse shaper. Using a single Michelson interferometer, the

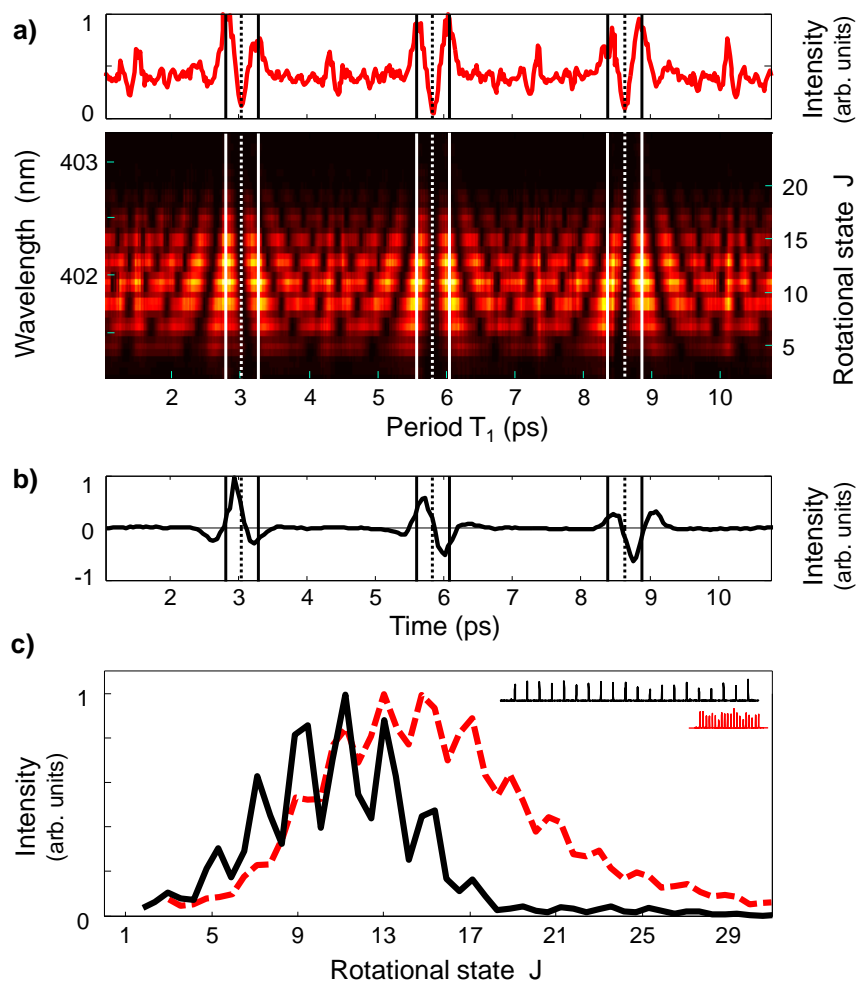


Figure 5.19: (a) Raman spectrogram for the rotational excitation by a sequence of two identical periodic pulse trains, five pulses each (same color map as Fig. 5.17(a)). The period of each train is fixed at T_{rev} , while the time delay T_1 between the two trains is scanned. The integrated signal above reveals the times of maximum total coherence. (b) Alignment-induced birefringence signal as a function of the probe delay after a weak transform-limited pump pulse. (c) Raman response after the rotational excitation by a sequence of 20 pulses: a periodic pulse train with $T = T_{\text{rev}}$ (black solid) and an optimized non-periodic pulse train (red dashed). The two trains are drawn schematically in the upper right corner.

train is then split in two parts, which are overlapped in space with the time delay T_1 between them (see Fig. 5.18(b) for the definition of time intervals T_1 and T_4). Similarly to the Raman spectrogram in Fig. 5.17(a), in Fig. 5.19(a) we plot the observed frequency-resolved Raman signal as a function of the delay T_1 between the two interleaved periodic pulse trains. As before, strong Raman peaks correspond to the time moments of enhanced rotational excitation. At some of those time moments marked with solid vertical lines, slightly before or after the $(\frac{1}{4}, \frac{1}{2}$ and $\frac{3}{4}) \times T_{\text{rev}}$ fractional revivals, the Raman response is simultaneously high for the largest number of rotational states, in exact analogy to the previously discussed response to the periodic excitation at the quantum resonance. We highlight this in the upper panel by plotting the same Raman signal integrated over wavelength. The latter is proportional to $\sum_J C_J^{(2)20}$ and should not be confused with the degree of transient molecular alignment which is plotted in Fig. 5.19(b) for comparison²¹. One can now interpret the optimal T_1 values in Fig. 5.19(a) as the times of the maximum positive derivative of the alignment signal, when the majority of molecules move towards the aligned state. A second kick, introduced at this time, accelerates the rotation further. In contrast, dashed vertical lines correspond to the maximum negative derivative of the alignment signal, when the majority of molecules move away from the aligned state. A second kick arriving at this time decelerates the rotation, lowering the degree of excitation, as reflected by the dips in the integrated coherence signal in panel (a).

The above analysis suggests a possibility of enhancing the rotational excitation by adding up to six pulses per every revival period [six vertical white lines in Fig. 5.19(a)]. Our pulse shaping scheme enables convenient scanning of four pulses per T_{rev} : near one full revival and three fractional revivals. We set the four variable delay times to the following optimal values taken from the integrated coherence signal in Fig. 5.19(a): $T_1 = 0.242 \cdot T_{\text{rev}}$, $T_2 = 0.519 \cdot T_{\text{rev}}$, $T_3 = 0.761 \cdot T_{\text{rev}}$ and $T_4 = 1.004 \cdot T_{\text{rev}} = 11.72$ ps, i.e. slightly above the full revival as explained earlier. We note that these optimized delays depend on the kick strength of the pulses in the train. The stronger the pulses, the higher the rotational excitation after each pulse, the larger the centrifugal distortion, the bigger the required shift from every fractional revival.

The result of the excitation by an optimized non-periodic train is shown in Fig. 5.19(c). By shortening the duration of the pulse train, while using the

²⁰Here, $C_J^{(2)}$ is the modulus squared of the coherences, described in Sec. 5.3.3.

²¹The alignment signal was recorded with a 130 fs probe pulse following a single kick.

same number of pulses ($N = 20$), we extend our reach from $J=17$ with one pulse per revival (black solid curve) to $J \approx 29$ with four pulses per revival (dashed red curve). Although the centrifugal limit of the periodic excitation has been circumvented, the efficiency of the non-periodic optimized pulse train is still well below its accumulated kick strength of $P_N = 140$. The main limitation is now the finite duration of the laser pulses, prohibiting further excitation.

5.4.3 Propagation effects

Long sequences of femtosecond pulses drive molecules to a highly coherent state. In a dense medium, it makes the latter a strong light modulator (for recent reviews of this effect, see [163, 14]). In this section, we study how pump and probe pulses are affected when propagating through a gas of rotationally excited molecules under high pressure. In oxygen at pressures up to 6.5 atmospheres, we observe the generation of frequency sidebands via the cascaded rotational Raman scattering [124]. We show that the molecular phase modulation (MPM) imparted on the probe pulse is maximized when its delay coincides with the full revival of the rotational wave packet, as well as if its timing is close to that of a fractional revival [15]. Here we demonstrate that when a non-periodic train is optimized for the efficient rotational excitation, the spectral bandwidth is increasingly broadened from pulse to pulse [128].

Cascaded Raman scattering

The rotational coherence in a molecular ensemble induced by our optimized pulse train is rather strong. This can be seen through Raman processes of higher orders, i.e. cascaded Raman scattering, which are especially pronounced at higher gas pressure. In Fig. 5.20(b), we plot the spectra of a weak probe pulse following a pulse train of 28 pulses at four different pressures ranging from 1.7 to 6.5 atm. The timing of the pulses in the train has been optimized at 6.5 atm so as to achieve the highest integrated coherence signal at $J > 17$, i.e. for maximizing the sum $\sum_{J>17} C_J^{(2)}$, by means of the same optimization procedure as described in the previous section 5.4.2.

With an optimized non-periodic pulse sequence, we count up to 250 Raman peaks. Note, that this number does not reflect the rotational quantum number reached by the end of the excitation process (indeed, at such high J values, the separation between the consecutive peaks should have decreased significantly due to the centrifugal distortion). Rather, large frequency shifts

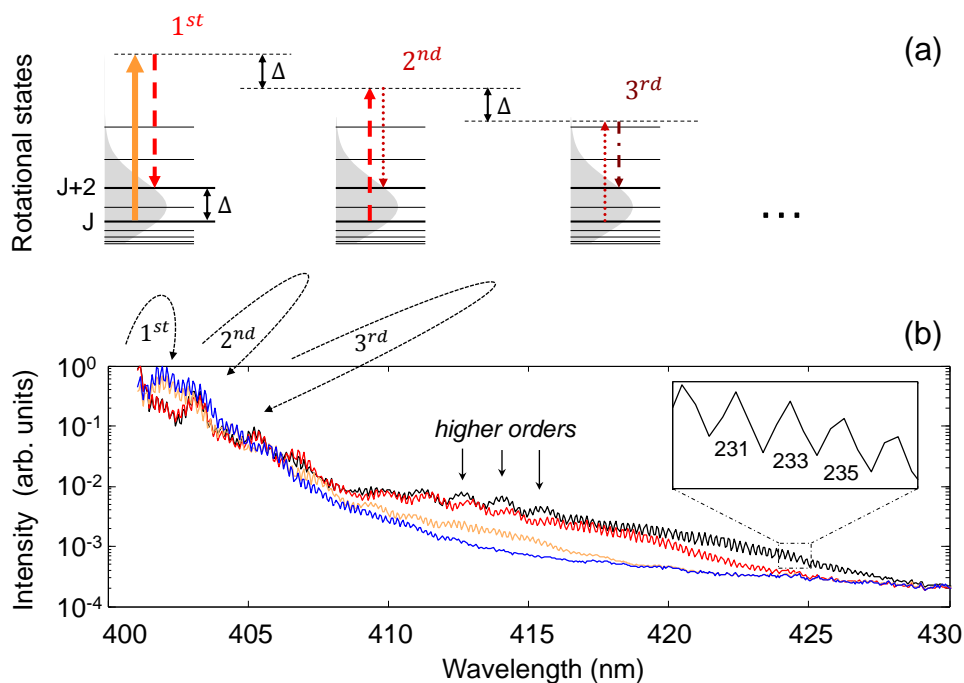


Figure 5.20: (a) Simplified illustration of the first three scattering orders in the process of cascaded Raman scattering. The grey profile represents the Boltzmann distribution of rotational population. (b) Rotational Raman spectra of oxygen gas excited by the optimized non-periodic train of 28 pulses. The four curves correspond to the gas pressures of 1.7 atm (lower blue), 2.4 atm (middle orange), 5.1 atm (higher red) and 6.5 atm (top black). First, second and higher orders of the cascaded Raman scattering are indicated with arrows. More than 235 Raman peaks are observed at higher pressure values, as shown in the inset.

are caused by the cascaded Raman scattering giving rise to multiple coherent sidebands [124]. The process is illustrated schematically in Fig. 5.20(a). A strong pump pulse (solid orange arrow) creates multiple coherences via several two-photon Raman processes (for clarity, only one Raman transition with an average frequency shift Δ is shown in the figure). The shape of the resulting Raman spectrum, which consists of a series of n red-shifted peaks, reflects the initial thermal distribution of molecules among the rotational states (grey profile). In the second-order process, all n emitted photons (dashed red arrow) re-scatter off the induced coherences, giving rise to the secondary set of n^2 Raman lines (dotted brown arrow), centered around 2Δ from the input laser frequency. The third-order process results in yet another red shift by Δ (dotted brown to dash-dotted black) and so on. This picture explains the repetitive broad spectral features in Fig. 5.20(b), e.g. those marked as “higher orders”, resembling the Raman spectrum observed after a single weak pulse, plotted earlier in Fig. 4.3. The features are separated by the frequency shift Δ corresponding to the peak of the Boltzmann distribution. The number of Raman processes in each order m of the cascaded scattering grows as n^m . We note, that the output spectrum consists of uniformly spaced Raman lines, owing to the repetitive scattering off the same set of coherences, induced by the strongest first-order interaction.

We verified experimentally that the conversion efficiency into the higher-order sidebands increases with the intensity of the pulse train and the number of molecules in the interaction region, both leading to the stronger rotational coherence in the system. Raising the density of molecules by increasing the gas pressure revealed an anticipated Bessel-like dependence of the strength of the Raman sidebands on the scattering order number [124]. For instance, as can be seen in Fig. 5.20(b), at $P = 5.1$ and 6.5 atm, the second-order coherences exceed those induced by the first-order scattering process.

Pulse broadening

Until now, we have used narrowband probe pulses for the state-resolved detection of the observed spectral broadening driven by the Raman transitions of multiple orders. In the time domain, the process can be described as the transient molecular phase modulation (MPM) owing to the periodically modulated refractive index of the medium. If a femtosecond pulse coincides with a full or a fractional wave packet revival, when the phase modulation is maximized, its frequency bandwidth is broadened [15]. The broadening effect has been theoretically predicted to accumulate from pulse to pulse in

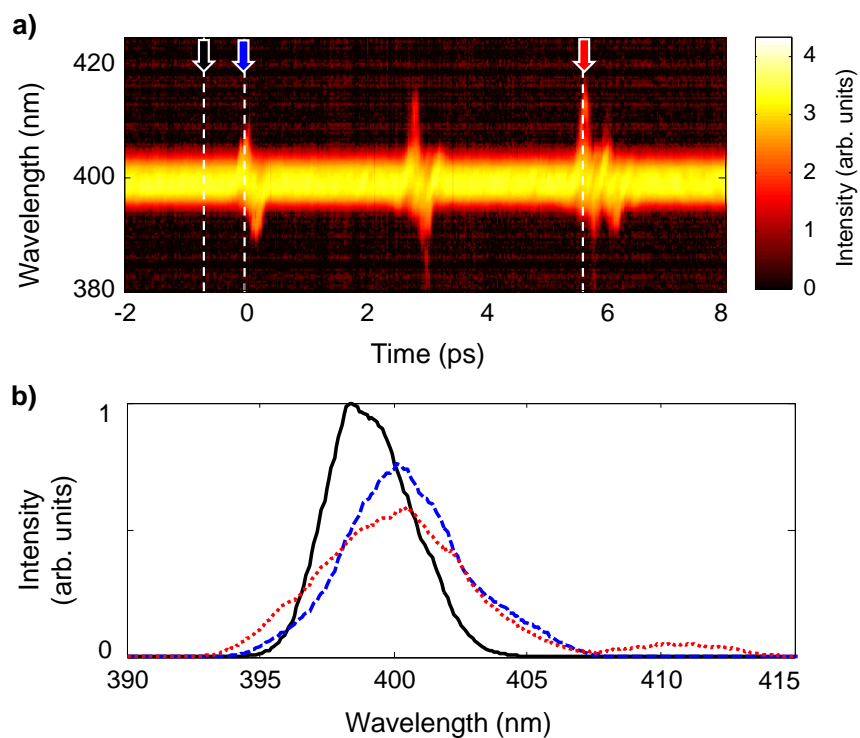


Figure 5.21: (a) Time-resolved Raman spectrogram (log scale) of oxygen gas excited by the optimized non-periodic train of 28 pulses under the pressure of 6.5 atm. (b) Raman spectra at the time moments indicated with arrows in the spectrogram: before the first kick (black solid), at the time of the first kick (blue dashed), and at the time of the third kick (red dotted).

a periodic sequence of pulses, as long as the train period is equal to the rotational revival time [128].

To demonstrate this accumulative broadening, we scan the time delay of a 130 fs probe pulse across the optimized non-periodic pulse train described earlier, while recording the probe spectrum. The results are plotted in Fig. 5.21(a) as a function of the probe delay with respect to the first pulse in the train. As expected, the spectrum of the probe pulse remains unchanged unless the latter coincides in time with a full or a fractional revival of the wave packet. The further down the pulse train we probe, the broader and more red-shifted the probe spectrum becomes, as illustrated in Fig. 5.21(b).

5.5 Conclusion

We investigated the excitation of molecular rotation using long pulse sequences of femtosecond pulses that are tailored to match the fractional and full quantum resonances. In the case of a pulse sequence with weak pulses spaced by a fractional revival time, we observe two-photon Rabi oscillations. The population oscillates in an effective two-level system of two rotational states as a function of the number of pulses. Once we change the periodicity to the full quantum resonance, the population efficiently moves up the “rotational ladder” until the inevitable centrifugal distortion prohibits further excitation. The consequence is oscillations in the angular momentum space, which can be related to the solid-state phenomenon of Bloch oscillations. We demonstrated the difficulties in the impulsive excitation of high rotational states and presented a strategy to partially mitigate the detrimental effect of the centrifugal distortion by adjusting the train period and by using non-periodic pulse sequences. The induced rotational coherence was significantly enhanced.

In theory, one could follow the rotational wave packet to higher states by continuously adjusting the train period. By avoiding the periodicity altogether, one would break the tight-binding analogy and might expect a continuous diffusive growth of the molecular angular momentum, limited only by the laser bandwidth. Non-periodic pulse sequences of this type are investigated in the following chapter 6.

We envision that our long pulse trains will be useful for all applications that require high transient molecular alignment at field-free conditions such as the generation of ultra-short laser pulses [15] or the control of high harmonic generation [174, 82]. It will be beneficial in impulsive gas heating [188]

5.5. *Conclusion*

or large amplitude plasma wave generation [172]. Similar effects have been studied in the context of propagation of intense femtosecond laser pulses in atmospheric air [173, 129, 128, 188].

Chapter 6

Dynamical localization in molecular rotation

The quantum kicked rotor is characterized by two qualitatively different regimes: In the last chapter 5 we examined the one when the kicking occurs on quantum resonances. In this chapter, the focus is on off-resonant periodic excitation, when the wave function of the quantum rotor undergoes dynamical localization. The wave function does not grow wider in the angular momentum space with every consecutive kick, but instead localizes near the initial rotational state due to the interference of quantum interaction pathways [31, 84]. An exponential distribution around the localization center is considered a necessary component and a distinct signature of dynamical localization. Although the phenomenon has been studied experimentally in Rydberg atoms [67, 16, 27, 65] and a cold-atom analogue of the QKR [121, 4, 43, 146, 145, 34], it has never been observed in a system of true quantum rotors.

Floss *et al.* theoretically demonstrated the possibility to observe dynamical localization in laser-kicked molecules [59, 63]. The first step toward that goal was reported in 2015, when an onset of localization was observed in laser-induced molecular alignment [88]. Here, we describe the direct observation of dynamical localization. We are able to show the hallmark features of the exponentially localized states and the suppressed growth of the rotational energy. An overview of all experimental observations, the underlying theory and a numerical analysis constitute this chapter.

Section 6.1 puts the work on dynamical localization into the context of the well-known effect of Anderson localization in disordered solids. Section 6.2 outlines the theoretical basis for our system. We analyse the tight-binding model, which is mapped onto the QKR, and explain the origin of the “disorder” in the rotational “lattice” that is responsible for the localization. Our experiment is described in Sec. 6.3. We will elaborate on our detection scheme and how we retrieve the angular momentum distribution from our measurement. Section 6.4 presents our key results: Cold initial

conditions and high-sensitivity detection enable us to observe the distribution of the molecular angular momenta evolving into an exponential line shape, characteristic of a localized state. We study the dependence of the localization on the number of kicks (6.4.1) and the strength of the kicks (6.4.2). Owing to the state-resolved detection we identify the suppressed growth of rotational energy (6.4.3). Dynamical localization is a coherent effect that relies on wave interferences. Therefore, we also implement two different types of noise in our studies to destroy the localization and to recover classical diffusion. Control over the position of the localization center is investigated (6.4.4). Section 6.5 builds a bridge between chapters 5 and 6 where we examine the transition from the quantum resonance to the regime of localization. Concluding remarks are found in Sec. 6.6.

6.1 Experiments on Anderson localization

In the last decades, there has been great interest and many achievements in studying Anderson localization in various systems of different dimensionality. Since the phenomenon relies on the wave character, it is ubiquitous and should also appear with classical waves. In fact, in our three-dimensional world the transition from diffusion to localization should occur for any type of classical or matter waves in any disordered media if the wavelength becomes comparable to the mean-free path between random scattering events [165].

After the proposal of localization with *electromagnetic waves* [86], it has been demonstrated with light in synthesized strong scattering materials [183, 165] and with microwaves [68, 42, 33]. Ultrasound was used to show localization of *acoustic waves* [178, 80]. All cited works used fully random potentials, without the presence of any lattice. With the realization of Anderson localization in *photonic crystals* [150, 99] experimentalists made another step toward the original Anderson model by superposing fluctuations onto a periodic structure.

Just as Bloch waves describe a quasi-free electron in an atomic crystal, *matter waves* can be placed in optical potentials created by laser interference patterns. Two common techniques are used to create disordered potentials, via the laser speckle patterns [39, 18] or by adding two optical lattices with incommensurable periods [50, 143] (see a review in Ref. [10]). More recently, much attention has been drawn by the studies of the mobility edge [94, 85, 153] and the effect of particle interaction on localization [38, 130, 149].

The QKR presents an alternative system to study Anderson localization,

and offers an interesting testing ground for new physics.

6.2 Theory

In section 2.4.6 we established the relationship between a quantum particle in a disordered solid and the periodically kicked rotor. The Schrödinger equation for the quantum rotor was derived in Eq. 2.52 as

$$T_J u_J + \sum_{J'} W_{J,J'} u_{J'} = 0 , \quad (6.1)$$

with the probability amplitude u_J to find the quantum rotor at the rotational state J of the angular momentum lattice. The two terms describe the *hopping term* $W_{J,J'}$ and the *on-site energy* $T_J = \tan(\phi_J)$ with $\phi_J = \frac{(\mathcal{E}_\alpha - E_J)T}{2\hbar}$.

If the function T_J is independent of the rotational states J , we arrive at the *tight-binding model* for a periodic lattice. The solutions are extended Bloch states [62]. This scenario has been discussed in the context of rotational Bloch oscillations in Sec. 5.3 and it will be further analysed in the context of dynamical localization in Sec. 6.5.1. If the on-site energies T_J are random, also referred to as “diagonal disorder”, we arrive at the *Anderson model*. In this case, the solution is given by quasi-energy states (Focket states) that are localized in the angular momentum space [52].

Next we look at the actual expression of T_J for linear molecules. We neglect the centrifugal term and use the rotational energy $E_J = hcBJ(J+1)$. If the period between kicks $T = \frac{p}{q}T_{\text{rev}}$ is a rational fraction (p, q are integers) of the revival time $T_{\text{rev}} = (2cB)^{-1}$

$$\phi(J) = \frac{\pi p}{2q} \left(\frac{\mathcal{E}_\alpha}{hcB} - J(J+1) \right) . \quad (6.2)$$

The variation of the on-site energy between neighbouring rotational states J and $J+2$ of the angular momentum lattice is therefore

$$\Delta\phi(J) = |\phi(J+2) - \phi(J)| = \pi \frac{p}{q} (2J+3) . \quad (6.3)$$

If $\frac{p}{q} = 1$, the lattice is strictly periodic ($T_J = \text{const.}$). For other rational values of p/q , we obtain a quasi-periodic lattice. Note, that the phase difference $\Delta\phi(J)$ has been analysed with the resonance map in Sec. 2.3.8, where each value of π corresponding to a fractional resonance was marked with a cross. In this chapter, we are interested in irrational values of T/T_{rev} , which are of order unity. Due to the periodicity of the tan-function, only $\Delta\phi$ modulo

π affects the variation of the on-site energy. Here, any rotational quantum number yields a magnitude of $\Delta\phi(J)$ that exceeds several π . This makes $T(J)$ a pseudo-random number [52], resulting in dynamical localization.

Two points are noteworthy: (1) The values of T_J are not truly random. They are calculated deterministically but they behave stochastically. It has been shown numerically, that “pseudo-random” energies are sufficient to observe Anderson localization in a one-dimensional system [52, 76]. For these reasons, the QKR is sometimes called the “pseudo-Anderson model” [76, 77]. (2) The rigid-rotor approximation is sufficient to describe the Anderson model. Adding the centrifugal term merely adds more randomness.

6.3 Experiment

Our approach to demonstrate dynamical localization with molecular rotors [63] bears a number of experimental challenges. First, the need to assess the shape of the rotational distribution calls for a sensitive detection method capable of resolving individual rotational states. According to the theoretical studies [63], the population of a few tens of rotational states must be measured with high sensitivity over the range of at least two orders of magnitude. Second, for the localized state not to be smeared out due to the averaging over the initial thermal distribution, the latter must be narrowed down to as close to a single rotational state as possible, requiring cold molecular samples. Finally, an important test of dynamical localization, the recovery of classical diffusion under the influence of noise and decoherence, demonstrated experimentally with atoms [27, 4, 92, 119, 127] and theoretically with molecular QKR [63], requires long sequences of more than 20 strong kicks.

We address all three of the above challenges and study the rotational dynamics of nitrogen molecules, cooled down to 25 K in a supersonic expansion and kicked by a periodic series of 24 laser pulses, whose kick strengths are as high as $P = 3$ per pulse. We use state-resolved coherent Raman spectroscopy, described in detail in Sec. 4.1 [Fig. 4.1(b)] to demonstrate the exponential shape of the created rotational wave packet, indicative of dynamical localization. The dependence of the rotational distribution on the number of pulses and their strength is investigated. Our ability to resolve individual rotational states allows for a direct extraction of the absorbed energy, whose growth is shown to cease completely after as few as three pulses. To confirm the coherent nature of the observed localization, we study the effect of both timing noise and amplitude noise, which are shown to yield

a non-exponential distribution of angular momenta and revive the diffusive growth of energy. Our results are in good agreement with the existing theoretical analysis [63] and our own numerical simulations.

6.3.1 Calibration of experimental parameters

The important experimental quantities in this study are the initial temperature of the molecular ensemble and the pulse train parameters: the number of pulses N , the train period T and the strength P of the individual pulses.

Temperature: The rotational temperature of our molecular sample is determined by fitting the Raman spectrum after a very weak kick, which to a good degree of approximation does not change the population distribution. The procedure and its results were discussed earlier in the technical section 4.2.3. We estimate an initial temperature around 25 K.

Pulse train parameters: The exact shape of the pulse train is set by the pulse shaper and the Michelson interferometers. We confirm the final pulse train parameters via an XFROG measurement, which was described in Sec. 3.2.1. This cross-correlation measurement, which is carried out immediately before sending the beams into the vacuum chamber, yields the temporal profile of each sequence. Besides the pulse number and the time separation between the pulses, we can also measure the relative pulse amplitudes, however their absolute values remain unknown.

Kick strength: We determine the exact pulse intensity in the interaction region with an additional measurement. We tune the period of the pulse train to $T = \frac{6}{7}T_{\text{rev}}$, indicated by the dashed line in Fig. 6.1. As discussed earlier, this timing coincides with the rotational period of a wave packet consisting of two rotational states with $J = 2$ and $J = 4$. Fitting the frequency of the ensuing Rabi oscillations between the two states provides an accurate way of measuring the intensity of the pump pulses. For the physical picture and more details, read section 5.2 on Rabi oscillations in molecular rotation. The pulse intensity is expressed in the dimensionless units of kick strength P , reflecting the typical amount of angular momentum (in units of \hbar) transferred from the laser pulse to the molecule [57]. By amplifying the sequence of 24 pulses in the multi-pass amplifier (MPA), we are able to reach kick strengths of up to $P = 3$ per pulse (2×10^{13} W/cm²). The standard deviation of the pulse energy fluctuations is below 15%.

6.3. Experiment

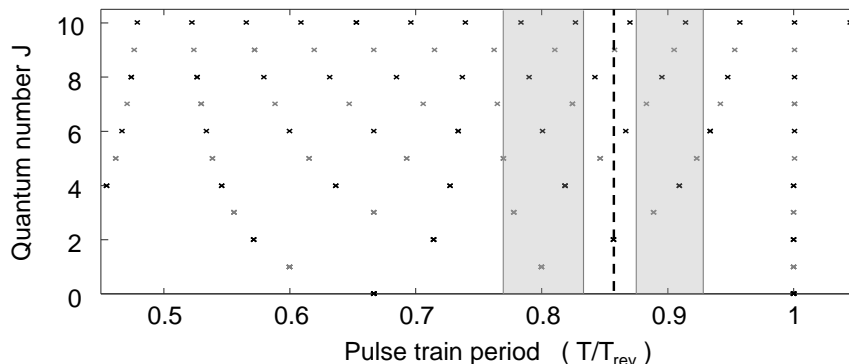


Figure 6.1: Resonance map with an illustration of the choice of pulse train periods. The period $T/T_{\text{rev}} = 6/7$ (dashed line) serves to induce Rabi oscillations between the states $J = 2$ and 4. Ten equidistant periods in each of the two shaded bands are chosen to observe dynamical localization in molecular rotation.

Pulse Period: Localized states in the quantum kicked rotor are known to exist away from the quantum resonances, i.e. when the time between kicks is not equal to a rational fraction of the revival period [52]. For molecular nitrogen $^{14}\text{N}_2$, the revival time is $T_{\text{rev}} = 8.38$ ps. As long as $T \neq \frac{p}{q}T_{\text{rev}}$, where p and q are integers, the behaviour of localization is universal [63]. To satisfy this condition, we choose 10 evenly spaced pulse train periods T in each of the two intervals, $10/13 < T/T_{\text{rev}} < 5/6$ and $7/8 < T/T_{\text{rev}} < 13/14$, seen in Fig. 6.1. Although we (partially) overlap with some fractional resonances, none of them are of low order, i.e. correspond to small integer values of q like $\frac{1}{2}, \frac{2}{3}, \frac{3}{4}$. Hence, their effect on the rotational excitation is rather negligible. Moreover, by taking the mean over all 20 Raman spectra, we reduce the influence of nearby quantum resonances and we achieve a better signal-to-noise ratio.

6.3.2 Population retrieval from the experiment

Dynamical localization of the QKR manifests itself in the exponential distribution of angular momentum around the localization center. The initial distribution of molecules in our supersonic jet is close to the rotational ground state. Therefore, we expect the population to fall off exponentially towards higher rotational quantum numbers. Our detection technique of Raman spectroscopy, however, does not provide a direct measure of the rotational population. Here, we describe our procedure to retrieve populations from

the measured Raman spectra.

In Sec. 2.3.6 we derived the intensity of the observed Raman peaks as $I_J \propto \sum_M \langle |c_J^{M*} c_{J+2}^M|^2 \rangle_{J',M'}$, the modulus squared of the induced coherence summed over the degenerate M -sublevels and averaged over the mixture of initially populated states $|J', M'\rangle$. If the initial ensemble contained only one populated level $|J' = J_0, M' = M_0\rangle$, the strength of the Raman signal would reduce to $I_J \propto P_{J,M_0} P_{J+2,M_0}$, where $P_{J,M} = |c_J^M|^2$ is the rotational population. For localized and non-localized dynamics of the QKR, we expect exponential or Gaussian population distributions, respectively [40, 92]. In either case, the Raman spectrum can be further simplified to $I_J \propto (P_{J,M_0})^2$, offering the direct measure of the rotational population. As we show below, this proportionality holds even at a non-zero temperature, when the Raman signal is produced by a number of independent rotational wave packets originating from different initial states. At 25 K most population is initially at $J' = 2$. Thus, the smallness of $M' = 0, \pm 1, \pm 2$ with respect to the angular momentum of the majority of states in the final wave packet results in an interaction Hamiltonian which to a good degree of approximation does not depend on M' . Having all molecules in the thermal ensemble respond to the laser field in an almost identical way enables us to extract rotational populations from the Raman signal as $P_J = a\sqrt{I_J}$, with the coefficients a found from normalizing the total population to unity.

6.4 Observation of dynamical localization

Figure 6.2(a) shows a set of 20 Raman spectra, obtained with the 20 different *periodic* pulse trains mentioned above. As before, the Raman frequency shift (horizontal axis) has been converted to the rotational quantum number J . All of the observed Raman signals I_J decay exponentially across 4 orders of magnitude and 15 rotational states, independent of the train period. The average Raman signal is plotted with the solid red line in Fig. 6.2(c). It has a distinctly different shape than the initial thermal distribution, plotted with the solid grey line²². The remaining oscillations are a consequence of the nuclear spin statistics of nitrogen, which dictates the 2:1 ratio for the two independent rotational progressions consisting of only even and only odd values of angular momentum. The exact shape of each individual distribution in Fig. 6.2(a) depends on the period of the corresponding train and is affected by its proximity to fractional quantum resonances of higher orders. In Fig. 6.2(d), the solid red line illustrates the distribution of the

²²The initial distribution was measured after a single weak pulse.

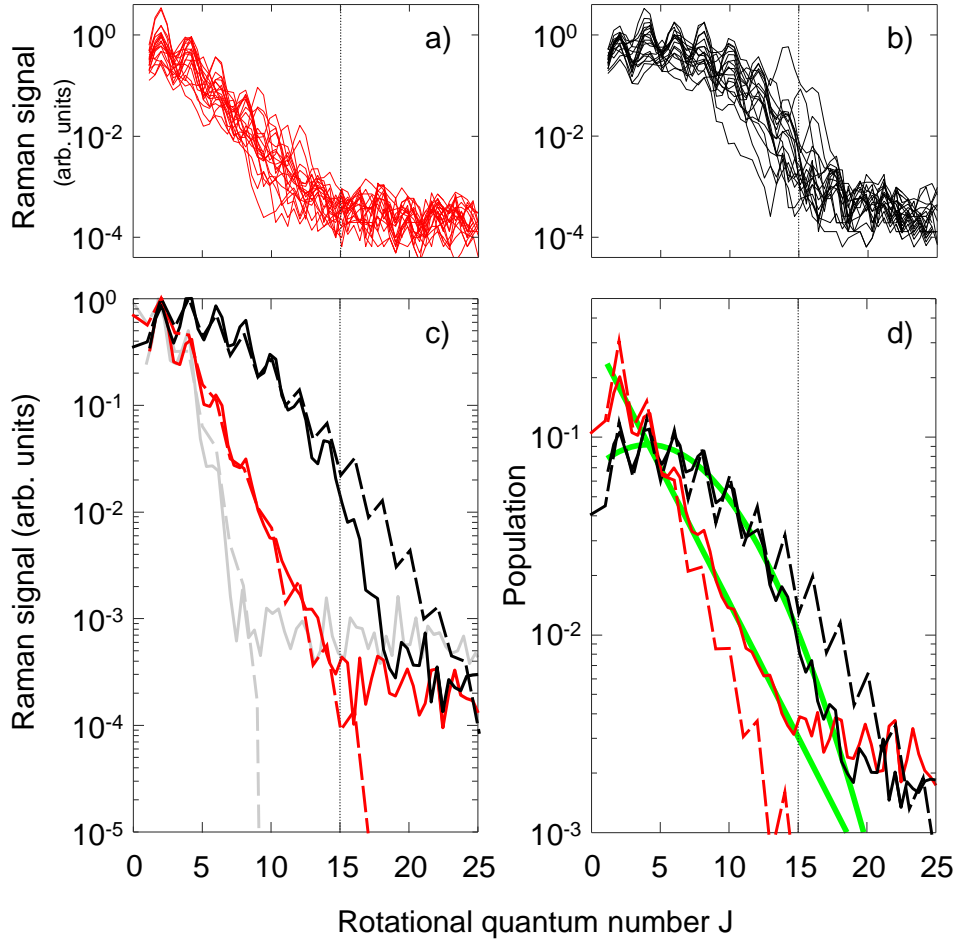


Figure 6.2: Rotational Raman spectrum of nitrogen molecules excited with a train of $N = 24$ pulses at a kick strength of $P = 2.3$ for 20 different (a) periodic and (b) non-periodic sequences. (c) The average experimental distributions (solid lines) are compared to the numerical simulations (dashed lines) for both the periodic (middle red lines) and the non-periodic (upper black lines) pulse trains. The initial distribution is shown by the lower grey lines. (d) The exact calculated populations (dashed lines) and the approximate populations (solid lines), retrieved from the experimental Raman signal. The retrieved populations are fitted with an exponential/Gaussian function (thick green lines). The dotted vertical line represents the excitation limit due to the finite pulse duration.

6.4. Observation of dynamical localization

rotational population, extracted from the average Raman signal according to $P_J \propto \sqrt{I_J}$. The evident exponential shape, highlighted by an exponential fit (thick green line) with a localization length ($1/e$ width) $J_{\text{loc}} = 3.2$, is a hallmark of Anderson localization in this true QKR system.

To confirm the coherent nature of the observed localization, we repeat the same measurement with a set of 20 *non-periodic* pulse trains. The kick strength is set to the same value of $P = 2.3$ per pulse, but the time intervals between the 24 pulses in each train is randomly distributed around the mean value of $0.85T_{\text{rev}}$ with a standard deviation of 33%. Here, all the individual Raman spectra, their average and the population distribution retrieved from it (solid black lines in Fig. 6.2**(b)**, **(c)** and **(d)**, respectively) show a qualitatively different non-exponential shape. As expected for a quantum kicked rotor, dynamical localization is destroyed by the timing noise. Classical diffusion, with its characteristic Gaussian distribution of angular momentum (thick green line) with a $1/e$ width of $J_{\text{diff}} = 7.4$, is recovered.

In Figures 6.2**(c)** and **(d)**, we also compare our experimental data to the results of numerical simulations, shown with dashed lines. The latter are carried out by solving the Schrödinger equation for nitrogen molecules interacting with a sequence of δ -kicks, as described in Sec. 2.3.6. We calculate the complex amplitudes $c_{J,M}$ of all rotational states in the wave packet created from each initially populated state $|J', M'\rangle$. Averaging over the initial thermal mixture, we simulate the expected Raman signals $I_J \propto \sum_M \langle |c_J^{M*} c_{J+2}^M|^2 \rangle_{J',M'}$, and find the exact populations $P_J = \sum_M \langle |c_J^M|^2 \rangle_{J',M'}$. In the case of a periodic sequence of kicks, the observed Raman line shape [Fig. 6.2**(c)**] is in good agreement with the numerical result down to the instrumental noise floor around $I_J \approx 10^{-4}$. Calculated populations [Fig. 6.2**(d)**] demonstrate the anticipated exponential decay with the rotational quantum number, but deviate slightly from the experimentally retrieved distribution. We attribute this discrepancy to the small finite thermal width of the initial rotational distribution, not accounted for in approximating the populations by $\sqrt{I_J}$, as discussed earlier.

When the timing noise is simulated numerically, both the calculated Raman response and the population distributions show a non-exponential shape and match the experimental observations below $J \approx 15$ (i.e. to the left of the dotted vertical line). The disagreement at higher values of angular momentum is because of the finite duration of our laser pulses, as discussed in Sec. 5.3.4. The dotted line represents this bandwidth limit.

Dynamical localization is also susceptible to amplitude noise. Rather

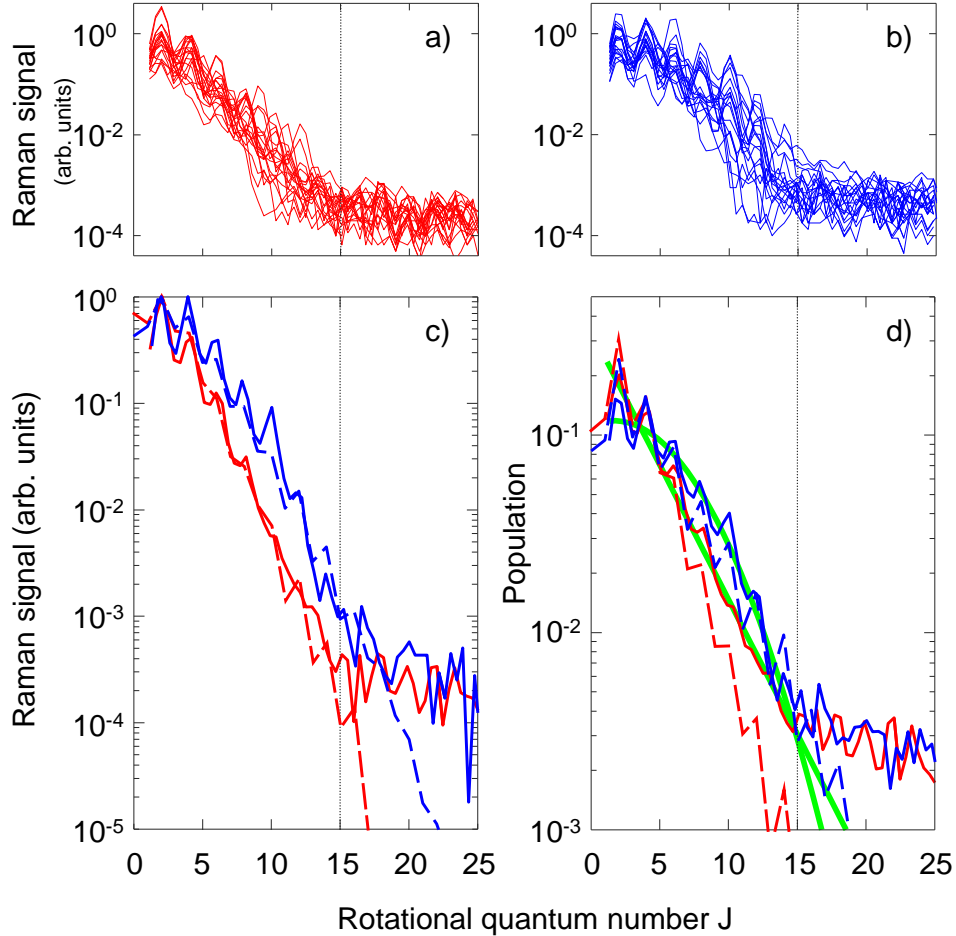


Figure 6.3: Rotational Raman spectrum of nitrogen molecules excited with a train of $N = 24$ pulses at a kick strength of $P = 2.3$ for 20 different periodic sequences **(a)** without amplitude noise and **(b)** with amplitude noise. **(c)** The average experimental distributions (solid lines) are compared to the numerical simulations (dashed lines) for both pulse trains, without noise (lower red lines) and with noise (upper blue lines). **(d)** The exact calculated populations (dashed lines) and the approximate populations (solid lines), retrieved from the experimental Raman signal. The retrieved populations are fitted with an exponential/Gaussian function (thick green lines). The dotted vertical line represents the excitation limit due to the finite pulse duration.

than introducing timing noise to our pulse sequence, we now randomly vary the pulse amplitudes within a sequence. The individual amplitudes are distributed around the mean kick strength of $P = 2.3$ with a standard deviation of 41%. We plot the results in Fig. 6.3. The red lines for the periodic pulse train without noise are identical to Fig. 6.2. The results for the pulse trains with amplitude noise are plotted with blue lines. We observe the same qualitative behaviour: noise destroys the localization. Again, the population distribution acquires a non-exponential shape, albeit not as pronounced as in the case of timing noise. Fitting a Gaussian distribution (thick green line) yields a smaller $1/e$ width of $J_{\text{diff}} = 6.9$. We conclude that the phenomenon of dynamical localization in molecular rotation is more susceptible to timing noise than to amplitude noise. In the context of demonstrating dynamical localization, this works in our favour since the timing noise of our experimental pulse trains can be suppressed much better than the remaining fluctuations in the pulse amplitudes.

In the whole section 6.4 we will use the same color coding: ‘red’ - periodic pulse train without noise, ‘blue’ - periodic pulse train with amplitude noise, ‘black’ - non-periodic pulse train due to timing noise. The amount of noise remains unchanged at 41% amplitude noise or 33% timing noise, given in standard deviation.

6.4.1 Dependence on the number of kicks

Figure 6.4 shows the evolution of the rotational distribution with the number of kicks N . For the case of a periodic pulse train illustrated in Fig. 6.4(a1), the distribution becomes exponential within a few kicks and hardly changes after that: $J_{\text{loc}} = 3.1, 3.3$ and 3.3 for $N = 8, 16$ and 24 , respectively. In sharp contrast, the line shapes in Fig. 6.4(b1&c1) remain non-exponential and keep broadening with increasing N in the case of periodic kicking with amplitude noise ($J_{\text{diff}} = 6.0, 7.2$ and 7.4) and non-periodic kicking due to timing noise ($J_{\text{diff}} = 5.6, 6.2$ and 7.9), respectively. This behaviour demonstrates the destruction of dynamical localization by noise and clearly distinguishes it from other mechanisms of suppressed rotational excitation.

We also give a comparison between the experimentally retrieved population in the left column (1) and the exact calculated population in the right column (2). Qualitatively, both sets are in agreement. Quantitatively, we observe two substantial deviations, as expected. First, the calculated localization lengths in Fig. 6.4(a2) with $J_{\text{loc}} = 2.1, 2.3$ and 2.3 for $N = 8, 16$ and 24 , respectively, are shorter than the experimentally retrieved ones. This discrepancy is a result of the single-initial-state approximation. Second, a

6.4. Observation of dynamical localization

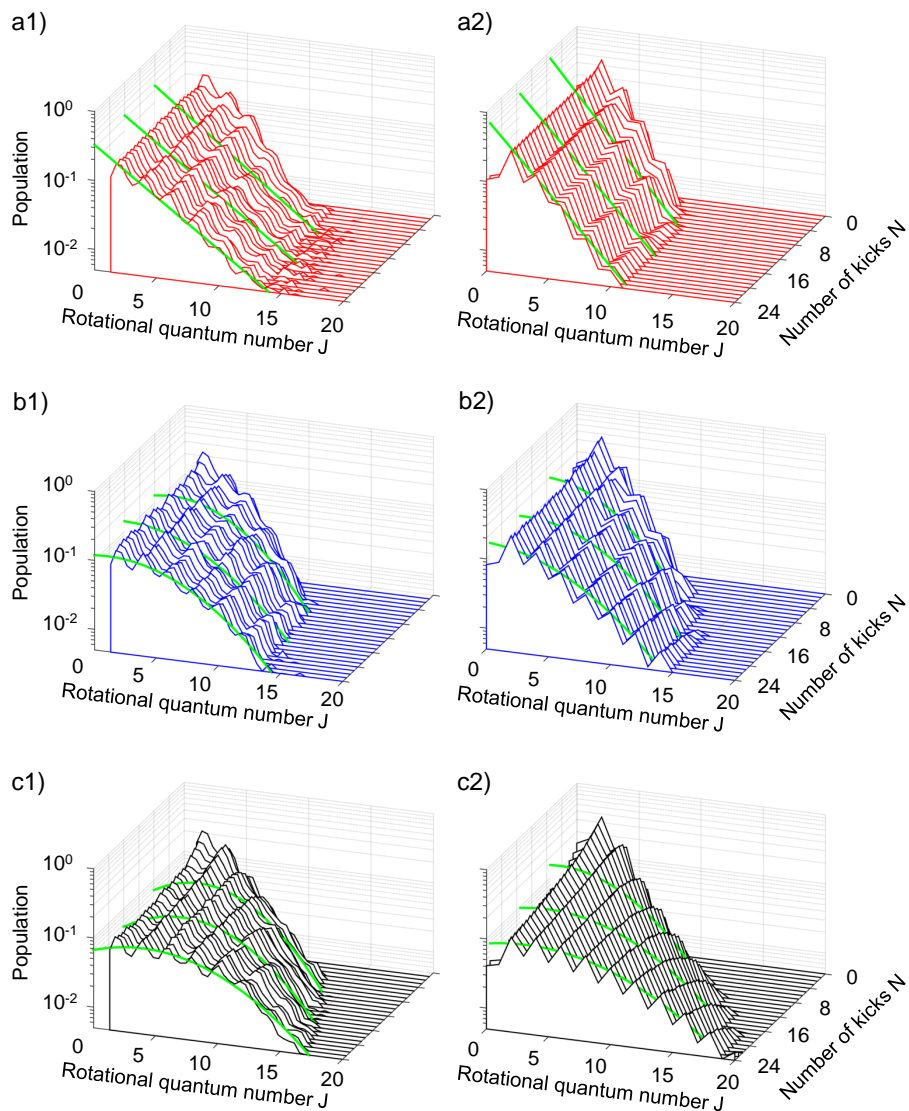


Figure 6.4: Evolution of the molecular angular momentum distribution with the number of kicks N for a periodic excitation without noise (**a**), with amplitude noise (**b**) and with time noise (**c**). The mean kick strength per pulse is $P = 2.3$. The left column (**1**) shows the populations retrieved from the experiment, the right column (**2**) are the numerically calculated ones. Exponential and Gaussian fits, respectively, indicate the changes of the distributions at $N = 8, 16$ and 24 (thick green lines).

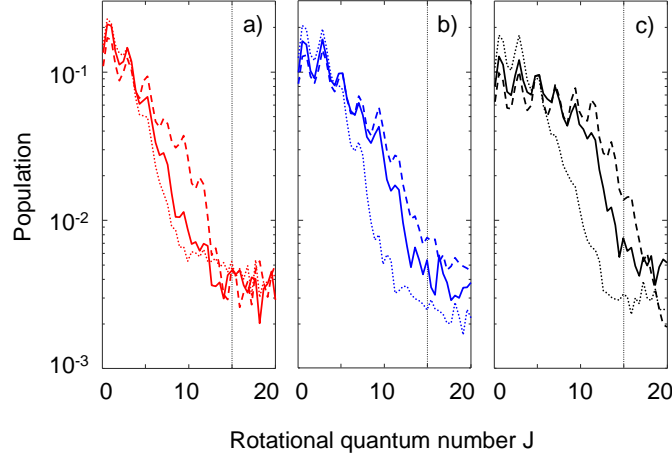


Figure 6.5: Dependence of the experimental populations on the kick strength P for an excitation with $N = 24$ kicks, that are periodic without noise (**a**), periodic with amplitude noise (**b**) and non-periodic (**c**). For each case, the kick strength is varied from $P = 1$ (dotted), $P = 2$ (solid) to $P = 3$ (dashed). The dotted vertical line represents the excitation limit due to the finite pulse duration.

substantial deviation is caused by the bandwidth limit in the experiment. Due to the final pulse duration, the effective kick strength in nitrogen diminishes for $J \gtrsim 15$. This limit in the excitation of rotational states is not present in the calculation with δ -kicks. In Fig. 6.4(**b2&c2**) the $1/e$ widths of the Gaussian distributions grow wider than the experimentally retrieved ones. In the case of a pulse train with amplitude noise $J_{\text{diff}} = 5.9, 6.8$ and 7.9 and for time noise $J_{\text{diff}} = 6.4, 8.0$ and 9.2 .

6.4.2 Dependence on the kick strength

The dependence of the rotational distribution on the strength of the kicks is shown in Fig. 6.5. For all three of the discussed scenarios, we show the population after a train of pulses with $P = 1$ (dotted line), $P = 2$ (solid line) and $P = 3$ (dashed line). As expected for a periodically kicked quantum rotor (**a**), the localization length grows with increasing P : $J_{\text{loc}} = 2.2, 2.9$ and 4.7 for $P = 1, 2$ and 3 , respectively. The line shape remains exponential below the cutoff value of $J \approx 15$ discussed earlier. For each kick strength, the Gaussian distribution after a noisy pulse sequence lies well above its localized counterpart, despite being equally affected by the cutoff, and thus confirming

the universality of the observed dynamics. The distributions obtained under the influence of timing noise (**c**) with $J_{\text{diff}} = 6.7, 7.5$ and 10.8 are broader than those corresponding to amplitude noise (**b**) with $J_{\text{diff}} = 5.1, 7.3$ and 9.0 , emphasizing the higher susceptibility to timing noise. For clarity, the fitted lines have not been included in Fig. 6.5.

6.4.3 Rotational energy

Owing to our state resolved detection, the total rotational energy of a molecule can be calculated as $\sum_J E_J P_J$, with populations P_J extracted from the observed Raman spectra I_J . The rotational energy is plotted as a function of the number of kicks for all three excitation scenarios in Fig. 6.6. For periodic kicking, the retrieved energy (red squares) increases during the first 3 kicks, after which its further growth is completely suppressed - a prominent feature of dynamical localization in the QKR. The same behaviour is reproduced in the simulation (red dashed line), with the difference of a systematic offset in the absolute energy. Numerically we can show that this offset is due to the approximations done to retrieve the populations. Random variations in the pulse amplitudes destroy the localization, which is manifested by the continuously increasing rotational energy of the rotors with the number of kicks. This is true for the experiment (blue triangles) and the exact simulation (blue dash-dotted line). Breaking the periodicity of the pulse sequence with timing noise results in an even stronger recovery of the classical diffusion (black circles). A linear growth rate is expected according to the calculations (black dotted line). The observed sub-linear growth is due to the finite duration of our laser pulses.

6.4.4 Dependence on the period

Previously, we pointed out the necessary condition for dynamical localization in the QKR: The period of the kicking field must not coincide with any fractional quantum resonances $T \neq \frac{p}{q} T_{\text{rev}}$ [52], where p and q are integers. However, we also stressed the influence of a finite pulse duration in terms of ‘partially’ overlapping with exactly those fractional resonances. In this section, we investigate how the exact choice of the pulse train period will affect the localization.

We switch our molecular sample to oxygen, where only one spin parity exists and only half of all fractional quantum resonances are of concern. This simplifies the interpretation of the results. We use a pulse sequence

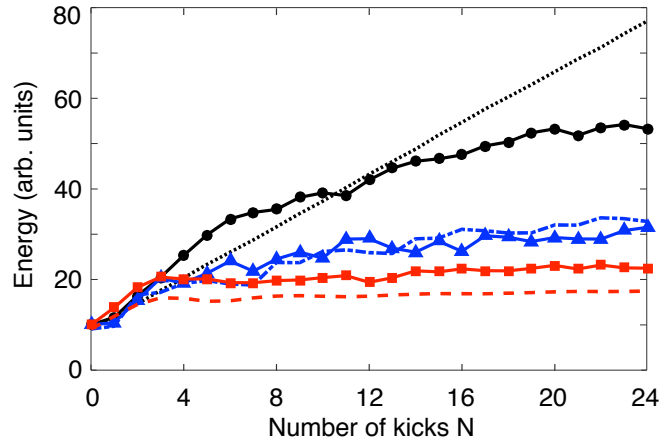


Figure 6.6: Rotational energy as a function of the number of kicks N with a mean strength of $P = 2.3$. Compared are the experimentally retrieved energies (connected symbols) with the numerically calculated ones (lines), for a periodic sequence (red squares, dashed line), and the same sequence after the introduction of amplitude noise (blue triangles, dash-dotted line) or timing noise (black circles, dotted line).

of 13 pulses with periods on the order of $T = \frac{1}{3}T_{\text{rev}}$. Experimentally, these sequences are produced without any Michelson interferometers. In the absence of polarization multiplexing in the latter, we can reduce the optical losses by a factor of two. This enables us to achieve stronger pulses with up to $P = 8$ per pulse. More details regarding the generation of pulse sequences can be found in chapter 3.

Figure 6.7(1a) shows an exponential distribution of angular momentum obtained after the molecules were exposed to such a pulse sequence. The distribution localizes after about 4 kicks. In order to smoothen the spectrum, we measured the distribution after each pulse N . Plotted is the mean distribution averaged over the measurements for $N = 6$ to 13. We also averaged over 10 pulse trains with equally spaced periods in the interval $0.26 \leq T/T_{\text{rev}} \leq 0.29$, marked in the resonance map (2a). These periods are chosen to not overlap with any fractional resonances associated with low-lying rotational states. As expected, the rotational population distribution falls off exponentially away from the initially populated states centred at $J = 1$. We compare three scenarios with pulses of different kick strengths $P = 4$ (dark-red, dashed line), $P = 6$ (light-red, dotted line) and $P = 8$ (red, solid line). The localization length increases with stronger kicks. Once the

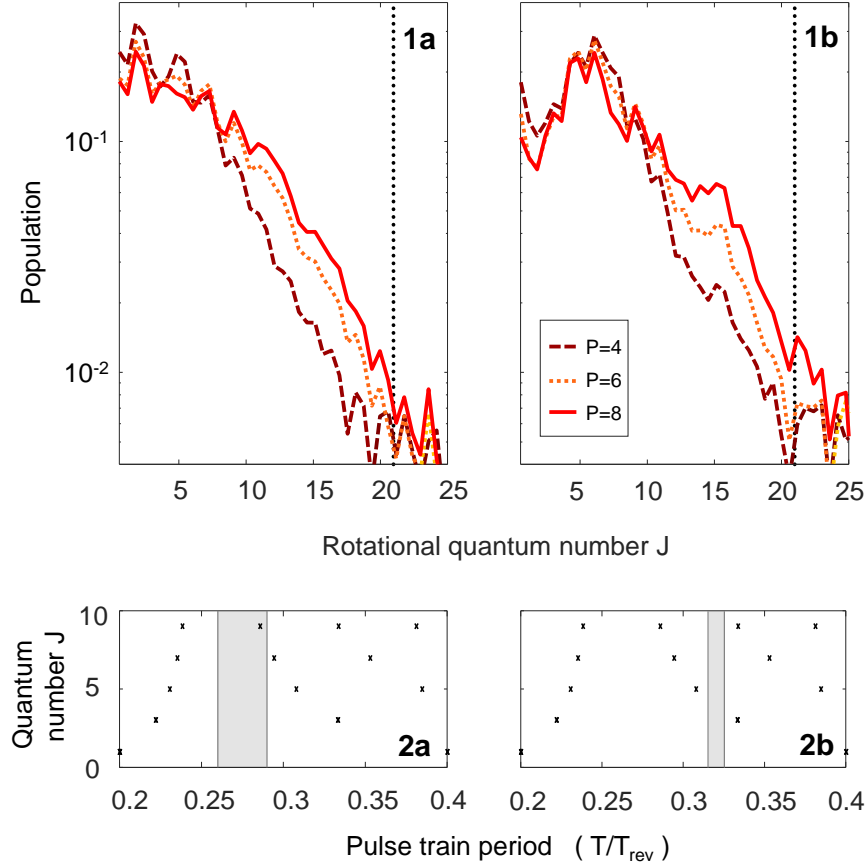


Figure 6.7: (**1a,1b**) Localized angular momentum distribution of oxygen molecules excited with a periodic train of 13 pulses for three selected kick strengths of $P = 4$ (dashed), $P = 6$ (dotted) and $P = 8$ (solid). The dotted vertical line represents the excitation limit due to the finite pulse duration. Shown are the mean distributions obtained from ten pulse trains with equidistant periods in the interval $0.26 \leq T/T_{\text{rev}} \leq 0.29$ (**2a**) and $0.315 \leq T/T_{\text{rev}} \leq 0.325$ (**2b**), marked in the resonance maps at the bottom.

6.4. Observation of dynamical localization

population is getting closer to the bandwidth limit at $J_{\text{lim}} \approx 21$ (dotted vertical line), we notice a sub-exponential tail due to the additional adiabatic localization.

Next, we compare the key parameters of the QKR: the kick strength P , the effective Planck constant τ and the stochasticity $K = \tau P$ (see Sec. 2.2.3), with respect to our previous study in nitrogen, i.e. Fig. 6.2 and Fig. 6.6. (1) The pulse train periods are smaller by about a factor of three. Therefore the effective Planck constant is reduced to $\tau \approx 2\pi\frac{1}{3} \approx 2$, which is still in the quantum regime of the QKR dynamics ($\tau > 1$). (2) Previously we were limited to $P_{(N_2)} = 3$. Now we reach $P_{(O_2)} = 8$, larger by about a factor of three. Owing to stronger kicks, we observe longer localization lengths. (3) The stochasticity parameter K of both studies is comparable. For all measurements presented in Fig. 6.7(1a) it is well in the classically chaotic regime $K \gtrsim 5$.

Figure 6.7(1b) shows the angular momentum distribution, obtained with the same procedure, but using 10 equally spaced periods in a different interval $0.315 \leq T/T_{\text{rev}} \leq 0.325$, marked in the resonance map (2b). Although these periods are non-resonant as well, the proximity of the resonances for $J = 3$ and 5 alter the shape of the distributions notably. The final population distribution is achieved similarly after about 4 kicks, but the localization center has shifted to $J \sim 5, 7$. Apparently, the vicinity of the fractional quantum resonances can (to some degree) facilitate the transfer of population into higher states when one uses laser kicks of non-zero length. Provided strong enough kicks, the center of the distribution initially moves up until it is further off all resonances, at which point the wave function once again localizes, but now with a shifted localization center.

The same principle applies to the diffusive growth of angular momentum that we observe under the influence of noise. In Fig. 6.8 we use the same 13 pulses as before but eliminate the periodicity with timing noise. The mean period remains at $\bar{T} \sim \frac{1}{3}T_{\text{rev}}$ with a standard deviation of $\sim 40\%$. For better statistics we again average over 10 different pulse trains. In direct analogy to Fig. 6.7(1a,1b), we compare the final population distribution after one ‘quasi’-random pulse train, which is engineered to avoid all quantum resonances that efficiently excite low-lying rotational states $J = 1, 3$ or 5, in Fig. 6.8(1a), and after another *fully random* pulse train in Fig. 6.8(1b). The 120 different periods belonging to each measurement are indicated in the respective resonance maps (2a,2b).

In both scenarios (1a,1b) we observe a non-exponential distribution that diffusively grows with the number of kicks, shown is the final distribution af-

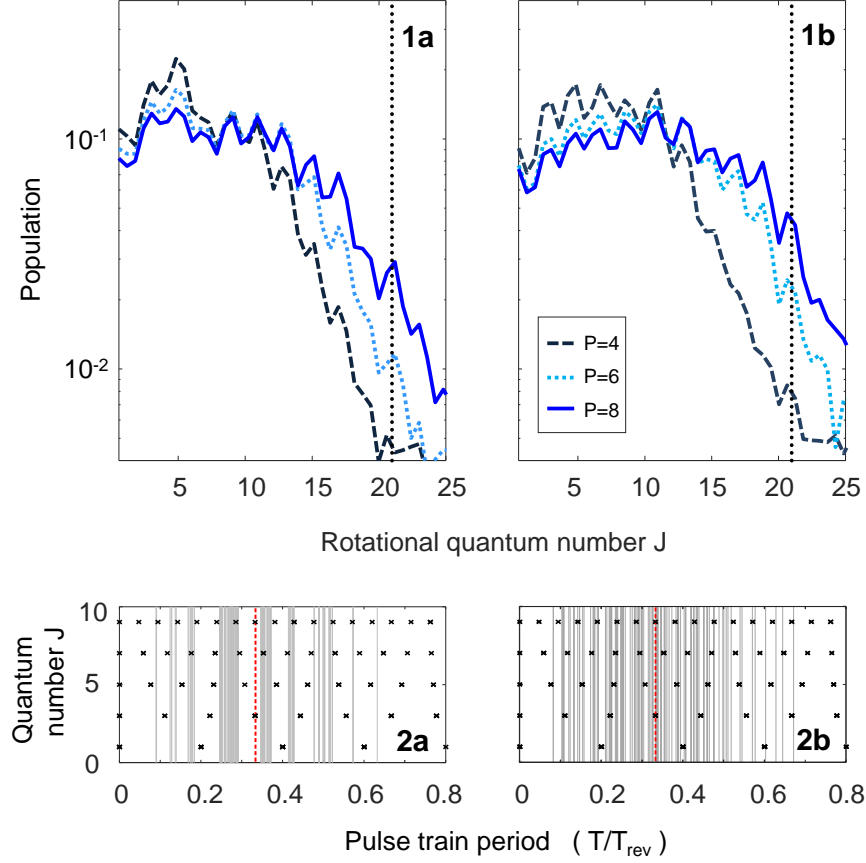


Figure 6.8: **(1a,1b)** Angular momentum distribution of oxygen molecules excited with a non-periodic train of 13 pulses for three selected kick strengths of $P = 4$ (dashed), $P = 6$ (dotted) and $P = 8$ (solid). The dotted vertical line represents the excitation limit due to the finite pulse duration. Shown are the average distributions obtained from ten different pulse trains. The random periods follow a Gaussian distribution with a mean and standard deviation of **(a)** $\bar{T}/T_{\text{rev}} = 0.34$ and 35%, **(b)** $\bar{T}/T_{\text{rev}} = 0.32$ and 43%, respectively. All 120 periods are marked in the resonance maps **(2)**. In case **(a)**, we make sure that no period is within 150 fs of any fractional resonance associated with $J = 1, 3$ or 5, whereas no such filtering is applied in case **(b)**. The dashed red line marks the $1/3$ resonance.

ter 13 pulses. With increasing kick strength from $P = 4$ (dark-blue, dashed line), $P = 6$ (light-blue, dotted line) and $P = 8$ (blue, solid line) the distribution grows wider. For the *quasi random* train the most populated states remain in the vicinity of the initial distribution. For the *fully random* train the distribution grows faster and the distribution center moves to $J \sim 11$. As the distribution becomes increasingly broader with more/stronger kicks, the difference between both cases will diminish. Then, the low-lying resonances play a minor role in the whole picture and full randomness is approached.

6.5 Transition from Bloch oscillations to dynamical localization

Here, we examine the phenomenon of localization in the vicinity of the quantum resonance. So far, we have analysed the excitation with periods far from the quantum resonance, leading to the dynamical localization of angular momentum (Sec. 6.4). We also analysed the excitation on or near resonance to study Bloch oscillations in angular momentum (Sec. 5.3). Now, we will revisit this regime, but with the intent to investigate the exponentially localized population distribution and how it is affected by the detuning. We will give an alternative explanation of Bloch oscillations where the resonant excitation is in fact limited by the dynamical localization at high quantum numbers. This transition between dynamical localization and a linear growth in momentum has been studied theoretically by Floss *et.al.* [184, 59, 63]. There exists no published experimental work with the QKR on this subject.

6.5.1 Anderson wall

The rotational tight-binding model makes it evident that the occurrence of Bloch oscillations in the angular momentum space is closely related to the phenomenon of dynamical localization. Beyond a critical value of the angular momentum, the “Anderson wall”, the wave function localizes. As a consequence, Bloch oscillations will appear in the molecular rotation only below the Anderson wall.

In this section we are investigating the QKR exposed to periodic resonant excitation with periods T in the proximity of the quantum resonance $T_{\text{rev}} = (2cB)^{-1}$ with

$$T = (1 + \delta) T_{\text{rev}} , \tag{6.4}$$

and the detuning $|\delta| \ll 1$. We start our theoretical treatment by revisiting

equation 2.57, the on-site energy term $T(J) = \tan[\phi(J)]$ of the rotational tight-binding model (Sec. 2.4.6), under our specific conditions

$$\begin{aligned}\phi(J) &= \frac{\pi}{2} \left(\frac{(1+\delta)\mathcal{E}}{hcB} - (1+\delta)J(J+1) + (1+\delta)\frac{D}{B}J^2(J+1)^2 \right) \\ \phi(J) &\approx \frac{\pi}{2} \left(\frac{(1+\delta)\mathcal{E}}{hcB} - \delta J(J+1) + \frac{D}{B}J^2(J+1)^2 \right).\end{aligned}\tag{6.5}$$

In the second line, we neglected the term, which is of second-order in both perturbations $|\delta| \ll 1$ and $\frac{D}{B} \ll 1$, as well as the term $\frac{\pi}{2}J(J+1)$ because multiples of π result in the same energy $T(J)$ [62].

We will explore four distinct scenarios, distinguishing a rigid rotor versus a non-rigid one, that is excited on quantum resonance or detuned from it.

Rigid rotor, resonant excitation ($\delta = 0$): In the rigid rotor approximation, the centrifugal term D in the energy expression is set to zero

$$\phi(J) = \frac{\pi}{2} \frac{\mathcal{E}}{hcB}.\tag{6.6}$$

The expression has no J -dependence and will result in a constant energy shift $T(J)$. Therefore, the tight-binding model presents a completely periodic lattice, which supports unlimited spreading of the rotational wave function, see Sec. 2.4.4. The quasi-energy states are extended over the rotational lattice [62], analogous to the Bloch states in crystalline solids.

The realization of this scenario leads to a “ballistic growth” of rotational energy. Starting from an initial wave packet that is close to the rotational ground state, the wave packet’s center will increase linearly in angular momentum, which translates into a quadratic growth of energy due to the $E(J) \propto J^2$ relation. This correlates with our intuitive understanding, that any rotational wave packet reproduces itself after an integer multiple of the revival time (see the description of the resonance map in Sec. 2.3.8). Thus, N kicks with the kick strength of P will add constructively and excite the molecule equivalently to a single kick with the strength NP .

Non-rigid rotor, resonant excitation ($\delta = 0$): In the experiment, we will observe a linear growth of the rotational population only for a limited number of pulses N , due to the non-rigidity of real molecules. Faster spinning of the molecule results in a stretching of the bond, i.e. centrifugal distortion. The increased moment of inertia will in turn modify the resonant frequency, making the quantum resonance J -dependent, which becomes most notable at higher quantum numbers.

In the picture of the tight-binding model, we gradually transition from a periodic lattice at low J -states to a pseudo-random lattice at higher J -states. Floss *et.al* have shown numerically that the phenomenon of dynamical localization will occur beyond a threshold value J_A , which they called the “Anderson wall” [60, 62]

$$\phi(J) = \frac{\pi}{2} \left(\frac{\mathcal{E}}{hcB} + \frac{D}{B} J^2 (J+1)^2 \right). \quad (6.7)$$

The quantity of importance is the change of the on-site energy between the neighbouring rotational states J and $J+2$ of the angular momentum lattice, which is carried through

$$\Delta\phi(J) = |\phi(J+2) - \phi(J)| \approx 4\pi \frac{D}{B} J^3. \quad (6.8)$$

We regard only the leading term that scales with J^3 . Once $\Delta\phi(J)$ reaches $\pi/2$, the $\tan(\Delta\phi)$ diverges. For larger J -values, the phase difference $\Delta\phi$ grows increasingly faster. However, only $\Delta\phi$ modulo π affects the variation of the on-site energy. The continued wrapping makes $T(J)$ a pseudo-random number. This statement is valid because D/B is irrational. The estimated position of the Anderson wall is [60, 62]

$$J_A \sim \frac{1}{2} \sqrt[3]{\frac{B}{D}}. \quad (6.9)$$

If the initial rotational wave packet consists of low-lying rotational states $J < J_A$, we anticipate a spreading of the angular momentum with the number of kicks, which is bounded by $J = 0$ below, and the Bloch wall $J_B \leq J_A$ above. The states at $J > J_A$ project onto localized quasi-energy states, which have no overlap with the initial wave packet, and therefore cannot be populated at any point in time. Instead of an unbounded spreading, one observes Bloch oscillations discussed earlier in Sec. 5.3. For oxygen and nitrogen molecules, the Anderson walls are expected around $J_A^{(O_2)} \sim 33$ and $J_A^{(N_2)} \sim 35$, respectively, way above our bandwidth limit.

Rigid rotor, non-resonant excitation ($\delta \neq 0$): A similar behaviour may be induced by detuning from the quantum resonance $T = (1 + \delta)T_{\text{rev}}$. If the detuning δ is large enough, the centrifugal term can be neglected and

$$\phi(J) = \frac{\pi}{2} \left(\frac{(1 + \delta)\mathcal{E}}{hcB} - \delta J(J+1) \right). \quad (6.10)$$

Again, we can distinguish two regimes, the one of extended states and the one of localized states, depending on

$$\Delta\phi(J) = \pi\delta(2J + 3) . \quad (6.11)$$

Owing to the linear dependence on J , the two regimes will alternate in the angular momentum space [62]. Whenever the rotational states are in the vicinity of $J_A^{(n)} \sim \frac{2n+1}{4\delta}$ such that $\Delta\phi(J) \sim \frac{2n+1}{2}\pi$ with integers n , the on-site energies are quasi-random for neighbouring J -states. We consider those states as effective Anderson walls. If the rotational states, however, are close to $J \sim \frac{2n}{4\delta}$ such that $\Delta\phi(J) \sim n\pi$, adjacent lattice sites have nearly equal energies, which corresponds to a periodic case with extended eigenstates.

In the experiment with the initial wave packet close to $J \approx 0$, it projects predominantly onto extended states ($n = 0$). The initial linear growth in the angular momentum is bound by the lowest Anderson wall $J_A^{(0)}$. For our experimental conditions with moderate kick strengths, we are not able to “jump” across this Anderson wall to the next set of extended states ($n = 1$). Qualitatively, we expect to observe the same Bloch oscillations mentioned above (in the case of a non-rigid rotor at $\delta = 0$), but this time we can control the location of the Anderson wall by adjusting the detuning δ .

Non-rigid rotor, non-resonant excitation ($\delta \neq 0$): This scenario is a combination of the last two. Using the same arguments, the term that dominates the expression of $\Delta\phi(J)$ with increasing J -states will determine the location of the Anderson wall.

The magnitude of the phase difference $\Delta\phi(J)$ determines whether the particular rotational states will map onto extended quasi-energy eigenstates ($\Delta\phi(J) \rightarrow 0$) or the localized ones ($\Delta\phi(J) \rightarrow \pi/2$). For a specific diatomic molecule ($D/B = \text{const.}$), the width and the location of these regions of extended and localized dynamics can be controlled by the detuning δ from the quantum resonance. The overlap of the initial states with either of the two regions will determine the dynamics of the QKR, i.e. whether it will dynamically localize or feature Bloch oscillations.

We note an important difference between the described behaviour of the QKR and the dynamics of a quantum particle in a disordered one-dimensional lattice. In the latter case, the particle will localize no matter how weak the disorder is. In a rotational lattice, however, introducing a small detuning from the resonance may not necessarily lead to the exponential localization of the wave function. The reason is the dependence of

the on-site energy on the site number J (cf. Eq. 6.11). Effectively, the “rotational disorder” increases with the distance from the edge of the lattice at $J = 0$. Hence, even though any detuning will result in the restricted growth of angular momentum, the distribution of the wave function will not necessarily be exponential.

6.5.2 Evolution of angular momentum

At first, we look at the angular momentum distribution and how it evolves with the number of kicks. The general procedure including the population retrieval from the Raman spectra is equivalent to the one described before. Figure 6.9 and 6.10 are a compilation of six different periodic pulse trains, whose periodicities are continuously tuned further below the quantum resonance. Shown are plots for the following detunings: **(a)** 0%, **(b)** -0.08% , **(c)** -0.16% , **(d)** -0.24% , **(e)** -0.5% and **(f)** -1.0% . The left column **(1)** of experimentally retrieved populations are compared to the calculated exact populations in the right column **(2)**. The kick strength of the pulses in a sequence of 24 kicks is set to $P = 0.9$. For nitrogen molecules this means that the bandwidth limit of $J_{\text{lim}} \approx 15$ will be reached at the end of the train ²³.

On the quantum resonance in Fig. 6.9**(a)**, the center of the population distribution linearly increases to higher J -states, as expected and seen in the calculations **(a2)**. At the end of the train the population reaches as far as the Anderson wall allows. For higher quantum numbers, the distribution falls off exponentially, owing to dynamical localization due to the centrifugal distortion of the non-rigid rotor. This concept was introduced in section 5.3 on Bloch oscillations. In the experiment **(a1)** the linear growth of angular momentum slows down towards the end of the train. For these higher quantum numbers, the effective kick strength decreases due to the finite pulse duration. It results in a stronger localization - a superposition of adiabatic localization and dynamical localization.

In the following rows **(b-f)** we detune the period increasingly further below the quantum resonance. According to the theory **(2)**, we push down the wall responsible for the turning point of Bloch oscillations. At a detuning between -0.16% **(c2)** and -0.24% **(d2)** the population distribution completes one full Bloch oscillation within 24 kicks. Eventually, at a detuning of -1% **(f2)**, the population distribution is barely distinguishable from its

²³For quantum numbers exceeding $J = 15$ the population is adiabatically localized. This particular value of the kick strength has been chosen to avoid multiple Bloch oscillations under the resonance condition.

6.5. Transition from Bloch oscillations to dynamical localization

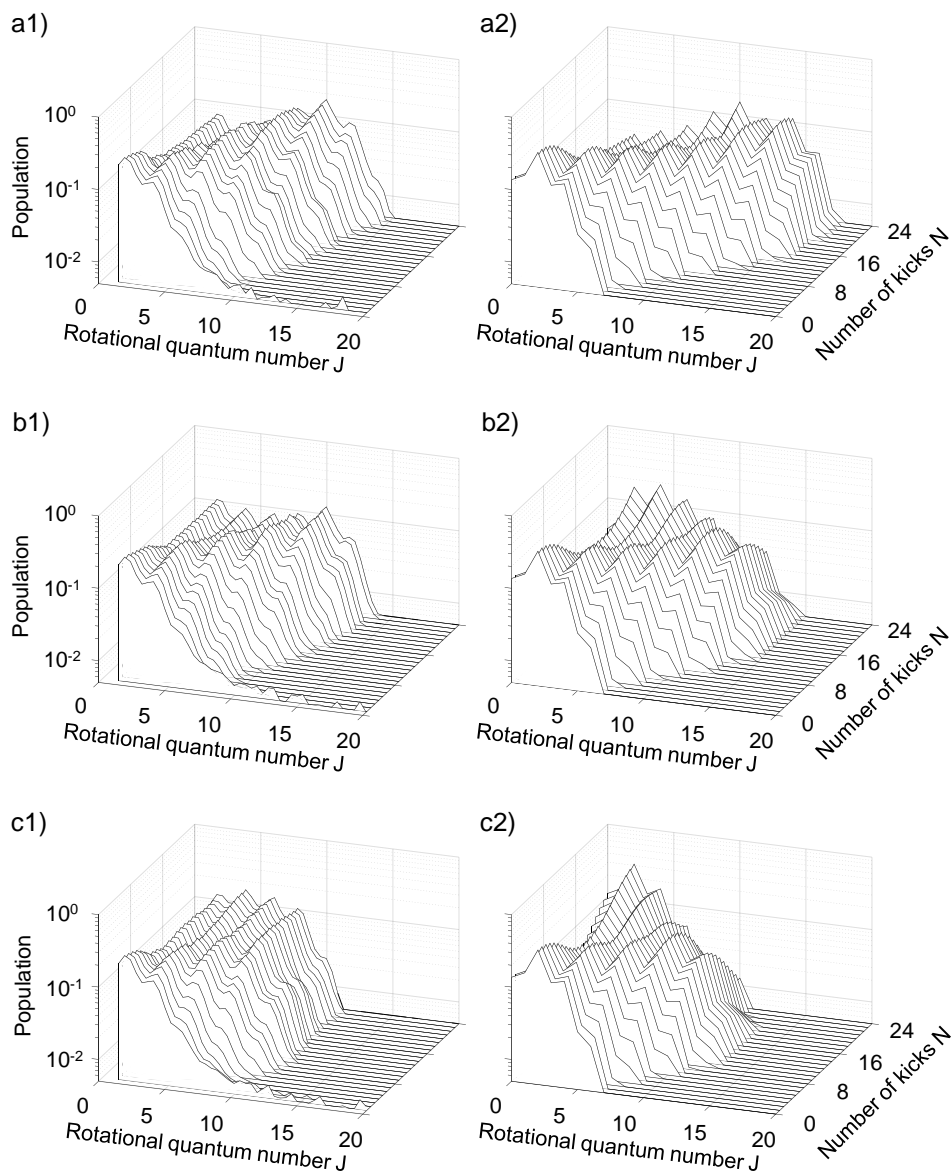


Figure 6.9: Evolution of the molecular angular momentum distribution with the number of kicks N for a periodic sequence. Each individual pulse carries the kick strength $P = 0.9$. Left column (1) contains the experimental results; right column (2) shows the corresponding numerical plots. The periodicity is continuously tuned further below the quantum resonance (a) with detunings of $\delta = -0.08\%$ (b) and -0.16% (c). (continued in Fig. 6.10.)

6.5. Transition from Bloch oscillations to dynamical localization

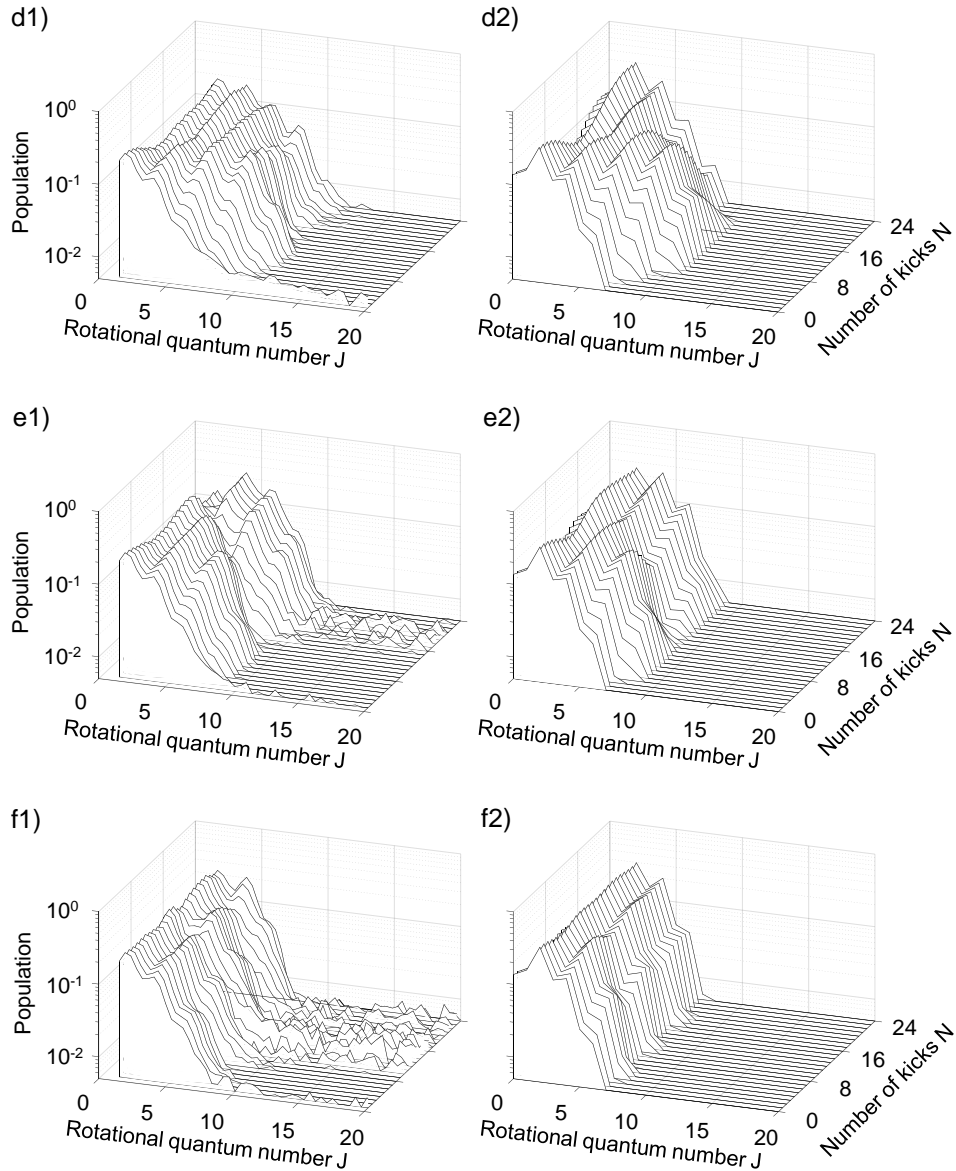


Figure 6.10: (Continuation of Fig. 6.9.) Evolution of the molecular angular momentum distribution with the number of kicks N for a periodic sequence. Each individual pulse carries the kick strength $P = 0.9$. Left column (1) contains the experimental results; right column (2) shows the corresponding numerical plots. The periodicity is continuously tuned further below the quantum resonance with detunings of $\delta = -0.24\%$ (d), -0.5% (e) and -1.0% (f).

6.5. Transition from Bloch oscillations to dynamical localization

initial distribution, apart from some residual fast Bloch oscillations. For detunings $> 1\%$ the system is completely governed by dynamical localization. The experimental results (**1**) demonstrate the same behaviour, i.e the Bloch wall location in the angular momentum space is continuously lowered, Bloch oscillations become visible (**d1**), and eventually the population distribution localizes and does not grow anymore (**f1**).

For large detunings from the quantum resonance our kick strength of $P = 0.9$ is not sufficient to significantly alter the initial thermal distribution. All states are localized, but the shape of the observed spectrum remains close to the thermal Boltzmann distribution.

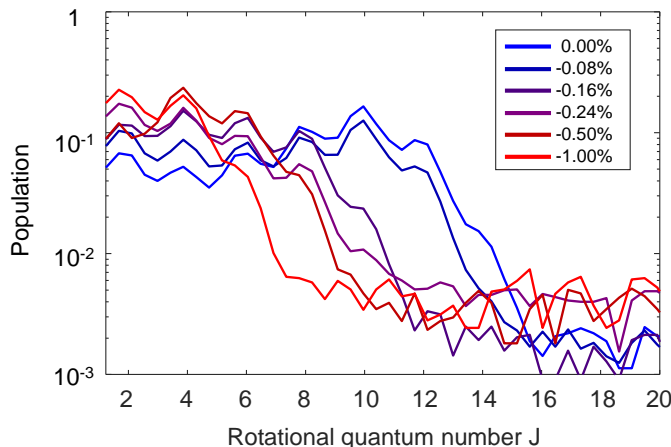


Figure 6.11: Populations, retrieved from the experimental Raman signal, after the excitation by 24 periodic pulses with a kick strength of $P = 0.9$ per pulse. The detuning from the quantum resonance ranges from 0 to -0.08% , -0.16% , -0.24% , -0.5% and -1.0% (blue to red coloured lines, see legend).

In Fig. 6.11 we plot the final population of the angular momentum states of nitrogen molecules after the excitation with 24 pulses. Shown are the distributions for all six periods with detunings from the quantum resonance ranging between 0% and -1% . The figure provides a good comparison to the same theoretical plot presented in Ref. [59, 63]. On resonance (blue line) the distribution is flat for $J \leq 12$ (on a logarithmic scale) before it sharply falls off. With increasing detuning, the extend of the plateau decreases, but the sharp drop remains. For the largest detuning (red line) the plateau has vanished and the population is localized. Owing to the weakness of

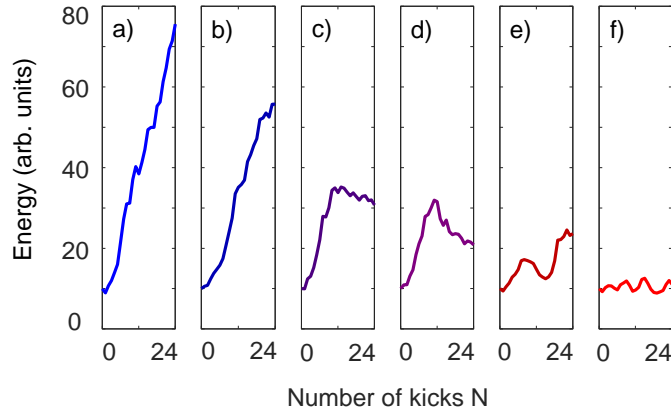


Figure 6.12: Rotational energy as a function of the number of kicks N with a strength of $P = 0.9$. Different panels show the dependence on the pulse train period: (a) on the quantum resonance, 0%, (b) -0.08% , (c) -0.16% , (d) -0.24% , (e) -0.5% and (f) -1.0% away from the quantum resonance.

the pulses at $P = 0.9$, the distribution resembles the initial Boltzmann distribution at 25 K.

6.5.3 Evolution of rotational energy

It is instructive to look at the total rotational energy in the system. We have seen in Fig. 6.6 that in the case of non-resonant periodic kicking, the energy diffusively grows for several kicks before the growth is suppressed by dynamical localization. In the case of resonant excitation the energy is expected to grow quadratically at first, before the centrifugal distortion will lead to oscillations in the total energy.

For the same six periodic pulse trains, we now calculate the rotational energy in the molecular system. In Fig. 6.12 the energy is given as a function of the number of pulses in the train. On resonance (a) the energy increases monotonically throughout all 24 pulses. With larger detunings, the total energy that the system accepts becomes smaller. The initial growth rate is the same, but the reduced Bloch wall forces the energy to oscillate. Finally, for a -1% detuning (f) the energy growth is completely suppressed. This is a powerful demonstration of the consequence of dynamical localization: Although in all six cases the energy of the pulse train is identical and the period changes by merely 1%, the total amount of energy that one can pump into the system differs by a factor of almost eight.

Besides the dependence on the detuning, we can also plot the dependence

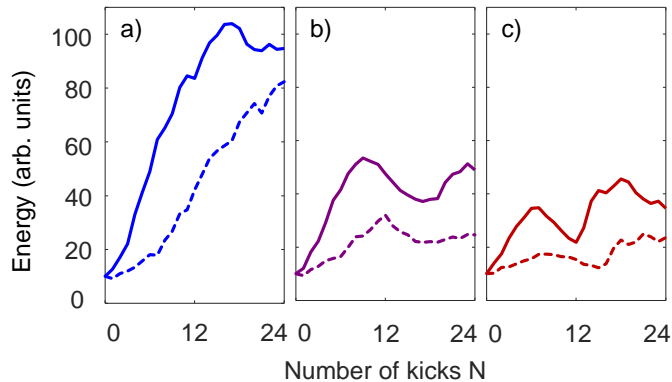


Figure 6.13: Rotational energy as a function of the number of kicks N with a strength of $P = 1.1$ (dashed lines) or $P = 2.3$ (solid lines). Different panels show the dependence on the pulse train period: (a) on the quantum resonance, 0%, (b) -0.24% , (c) -1.0% away from the quantum resonance.

on the kick strength. In Fig. 6.13, for three values of the detunings [(a) 0%, (b) -0.24% , (c) -1.0%], we plot the observed energy growth for two kick strengths of $P = 1.1$ (dashed line) and $P = 2.3$ (solid line). Stronger pulses lead to a more rapid growth of energy and to a higher maximum energy value. The reason has already been given in the context of Bloch oscillations in Sec. 5.3 when we demonstrated that the amplitude of the oscillations in the angular momentum space increases with the kick strength. The initial growth of energy has to be quadratic, which can be observed most clearly in panel (a). For the largest detuning in panel (c), there are about two complete oscillations. According to the theory, one would expect clean oscillations with maximum contrast: the energy at the minimum of each oscillation should equal the initial energy of the molecule. This is not the case in the experimental data. The most likely suspect for the mismatch is that averaging over the spatial beam profiles washes out the oscillations. Similar contrast in Bloch oscillations were reported by Kamalov *et.al.* with a different detection technique [88].

6.6 Conclusion

We presented the first experimental demonstration of the quantum phenomenon of dynamical localization in the angular momentum space of a periodically kicked rotor.

We showed that laser-kicked molecules have the potential of a testing

6.6. Conclusion

ground for a number of new physical phenomena. Some of them have been previously studied in AOKR, e.g. dynamical localization, the quantum resonance, the susceptibility to noise. At the same time, the QKR system offers new perspectives. The molecular angular momenta are quantized, whereas continuous translational atomic momenta hinder a clear observation of momentum distributions. Cold temperatures achieved in standard supersonic expansions are sufficient to reach the rotational ground state, while the AOKR requires ultracold atoms, obtained in complex experimental setups. The periodic excitation of real rotors also leads to some unique phenomena, e.g. the occurrence of Bloch oscillations due to centrifugal distortion (Sec. 5.3) or the predicted and yet-to-be-demonstrated edge states[61].

Chapter 7

Coherent control of quantum chaos

Control of molecular dynamics with external fields is a long-standing goal of physics and chemistry research. Great progress has been made by exploiting the coherent nature of light-matter interaction. At the heart of coherent control is the interference of quantum pathways leading to the desired target state from a well-defined initial state [158, 157]. In this context, an exponential sensitivity to the initial conditions, characteristic for classically chaotic systems, poses an important question about the controllability in the quantum limit (for a comprehensive review of this topic, see [71]). As the underlying classical ro-vibrational dynamics of the majority of large polyatomic molecules is often chaotic, the answer to this question has far reaching implications for the ultimate prospects of using coherence to control chemical reactions.

Success in steering the outcome of chemical reactions by the means of feedback-based adaptive algorithms [11], using the methods of optimal control theory [87], proved that such control is feasible. Theoretical works on quantum controllability in the presence of chaos, both in general [142] and with regard to specific molecular systems [70, 3], pointed at the importance of coherent evolution. To investigate the roles of coherence, stochasticity and quantumness further, Gong and Brumer considered the quantum kicked rotor to study quantum effects on classically chaotic dynamics [69, 70, 71]. They demonstrated that the energy of the localized state can be controlled by modifying the initial wave packet. Quantum coherences, as opposed to the classical structures in the rotor's phase space, are indeed responsible for the achieved control over the chaotic dynamics of the QKR [154].

In this chapter, we present an experimental proof of the Gong-Brumer control scheme. We prepare oxygen molecules in a coherent rotational wave packet and control the localization process of the QKR by varying the relative phases of the initial states. In Sec. 7.1, we outline relevant theoretical concepts and discuss the transition from quantum to classical regimes of the

QKR dynamics. We give a brief overview of the experiment in Sec. 7.2 and present all results in Sec. 7.3. The conclusions are in Sec. 7.4.

7.1 Theory

The main experimental approach is based on the effect of dynamical localization, described in detail in chapter 6.

7.1.1 Coherent control

The general concept of “coherent control” is based on the availability of quantum interferences, which can be altered in order to change the probability of reaching the desired target state [157]. Until now, coherent control has been used most frequently in atomic or molecular systems exhibiting relatively simple, e.g. periodic, dynamics [71, 157]. The focus of this work is on the control of quantum objects, whose underlying classical dynamics is chaotic.

7.1.2 Quantum-to-classical transition

The transition from classical behaviour to quantum behaviour can be defined by comparing the Planck’s constant \hbar with the classical action of the system [53]. In the case of the quantum kicked rotor, the latter can be expressed as (I/T) , the moment of inertia divided by the period of kicking [77]. Thus, the effective Planck constant $\tau = \hbar(I/T)^{-1}$, from Eq. 2.5, provides a simple estimate of the degree of “quantumness”. For $\tau \rightarrow 0$, the system approaches the classical limit, whereas for $\tau > 1$ it is expected to show its quantum nature [77, 138].

The fact that the stochasticity $K = \tau P$ of the QKR is comprised of two individual parameters, the effective Planck constant and the kick strength, allows for a unique control knob. One can fix K in the deeply chaotic regime and observe the quantum-to-classical transition by reducing τ from values greater than one towards zero. However, even if a quantum system can initially be described by means of the classical equations of motion, quantum effects will still accumulate with time, making the system deviate from its classical counterpart after the “quantum break time” [53]. In other words, the ability to tune τ to smaller values results in a larger window where the classical behaviour can be observed. The correspondingly larger values of the kick strength P for a constant stochasticity K , result in a longer localization length. Therefore, it takes more pulses for the QKR

to diffuse over a distance comparable to the localization length. But once it has diffused that far, quantum effects will again lead to the dynamical localization.

The conjugate variables of the QKR are the angle and the angular momentum, which obey the commutation relation $[J, \theta] = -i\hbar$ [77]. The classical trajectory, described by the standard map, is presented via the scaled angular momentum $\tilde{J} = J(I/T)^{-1} = J\tau/\hbar$, which yields the dimensionless commutation relation $[\tilde{J}, \theta] = -i\tau$.

In the following we give an intuitive explanation of the classical to quantum transition, which is adapted from Ref. [53]. (1) An initial state of a quantum system is assumed to be a localized wave packet, i.e. a small area in the available phase space. Its minimum size, a ‘‘Planck cell’’, is limited by the Heisenberg uncertainty principle and according to the commutation relation is given by τ . The corresponding classical system consists of several points in the phase space occupying the same area. (2) As a function of time, the wave packet spreads diffusively, with each initial point following its classical trajectory. (3) After the quantum break time, the wave packet has spread so much, that its different parts start overlapping, and hence interfering, with one another. The resulting interference is purely a quantum phenomenon.

The true transition to a classical kicked rotor can be implemented by introducing noise, as we showed in Sec. 6.4, or other decoherence mechanisms, e.g. collisions between the molecules. This will destroy the quantum coherences in the system irrevocably such that dynamical localization can no longer occur.

7.2 Experiment

The setup and the experimental procedure is mostly identical to the ones used to observe dynamical localization (Ch. 6). The only crucial difference is the shape of the femtosecond pulse train. A sequence of 15 high-intensity laser pulses is generated in the combined setup of a pulse shaper and a multi-pass amplifier (MPA). It consists of two independent parts, shown in Fig. 7.1. The first three ‘‘preparation’’ pulses are separated in time by $T_{\text{pre}} = 0.237 T_{\text{rev}}$, close to a fractional quantum resonance at $T = 1/4 T_{\text{rev}}$, and are used to excite a broad rotational wave packet, defined by the resonant process studied in Sec. 5.4. The period T_{loc} of the second ‘‘localizing’’ train of 12 pulses is chosen between $0.26 T_{\text{rev}}$ and $0.27 T_{\text{rev}}$, corresponding to the

7.3. Demonstration of coherent control in quantum chaotic system

effective Planck constant of $1.6 < \tau < 1.7$. This window is chosen so as to avoid strong fractional quantum resonances of low orders.

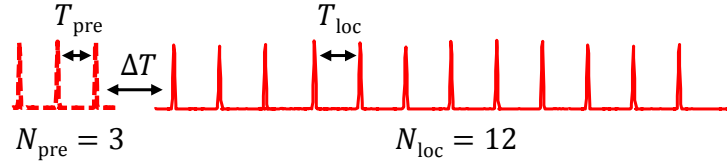


Figure 7.1: Train of fifteen laser pulses, with three variable time constants indicated by horizontal arrows.

The experiments are done with oxygen, whose nuclear spin statistics (Sec. 2.3.9) make only half of all fractional resonances relevant. Figure 7.2 visualizes pulse train periods with respect to the position of the fractional resonances. The time delay ΔT between the two pulse trains, and hence the relative quantum phases of the initial states, serves as a “control knob”. It will be used to control the amount of the rotational energy that is absorbed by the molecules before its further growth is suppressed by localization.

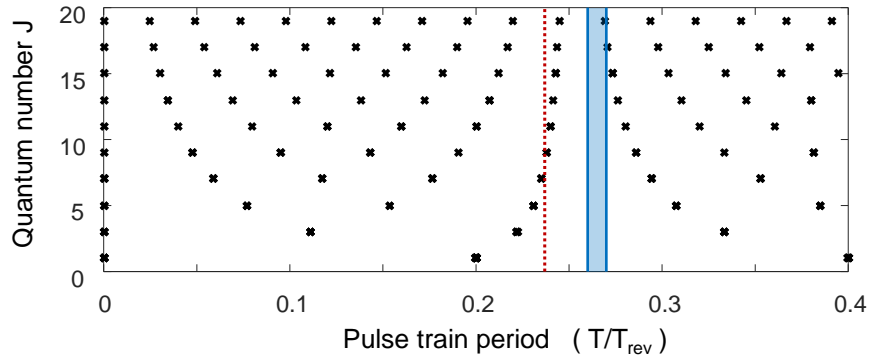


Figure 7.2: Resonance map indicating all relevant times: $T_{\text{pre}} = 0.237 T_{\text{rev}}$ (red dotted line) and $0.26 T_{\text{rev}} < T_{\text{loc}} < 0.27 T_{\text{rev}}$ (blue area).

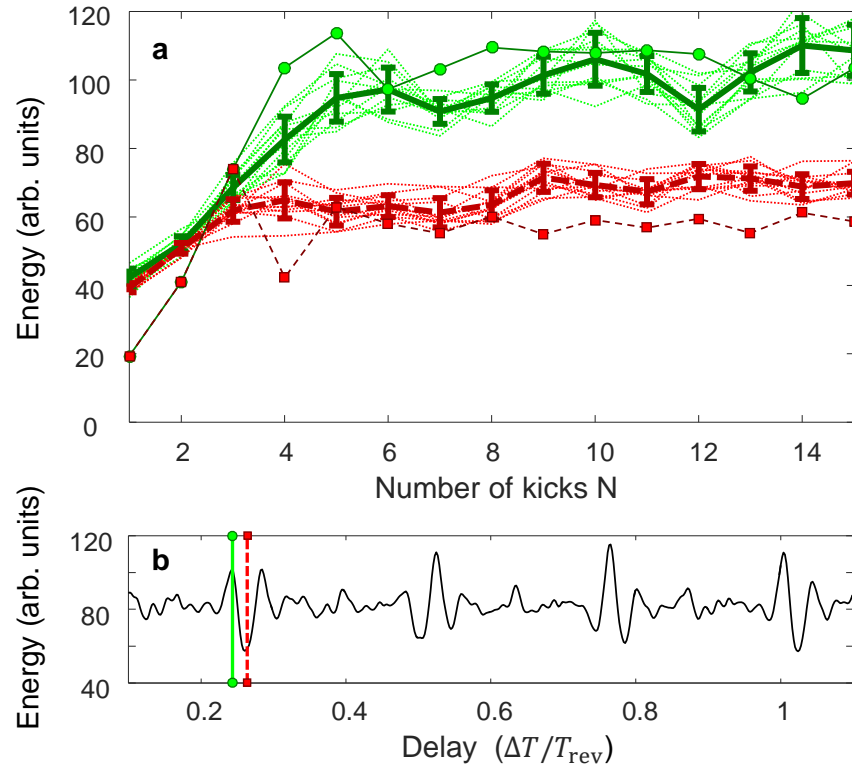


Figure 7.3: (a) Rotational energy of oxygen molecules as a function of the number of kicks N . Shown are thirteen experimental realizations (dotted lines) for each of the two control scenarios corresponding to a maximum (upper green lines, at $\Delta T_1 = 0.243 T_{\text{rev}}$) and a minimum in the absorbed rotational energy (lower red lines, at $\Delta T_2 = 0.264 T_{\text{rev}}$). The corresponding average values are plotted as the green solid line and the red dashed line, respectively, with error bars representing one standard deviation. In comparison, the numerical calculations are indicated by connected green circles (ΔT_1) and red squares (ΔT_2). (b) Numerically calculated dependence of the final rotational energy on the delay ΔT . Two vertical lines mark the experimental delays ΔT_1 (solid green) and ΔT_2 (dashed red).

7.3 Demonstration of coherent control in quantum chaotic system

Our main result is shown in Fig. 7.3(a), where we plot the rotational energy of oxygen molecules, measured after each of 15 laser pulses for a number of pulse trains, all with $T_{\text{loc}} = 0.267 T_{\text{rev}}$. The kick strength is set to $P = 3.8$, which corresponds to a stochasticity parameter $K = 6.4$ lying deep in the classically chaotic regime. By design, the first three preparation pulses in all trains lead to a fast growth of molecular energy. The time delay ΔT between the three preparation pulses and the localizing train of 12 pulses is scanned around the quarter revival time, between $\Delta T/T_{\text{rev}} = 0.223$ and 0.284 , where we anticipate the highest degree of control, as discussed below.

When the delay is set to $\Delta T_1 = 0.243 T_{\text{rev}}$ (upper green lines), the energy growth continues for a few more kicks and ceases after that, reflecting dynamical localization of the molecular angular momentum, investigated in chapter 6. Different thin lines correspond to different experimental runs, with their average indicated by the thick green curve. On the other hand, when the very same localizing pulse sequences are separated from the preparation pulses by $\Delta T_2 = 0.264 T_{\text{rev}}$, the suppression of the energy growth occurs much earlier and results in a lower (by $40 \pm 7\%$) energy of the final localized states (lower red lines).

In Fig. 7.3(a) we also show the results of the equivalent numerical calculations by connected green circles for the delay ΔT_1 and red squares for ΔT_2 . Despite the used approximation of infinitely short δ -kicks, the numerical results are in good qualitative agreement with the observations. We further exploit the numerical model for calculating the dependence of the rotational energy on the single control parameter ΔT , plotted in Fig. 7.3(b). The availability of control is apparent around fractional revivals, $\Delta T/T_{\text{rev}} = 1/4, 1/2, 3/4$ and 1 , which suggests an intuitive picture of its mechanism. The first kick from the localizing pulse train either continues the quantum-resonant excitation of the preparation sequence or opposes it, affecting the energy level, at which the rest of the train localizes the system. The dephasing of the rotational states in the prepared wave packet leads to a loss of control between the fractional revivals. The two vertical lines mark our experimental values of ΔT in Fig. 7.3(a).

The described control mechanism is also evident from the experimentally retrieved average distributions of the localized angular momentum, shown in Fig. 7.4 by thick lines with no markers. Solid green and dashed red traces

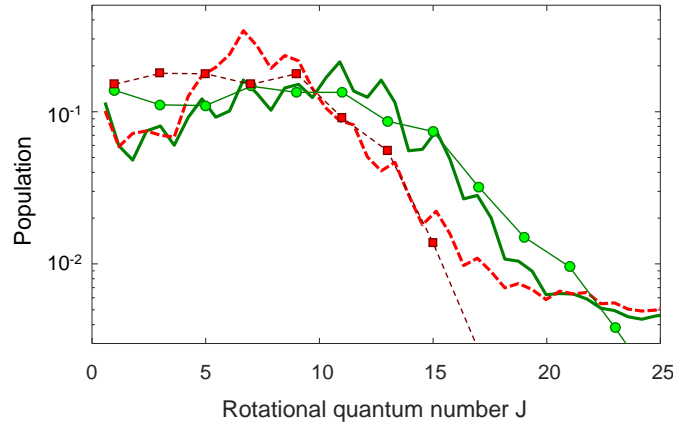


Figure 7.4: Localized population distribution of oxygen molecules excited by a train of 15 pulses with $P = 3.8$. Plotted is the experimentally retrieved average population distribution (thick lines, no markers) and the numerically calculated one (markers, connected by thin lines). The distributions correspond to the high (upper green lines, $\Delta T_1 = 0.243 T_{\text{rev}}$) and low (lower red lines, $\Delta T_2 = 0.264 T_{\text{rev}}$) localization energy in Fig. 7.3.

correspond to the localized wave packets with higher and lower rotational energies, respectively. As the higher energy clearly correlates with the broader wave packet, the achieved control can be attributed to populating different sets of quasienergy (Floquet) states [63]. Because each wave packet contains more than a single quasienergy state, the distributions are not expected to (and, indeed, do not) exhibit exponential line shapes [69].

Numerically calculated population distributions, corresponding to the experimental parameters for the high and low energy localized wave packets, are shown in Fig. 7.4 with connected green circles and red squares, respectively. The simulated and experimental distributions show qualitative agreement down to the instrumental noise floor around $P_J \approx 5 \cdot 10^{-3}$. The systematic underestimation of the experimentally extracted population at low rotational states is attributed to two effects. First, the approximations in the population retrieval from the measured Raman spectra neglects the dependence on the magnetic quantum number and the thermal population of multiple rotational states, as discussed in Sec. 6.3.2. Second, the effect of spin-rotation coupling in oxygen (Sec. 4.2.3) leads to a more rapid dephasing of the Raman signal at low J -states, which is not taken into account in the numerics.

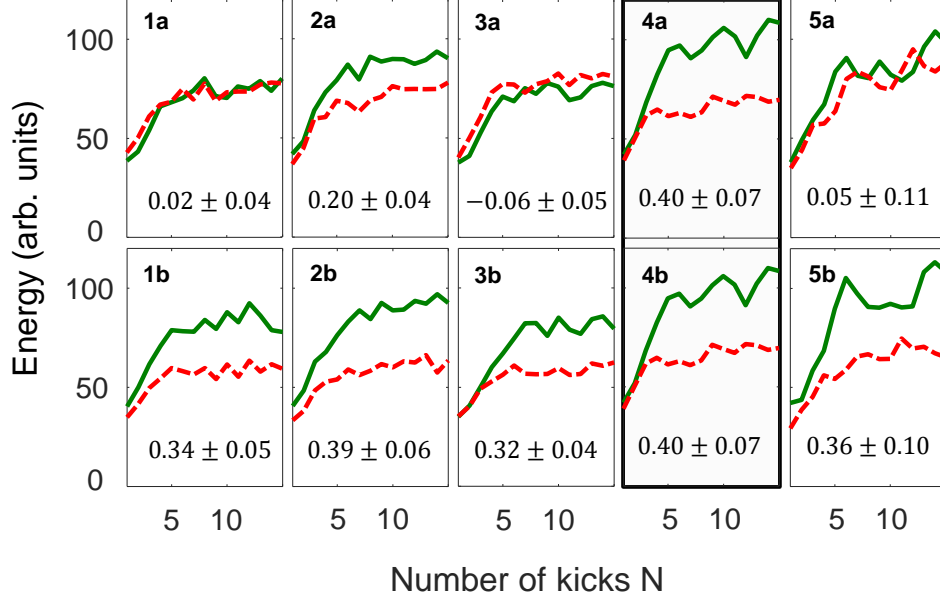


Figure 7.5: Top row (a): rotational energy for both time delays, $\Delta T_1 = 0.243 T_{\text{rev}}$ (solid green line) and $\Delta T_2 = 0.264 T_{\text{rev}}$ (dashed red line) for a set of five different T_{loc} periods (1)-(5), given in the text. Other parameters of the localizing train remain unchanged. Bottom row (b): for the same five values of T_{loc} , delays ΔT_1 and ΔT_2 are individually adjusted for the respectively highest and lowest energy of the localized state. The degree of control is given in each plot. Column (4) is equivalent to Fig. 7.3.

7.3.1 Robustness of control

The stability of the implemented control scheme with respect to the underlying classically chaotic dynamics is analysed in Fig. 7.5. In the top row (a) we show the dependence of the rotational energy on the period of the localizing train T_{loc} . As earlier, the value of the control parameter is either $\Delta T_1 = 0.243 T_{\text{rev}}$ (solid green line) or $\Delta T_2 = 0.264 T_{\text{rev}}$ (dashed red line). Shown is a representative set for five values of $T_{\text{loc}}/T_{\text{rev}}$: (1) 0.260, (2) 0.261, (3) 0.263, (4) 0.267 and (5) 0.270. The respective degree of control, defined as $\frac{E_1 - E_2}{(E_1 + E_2)/2}$ with E_i being the final rotational energy for the delay ΔT_i , is shown at the bottom of each plot. We observe wide fluctuations from a total loss of control in panels (1a, 3a, 5a) to the maximum control of about 40% in panel (4a).

High sensitivity of the QKR dynamics to the exact train period is well ex-

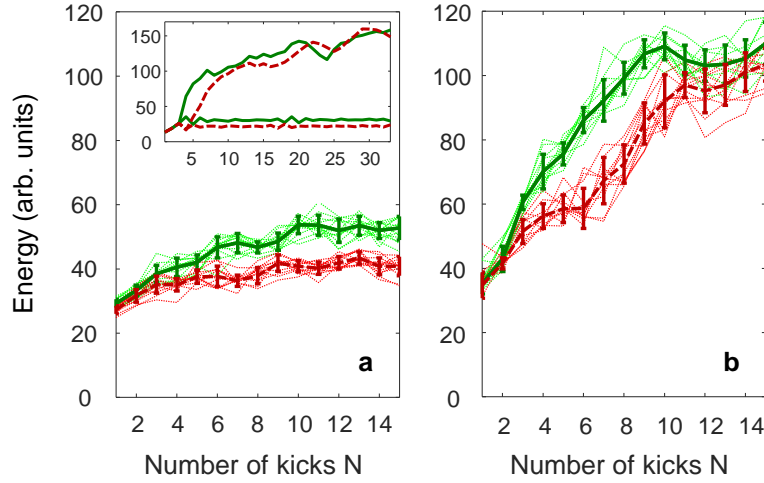


Figure 7.6: Same as Fig.7.3, but for two different values of the effective Planck constant: $\tau = 1.7$ (a) and $\tau = 0.6$ (b). The stochasticity parameter is held constant at $K = 3.4$. The inset gives a numerical comparison of both regimes, with lower (top) and higher (bottom) value of τ , for longer sequences of infinitely short δ -kicks.

pected [154] and can be attributed to the existence of fractional resonances, $T_{\text{loc}}/T_{\text{rev}} = p/q$, where quantum diffusion is accelerated. Yet despite the observed sensitivity of the control, we found that it can be successfully regained by optimizing the control parameter, i.e. the delay time ΔT , for each individual realization of the localizing train. In the bottom row (b) of Fig. 7.5 we demonstrate this sustained controllability, which supports the assumption of its coherent nature. We note that our numerical calculations of the molecular response to the localizing train of infinitely short δ -kicks (not plotted) show more stable control, which suggests that the finite experimental pulse width may also contribute to the observed sensitivity.

7.3.2 Quantum-to-classical transition

To distinguish between the quantum and classical mechanisms of the achieved control, we analyse its dependence on the effective Planck constant τ . Smaller values of τ , realized with shorter periods of the pulse train, take us closer to the classical limit (i.e. the well-known standard map [31]), at which the dynamics is less sensitive to the discreteness of the QKR spectrum. We keep the stochasticity parameter constant at $K = \tau P = 3.4$, large enough

7.4. Conclusion

to remain in the fully chaotic regime, and reduce τ while increasing the kick strength P proportionally. As demonstrated in Fig. 7.6(a), for $\tau = 1.7$, the localized states are reached after about 10 kicks. The quantum break time is longer than the one in Fig. 7.3(a) due to the lower kick strength ($P = 2$ vs. 3.8). The maximum degree of control ($25 \pm 3\%$) is established between $\Delta T_1 = 0.232 T_{\text{rev}}$ (solid green line) and $\Delta T_2 = 0.263 T_{\text{rev}}$ (dashed red line).

Figure 7.6(b) shows the result of the same experiment with $\tau = 0.6$ and $P = 5.6$. Owing to much stronger kicks, the quantum break time has become longer than the available number of pulses, such that the kicked rotor behaves classically within the observable time frame. Although the dynamics is still sensitive to ΔT , the unbounded growth of rotational energy results in the decreasing relative difference between the two cases and, therefore, diminishing degree of coherent control. The apparent energy saturation at later times is due to the finite duration of our laser pulses. It results in the suppressed excitation of rotational states with $J \gtrsim 21$, as we explained at the end of Sec. 5.3.4. Numerical simulations with a larger number of δ -kicks, shown in the inset, better illustrate the transition between the controlled localization at $\tau = 1.7$ (bottom two lines) and the uncontrolled classical diffusion at $\tau = 0.6$ (top two lines). Evidently, the latter effective Planck constant is small enough for the diffusive energy growth to persist. This behaviour is universal if the two periods are both chosen to be in the off-resonance regime.

7.4 Conclusion

In summary, we used oxygen molecules exposed to a sequence of strong laser pulses as true quantum kicked rotors. We demonstrated that despite the exponential loss of memory about the initial conditions in the classically chaotic limit, the relative phases in the initial coherent superposition of rotational states can be used to control the QKR dynamics in the absence of noise or decoherence. Adjusting a single control parameter results in the changing rotational distribution of the final localized state: its peak is shifted from a low (here, $J = 7$) to a high ($J = 11$) angular momentum. This corresponds to a relative change in the rotational energy, absorbed by the laser-kicked molecules. The coherent quantum nature of the control mechanism is evident from the demonstrated high sensitivity of the localized wave packet to the exact period of the pulse train, and the ability to regain control for any value of that parameter. Driving the system closer to the classical limit, while maintaining the same degree of stochasticity, results in

7.4. Conclusion

a gradual loss of control.

This proof-of-principle experiment in a simple chaotic system marks a first step towards the control of more complex systems.

Chapter 8

Outlook

In this thesis, we described the recent progress in the experimental studies of the quantum kicked rotor. Linear molecules, i.e. diatomic oxygen or nitrogen, served as quantum rotors and were exposed to periodic sequences of high-energy femtosecond laser pulses. The main achievements were the direct observation of *dynamical localization* and the ability to execute the methods of *coherent control* in the regime of *quantum chaos*. We analysed the dependence of the localization phenomenon on various kicking parameters, i.e. kick strength, number of pulses, pulse duration and pulse period. We studied the effect of the quantum resonances and investigated rotational Bloch oscillations and rotational Rabi oscillations. In addition, the quantum nature of the observed phenomena was tested and confirmed. We transitioned from the quantum to the classical limit in two fundamentally different ways, by introducing noise or by reducing the time period and with it, the effective Planck constant of the QKR. Upon this transition, the classically chaotic behaviour was recovered and the possibility of control was lost. A more detailed summary of each separate topic can be found in the conclusion sections of the experimental chapters 5, 6 and 7.

Most of the observations were made possible due to the development of new excitation and detection technologies, described in the chapters 3 and 4. Our work paves the way to many interesting studies. We outline some of them in the next closing pages of this thesis.

Edge states

An interesting theoretical prediction is the existence of the localized edge states [61]. The rotational quantum number of a three-dimensional rotor has an effective edge at $J = 0$ in the rotational lattice. Floss *et.al.* showed that under certain conditions, the quantum rotor can be localized at this edge, similarly to the localization of a particle near the edge of a real lattice.

According to the calculations, we can meet all the necessary requirements to observe this new effect. We did manage to see the glimpse of the edge state in O_2 but the definitive demonstration would require heavier molecules

like N_2O or CO_2 . Such demonstration is of interest because it represents a phenomenon, which is unique to three-dimensional rotors and does not exist in the AOKR.

Coherent control of quantum chaos

We studied the Gong-Brumer control scheme where the phases of the initial rotational states are used to control the dynamical localization [70, 69]. However, changing the phases of the initial states does not affect the Floquet evolution operator. This means that the average localization length, which is determined by the quasi-energy eigenstates, cannot be changed.

Other control scenarios have been studied theoretically, which do allow more drastic changes of the QKR dynamics. For example, the modified kicked rotor (MKR), where the kicking field is reversed every n kicks, can control the localization length and the shape of the localized distribution [73]. The energy absorption of the MKR can be significantly accelerated compared to the underlying classical anomalous diffusion [72]. The MKR would be easy to implement experimentally. The periodic field reversal is equivalent to a π phase shift, which can be executed by introducing an appropriate time delay between the kicks. The pulse train with a field reversal at every second kick ($n = 2$), could easily be designed with the Michelson interferometers by shifting the time delay of one arm of an interferometer. One needs to verify, however, whether the limited amount of pulses is sufficient to show the predicted effects.

Decoherence

We investigated the effect of noise on the QKR. Timing noise or amplitude noise in the periodic kicking is essentially destroying the analogy with the tight-binding model of a one-dimensional periodic lattice. Therefore, the system no longer corresponds to an Anderson model and dynamical localization gives way to classical diffusion.

Instead of introducing noise, one could couple the QKR system to the environment, which would leave the Anderson model intact. Studying the effects of true decoherence on quantum chaos could yield important insights into the quantum-classical transition and the question of controllability. A practical way to induce decoherence in the experiment is through collisions. A background gas with tunable pressure can be leaked into the vacuum chamber to create an adjustable decoherence mechanism.

Dynamical localization in three dimensions

An interesting future direction is the generalization of the QKR to higher dimensions. It was shown that using several driving fields with incommensurable frequencies is equivalent to higher dimensions of the Anderson model [32]. Each frequency corresponds to a spatial coordinate in the Anderson model. Such quasi-periodic pulse sequences have been realized in the AOKR [34, 106, 110], enabling for example the study of the metal-insulator phase transition.

Work in this direction will likely require an improvement or modification of our current pulse shaping setup. Rather than just using the technique of pulse multiplexing via Michelson interferometers, it might be beneficial to combine several pulse shapers to create the required multiple frequencies.

Multi-pulse excitation schemes

Our unique setup could be used to explore other multi-pulse excitation schemes, following goals that are not related to dynamical localization.

For instance, one can use long pulse sequences to improve the degree of molecular alignment. One could follow the proposal of Averbukh [12] or, as mentioned in Sec. 5.5, adjust the train period from kick to kick. It would be best to try these optimization schemes in heavier molecules where the bandwidth limit is of no concern.

More interesting is the alignment or orientation of larger and asymmetric molecules. In a recent work, three pulses have been used for the three-dimensional alignment of asymmetric top molecules [139]. It has been shown that the alignment factor will get better with an increasing number of kicks.

Improvement of the setup

Apart from different research directions, the experimental setup can be improved in several ways. For instance, by reaching colder temperatures with the goal of starting the excitation from a single rotational state, or by adapting the developed techniques to a laser system with shorter pulses. Numerically, the calculations should be refined by including the laser bandwidth to get better comparison with the experimental data.

Bibliography

- [1] R. Abou-Chacra, D. J. Thouless, and P. W. Anderson. A self-consistent theory of localization. *Journal of Physics C: Solid State Physics*, 6(10):1734, 1973.
- [2] E. Abrahams, P. W. Anderson, D. C. Licciardello, and T. V. Ramakrishnan. Scaling theory of localization: Absence of quantum diffusion in two dimensions. *Physical Review Letters*, 42(10):673–676, 1979.
- [3] D. G. Abrashkevich, M. Shapiro, and P. Brumer. Coherent control of the $\text{CH}_2\text{Br}+\text{I} \leftarrow \text{CH}_2\text{BrI} \rightarrow \text{CH}_2\text{I}+\text{Br}$ branching photodissociation reaction. *The Journal of Chemical Physics*, 116(13):5584–5592, 2002.
- [4] H. Ammann, R. Gray, I. Shvarchuck, and N. Christensen. Quantum delta-kicked rotor: Experimental observation of decoherence. *Physical Review Letters*, 80(19):4111–4115, 1998.
- [5] J. B. Anderson. *Molecular Beam and low density gas dynamics*. Decker, New York, 1974.
- [6] P. W. Anderson. Absence of diffusion in certain random lattices. *Physical Review*, 109(5):1492–1505, 1958.
- [7] P. W. Anderson. Local moments and localized states. *Reviews of Modern Physics*, 50(2):191–201, 1978.
- [8] C. Asawaroengchai and G. M. Rosenblatt. Rotational Raman intensities and the measured change with internuclear distance of the polarizability anisotropy of H_2 , D_2 , N_2 , O_2 , and CO . *The Journal of Chemical Physics*, 72(4):2664–2669, 1980.
- [9] N. W. Ashcroft and N. D. Mermin. *Solid State Physics*. Holt, Rinehart and Winston, New York, 1976.
- [10] A. Aspect and M. Inguscio. Anderson localization of ultracold atoms. *Physics Today*, 62(8):30–35, 2009.

- [11] A. Assion, T. Baumert, M. Bergt, T. Brixner, B. Kiefer, V. Seyfried, M. Strehle, and G. Gerber. Control of chemical reactions by feedback-optimized phase-shaped femtosecond laser pulses. *Science*, 282(5390):919–922, 1998.
- [12] I. S. Averbukh and R. Arvieu. Angular focusing, squeezing, and rainbow formation in a strongly driven quantum rotor. *Physical Review Letters*, 87(16):163601, 2001.
- [13] I. S. Averbukh and N. F. Perelman. Fractional revivals: Universality in the long-term evolution of quantum wave packets beyond the correspondence principle dynamics. *Physics Letters A*, 139(9):449–453, 1989.
- [14] S. Baker, I. A. Walmsley, J. W. G. Tisch, and J. P. Marangos. Femtosecond to attosecond light pulses from a molecular modulator. *Nature Photonics*, 5(11):664–671, 2011.
- [15] R. A. Bartels, T. C. Weinacht, N. Wagner, M. Baertschy, C. H. Greene, M. M. Murnane, and H. C. Kapteyn. Phase modulation of ultrashort light pulses using molecular rotational wave packets. *Physical Review Letters*, 88(1):013903, 2001.
- [16] J. E. Bayfield, G. Casati, I. Guarneri, and D. W. Sokol. Localization of classically chaotic diffusion for hydrogen atoms in microwave fields. *Physical Review Letters*, 63(4):364–367, 1989.
- [17] M. Ben Dahan, E. Peik, J. Reichel, Y. Castin, and C. Salomon. Bloch oscillations of atoms in an optical potential. *Physical Review Letters*, 76(24):4508–4511, 1996.
- [18] J. Billy, V. Josse, Z. Zuo, A. Bernard, B. Hambrecht, P. Lugan, D. Clément, L. Sanchez-Palencia, P. Bouyer, and A. Aspect. Direct observation of Anderson localization of matter waves in a controlled disorder. *Nature*, 453(7197):891–894, 2008.
- [19] C. Z. Bisgaard, M. D. Poulsen, E. Peronne, S. S. Viftrup, and H. Stapelfeldt. Observation of enhanced field-free molecular alignment by two laser pulses. *Physical Review Letters*, 92(17):173004, 2004.
- [20] M. Bitter and V. Milner. Control of quantum localization and classical diffusion in laser-kicked molecular rotors. *arXiv:1610.04193*, 2016.

Bibliography

- [21] M. Bitter and V. Milner. Experimental demonstration of coherent control in quantum chaotic systems. *arXiv:1606.06805*, 2016.
- [22] M. Bitter and V. Milner. Experimental observation of dynamical localization in laser-kicked molecular rotors. *Physical Review Letters*, 117(14):144104, 2016.
- [23] M. Bitter and V. Milner. Generating long sequences of high-intensity femtosecond pulses. *Applied Optics*, 55(4):830–833, 2016.
- [24] M. Bitter and V. Milner. Rotational excitation of molecules with long sequences of intense femtosecond pulses. *Physical Review A*, 93(1):013420, 2016.
- [25] F. Bloch. Über die Quantenmechanik der Elektronen in Kristallgittern. *Zeitschrift für Physik*, 52(7):555–600, 1929.
- [26] N. Bloembergen, K.-H. Chen, C.-Z. L, and E. Mazur. Multiplex pure rotational coherent anti-stokes Raman spectroscopy in a molecular beam. *Journal of Raman Spectroscopy*, 21(12):819–825, 1990.
- [27] R. Blümel, A. Buchleitner, R. Graham, L. Sirko, U. Smilansky, and H. Walther. Dynamical localization in the microwave interaction of rydberg atoms: The influence of noise. *Physical Review A*, 44(7):4521–4540, 1991.
- [28] R. Blümel, S. Fishman, and U. Smilansky. Excitation of molecular rotation by periodic microwave pulses. a testing ground for Anderson localization. *The Journal of Chemical Physics*, 84(5):2604–2614, 1986.
- [29] R. W. Boyd. *Nonlinear Optics*. Academic Press, Boston, 2nd edition, 1992.
- [30] J. Cao, C. J. Bardeen, and K. R. Wilson. Molecular “ π pulse” for total inversion of electronic state population. *Physical Review Letters*, 80(7):1406–1409, 1998.
- [31] G. Casati, B. Chirikov, F. Izraelev, and J. Ford, editors. *Stochastic Behavior in Classical and Quantum Hamiltonian Systems, Lecture Notes in Physics*, volume 93. Springer, Berlin, 1979.
- [32] G. Casati, I. Guarneri, and D. L. Shepelyansky. Anderson transition in a one-dimensional system with three incommensurate frequencies. *Physical Review Letters*, 62(4):345–348, 1989.

- [33] A. A. Chabanov, M. Stoytchev, and A. Z. Genack. Statistical signatures of photon localization. *Nature*, 404(6780):850–853, 2000.
- [34] J. Chabé, G. Lemarié, B. Grémaud, D. Delande, P. Szriftgiser, and J. C. Garreau. Experimental observation of the Anderson metal-insulator transition with atomic matter waves. *Physical Review Letters*, 101(25):255702, 2008.
- [35] B. Chirikov. Research concerning the theory of nonlinear resonance and stochasticity. *Preprint N 267, Institute of Nuclear Physics, Novosibirsk*, (Engl. Trans., CERN Trans. 71-40 (1971)), 1969.
- [36] B. V. Chirikov. A universal instability of many-dimensional oscillator systems. *Physics Reports*, 52(5):263–379, 1979.
- [37] D. N. Christodoulides, F. Lederer, and Y. Silberberg. Discretizing light behaviour in linear and nonlinear waveguide lattices. *Nature*, 424(6950):817–823, 2003.
- [38] D. Clément, A. F. Varón, M. Hugbart, J. A. Retter, P. Bouyer, L. Sanchez-Palencia, D. M. Gangardt, G. V. Shlyapnikov, and A. Aspect. Suppression of transport of an interacting elongated Bose-Einstein condensate in a random potential. *Physical Review Letters*, 95(17):170409, 2005.
- [39] D. Clément, A. F. Varon, J. A. Retter, L. Sanchez-Palencia, A. Aspect, and P. Bouyer. Experimental study of the transport of coherent interacting matter-waves in a 1d random potential induced by laser speckle. *New Journal of Physics*, 8(8):165, 2006.
- [40] D. Cohen. Quantum chaos, dynamical correlations, and the effect of noise on localization. *Physical Review A*, 44(4):2292–2313, 1991.
- [41] J. P. Cryan, P. H. Bucksbaum, and R. N. Coffee. Field-free alignment in repetitively kicked nitrogen gas. *Physical Review A*, 80(6):063412, 2009.
- [42] R. Dalichaouch, J. P. Armstrong, S. Schultz, P. M. Platzman, and S. L. McCall. Microwave localization by two-dimensional random scattering. *Nature*, 354(6348):53–55, 1991.
- [43] M. B. d’Arcy, R. M. Godun, M. K. Oberthaler, D. Cassettari, and G. S. Summy. Quantum enhancement of momentum diffusion in the delta-kicked rotor. *Physical Review Letters*, 87(7):074102, 2001.

- [44] W. Demtröder. *Laser Spectroscopy Vol. 1*. Springer, 4th edition, 2008.
- [45] P. W. Dooley, I. V. Litvinyuk, K. F. Lee, D. M. Rayner, M. Spanner, D. M. Villeneuve, and P. B. Corkum. Direct imaging of rotational wave-packet dynamics of diatomic molecules. *Physical Review A*, 68(2):023406, 2003.
- [46] N. Dudovich, D. Oron, and Y. Silberberg. Single-pulse coherently controlled nonlinear Raman spectroscopy and microscopy. *Nature*, 418(6897):512–514, 2002.
- [47] M. A. Dugan, J. X. Tull, and W. S. Warren. High-resolution acousto-optic shaping of unamplified and amplified femtosecond laser pulses. *Journal of the Optical Society of America B*, 14(9):2348–2358, 1997.
- [48] A. Efimov, M. D. Moores, N. M. Beach, J. L. Krause, and D. H. Reitze. Adaptive control of pulse phase in a chirped-pulse amplifier. *Optics Letters*, 23(24):1915–1917, 1998.
- [49] A. Efimov and D. H. Reitze. Programmable dispersion compensation and pulse shaping in a 26-fs chirped-pulse amplifier. *Optics Letters*, 23(20):1612–1614, 1998.
- [50] L. Fallani, J. E. Lye, V. Guarrera, C. Fort, and M. Inguscio. Ultracold atoms in a disordered crystal of light: Towards a Bose glass. *Physical Review Letters*, 98(13):130404, 2007.
- [51] J. Feldmann, K. Leo, J. Shah, D. A. B. Miller, J. E. Cunningham, T. Meier, G. von Plessen, A. Schulze, P. Thomas, and S. Schmitt-Rink. Optical investigation of Bloch oscillations in a semiconductor superlattice. *Physical Review B*, 46(11):7252–7255, 1992.
- [52] S. Fishman, D. R. Grempel, and R. E. Prange. Chaos, quantum recurrences, and Anderson localization. *Physical Review Letters*, 49(8):509–512, 1982.
- [53] S. Fishman, D. R. Grempel, and R. E. Prange. Temporal crossover from classical to quantal behavior near dynamical critical points. *Physical Review A*, 36(1):289–305, 1987.
- [54] S. Fleischer, I. S. Averbukh, and Y. Prior. Isotope-selective laser molecular alignment. *Physical Review A*, 74(4):041403, 2006.

- [55] S. Fleischer, I. S. Averbukh, and Y. Prior. Selective alignment of molecular spin isomers. *Physical Review Letters*, 99(9):093002, 2007.
- [56] S. Fleischer, Y. Khodorkovsky, E. Gershnel, Y. Prior, and I. S. Averbukh. Molecular alignment induced by ultrashort laser pulses and its impact on molecular motion. *Israel Journal of Chemistry*, 52(5):414–437, 2012.
- [57] S. Fleischer, Y. Khodorkovsky, Y. Prior, and I. S. Averbukh. Controlling the sense of molecular rotation. *New Journal of Physics*, 11(10):105039, 2009.
- [58] G. Floquet. Sur les équations différentielles linéaires à coefficients périodiques. *Annales scientifiques de l'École Normale Supérieure*, 12:47–88, 1883.
- [59] J. Floß and I. S. Averbukh. Quantum resonance, Anderson localization, and selective manipulations in molecular mixtures by ultrashort laser pulses. *Physical Review A*, 86(2):021401, 2012.
- [60] J. Floß and I. S. Averbukh. Anderson wall and Bloch oscillations in molecular rotation. *Physical Review Letters*, 113(4):043002, 2014.
- [61] J. Floß and I. S. Averbukh. Edge states of periodically kicked quantum rotors. *Physical Review E*, 91(5):052911, 2015.
- [62] J. Floß and I. S. Averbukh. Exciting molecules close to the rotational quantum resonance: Anderson wall and rotational Bloch oscillations. *The Journal of Physical Chemistry A*, 120(19):3206–3217, 2016.
- [63] J. Floß, S. Fishman, and I. S. Averbukh. Anderson localization in laser-kicked molecules. *Physical Review A*, 88(2):023426, 2013.
- [64] J. Floß, A. Kamalov, I. S. Averbukh, and P. H. Bucksbaum. Observation of Bloch oscillations in molecular rotation. *Physical Review Letters*, 115(20):203002, 2015.
- [65] M. T. Frey, F. B. Dunning, C. O. Reinhold, S. Yoshida, and J. Burgdörfer. Realization of the kicked atom. *Physical Review A*, 59(2):1434–1443, 1999.
- [66] B. Friedrich and D. Herschbach. Alignment and trapping of molecules in intense laser fields. *Physical Review Letters*, 74(23):4623–4626, 1995.

- [67] E. J. Galvez, B. E. Sauer, L. Moorman, P. M. Koch, and D. Richards. Microwave ionization of H atoms: Breakdown of classical dynamics for high frequencies. *Physical Review Letters*, 61(18):2011–2014, 1988.
- [68] A. Z. Genack and N. Garcia. Observation of photon localization in a three-dimensional disordered system. *Physical Review Letters*, 66(16):2064–2067, 1991.
- [69] J. Gong and P. Brumer. Coherent control of quantum chaotic diffusion. *Physical Review Letters*, 86(9):1741–1744, 2001.
- [70] J. Gong and P. Brumer. Coherent control of quantum chaotic diffusion: Diatomic molecules in a pulsed microwave field. *The Journal of Chemical Physics*, 115(8):3590–3597, 2001.
- [71] J. Gong and P. Brumer. Quantum chaos meets coherent control. *Annual Review of Physical Chemistry*, 56(1):1–23, 2005.
- [72] J. Gong, H. J. Woerner, and P. Brumer. Coherent manipulation of quantum δ -kicked dynamics: Faster-than-classical anomalous diffusion. *Physical Review E*, 68(2):026209, 2003.
- [73] J. Gong, H. J. Woerner, and P. Brumer. Control of dynamical localization. *Physical Review E*, 68(5):056202, 2003.
- [74] R. Graham, M. Schlautmann, and P. Zoller. Dynamical localization of atomic-beam deflection by a modulated standing light wave. *Physical Review A*, 45(1):R19–R22, 1992.
- [75] J. M. Greene. A method for determining a stochastic transition. *Journal of Mathematical Physics*, 20(6):1183–1201, 1979.
- [76] D. R. Grempel, R. E. Prange, and S. Fishman. Quantum dynamics of a nonintegrable system. *Physical Review A*, 29(4):1639–1647, 1984.
- [77] F. Haake. *Quantum Signatures of Chaos*. Springer, 3rd edition, 2010.
- [78] P. Hänggi. Driven quantum systems. In *Quantum Transport and Dissipation*. Wiley-vch, 1998.
- [79] G. Herzberg. *Molecular Spectra and Molecular Structure*, volume I. Spectra of Diatomic Molecules. D. Van Nostrand Company, Inc., 1950.

- [80] H. Hu, A. Strybulevych, J. H. Page, S. E. Skipetrov, and B. A. van Tiggelen. Localization of ultrasound in a three-dimensional elastic network. *Nature Physics*, 4(12):945–948, 2008.
- [81] K. Huber and G. Herzberg. *NIST Chemistry WebBook, NIST Standard Reference Database*, volume 69 of *Constants of Diatomic Molecules*. National Institute of Standards and Technology, Gaithersburg MD, 2012.
- [82] J. Itatani, D. Zeidler, J. Levesque, M. Spanner, D. M. Villeneuve, and P. B. Corkum. Controlling high harmonic generation with molecular wave packets. *Physical Review Letters*, 94(12):123902, 2005.
- [83] F. M. Izrailev. Simple models of quantum chaos: Spectrum and eigenfunctions. *Physics Reports*, 196(56):299–392, 1990.
- [84] F. M. Izrailev and D. L. Shepelyanskii. Quantum resonance for a rotator in a nonlinear periodic field. *Theoretical and Mathematical Physics*, 43(3):553–561, 1980.
- [85] F. Jendrzejewski, A. Bernard, K. Müller, P. Cheinet, V. Josse, M. Piraud, L. Pezzé, L. Sanchez-Palencia, A. Aspect, and P. Bouyer. Three-dimensional localization of ultracold atoms in an optical disordered potential. *Nature Physics*, 8(5):398–403, 2012.
- [86] S. John. Electromagnetic absorption in a disordered medium near a photon mobility edge. *Physical Review Letters*, 53(22):2169–2172, 1984.
- [87] R. S. Judson and H. Rabitz. Teaching lasers to control molecules. *Physical Review Letters*, 68(10):1500–1503, 1992.
- [88] A. Kamalov, D. W. Broege, and P. H. Bucksbaum. Dynamical localization in molecular alignment of kicked quantum rotors. *Physical Review A*, 92(1):013409, 2015.
- [89] J. Karczmarek, J. Wright, P. Corkum, and M. Ivanov. Optical centrifuge for molecules. *Physical Review Letters*, 82(17):3420–3423, 1999.
- [90] K. Kitano, H. Hasegawa, and Y. Ohshima. Ultrafast angular momentum orientation by linearly polarized laser fields. *Physical Review Letters*, 103(22):223002, 2009.

Bibliography

- [91] C. Kittel. *Introduction to solid state physics*. John Wiley & Sons, Hoboken, NJ, 2005.
- [92] B. G. Klappauf, W. H. Oskay, D. A. Steck, and M. G. Raizen. Observation of noise and dissipation effects on dynamical localization. *Physical Review Letters*, 81(6):1203–1206, 1998.
- [93] A. R. Kolovsky and H. J. Korsch. Bloch oscillations of cold atoms in optical lattices. *International Journal of Modern Physics B*, 18(09):1235–1260, 2004.
- [94] S. S. Kondov, W. R. McGehee, J. J. Zirbel, and B. DeMarco. Three-dimensional Anderson localization of ultracold matter. *Science*, 334(6052):66–68, 2011.
- [95] O. Korech, U. Steinitz, R. J. Gordon, I. S. Averbukh, and Y. Prior. Observing molecular spinning via the rotational doppler effect. *Nature Photonics*, 7(9):711–714, 2013.
- [96] A. Korobenko, A. A. Milner, and V. Milner. Direct observation, study, and control of molecular superrotors. *Physical Review Letters*, 112(11):113004, 2014.
- [97] B. Kramer and A. MacKinnon. Localization: theory and experiment. *Reports on Progress in Physics*, 56(12):1469, 1993.
- [98] A. Lagendijk, B. v. Tiggelen, and D. S. Wiersma. Fifty years of Anderson localization. *Physics Today*, 62(8):24–29, 2009.
- [99] Y. Lahini, A. Avidan, F. Pozzi, M. Sorel, R. Morandotti, D. N. Christodoulides, and Y. Silberberg. Anderson localization and nonlinearity in one-dimensional disordered photonic lattices. *Physical Review Letters*, 100(1):013906, 2008.
- [100] D. E. Leaird and A. M. Weiner. Femtosecond optical packet generation by a direct space-to-time pulse shaper. *Optics Letters*, 24(12):853–855, 1999.
- [101] K. F. Lee, I. V. Litvinyuk, P. W. Dooley, M. Spanner, D. M. Villeneuve, and P. B. Corkum. Two-pulse alignment of molecules. *Journal of Physics B: Atomic, Molecular and Optical Physics*, 37(3):L43, 2004.

- [102] K. F. Lee, D. M. Villeneuve, P. B. Corkum, A. Stolow, and J. G. Underwood. Field-free three-dimensional alignment of polyatomic molecules. *Physical Review Letters*, 97(17):173001, 2006.
- [103] M. Leibscher, I. S. Averbukh, and H. Rabitz. Molecular alignment by trains of short laser pulses. *Physical Review Letters*, 90(21):213001, 2003.
- [104] M. Leibscher, I. S. Averbukh, and H. Rabitz. Enhanced molecular alignment by short laser pulses. *Physical Review A*, 69(1):013402, 2004.
- [105] C. Leichtle, I. S. Averbukh, and W. P. Schleich. Generic structure of multilevel quantum beats. *Physical Review Letters*, 77(19):3999–4002, 1996.
- [106] G. Lemarié, H. Lignier, D. Delande, P. Szriftgiser, and J. C. Garreau. Critical state of the Anderson transition: Between a metal and an insulator. *Physical Review Letters*, 105(9):090601, 2010.
- [107] S. Linden, H. Giessen, and J. Kuhl. XFROG - a new method for amplitude and phase characterization of weak ultrashort pulses. *physica status solidi (b)*, 206(1):119–124, 1998.
- [108] I. V. Litvinyuk, K. F. Lee, P. W. Dooley, D. M. Rayner, D. M. Villeneuve, and P. B. Corkum. Alignment-dependent strong field ionization of molecules. *Physical Review Letters*, 90(23):233003, 2003.
- [109] X. Liu, R. Wagner, A. Maksimchuk, E. Goodman, J. Workman, D. Umstadter, and A. Migus. Nonlinear temporal diffraction and frequency shifts resulting from pulse shaping in chirped-pulse amplification systems. *Optics Letters*, 20(10):1163–1165, 1995.
- [110] M. Lopez, J.-F. Clément, P. Szriftgiser, J. C. Garreau, and D. Delande. Experimental test of universality of the Anderson transition. *Physical Review Letters*, 108(9):095701, 2012.
- [111] V. V. Lozovoy, I. Pastirk, and M. Dantus. Multiphoton intrapulse interference.iv.ultrashort laser pulse spectral phase characterization and compensation. *Optics Letters*, 29(7):775–777, 2004.
- [112] S. Mackenzie. Lecture notes: Section 6 Raman scattering.

- [113] V. S. Malinovsky and J. L. Krause. Efficiency and robustness of coherent population transfer with intense, chirped laser pulses. *Physical Review A*, 63(4):043415, 2001.
- [114] L. Matsuoka. Unified parameter for localization in isotope-selective rotational excitation of diatomic molecules using a train of optical pulses. *Physical Review A*, 91(4):043420, 2015.
- [115] D. R. Miller. *Atomic and Molecular Beam Methods*. Oxford University Press, New York, 1988.
- [116] J. D. Miller, S. Roy, J. R. Gord, and T. R. Meyer. Communication: Time-domain measurement of high-pressure N₂ and O₂ self-broadened linewidths using hybrid femtosecond/picosecond coherent anti-Stokes Raman scattering. *The Journal of Chemical Physics*, 135(20):201104, 2011.
- [117] A. A. Milner, A. Korobenko, J. W. Hepburn, and V. Milner. Effects of ultrafast molecular rotation on collisional decoherence. *Physical Review Letters*, 113(4):043005, 2014.
- [118] V. Milner and J. W. Hepburn. Control of molecular rotation in the limit of extreme rotational excitation. *submitted*, arXiv:1501.02739, 2015.
- [119] V. Milner, D. A. Steck, W. H. Oskay, and M. G. Raizen. Recovery of classically chaotic behavior in a noise-driven quantum system. *Physical Review E*, 61(6):7223–7226, 2000.
- [120] P. W. Milonni and J. H. Eberly. *Laser Physics*. John Wiley and Sons, Inc., 2010.
- [121] F. L. Moore, J. C. Robinson, C. F. Bharucha, B. Sundaram, and M. G. Raizen. Atom optics realization of the quantum δ -kicked rotor. *Physical Review Letters*, 75(25):4598–4601, 1995.
- [122] R. Morandotti, U. Peschel, J. S. Aitchison, H. S. Eisenberg, and Y. Silberberg. Experimental observation of linear and nonlinear optical Bloch oscillations. *Physical Review Letters*, 83(23):4756–4759, 1999.
- [123] O. Morsch, J. H. Müller, M. Cristiani, D. Ciampini, and E. Arimondo. Bloch oscillations and mean-field effects of Bose-Einstein condensates in 1d optical lattices. *Physical Review Letters*, 87(14):140402, 2001.

- [124] A. Nazarkin, G. Korn, M. Wittmann, and T. Elsaesser. Generation of multiple phase-locked Stokes and anti-Stokes components in an impulsively excited Raman medium. *Physical Review Letters*, 83(13):2560–2563, 1999.
- [125] E. T. J. Nibbering, G. Grillon, M. A. Franco, B. S. Prade, and A. Mysyrowicz. Determination of the inertial contribution to the nonlinear refractive index of air, N₂, and O₂ by use of unfocused high-intensity femtosecond laser pulses. *Journal of the Optical Society of America B*, 14(3):650–660, 1997.
- [126] Y. Ohshima and H. Hasegawa. Coherent rotational excitation by intense nonresonant laser fields. *International Reviews in Physical Chemistry*, 29(4):619–663, 2010.
- [127] W. H. Oskay, D. A. Steck, and M. G. Raizen. Timing noise effects on dynamical localization. *Chaos, Solitons & Fractals*, 16(3):409–416, 2003.
- [128] J. P. Palastro, T. M. Antonsen, and H. M. Milchberg. Compression, spectral broadening, and collimation in multiple, femtosecond pulse filamentation in atmosphere. *Physical Review A*, 86(3):033834, 2012.
- [129] J. P. Palastro, T. M. Antonsen, S. Varma, Y. H. Chen, and H. M. Milchberg. Simulations of femtosecond atmospheric filaments enhanced by dual pulse molecular alignment. *Physical Review A*, 85(4):043843, 2012.
- [130] M. Pasienski, D. McKay, M. White, and B. DeMarco. A disordered insulator in an optical lattice. *Nature Physics*, 6(9):677–680, 2010.
- [131] I. Pastirk, B. Resan, A. Fry, J. MacKay, and M. Dantus. No loss spectral phase correction and arbitrary phase shaping of regeneratively amplified femtosecond pulses using miips. *Optics Express*, 14(20):9537–9543, 2006.
- [132] A. Pe’er, E. A. Shapiro, M. C. Stowe, M. Shapiro, and J. Ye. Precise control of molecular dynamics with a femtosecond frequency comb. *Physical Review Letters*, 98(11):113004, 2007.
- [133] T. Pertsch, P. Dannberg, W. Elflein, A. Bräuer, and F. Lederer. Optical Bloch oscillations in temperature tuned waveguide arrays. *Physical Review Letters*, 83(23):4752–4755, 1999.

- [134] D. Pestov, V. V. Lozovoy, and M. Dantus. Multiple independent comb shaping (MICS): Phase-only generation of optical pulse sequences. *Optics Express*, 17(16):14351–14361, 2009.
- [135] M. G. Raizen. Quantum chaos with cold atoms. In B. Benjamin and W. Herbert, editors, *Advances In Atomic, Molecular, and Optical Physics*, volume Volume 41, pages 43–81. Academic Press, 1999.
- [136] M. G. Raizen and D. A. Steck. Cold atom experiments in quantum chaos. *Scholarpedia*, 6:10468, 2011.
- [137] A. Ramos, B. Maté, G. Tejada, J. M. Fernández, and S. Montero. Raman spectroscopy of hypersonic shock waves. *Physical Review E*, 62(4):4940–4945, 2000.
- [138] L. E. Reichl. *The Transition to Chaos: Conservative Classical Systems and Quantum Manifestations*. Springer New York, 2nd edition, 2004.
- [139] X. Ren, V. Makhija, and V. Kumarappan. Multipulse three-dimensional alignment of asymmetric top molecules. *Physical Review Letters*, 112(17):173602, 2014.
- [140] M. Renard, R. Chaux, B. Lavorel, and O. Faucher. Pulse trains produced by phase-modulation of ultrashort optical pulses: tailoring and characterization. *Optics Express*, 12(3):473–482, 2004.
- [141] V. Renard, M. Renard, S. Gurin, Y. T. Pashayan, B. Lavorel, O. Faucher, and H. R. Jauslin. Postpulse molecular alignment measured by a weak field polarization technique. *Physical Review Letters*, 90(15):153601, 2003.
- [142] S. A. Rice. Active control of molecular dynamics: Coherence versus chaos. *Journal of Statistical Physics*, 101(1):187–212, 2000.
- [143] G. Roati, C. D’Errico, L. Fallani, M. Fattori, C. Fort, M. Zaccanti, G. Modugno, M. Modugno, and M. Inguscio. Anderson localization of a non-interacting Bose-Einstein condensate. *Nature*, 453(7197):895–898, 2008.
- [144] F. Rosca-Pruna and M. J. J. Vrakking. Experimental observation of revival structures in picosecond laser-induced alignment of I_2 . *Physical Review Letters*, 87(15):153902, 2001.

- [145] C. Ryu, M. F. Andersen, A. Vaziri, M. B. d'Arcy, J. M. Grossman, K. Helmerson, and W. D. Phillips. High-order quantum resonances observed in a periodically kicked Bose-Einstein Condensate. *Physical Review Letters*, 96(16):160403, 2006.
- [146] M. Sadgrove, S. Wimberger, S. Parkins, and R. Leonhardt. Ballistic and localized transport for the atom optics kicked rotor in the limit of a vanishing kicking period. *Physical Review Letters*, 94(17):174103, 2005.
- [147] J. J. Sakurai. *Modern Quantum Mechanics*. Addison-Wesley Publishing Company, Inc., 1994.
- [148] R. Sapienza, P. Costantino, D. Wiersma, M. Ghulinyan, C. J. Oton, and L. Pavesi. Optical analogue of electronic Bloch oscillations. *Physical Review Letters*, 91(26):263902, 2003.
- [149] M. Schreiber, S. S. Hodgman, P. Bordia, H. P. Lüschen, M. H. Fischer, R. Vosk, E. Altman, U. Schneider, and I. Bloch. Observation of many-body localization of interacting fermions in a quasirandom optical lattice. *Science*, 349(6250):842–845, 2015.
- [150] T. Schwartz, G. Bartal, S. Fishman, and M. Segev. Transport and Anderson localization in disordered two-dimensional photonic lattices. *Nature*, 446(7131):52–55, 2007.
- [151] T. Seideman. Revival structure of aligned rotational wave packets. *Physical Review Letters*, 83(24):4971–4974, 1999.
- [152] T. Seideman, E. Hamilton, P. R. Berman, and C. C. Lin. Nonadiabatic alignment by intense pulses. concepts, theory, and directions. In *Advances In Atomic, Molecular, and Optical Physics*, volume 52, pages 289–329. Academic Press, 2005.
- [153] G. Semeghini, M. Landini, P. Castilho, S. Roy, G. Spagnolli, A. Trenkwalder, M. Fattori, M. Inguscio, and G. Modugno. Measurement of the mobility edge for 3D Anderson localization. *Nature Physics*, 11(7):554–559, 2015.
- [154] E. A. Shapiro, V. Milner, C. Menzel-Jones, and M. Shapiro. Piecewise adiabatic passage with a series of femtosecond pulses. *Physical Review Letters*, 99(3):033002, 2007.

- [155] E. A. Shapiro, V. Milner, and M. Shapiro. Complete transfer of populations from a single state to a preselected superposition of states using piecewise adiabatic passage: Theory. *Physical Review A*, 79(2):023422, 2009.
- [156] E. A. Shapiro, A. Pe'er, J. Ye, and M. Shapiro. Piecewise adiabatic population transfer in a molecule via a wave packet. *Physical Review Letters*, 101(2):023601, 2008.
- [157] M. Shapiro and P. Brumer. *Quantum Control of Molecular Processes*. Wiley, Weinheim, Germany, 2012.
- [158] M. Shapiro, P. Brumer, B. Benjamin, and W. Herbert. Coherent control of atomic, molecular, and electronic processes. In *Advances In Atomic, Molecular, and Optical Physics*, volume 42, pages 287–345. Academic Press, 2000.
- [159] B. W. Shore, K. Bergmann, J. Oreg, and S. Rosenwaks. Multilevel adiabatic population transfer. *Physical Review A*, 44(11):7442–7447, 1991.
- [160] C. W. Siders, J. L. W. Siders, A. J. Taylor, S.-G. Park, and A. M. Weiner. Efficient high-energy pulse-train generation using a 2n-pulse Michelson interferometer. *Applied Optics*, 37(22):5302–5305, 1998.
- [161] S. H. Simon. Lecture notes for solid state physics, 2012.
- [162] J. Singleton. *Band theory and electronic properties of solids*. Oxford University Press, 2001.
- [163] A. V. Sokolov and S. E. Harris. Ultrashort pulse generation by molecular modulation. *Journal of Optics B: Quantum and Semiclassical Optics*, 5(1):R1, 2003.
- [164] H. Stapelfeldt and T. Seideman. Colloquium: Aligning molecules with strong laser pulses. *Reviews of Modern Physics*, 75(2):543–557, 2003.
- [165] M. Störzer, P. Gross, C. M. Aegerter, and G. Maret. Observation of the critical regime near Anderson localization of light. *Physical Review Letters*, 96(6):063904, 2006.
- [166] D. Sugny, A. Keller, O. Atabek, D. Daems, C. M. Dion, S. Gurin, and H. R. Jauslin. Control of mixed-state quantum systems by a train of short pulses. *Physical Review A*, 72(3):032704, 2005.

- [167] G. Tejada, B. Maté, J. M. Fernández-Sánchez, and S. Montero. Temperature and density mapping of supersonic jet expansions using linear Raman spectroscopy. *Physical Review Letters*, 76(1):34–37, 1996.
- [168] C. Trallero-Herrero, J. L. Cohen, and T. Weinacht. Strong-field atomic phase matching. *Physical Review Letters*, 96(6):063603, 2006.
- [169] R. Trebino. *Frequency-Resolved Optical Gating: The Measurement of Ultrashort Laser Pulses*. Springer, 1 edition, 2000.
- [170] H. Trompeter, W. Krolikowski, D. N. Neshev, A. S. Desyatnikov, A. A. Sukhorukov, Y. S. Kivshar, T. Pertsch, U. Peschel, and F. Lederer. Bloch oscillations and Zener tunneling in two-dimensional photonic lattices. *Physical Review Letters*, 96(5):053903, 2006.
- [171] T. Udem, R. Holzwarth, and T. W. Hansch. Optical frequency metrology. *Nature*, 416(6877):233–237, 2002.
- [172] D. Umstadter, E. Esarey, and J. Kim. Nonlinear plasma waves resonantly driven by optimized laser pulse trains. *Physical Review Letters*, 72(8):1224–1227, 1994.
- [173] S. Varma, Y. H. Chen, and H. M. Milchberg. Trapping and destruction of long-range high-intensity optical filaments by molecular quantum wakes in air. *Physical Review Letters*, 101(20):205001, 2008.
- [174] R. Velotta, N. Hay, M. B. Mason, M. Castillejo, and J. P. Marangos. High-order harmonic generation in aligned molecules. *Physical Review Letters*, 87(18):183901, 2001.
- [175] D. M. Villeneuve, S. A. Aseyev, P. Dietrich, M. Spanner, M. Y. Ivanov, and P. B. Corkum. Forced molecular rotation in an optical centrifuge. *Physical Review Letters*, 85(3):542–545, 2000.
- [176] N. V. Vitanov, T. Halfmann, B. W. Shore, and K. Bergmann. Laser-induced population transfer by adiabatic passage techniques. *Annual Review of Physical Chemistry*, 52(1):763–809, 2001.
- [177] J. Voll and R. d. Vivie-Riedle. Pulse trains in molecular dynamics and coherent spectroscopy: a theoretical study. *New Journal of Physics*, 11(10):105036, 2009.
- [178] R. L. Weaver. Anderson localization of ultrasound. *Wave Motion*, 12(2):129–142, 1990.

Bibliography

- [179] M. M. Wefers and K. A. Nelson. Programmable phase and amplitude femtosecond pulse shaping. *Optics Letters*, 18(23):2032–2034, 1993.
- [180] A. M. Weiner. Femtosecond pulse shaping using spatial light modulators. *Review of Scientific Instruments*, 71(5):1929–1960, 2000.
- [181] A. M. Weiner and D. E. Leaird. Generation of terahertz-rate trains of femtosecond pulses by phase-only filtering. *Optics Letters*, 15(1):51–53, 1990.
- [182] A. M. Weiner, S. Oudin, D. H. Reitze, and D. E. Leaird. Shaping of femtosecond pulses using phase-only filters designed by simulated annealing. *Journal of the Optical Society of America A*, 10(5):1112–1120, 1993.
- [183] D. S. Wiersma, P. Bartolini, A. Lagendijk, and R. Righini. Localization of light in a disordered medium. *Nature*, 390(6661):671–673, 1997.
- [184] S. Wimberger, I. Guarneri, and S. Fishman. Quantum resonances and decoherence for δ -kicked atoms. *Nonlinearity*, 16(4):1381, 2003.
- [185] S. Wimberger, I. Guarneri, and S. Fishman. Classical scaling theory of quantum resonances. *Physical Review Letters*, 92(8):084102, 2004.
- [186] M. Wollenhaupt, A. Präkelt, C. Sarpe-Tudoran, D. Liese, T. Bayer, and T. Baumert. Femtosecond strong-field quantum control with sinusoidally phase-modulated pulses. *Physical Review A*, 73(6):063409, 2006.
- [187] A. G. York and H. M. Milchberg. Broadband terahertz lasing in aligned molecules. *Optics Express*, 16(14):10557–10564, 2008.
- [188] S. Zahedpour, J. K. Wahlstrand, and H. M. Milchberg. Quantum control of molecular gas hydrodynamics. *Physical Review Letters*, 112(14):143601, 2014.
- [189] Y. B. Zel’dovich. The quasienergy of a quantum-mechanical system subjected to a periodic action. *Soviet Physics JETP*, 24(5):1006, 1967.
- [190] C. Zener. A theory of the electrical breakdown of solid dielectrics. *Proceedings of the Royal Society of London A: Mathematical, Physical and Engineering Sciences*, 145(855):523–529, 1934.

- [191] S. Zhdanovich. Control of atoms and molecules with shaped broadband pulses. *PhD dissertation*, 2012.
- [192] S. Zhdanovich, C. Bloomquist, J. Floß, I. S. Averbukh, J. W. Hepburn, and V. Milner. Quantum resonances in selective rotational excitation of molecules with a sequence of ultrashort laser pulses. *Physical Review Letters*, 109(4):043003, 2012.
- [193] S. Zhdanovich, A. A. Milner, C. Bloomquist, J. Floß, I. S. Averbukh, J. W. Hepburn, and V. Milner. Control of molecular rotation with a chiral train of ultrashort pulses. *Physical Review Letters*, 107(24):243004, 2011.
- [194] S. Zhdanovich, E. A. Shapiro, M. Shapiro, J. W. Hepburn, and V. Milner. Population transfer between two quantum states by piecewise chirping of femtosecond pulses: Theory and experiment. *Physical Review Letters*, 100(10):103004, 2008.
- [195] S. Zhou, D. Ouzounov, H. Li, I. Bazarov, B. Dunham, C. Sinclair, and F. W. Wise. Efficient temporal shaping of ultrashort pulses with birefringent crystals. *Applied Optics*, 46(35):8488–8492, 2007.
- [196] S. Zhou, F. W. Wise, and D. G. Ouzounov. Divided-pulse amplification of ultrashort pulses. *Optics Letters*, 32(7):871–873, 2007.

Appendix A

List of Publications

1. **M. Bitter** and V. Milner. Generating long sequences of high-intensity femtosecond pulses. *Applied Optics*, 55, 830, 2016 [23].
2. **M. Bitter** and V. Milner. Rotational excitation of molecules with long sequences of intense femtosecond pulses. *Physical Review A*, 93, 013420, 2016 [24].
3. **M. Bitter** and V. Milner. Experimental Observation of Dynamical Localization in Laser-Kicked Molecular Rotors. *Physical Review Letters*, 117, 144104, 2016 [22].
4. **M. Bitter** and V. Milner. Experimental demonstration of coherent control in quantum chaotic systems. *arXiv:1606.06805*, 2016 [21], *submitted*.
5. **M. Bitter** and V. Milner. Control of quantum localization and classical diffusion in laser-kicked molecular rotors. *arXiv:1610.04193*, 2016 [20], *submitted*.

During my PhD, prior to the work on the quantum kicked rotor, I studied ro-vibrational dynamics of diatomic molecules via coherent anti-Stokes Raman spectroscopy (CARS). I also investigated various pulse shaping techniques to enhance molecular vibrations in the regime of strong ultra-short pulses. The results are summarized in three publications. I decided not to include this work in this thesis.

6. **M. Bitter**, E. A. Shapiro and V. Milner. Enhancing strong-field-induced molecular vibration with femtosecond pulse shaping. *Physical Review A*, 86, 043421, 2012.
7. **M. Bitter**, E. A. Shapiro and V. Milner. Coherent rovibrational revivals in a thermal molecular ensemble. *Physical Review A*, 85, 043410, 2012.

Appendix A. List of Publications

8. **M. Bitter** and V. Milner. Coherent anti-Stokes Raman spectroscopy in the presence of strong resonant signal from background molecules. *Optics Letters*, 38, 2050, 2013.

Appendix B

Classical dynamics of the kicked rotor

B.1 Equations of motion

We derive the equations of motion for a classical kicked rotor starting from the classical version of the Hamiltonian in Eq. 2.1

$$H = \frac{I}{2}\dot{\theta}^2 + V(\theta) , \quad (\text{B.1})$$

with the potential energy term $V(\theta) = -\hbar P \cos^2(\theta) \sum_{n=0}^{N-1} \delta(t - nT)$. Newton's second law for the rotating KR is of the form $I \frac{d^2\theta}{dt^2} = -\frac{dV(\theta)}{d\theta}$, which results in

$$I \frac{d^2\theta}{dt^2} = -\hbar P \sin(2\theta) \sum_{n=0}^{N-1} \delta(t - nT) . \quad (\text{B.2})$$

Here, we used the identity $2 \sin(\theta) \cos(\theta) = \sin(2\theta)$. We define $\xi = t/T$, which effectively counts the periods, and a dimensionless angular momentum

$$\tilde{J} = J \frac{T}{I} = \left(I \frac{d\theta}{dt} \right) \frac{T}{I} = \frac{d\theta}{d\xi} . \quad (\text{B.3})$$

Substituting the scaled angular momentum into the differential equation yields

$$\frac{d\tilde{J}}{d\xi} = -P\hbar \frac{T^2}{I} \sin(2\theta) \sum_{n=0}^{N-1} \delta(t - nT) \quad (\text{B.4})$$

$$= -P\tau \sin(2\theta) \sum_{n=0}^{N-1} T\delta(t - nT) , \quad (\text{B.5})$$

where we used the dimensionless time $\tau = \hbar T/I$. The stochasticity parameter is $K = \tau P$. Another identity $T\delta(t - nT) = \delta(t/T - n)$ is needed to reach

B.1. Equations of motion

the final form, the two coupled equations of motion

$$\begin{aligned}\frac{d\theta}{d\xi} &= \tilde{J} \\ \frac{d\tilde{J}}{d\xi} &= -K \sin(2\theta) \sum_{n=0}^{N-1} \delta(\xi - n) .\end{aligned}\tag{B.6}$$

The equivalent formulation in the form of a discrete mapping gives a standard map

$$\begin{aligned}\theta_N &= \theta_{N-1} + \tilde{J}_N \\ \tilde{J}_N &= \tilde{J}_{N-1} - K \sin(2\theta_{N-1}) ,\end{aligned}\tag{B.7}$$

with the canonical variables after each kick N .

Appendix C

Spectral decomposition of the kicked rotor wave function

C.1 The kicked rotor

The procedure described here follows the Ref. [63]. We solve the Schrödinger equation for a kicked rotor after a single Gaussian pulse

$$i\hbar \frac{\partial}{\partial t} |\psi^M(t)\rangle = \left[\frac{\hat{J}^2}{2I} - \frac{P\hbar}{\sqrt{\pi}\sigma} \cos^2 \theta e^{-t^2/\sigma^2} \right] |\psi^M(t)\rangle. \quad (\text{C.1})$$

We insert the wave function of Eq. 2.16 and evaluate the left-hand side (*lhs*) and the right-hand side (*rhs*) individually.

$$\begin{aligned} (\text{lhs}) &= \sum_J \left(i\hbar \frac{\partial c_J^M}{\partial t} e^{-iE_J t/\hbar} + E_J c_J^M e^{-iE_J t/\hbar} \right) |J, M\rangle \\ (\text{rhs}) &= \sum_J \left[E_J - \frac{P\hbar}{\sqrt{\pi}\sigma} \cos^2 \theta e^{-t^2/\sigma^2} \right] c_J^M e^{-iE_J t/\hbar} |J, M\rangle \end{aligned} \quad (\text{C.2})$$

The (*lhs*) was obtained with the product rule, whereas the (*rhs*) made use of the relation $\hat{J}^2 |J, M\rangle = \hbar^2 J(J+1) |J, M\rangle$ and the definition of rotational energy E_J . Now, the kinetic energy terms on both sides cancel.

$$\sum_J \frac{\partial c_J^M}{\partial t} e^{-iE_J t/\hbar} |J, M\rangle = \frac{iP}{\sqrt{\pi}\sigma} \cos^2 \theta e^{-t^2/\sigma^2} \sum_J c_J^M e^{-iE_J t/\hbar} |J, M\rangle \quad (\text{C.3})$$

We multiply $\langle J', M' | \times$ from the left to both sides, knowing that the spherical harmonics form an orthonormal basis $\langle J', M' | J, M\rangle = \delta_{JJ'} \delta_{MM'}$ with the Kronecker delta $\delta_{JJ'} = 1$ for $J = J'$ and zero in all other cases, and $\delta_{MM'} = 1$ since $M = M'$.

$$\frac{\partial c_{J'}^{M'}}{\partial t} = \frac{iP}{\sqrt{\pi}\sigma} e^{-t^2/\sigma^2} \sum_J c_J^M e^{-i(E_J - E_{J'})t/\hbar} \langle J', M' | \cos^2 \theta | J, M\rangle \quad (\text{C.4})$$

This set of coupled differential equations can be solved numerically to get the complex amplitudes of the wave function.

C.2 The periodically kicked rotor

This section is based on Ref. [57] and the quantum mechanics book by Sakurai [147].

C.2.1 The wave function ψ^+

First, we prove that $|\psi^+\rangle = \exp(iP \cos^2 \theta) |\psi^-\rangle$ (Eq. 2.21) is indeed a solution to the Schrödinger equation of a δ -kicked rotor (Eq. 2.20) by differentiating ψ^+ with respect to time.

$$\begin{aligned}
 i\hbar \frac{\partial |\psi^+\rangle}{\partial t} &= i\hbar \left(i \cos^2 \theta \frac{\partial P}{\partial t} \exp(iP \cos^2 \theta) |\psi^-\rangle + \exp(iP \cos^2 \theta) \frac{\partial |\psi^-\rangle}{\partial t} \right) \\
 &= -\hbar \cos^2 \theta \frac{\partial P}{\partial t} |\psi^+\rangle \\
 &= -\hbar \cos^2 \theta \left(\frac{\Delta \alpha}{4\hbar} \mathcal{E}^2(t) \right) |\psi^+\rangle \\
 &= V(\theta, t) |\psi^+\rangle
 \end{aligned} \tag{C.5}$$

In the first line, we used the product rule of differentiation, whereas the second term vanishes, because the initial wave function $|\psi^-\rangle$ does not depend on time. The second line uses the definition of $|\psi^+\rangle$, the third one the derivative of the kick strength P defined in Eq. 2.11. As desired, this describes the Schrödinger equation (without the kinetic part).

C.2.2 Decomposition of ψ^+

The transformation of $|\psi^+\rangle$ into spherical harmonics is done by introducing an artificial time τ . Immediately before the kick ($\tau = 0$) only the initial state $|\psi^-\rangle = |J_0, M_0\rangle$ is populated. This translates to $c_J^M(\tau = 0) = 1$ for $|J, M\rangle = |J_0, M_0\rangle$ and zero for all other $|J, M\rangle$. Immediately after the kick ($\tau = 1$) the wave function is $|\psi^+\rangle$. We start with setting the two equation for $|\psi^+(\tau)\rangle$ equal, Eq. 2.21 and Eq. 2.22,

$$\exp(iP \cos^2 \theta \cdot \tau) |J_0, M_0\rangle = \sum_{J, M} c_J^M(\tau) |J, M\rangle. \tag{C.6}$$

Note, that the artificial time has been introduced. We differentiate Eq. C.6 with respect to τ

$$\begin{aligned} \sum_{J,M} \frac{\partial c_J^M}{\partial \tau} |J, M\rangle &= iP \cos^2 \theta \exp(iP \cos^2 \theta \cdot \tau) |J_0, M_0\rangle \\ &= iP \cos^2 \theta \sum_{J,M} c_J^M |J, M\rangle \end{aligned} \quad (\text{C.7})$$

and project both sides onto $\langle J', M' | \times$

$$\frac{\partial}{\partial t} c_{J'}^{M'}(\tau) = iP \sum_{J,M} c_J^M \langle J', M' | \cos^2 \theta | J, M \rangle . \quad (\text{C.8})$$

As in appendix C.1 we used the orthonormality of the spherical harmonics basis set.

C.2.3 The coupling matrix

In this section we study Eq. 2.23 / C.8 and look at the coupling matrix, that couples the quantum numbers before the kick (J, M) with the ones after the kick (J', M') . At first, however, we will establish some basics for the addition of angular momenta $\mathbf{J} = \mathbf{J}_1 + \mathbf{J}_2$, with the angular momentum operators \mathbf{J}_1 and \mathbf{J}_2 . The entire system has two obvious options for a basis. One basis is $|J_1 J_2; M_1 M_2\rangle$ which is simultaneously an eigenfunction for \mathbf{J}_1^2 , \mathbf{J}_2^2 , \mathbf{J}_{1z} and \mathbf{J}_{2z} . The other basis is $|J_1 J_2; JM\rangle$ which is simultaneously an eigenfunction for \mathbf{J}_1^2 , \mathbf{J}_2^2 , \mathbf{J}^2 and \mathbf{J}_z . Both bases are connected via a unitary transformation [147].

$$|J_1 J_2; JM\rangle = \sum_{M_1} \sum_{M_2} |J_1 J_2; M_1 M_2\rangle \langle J_1 J_2; M_1 M_2 | J_1 J_2; JM \rangle . \quad (\text{C.9})$$

The elements of the transformation matrix $\langle J_1 J_2; M_1 M_2 | J_1 J_2; JM \rangle$ are called the *Clebsch-Gordan coefficients* (CGC). The transformation matrix itself is a unitary matrix, which means that all CGC must be real values. Some important properties of the CGC are

$$M = M_1 + M_2 \quad (\text{C.10})$$

$$|J_1 - J_2| \leq J \leq J_1 + J_2 \quad (\text{C.11})$$

If these conditions are not fulfilled the CGC are zero. For a proof see the book by Sakurai [147].

C.2. The periodically kicked rotor

Now, we switch back to Eq. 2.23 and C.8. We transform the elements of the coupling matrix $\langle J', M' | \cos^2 \theta | J, M \rangle$ by translating $\cos^2 \theta$ into spherical harmonics $|J, M\rangle = |Y_J^M(\theta, \phi)\rangle$. To do that we use the formal definition of $Y_2^0 = \frac{1}{4}\sqrt{\frac{5}{\pi}}(3\cos^2\theta - 1)$. The new expression reads as

$$\langle J', M' | \cos^2 \theta | J, M \rangle = \frac{4}{3}\sqrt{\frac{\pi}{5}}\langle Y_{J'}^{M'} | Y_2^0 | Y_J^M \rangle + \frac{1}{3}\langle Y_{J'}^{M'} | Y_J^M \rangle \quad (\text{C.12})$$

The second term yields only diagonal matrix elements, i.e. when $J' = J$ and $M' = M$. The more interesting first term contains a product of three spherical harmonics. There exists a helpful relation between such a product and the Clebsch-Gordan coefficients (CGC) [147].

$$\int_0^{2\pi} \int_0^\pi Y_J^{M*} Y_{J_1}^{M_1} Y_{J_2}^{M_2} \sin\theta \, d\theta d\phi = \sqrt{\frac{(2J_1+1)(2J_2+1)}{4\pi(2J+1)}} \langle J_1 J_2; 00 | J_1 J_2; J0 \rangle \langle J_1 J_2; M_1 M_2 | J_1 J_2; JM \rangle \quad (\text{C.13})$$

The notation is as introduced above. The square root and the first CGC are independent of M_1 and M_2 (independent of the molecular orientation θ). The second CGC describes the angular momentum summation. Matching this relation to our product in Eq. C.12 yields

$$\langle Y_{J'}^{M'} | Y_2^0 | Y_J^M \rangle = \sqrt{\frac{5(2J+1)}{4\pi(2J'+1)}} \langle 2J; 00 | 2J; J'0 \rangle \langle 2J; 0M | 2J; J'M' \rangle \quad (\text{C.14})$$

The values of CGC are well known and can be looked up or calculated. One important revelation from this angular momentum algebra are the selection rules that apply to our system of a kicked rotor. The CGC properties (Eq. C.10 and C.11) for our system simplify to

$$M' = M \quad (\text{C.15})$$

$$|J-2| \leq J' \leq J+2 \quad (\text{C.16})$$

It also follows that only J quantum numbers of the same parity are coupled. We summarize: The magnetic quantum number has to be preserved $\Delta M = M' - M = 0$, and the angular momenta are only coupled between states of the same parity that satisfy the condition $\Delta J = J' - J = 0, \pm 2$.

Appendix D

Fourier transform of shaped pulses

Ultra-short pulses contain a broad frequency spectrum; the shorter the pulses the wider the spectrum. Depending on the circumstances, it can be beneficial or more intuitive to solve a problem or to understand some physical concept by looking at the pulses either in the spectral domain or alternatively in the time domain. In general, the mathematical transformation that is applied to switch from one domain to the other is called the *Fourier transform*. It is equally valid for a transformation in both directions. In our case, we will look at the Fourier transform of a function $F(\omega)$ in the frequency domain into the time domain $f(t)$, and vice versa

$$F(\omega) = \int_{-\infty}^{+\infty} f(t) \exp(-i\omega t) dt \quad (\text{D.1})$$

$$f(t) = \frac{1}{2\pi} \int_{-\infty}^{+\infty} F(\omega) \exp(i\omega t) d\omega. \quad (\text{D.2})$$

We also want to introduce the *Fourier transform shift theorem*

$$F\{f(t - t_k)\} = \exp(-i\omega t_k) \cdot F\{f(t)\}, \quad (\text{D.3})$$

which is essential in the transformation of pulse sequences with individual pulses at the timings t_k (App. D.3).

D.1 Fourier transform of a TL pulse

We start with the spectrum of a Gaussian pulse (Eq. 3.1) and do a Fourier transform (Eq. D.2) to obtain the electric field in the time domain

$$\begin{aligned} \mathcal{E}(t) &\stackrel{\text{D.2}}{=} \frac{1}{2\pi} \int_{-\infty}^{+\infty} \mathcal{E}(\omega) \exp(i\omega t) d\omega \\ &\stackrel{\text{3.1}}{=} \frac{1}{2\pi} A_0 \cdot \int_{-\infty}^{+\infty} \exp\left(-\frac{(\omega - \omega_0)^2}{2\Gamma^2} + i\omega t\right) d\omega. \end{aligned} \quad (\text{D.4})$$

D.2. Fourier transform of a chirped pulse

Using the substitution $\beta = \frac{\omega - \omega_0}{\sqrt{2}\Gamma} - i\frac{\Gamma t}{\sqrt{2}}$ we can rewrite the exponential

$$\frac{(\omega - \omega_0)^2}{2\Gamma^2} - i(\omega - \omega_0)t - i\omega_0 t = \beta^2 + \frac{\Gamma^2 t^2}{2} - i\omega_0 t. \quad (\text{D.5})$$

Using the derivative $d\beta/d\omega = 1/\sqrt{2}\Gamma$ the expression of the electric field can be transformed to

$$\begin{aligned} \mathcal{E}(t) &= \frac{1}{2\pi} A_0 \cdot \int_{-\infty}^{+\infty} \exp\left(-\beta^2 - \frac{\Gamma^2 t^2}{2} + i\omega_0 t\right) \cdot \sqrt{2}\Gamma d\beta \\ &= \frac{\Gamma}{\sqrt{2}\pi} A_0 \cdot \exp\left(-\frac{\Gamma^2 t^2}{2} + i\omega_0 t\right) \cdot \int_{-\infty}^{+\infty} \exp(-\beta^2) d\beta. \end{aligned} \quad (\text{D.6})$$

The solution of the integral is $\sqrt{\pi}$. This yields the analytic expression of the electric field of a TL Gaussian pulse in the time domain

$$\mathcal{E}(t) = \mathcal{E}_0 \cdot \exp\left(-\frac{t^2}{2\tau^2}\right) \cdot \exp(i\omega_0 t) \quad (\text{D.7})$$

with the amplitude $\mathcal{E}_0 = A_0\Gamma/\sqrt{2\pi}$ and the duration $\tau = 1/\Gamma$.

D.2 Fourier transform of a chirped pulse

Again, we start with the electric field in the spectral domain (Eq. 3.5) and obtain the time domain via the Fourier transform (Eq. D.2)

$$\begin{aligned} \mathcal{E}(t) &\stackrel{\text{D.2}}{=} \frac{1}{2\pi} \int_{-\infty}^{+\infty} \mathcal{E}(\omega) \exp(i\omega t) d\omega \\ &\stackrel{3.5}{=} \frac{1}{2\pi} A_0 \cdot \int_{-\infty}^{+\infty} \exp\left(-\frac{(\omega - \omega_0)^2}{2\Gamma^2} + i\alpha' \frac{(\omega - \omega_0)^2}{2} + i\omega t\right) d\omega \quad (\text{D.8}) \\ &= \frac{1}{2\pi} A_0 \cdot \int_{-\infty}^{+\infty} \exp\left(-\frac{(\omega - \omega_0)^2}{2\Gamma^2} (1 - i\alpha'\Gamma^2) + i\omega t\right) d\omega. \end{aligned}$$

We define the constant $x^2 = (1 - i\alpha'\Gamma^2)$ and do a similar substitution as before $\beta = x\frac{\omega - \omega_0}{\sqrt{2}\Gamma} - i\frac{\Gamma t}{x\sqrt{2}}$ such that the exponential can be rewritten as

$$x^2 \frac{(\omega - \omega_0)^2}{2\Gamma^2} - i(\omega - \omega_0)t - i\omega_0 t = \beta^2 + \frac{\Gamma^2 t^2}{2x^2} - i\omega_0 t. \quad (\text{D.9})$$

D.3. Fourier transform of a pulse train

Making use of the derivative $d\beta/d\omega = x/\sqrt{2}\Gamma$, the altered expression of the electric field becomes

$$\begin{aligned}\mathcal{E}(t) &= \frac{1}{2\pi} A_0 \cdot \int_{-\infty}^{+\infty} \exp\left(-\beta^2 - \frac{\Gamma^2 t^2}{2x^2} + i\omega_0 t\right) \cdot \frac{\sqrt{2}\Gamma}{x} d\beta \\ &= \frac{\Gamma}{\sqrt{2\pi}x} A_0 \cdot \exp\left(-\frac{\Gamma^2 t^2}{2x^2}\right) \cdot \exp(i\omega_0 t) \cdot \int_{-\infty}^{+\infty} \exp(-\beta^2) d\beta.\end{aligned}\quad (\text{D.10})$$

The solution of the integral is $\sqrt{\pi}$. We still need to re-substitute x . The first exponential in eq. D.10 turns into

$$\begin{aligned}\frac{\Gamma^2 t^2}{2x^2} &= \frac{\Gamma^2 t^2}{2(1 - i\alpha'\Gamma^2)(1 + i\alpha'\Gamma^2)} \\ &= \frac{\Gamma^2 t^2}{2(1 + \alpha'^2\Gamma^4)} + i\frac{\alpha'\Gamma^4}{2(1 + \alpha'^2\Gamma^4)} t^2 \\ &= \frac{t^2}{2\tau^2} + i\frac{\alpha}{2} t^2\end{aligned}\quad (\text{D.11})$$

where we defined the duration τ and the temporal chirp α

$$\tau^2 = \frac{1}{\Gamma^2}(1 + \alpha'^2\Gamma^4) \quad (\text{D.12})$$

$$\alpha = \alpha' \frac{\Gamma^4}{1 + \alpha'^2\Gamma^4} = \alpha' \frac{\Gamma^2}{\tau^2}. \quad (\text{D.13})$$

In the limit of large chirps, we can approximate $\alpha \approx 1/\alpha'$. The final version of eq. D.10 yields the electric field of a linearly chirped Gaussian pulse in the time domain

$$\mathcal{E}(t) = \mathcal{E}_0 \cdot \exp\left(-\frac{t^2}{2\tau^2}\right) \exp\left(i\omega_0 t - i\frac{\alpha}{2} t^2\right) \quad (\text{D.14})$$

with the complex amplitude $\mathcal{E}_0 = A_0\Gamma/(\sqrt{2\pi} \cdot \sqrt{1 - i\alpha'\Gamma^2})$.

D.3 Fourier transform of a pulse train

We have built the desired pulse train in the time domain with the electric field given in equation 3.8. Now, we will perform a Fourier transform (Eq. D.1) to get the electric field in the spectral domain. Once we have the knowledge of amplitude and phase in the frequency representation we are

D.3. Fourier transform of a pulse train

able to send the corresponding masks to our SLM and create this pulse train with the shaper.

$$\begin{aligned}
\mathcal{E}(\omega) &\stackrel{\text{D.1}}{=} \int_{-\infty}^{+\infty} \mathcal{E}(t) \exp(-i\omega t) dt \\
&\stackrel{\text{3.8}}{=} \sum_k \mathcal{E}_0 \int_{-\infty}^{+\infty} e^{-\frac{(t-t_k)^2}{2\tau^2}} e^{i\omega_0 t} e^{i\frac{\beta}{2}k^2} \exp(-i\omega t) dt \\
&= \sum_k \mathcal{E}_0 \underbrace{\int_{-\infty}^{+\infty} e^{-\frac{(t-t_k)^2}{2\tau^2}} e^{i\omega_0(t-t_k)} e^{-i\omega t} dt}_{F\{f(t-t_k)\}} \cdot e^{i\omega_0 t_k} e^{i\frac{\beta}{2}k^2}
\end{aligned} \tag{D.15}$$

We use the FT shift theorem (Eq. D.3) with the function $f(t - t_k) = \exp\left(-\frac{(t-t_k)^2}{2\tau^2} + i\omega_0(t - t_k)\right)$

$$F\{f(t - t_k)\} = \exp(-i\omega t_k) \int_{-\infty}^{+\infty} e^{-\frac{t^2}{2\tau^2}} e^{i\omega_0 t} e^{-i\omega t} dt. \tag{D.16}$$

Now, we eliminated all k -dependences inside the integral

$$\mathcal{E}(\omega) = \sum_k e^{-i\omega t_k} \left(\mathcal{E}_0 \int_{-\infty}^{+\infty} e^{-\frac{t^2}{2\tau^2}} e^{i\omega_0 t} e^{-i\omega t} dt \right) e^{i\omega_0 t_k} e^{i\frac{\beta}{2}k^2}. \tag{D.17}$$

We pull everything in brackets in front of the sum and solve the integral. Under closer inspection it can be seen that the integral is merely the Fourier transform (Eq. D.1) of a TL pulse (Eq. 3.2 or Eq. D.7)

$$\int_{-\infty}^{+\infty} \mathcal{E}_0 e^{-\frac{t^2}{2\tau^2}} e^{i\omega_0 t} e^{-i\omega t} dt \stackrel{\text{3.2}}{=} \int_{-\infty}^{+\infty} \mathcal{E}(t) e^{-i\omega t} dt \stackrel{\text{D.1}}{=} \mathcal{E}(\omega) \tag{D.18}$$

whose expression we gave earlier in Eq. 3.1. Thus, the analytic expression for the electric field of a periodic and flat pulse train in the spectral domain is given as

$$\mathcal{E}(\omega) = A_0 \exp\left(-\frac{(\omega - \omega_0)^2}{2\Gamma^2}\right) \cdot \sum_k \exp\left(-i(\omega - \omega_0)t_k + i\frac{\beta}{2}k^2\right) \tag{D.19}$$

with the amplitude $A_0 = \mathcal{E}_0\sqrt{2\pi}/\Gamma$. The term in front of the sum gives the spectrum of the unshaped, TL pulse as in Eq. 3.1. Once we evaluate the sum, it will tell us how we have to shape the amplitude and phase in order to obtain the pulse train.

D.4 Convolution theorem

The convolution theorem states that the Fourier transform of a convolution is equal to the point-wise product of Fourier transforms. We denote \mathcal{F} as the Fourier transform operator. Let us use two functions $f(t)$ and $g(t)$ as a function of time t . Their respective Fourier transforms are $F(\omega) = \mathcal{F}\{f(t)\}$ and $G(\omega) = \mathcal{F}\{g(t)\}$ as a function of frequency ω , defined in Eq. D.1.

$$\mathcal{F}\{f(t) \otimes g(t)\} = F(\omega) \cdot G(\omega) \quad (\text{D.20})$$

$$\mathcal{F}\{F(\omega) \otimes G(\omega)\} = f(t) \cdot g(t) \quad (\text{D.21})$$

The symbol \otimes denotes *convolution*.

Appendix E

Semi-classical model of rotational Bloch oscillations

We derive a semi-classical model to describe the phenomenon of Bloch oscillations in rotating molecules. We start with a stroboscopic description of the rotor after each kick n . The wave function is a linear combination of free-rotor eigenstates

$$|\Psi^{(n)}\rangle = \sum_J c_J^{(n)} |J\rangle, \quad (\text{E.1})$$

where we neglect the magnetic quantum number M since it does not change in the interaction. The wave function right after a δ -kick is governed by

$$|\Psi^{(n+1)}\rangle = e^{iP \cos^2 \theta} e^{-iE_J T/\hbar} |\Psi^{(n)}\rangle. \quad (\text{E.2})$$

Here, the one-cycle operator contains the kicking operator, see Sec. C.2.1, and a free-evolution term. Insert Eq. E.1 as a function of J' into Eq. E.2 and multiply $\langle J|$ from the left side to get an expression for the amplitude coefficients

$$c_J^{(n+1)} = \sum_{J'} c_{J'}^{(n)} \langle J| e^{iP \cos^2 \theta} |J'\rangle e^{-iE_{J'} T/\hbar} \quad (\text{E.3})$$

The following derivation from Ref. [62] assumes pulses of $P \ll 1$. However, the same result is obtained in the “ ϵ -classics” approach [184, 185], which is more involved but does not rely on the weak pulse approximation. A Taylor expansion yields

$$c_J^{(n+1)} = \sum_{J'} c_{J'}^{(n)} \langle J| 1 + iP \cos^2 \theta |J'\rangle e^{-iE_{J'} T/\hbar}. \quad (\text{E.4})$$

Further, we investigate two distinct scenarios.

E.1 Non-rigid rotor on quantum resonance

Taking into account centrifugal distortion the free evolution term with a period $T = T_{\text{rev}} = (2cB)^{-1}$ breaks down into

$$e^{-iE_{J'}T_{\text{rev}}/\hbar} = e^{-i\pi J'(J'+1)} e^{i\pi \frac{D}{B} J'^2(J'+1)^2} \approx 1 + i\pi \frac{D}{B} J'^2(J'+1)^2 \quad (\text{E.5})$$

where the first exponential is equal to unity and the second one is expanded in another Taylor series around $\frac{D}{B} \ll 1$. We insert the expression into Eq. E.4 and neglect the $(P\frac{D}{B})$ -term

$$c_J^{(n+1)} = c_J^{(n)} + i\pi \frac{D}{B} J^2(J+1)^2 c_J^{(n)} + iP \sum_{J'} c_{J'}^{(n)} \langle J | \cos^2 \theta | J' \rangle. \quad (\text{E.6})$$

The \cos^2 term is approximated as [62]

$$\langle J | \cos^2 \theta | J' \rangle = \begin{cases} 1/2 & \text{for } J' = J \\ 1/4 & \text{for } J' = J \pm 2 \\ 0 & \text{else} \end{cases} \quad (\text{E.7})$$

and we obtain

$$-i \left[c_J^{(n+1)} - c_J^{(n)} \right] = \left[\pi \frac{D}{B} J^2(J+1)^2 + \frac{P}{2} \right] c_J^{(n)} + \frac{P}{4} \left[c_{J+2}^{(n)} + c_{J-2}^{(n)} \right]. \quad (\text{E.8})$$

Finally, since each kick is very weak and hardly changes the angular momentum distribution, we replace the difference term $c_J^{(n+1)} - c_J^{(n)}$ by a differential $dc_J(n)/dn$. The result is a Schrödinger equation for the rotational tight-binding model with a continuous dimensionless time n

$$i \frac{dc_J(n)}{dn} = \left[-\pi \frac{D}{B} J^2(J+1)^2 - \frac{P}{2} \right] c_J^{(n)} - \frac{P}{4} \left[c_{J+2}^{(n)} + c_{J-2}^{(n)} \right]. \quad (\text{E.9})$$

E.2 Rigid rotor detuned from quantum resonance

If we neglect the centrifugal distortion but consider a detuning δ from the resonance $T = (1 + \delta)T_{\text{rev}}$ the free evolution term has the form

$$e^{-iE_{J'}(1+\delta)T_{\text{rev}}/\hbar} = e^{-i\pi J'(J'+1)} e^{-i\pi\delta J'(J'+1)} \approx 1 - i\pi\delta J'(J'+1). \quad (\text{E.10})$$

All the other steps are identical to Sec. E.1, and the final differential equation will be

$$i \frac{dc_J(n)}{dn} = [\pi\delta J(J+1)] c_J^{(n)} - \frac{P}{4} \left[c_{J+2}^{(n)} + c_{J-2}^{(n)} \right]. \quad (\text{E.11})$$